Ph.D. Dissertation

Design of Multi-feed UWB Antennas using the Theory of Characteristic Modes

Universitat Politècnica de València

Departamento de Comunicaciones

Author

Carlos Ramiro Peñafiel Ojeda

Advisors

Prof. Dr. Miguel Ferrando Bataller
Prof. Dra. Marta Cabedo Fabrès

Valencia, May 2021

To my Lord and my Family

Agradecimientos

Inocente por mi parte haber dejado esto para el final, me resulta casi imposible poder empezar... Llegar a este punto luego de haber recorrido este camino durante los últimos años, realmente ha sido una de las mejores cosas que he hecho en mi vida. Se me viene a la mente el primer día en Valencia, un poco perdido por llegar a un lugar nuevo, pero con la convicción a tope, a medida que ha ido pasando el tiempo he llegado a querer a esta hermosa ciudad como que fuese mía, me ha regalado casi todo, y ahora que estoy lejos de ella la extraño mucho. Seguro la visitaré con mucha frecuencia.

Nunca olvidaré el primer día que llegué a la UPV, no logré encontrar el despacho de mi tutor (hasta ese momento no tenía ni idea que esa reunión cambiaría mi vida), con un poco de retraso, el jetlag y preguntado de oficina en oficina llegue casi que corriendo a la cita. Si, de esta forma conocí a una persona que considero como un Papá, Gracias Profe Miguel como le digo, ha sabido ser mas que un tutor, me ha guiado y con mucha paciencia me ha enseñado a caminar en este mundo de las Antenas, toda la vida le viviré agradecido y trataré con todas mis fuerzas de estar siempre a la altura. No puedo dejar a un lado una anécdota que marcó mucho en mi vida, en el 2017 vino al mundo Mikaela, y luego de unos días al intentar salir de la Clínica, me dieron la noticia que debía pagar una fuerte cantidad, argumentado que el seguro lamentablemente no podría cubrir el gasto del parto (nos falto 8 días para cumplir el tiempo). Sin tener dinero y con una desesperación muy grande, le llame a Miguel, sin poner escusas y sin dudarlo en ningún momento, me ofreció su tarjeta para cubrir la cuenta, obviamente luego de unos días le devolví (caso contrario esto no sería una realidad).

Además, quiero agradecer a mi Tutora Marta, por darme siempre un espacio, he aprendido mucho de usted, gracias por sus consejos y sus acertados comentarios, muchas veces haciéndome poner los pies sobre la tierra. Gracias también a Eva, una mujer que me ha enseñado que con constancia, sacrifico y perseverancia se logra cumplir los sueños. Gracias a las dos por permitirme coincidir en este tiempo.

Este trabajo no podría haber llegado a un buen fin sin una buena base y el aporte de los amigos. Muchas gracias Daniel Sánchez, Sheldom como te he bautizado (espero no te enojes), nunca me negaste tu ayuda y siempre estuviste dispuesto, eres un crack Dani. Gracias a la familia del laboratorio: Miguel Jr., Nora, Daniel, Jaime, Marc, Zakaria, Yousra, Hamza, María, Toni, Tomás, Toni Vila, Bernat y Felipe. A los de Argentina: Juan Pablo, Alberto y Guillermo. Todos han sido un gran aporte para cumplir con este objetivo. A mi amigo Aníbal, gracias panela por los días de trabajo, piscina, gimnasio, y sobre todo por los gratos momentos compartidos en casa.

También parte de este trabajo ha sido posible gracias al apoyo de los amigos de Queen Mary University de Londres. Gracias Profesor Yang, realmente un lujo poder trabajar en tu equipo. A Henry, Darryl, Isidoro, Joe, Benjamin, Andy, Robert y en especial al gran Max Muñoz, gracias Max por tu amistad y las largas horas de conversación en el Laborario, me has enseñado que se puede llegar tan lejos con trabajo.

Sin la fortaleza espiritual no se llegaría a ningún lado, muchas gracias a los hermanos de la séptima comunidad de la Parroquia Preciosisima Sangre, habéis sido mi fortaleza y mi compañía en los momentos mas difíciles, Dios les Bendiga infinitamente.

Gracias a Gabriel, Daniel Maldonado y su familia por acogerme. A mi familia en New York, en especial a mi tío Jesús y su familia, gracias por haberme brindado un espacio y no permitir que jamás me sienta solo, gracias por todo Brother, nunca olvidaré esos 2 meses maravillosos, seguro habrán muchos más. A la familia en Londres, me habéis hecho sentir como en casa, siempre cuenten conmigo.

Quiero hacer un agradecimiento muy especial a mi Esposa, una mujer maravillosa. Gracias mi Amor por haber sido mi sostén y mi apoyo en este proceso, por tu paciencia, fortaleza y esfuerzo al haberte hecho cargo de nuestro hogar sobre todo en esta crisis sanitaria que atraviesa el mundo. Gracias morenita por darme el lujo de ser Papá y de tener unas hermosas princesas. Ten por seguro que siempre estaré a tu lado, seguiremos siendo ese gran equipo para seguir cumpliendo nuestros sueños juntos. A Mikaela y Analía,

todo lo que he hecho ha sido por ustedes, perdónenme hijas mías por haber sacrificado su tiempo, quizá cuando sean grandes podrán entenderme. Lo que sí, ni un solo día he dejado de amarlas, cada noche que pase en la soledad de mi escritorio pensaba en ustedes y me motivaba cada vez más. Gracias mis hijas por se mi alegría, mi motor y mi inspiración. Papá siempre estará con ustedes y les amará para toda la vida.

Finalmente, un agradecimiento a mi Papi Lucho y mi Mami Alicia, gracias por no haberme nunca dejado solo, en cualquier parte de mundo en donde estado, siempre han ido a mi encuentro. Por ustedes he llegado a este punto, gracias por su sacrificio, constancia y apoyo, nunca les abandonaré. A Adriana, Pablo y Amanda, gracias hermanitos por aguantar todo, nunca darme la espalda y estar en todo momento. A la Mami Maya, por siempre tener tiempo para mi, ha sido una gran ayuda en este proceso, siempre cuente conmigo. A Irvin, Gaby, Joaquín, Mía y Alex, gracias por su soporte y oraciones. Dios le conceda mucho.

A mi querida Universidad Nacional de Chimborazo, por haber confiado en mí al otorgarme una beca de estudios.

Bueno, en fin, a toda la familia y amigos que han sido parte de este proceso. Gracias.

Abstract

The Theory of Characteristic Modes (TCM), developed by R.F. Harrington in the mid 1960's, has become, since the beginning of the 21^{st} century, a fundamental tool for systematic antenna design, thanks to the physical vision it provides of radiation phenomena. Currently, many research groups worldwide have adopted this theory as part of their design methodology. However, the theory of characteristic modes has been used mainly for the analysis of planar structures, and there are few examples of application of the theory to 3D structures, given the difficulty involved in its analysis.

This thesis aims to design multi-fed antennas with high bandwidth using TCM. The main novelty contribution is providing the application of characteristic modes theory to the analysis of 3D structures and the use of multi-feed to selectively excite specific radiation modes. Initially, an analysis of plane structures that interact with each other is presented, and a combination of ports is used to force the excitation of certain modes with good radiant behavior. Furthermore, it is shown that the resonances of an antenna are not only caused by a resonance mode, but also appear as a result of the combination of magnetic and electrical modes.

The thesis proposes antenna designs with very low profile, obtained from the progressive folding of the previously studied planar structures. With the folding techniques, compact and low-profile antennas are designed, easily integrated, with very good radiation characteristics and a simple form of excitation.

A systematic study of 3-dimensional canonical structures, such as rectangular and circular waveguides, is carried out. First, the waveguides and equivalent cavities with a classical approach are analyzed, obtaining the transverse electric TE and transverse magnetic TM field modes. Then, the same waveguides and cavities are analyzed applying the theory of characteristic modes, unifying and comparing for the first time the two types of analysis. The conclusions drawn from the analysis of the rectangular and circular waveguides have been applied to design two types of antennas, which provide

good bandwidth and optimal radiation characteristics for 5G applications.

The thesis includes a chapter in which different antenna prototypes are proposed, designed from the application of the characteristic modes theory. The conclusions obtained in each chapters of the thesis are taken advantage of and applied to specific designs, showing that using TCM, it is possible to design antennas that have good radiation characteristics and that can be easily integrated into devices that operate with new technologies. like 5G or IoT.

Resumen

La Teoría de Modos Característicos (TCM), desarrollada por R.F. Harrington a mediados de los años 60, se ha convertido desde los inicios del siglo XXI, en una herramienta fundamental para el diseño sistemático de antenas, gracias a la visión física que aporta de los fenómenos de radiación. Actualmente, numerosos grupos de investigación a nivel mundial han adoptado esta teoría dentro de su metodología de diseño. No obstante, la teoría de modos característicos ha sido utilizada mayormente para el análisis de estructuras planas, existiendo pocos ejemplos de aplicación de la teoría a estructuras 3D, dada la dificultad que implica su análisis.

Esta tesis tiene como objetivo diseñar antenas multi-alimentadas con un gran ancho de banda usando la TMC. La principal novedad que aporta, es la aplicación de la teoría de modos característicos al análisis de estructuras 3D y el empleo de multi alimentación para excitar de forma selectiva modos concretos de radiación. Inicialmente se presenta un análisis de estructuras planas que interactúan entre sí, y se utiliza una combinación de puertos para forzar la excitación de ciertos modos con buen comportamiento radiante. Además, se demuestra que las resonancias de una antena, no solamente son causadas por un modo en resonancia, sino que también aparecen como resultado de la combinación de modos magnéticos y eléctricos.

En la tesis se proponen diseños de antenas con muy bajo perfil, obtenidas a partir del plegado progresivo de las estructuras planas previamente estudiadas. Con las técnicas de plegado se consiguen antenas compactas y de bajo perfil, fácilmente integrables, que presentan muy buenas características de radiación y una forma de excitación sencilla.

Se realiza un estudio sistemático de estructuras canónicas en 3 dimensiones, como las guías de onda rectangular y circular. En primer lugar, las guías de onda y cavidades equivalentes se analizan con un enfoque clásico, obteniendo los modos de campo transversal eléctrico TE y transversal magnético TM. A continuación, se analizan las mismas guías y cavidades aplicando la teoría de modos característicos, unificando y comparando por primera vez los

dos tipos de analisis. Las conclusiones extraídas del análisis de las guías de onda rectangular y circular, se han aplicado para diseñar dos tipos de antenas, que proporcionan buen ancho de banda y características de radiación óptimas para aplicaciones 5G.

La tesis incluye un capítulo en el que se proponen distintos prototipos de antenas, diseñados a partir de la aplicación de la teoría de modos característicos. Se aprovechan las conclusiones obtenidas en cada uno de los capítulos de la tesis y se aplican a diseños específicos, demostrando que empleando la TCM, es posible diseñar antenas que tengan buenas características de radiación y que pueden integrarse fácilmente en dispositivos que operen con nuevas tecnologías, como 5G o IoT.

Resum

La Teoria de Modes Característics (TCM), desenvolupada per R.F. Harrington a mitjans dels anys 60, s'ha convertit des dels inicis de segle XXI, en una eina fonamental per al disseny sistemàtic d'antenes, gràcies a la visió física que aporta dels fenòmens de radiació. Actualment, nombrosos grups d'investigació a nivell mundial han adoptat aquesta teoria dins de la seva metodologia de disseny. No obstant això, la teoria de modes característics ha estat utilitzada majorment per l'anàlisi d'estructures planes, i hi ha pocs exemples d'aplicació de la teoria a estructures 3D, donada la dificultat que implica el su anàlisi.

Aquesta tesi té com a objectiu dissenyar antenes multi-alimentades amb un gran ample de banda usant la TMC. La principal novetat que aporta és l'aplicació de la teoria de modes característics a l'anàlisi d'estructures 3D i l'us de multi alimentació per excitar de forma selectiva modes concrets de radiació. Inicialment es presenta un anàlisi d'estructures planes que interactuen entre si, i s'utilitza una combinació de ports per forar l'excitació de determinats modes amb bon comportament radiant. A més, es demostra que les ressonàncies d'una antena, no solament són causades per un mode en ressonància, sinó que també apareixen com a resultat de la combinació de modes magnètics i elèctrics.

A la tesi es proposen dissenys d'antenes amb molt baix perfil, obtingudes a partir del plegat progressiu de les estructures planes prèviament estudiades. Amb les tècniques de plegat s'aconsegueixen antenes compactes i de baix perfil, fàcilment integrables, que presenten molt bones característiques de radiació i una forma d'excitació senzilla.

Es realitza un estudi sistemàtic d'estructures canòniques en 3 dimensions, com les guies d'ona rectangular i circular. En primer lloc, les guies d'ona i cavitats equivalents s'analitzen amb un enfocament clàssic, obtenint els modes de camp transversal elèctric ET i transversal magnètic TM. A continuació, s'analitzen les mateixes guies i cavitats aplicant la teoria de modes característics, unificant i comparant per primera vegada els dos tipus d'anàlisi. Les conclusions extretes de l'anàlisi de les guies d'ona rectangular i circular,

s'han aplicat per dissenyar dos tipus d'antenes, que proporcionen bon ample de banda i característiques de radiació òptimes per a aplicacions 5G.

La tesi inclou un capítol en el qual es proposen diferents prototips d'antenes, dissenyats a partir de l'aplicació de la teoria de modes característics. S'aprofiten les conclusions obtingudes en cada un dels capítols de la tesi i s'apliquen a dissenys específics, demostrant que emprant la TCM, és possible dissenyar antenes que tinguen bones característiques de radiació i que poden integrar-se fàcilment en dispositius que operen amb noves tecnologies, com 5G o IoT.

Table of contents

List of Figures

List of Tables

Chapter 1

Introduction

"*Unless someone like you cares a whole awful lot, nothing is going to get better. It's not*" "

— Dr. Seuss.

1.1 Introduction

From the beginnings of the 1G technology launched in the 70s to the 4G technology it has been seen that from one generation to the next there has been a substantial evolution, but following the same line of speed increase [3, 4]. However, the fifth generation wants to completely revolutionize the system and not simply as an evolution of the previous technology. The main objective of 5G is not only to increase the speed of the service, but to generate a framework that encompasses the integration of many networks and technologies with different characteristics, also including the user to be part of the system through their interaction with a better quality of experience [5].

In 2002, the Federal Communication Commission (FCC) approved a ruling that UWB (Ultrawideband) could be used for data communications as well as for radar and safety applications, the available frequencies range are between 3.1 GHz to 10.6 GHz with a maximum power spectral density of -41.25 dBm/MHz and a maximum transmit power of -2.5 dBm [6–8]. Since that time, a number of antennas capable of working under UWB conditions for various applications have been developed by researchers in the worldwide.

Curiously, in 2002, the Universitat Politècnica de Valencia, through the Grupo de Radiación Electromagnética, began to introduce in its research field a theory that had been abandoned since it was presented in 1968. It went from being a theory in disuse to become a very important tool for antenna design, due to the important information it provides. Nowadays, there is a high interest in using this theory for the design of antennas that can be easily integrated to mobile devices, base stations, biomedical applications, satellite communications, etc.

Therefore, during the development of this thesis, some options will be proposed that can be integrated in the above mentioned applications. It will start from an analysis of planar structures of arbitrary shape, to describe the behavior of 3-dimensional structures derived from canonical shapes.

1.2 State of art

The study of the Theory of Characteristic Modes was carried out for the first time by Garbacz in 1968 [9], who showed that Characteristic Modes can be defined on conductive bodies in arbitrary structures by diagonalizing the scattering matrix. However, obtaining these modes was not an easy task due to their complexity [10]. Later it was improved by Harrington and Mautz [11] where they came to obtain the same modes through the diagonalization of the generalized impedance matrix of the bodies [11, 12].

Harrington in his future works succeeded by introducing the concept of the Method of Moments for solving an electromagnetism problem. This method facilitates the solution of the eigenvalue problem, which at the time of its resolution provides a set of modes of real currents, called Characteristic Modes [13]. Studies have not only been carried out for conductive bodies but also for magnetic and dielectric materials [14], and even for materials with losses [14,15].

This theory has long been out of use. However, in 2002 the Electromagnetic Radiation Group (GRE) of the Universitat Politècnica de València again took up the subject, carrying out studies on the characteristic modes of an elliptical loop and the characteristics of patch-type antennas [16, 17], developing an analysis method for designs in some applications of antennas for mobile telephony, MIMO and UWB [16–24]. Thus demonstrating that the Theory of Characteristic Modes is a very suitable method to carry out systematic designs using different types of antennas [25], this scientific contribution, since its publication has become the most cited, becoming the reference document in terms of Modes Characteristic in recent years.

Some simple structures have been studied and analyzed in depth [26–32], thus opening a wide field of study of great interest. The characteristic modes are of great importance because they help us to know the characteristic current distribution of a structure [25], offering information such as the resonance frequency of the antenna, impedance matching level, radiation pattern, etc. In addition to analyzing the characteristic modes of a simple structure, it is necessary to consider when the structures are fed. One of the existing methods for analyzing a structure is the method of characteristic basic functions [33].

Due to interest [34], the companies that develop electromagnetic simulators such as: FEKO, CST Suite Studio and HFSS, have incorporated the analysis of characteristic modes in their products. This analysis tool has meant a very notable increase in the use of commercial software, that is why these simulators will be the tool for the development of this work. In addition, the use of the own code to analyze the characteristic modes of structures with infinite dielectrics that the GRE of the UPV has developed has be considered.

However, is necessary to highlight that simulators present numerical calculation problems when the geometry is complex or has reactive elements [35]. At the time of tracking the eigenvalue, an inevitable effect called Crossing Avoidance is generated. [36], the current distribution in surface of specific modes changes dramatically and appears asymmetrically at isolated frequency points [37]. This effect is closely related to equal eigenvalues at certain frequency points [38]. Some algorithms have been developed to compensate for this effect [39, 40].

Due to the emergence of new technologies and the development of future 5th Generation (5G) mobile services. A large number of applications have been developed in recent years in order to meet the needs of the system. The interconnection of mobile devices with ultra high data rates, very low latency, more capacity and good quality of service [41, 42], have forced the scientific community to explore new alternatives to antennas design. Also, the challenge of integrating antennas in structures and with a reduced size for the digital interconnection of everyday objects with the Internet (Internet of Things IoT) [41, 42].

Thus, UWB antennas have become attractive for 5G systems [43, 44], however, these are difficult to achieve. In general, patch antennas with microstrip technology are the most commonly used [45], but they are not the most appropriate for multi-service systems due to their limited features [46]. Monopole antennas [47–51] have been widely studied for many years since they provide optimum performance, offering good bandwidth with an omnidirectional radi-

ation pattern. Some antenna designs have been experimented with in order to further improve its characteristics as a single element, an example is the use of two feed ports [52, 53], use of cavities [54, 55], vivaldi antennas [56–58] or even fractal antennas [59, 60].

Currently, using the theory of characteristic modes, a lot of types of antennas have been designed. Starting from the simplest antennas such as dipoles [61–63] these dipoles can generate good bandwidth and radiation patterns in specific directions. For example, inserting a pair of orthogonal stubs at 0.1 λ from the ends of a dipole, it is possible to force the excitation of the J_3 and J_5 modes. Due to the antenna configuration, the resonance frequencies J_3 and J_5 are very close [62], generating good bandwidth. In order to generate the radiation pattern in the endfire direction, 2 similar dipoles with a complementary fold have been used, but only one of them is being excited [63].

After dipoles, antennas that begin from a planar structure have been the most developed [64–67], in some cases using external elements to excite them [64, 66]. However, a common form of excitation is to embed slots on a planar finite ground plane [68, 69]. Its principle of operation is based basically on the interaction of magnetic modes of the slot and the electrical modes of a ground plane. If the slot shapes are modified (H or I shape) and using multiple power points, a reconfigurable polarization can be generated [70], being able to improve its bandwidth by systematically increasing the dimensions of the slots [71]. In addition, structures have been designed that are capable of Radar Cross Section reduction [72].

To generate multiple beams, and achieve that the planar structure can be used to work in MIMO technology, multiple feeding ports must be inserted. Therefore, based on the use of symmetry of the structures to insert multiple feeds with an orthogonal port, the location points for the feeds will be obtained [73–75]. Inductive excitation slots have been used to excite the planar structure. Consequently, it will be possible to achieve multimode antennas that are capable of working at high speeds. Obviously, there are other forms to design MIMO antennas using the Theory of characteristics modes information. According the characteristics currents in the surface of a rectangular planar structure, a multiples capacitive elements can be inserted in the current nulls [76].

In order to reduce the dimensions of the structure, improve bandwidth and radiation performance, uniform and nonuniform array 2D metasurfaces are used. [77–85]. Where, the Characteristic Mode Analysis (CMA) is an ap-

propriate antenna design approach, helping to optimize the metasurfaces and allowing to obtain the optimal points for their excitation.

For Internet of Things applications. TCM has also proved to be a great ally. Through its analysis, new types of RFID tags have been designed [86,87]. For example, the new RFID antenna for labeling commercial metal cans in a refrigerator. The tag is designed by taking advantage of the structure of the metal can as the main radiator [88].

In many telecommunications applications, covering a wide working area is extremely important. That is why the use of beamforming networks (BFN) for an array antennas is a form to cover a wider radiation space. Beamforming networks allow multiple radiation patterns to be generated, and their operation is as simple as a beam switch to form a continuous beam. BFN's can be divided into 3 groups: transmission lines based (transmission lines BFN), quasioptical lens based (quasioptical BFN) and digital data processing network based (Digital BFN).

One of the most important designs within transmission line-based BFN's are Butler matrix. [89,90] and Rotman lenses [91]. The N x N port Butler matrix is a combination of power dividers with broadband phase shifters, which is why a Butler Matrix is composed of hybrid couplers at -3dB, crossovers and 45° phase shifters. In recent years these elements have been experimented by virtue of improving their characteristics [92,93]. The UWB Butler matrices [94–98] have started to be developed, the systems in which this type of design is applied are: satellite communications [99], radar applications, unmanned aerial vehicles, etc.

1.3 Motivation

In April 2016, after a devastating earthquake destroyed a large part of the coastline in Ecuador, all high-speed guided communications to the devastated areas were compromised, leaving only radio communications as the only alternative for emergency communication. The affected people were trying to communicate with their families but it was almost impossible due to the heavy traffic and technological limitations. [100].

However, despite the difficulties shown, radio communications will always be the best option for communication in times of natural disasters. Being of great interest at present the development of devices that can provide a very high speed communication, low latency and jitter. On the other hand, it must have the ability to integrate with the systems that are currently being assembled around the world, as is the case of fifth generation networks 5G.

the Grupo de Radiación Electromagnética at Universitat Politècnica de València, for some time has been working on the development of devices that may be able to integrate this technology. Since the presentation of 2 doctoral theses in 2008 [26, 27], has been using the theory of Characteristic Modes as a tool for the design of antennas. Therefore, the thesis is also motivated by the previous experience that the research group has in the subject of the Characteristic Modes Theory.

Finally, it must be a highlight that this thesis has been developed in collaboration between the Universitat Politècnica de València (UPV) through the Grupo de Radiación Electromagnética (GRE) that is part of the Instituto de Telecomunicaciones y Aplicaciones Multimedia (iTEAM) and the Grupo de Investigación en Radiación Electromagnética, Sistemas Electrónicos Aplicados y Redes de Comunicaciones Híbridas (G-RESEARCH) of the Universidad Nacional de Chimborazo (UNACH) in Ecuador. In addition, this work has been supported by a doctoral studies scholarship of the UNACH, by the Spanish Ministry of Science, Innovation, and Universities (Ministerio de Ciencia, Innovación y Universidades de España) under the project PID2019-107885GB-C32, and by the Generalitat Valenciana GV/2015/065.

1.4 Objectives

The objectives that have been set for the development of this research work are:

1.4.1 Main Objective

The overall objective is to develop new antenna designs with wide bandwidth, low profile, compact and generate stable unidirectional radiation patterns, using different geometries and multiple feeds, applying a design methodology based on Characteristic Mode Theory.

The general objective also addresses theoretical investigations through mathematical formulation, numerical analysis using simulators and evaluation of the prototypes. Therefore, it will be necessary to work on certain specific objectives to fulfill the general one.

1.4.2 Specific Objectives

1. Analyze the characteristic modes of the structure and feeding incidence in arbitrary 2D and 3D figures.

- ✓ Analysis of structures and simple planar geometries.
- ✓ Analysis of different types of 2D structures as circles, rectangles, ellipses, circular and rectangular rings.
- ✓ Analysis of different types of 3D structures as rectangular waveguides, circular waveguides, cube, structures folded on themselves.
- ✓ Feeding effects analysis.
- ✓ Combination of electric and magnetic modes for resonance generation.

2. Multiple modes excitation using multiple feeding ports to achieve antennas with the following properties:
   - ✓ Ultra Wide Band (UWB)
   - ✓ Unidirectional radiation pattern with stability in the pattern
3. Study beamforming networks (BFNs) for array antennas
   - ✓ New concepts of broadband Butler Matrices
   - ✓ Array antennas for WIFI applications
4. Manufacture, characterization and experimental validation of prototypes.

1.5 Metodology

The methodology used for the development of this research work is described as follows:

1. **Compilation and bibliographic review**

   The first phase of the thesis has been dedicated to the collection of information and bibliographic review, starting from a basic study until reaching specific definitions as the thesis develops. The consultation and updating of the state of the art will be done through scientific data repositories such as IEEE Xplore or through databases indexed in WoS (Web of Science) specialized in antennas and microwaves topics. In addition to the information provided by data collection, the program has been supported by active participation in conferences related to the subject at national and international level.

   The conferences have provided updated information on the advances and news that occur on the subject in other research centers worldwide. Likewise, I have been an active participant in training courses and a short-term stay in an international research center of the highest prestige, since

these activities have been of great benefit in the acquisition of basic information for the development of the thesis. Parallel to the compilation and bibliographic review, the behavior of some arbitrary structures has been studied using the theory of Characteristic Modes.

2. **Modal analysis for antenna designs**

   This phase of the development of the thesis has been dedicated to the analysis and development of design techniques and optimization of simple structures through the use of the Theory of characteristic modes, this has been done to achieve antennas that have a low profile, a large bandwidth, a good impedance matching and above all that a unidirectional radiation pattern is generated with stability in its radiation pattern.

   The modal analysis for antenna design has been carried out through several arbitrary shapes in 2D and 3D, the first analysis has been performed in a structure without including the power ports, but only illuminating with a plane wave, and the second case has used one or multiple feed points. The fundamental aspects to analyze are: the distribution of induced currents in the structure, multimodal input impedance at the feeding point, the stability of the radiation patterns due to the modes in the structure and the contribution percentages of the modes to generate the resonance.

3. **Prototyping and experimental characterization**

   The practical validation of the designed devices has been carried out through the fabrication and characterization of these structures. The laboratory of Grupo de Radiación Electromagnética (GRE) del Instituto de Telecomunicaciones y Aplicaciones Multimedia (iTEAM) at Univesidad Politècnica de Valencia, and the laboratory of the Antenna and Electromagnetism Research Group at the Queen Mary University of London have been provide the necessary equipment to carry out the device manufacturing and devices characterization, thus validating the results obtained in the previous phases through electromagnetic simulators.

   Analogous to the development of the thesis, the most relevant results due to their theoretical or design content, which imply a novelty in the field, have been disseminated to the scientific community through papers in indexed journals and conferences related to the research topic. In addition, during the course of the thesis, new technologies that has been contribute to the development of the thesis have been explored through

an academic visit in the Antenna and Electromagnetism Research Group at the Queen Mary University of London.

1.6 Structure of the thesis

This thesis has been organized through seven chapters, their description as depicted below:

- ⇝ **Chapter 2.- Theory of Characteristic Modes**

  A brief introduction to the Theory of Characteristic Modes (TMC) is presented. These modes are important to analyze the current distribution and describe the resonance frequency of an arbitrary metallic structure in the absence of feeding points but illuminated by an incident field (plane wave). A mathematical formulation is introduced to describe the behavior of the structure through the solution of integral equations using the method of moments. A description of the physical interpretation of the modes is presented, for which the characteristic angles α_n, eigenvalues λ_n and modal significance MS_n are analyzed. Finally, an example of a modal analysis for a planar structure is presented.

- ⇝ **Chapter 3.- TCM in planar structures** In this chapter the analysis of several planar structures in isolation using the tcm is made, in addition to the behavior when two or more structures interact with each other, with this information then you can determine the shape and the number of feed points that can be used to force certain modes. Some examples are presented where 1 or several feeding points are inserted, it is also shown that resonance obtained with a full wave analysis is not necessarily linked to a single mode, but it is shown that it is the result of a combination of modes.

- ⇝ **Chapter 4.- Folded structures**

  The behavior of a pair of planar structures (a rectangular plate and an ellipse) is described using the TCM, to take advantage of their dimensions, these structures are subjected to a progressive folding until reaching the point where their two ends almost come together, a complete analysis of the behavior of the characteristic angles as the folding is performed is provided. With this information we proceed to insert the feeding points to convert them into antennas. A couple of prototypes are fabricated that achieve unidirectional radiation patterns and a very considerable bandwidth.

- ⇝ **Chapter 5.- TCM in 3D structures**

Once the planar structures, the interaction between them, and the folding on itself were analyzed. This chapter is dedicated to carrying out a study of the structures in 3 dimensions, the analyzed 3D structures are the waveguides, cavities closed at both ends and a cavity with a half-height structure with an open circuit and a short circuit at the ends. Two types of analysis are used, the first corresponds to the study of guide modes, i.e. to study the fields propagation inside a waveguide, their cutoff frequencies and the resonances for each of the proposed cavities.On the other hand, an analysis of the same structure is made using the characteristic modes theory, to describe how the currents behave, the radiation pattern and the resonance frequency when is excited by a feeding point. It is also presented two types of devices that have been inspired by the analyzed 3D structures, using a combination between the feeding ports, a large bandwidth, stable unidirectional radiation pattern is generated.

⇝ **Chapter 6.- Applications**

In the applications chapter, the validation of some devices that have been manufactured during the development of the thesis is shown, a comparative analysis is carried out between the results obtained through simulations and measurement instruments. The propotypes shown are:

- Butler matrix designed to generate four beams independently at a center frequency of 2.45 GHz
- Antenna composed of 4 asymmetric semi-cavities designed with SIW technology (Substrate Integrate Waveguide) with a very low profile, the structure is excited by a capacitive feed point that has a cross shape, each one of the semi-cavities generates a resonance, therefore , with the 4 semi-cavities a great bandwidth is generated. On the other hand, using the same design concept, an antenna with circular semi-cavities that can be integrated into a smart watch, it has 4 feeding points, 2 antennas work at 2.5 Ghz and the other 2 at 3.6 GHz. The port isolation is very good and, combined them multiple beams can be generated.
- Two proposals for antennas that are integrated into a chassis of a mobile device (a tablet specifically) and can cover the frequencies of 2.5 GHz and 3.6 GHz are presented, the first proposal starts from an elliptical plate folded on itself by the section of the semi minor axis, is fed capacitively from the curved edge, for the generation of the other frequency its dimensions are optimized. A 4 x 2 antenna array has been placed on the chassis so that the device works in MIMO technology. The second proposal is very similar to the first one, but to generate the second resonance a slot is added to the upper layer of

the structure and the capacitive feed point is placed in the inserted slot.

- An arbitrary structure is analyzed using TCM, a scaled air-plane is taken as a reference, and a pair of feed points are inserted in specific areas for the generation and control of the radiation pattern.
- A periodic metasurface antenna absorber is presented, to find the optimal power points, it starts from the analysis of a unit cell using the TCM, the impedance values are found that are later replaced by resistive loads, with this a maximum power transfer will be made.

⇝ **Chapter 7.- Conclusions and Future works**

In this chapter, the conclusions reached with the development of this research work have been presented, in addition, a perspective of the future works that can be derived from this research line has been provided.

Chapter 2

Theory of Characteristic Modes

> "*The charms of this sublime science, mathematics, are only revealed to those who have the courage to deepen it.*"
>
> — Carl Friedrich Gauss

2.1 Introduction

The Theory of Characteristic Modes (TCM) in last years has been used as a great tool for the design of antennas because of the important information provided [34, 101]. TCM was analyzed for first time by Garbacz in 1968 [9], in these work, the author demonstrated that with the diagonalizing the scattering matrix of the bodies conductor with arbitrary shapes the characteristic modes can be described. However, obtaining these modes was not a simple task due to its complexity [10].

Later it was improved by Harrington and Mautz [11] where they got to obtain the same modes through the diagonalization of the generalized impedance matrix of the bodies [11, 12], Harrington in his future works managed to succeed by introducing the concept of Moments Method for solving a problem of electromagnetism [102], this method facilitates the solution of the problem of eigenvalues, which at the moment of its resolution provides a set of real current modes, called Characteristic Modes [13]. TCM not only have been studied for

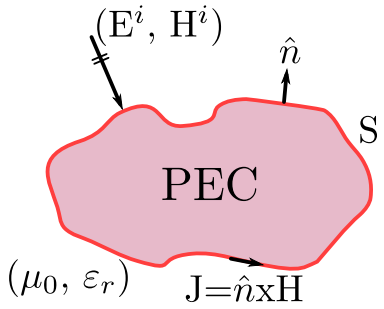

Figure 2.1: 3D PEC general arbitrary surface.

conductive bodies but also for magnetic materials and dielectrics [14], and even for materials with losses [14, 15, 103].

Although the Theory of Characteristic Modes has been described in great detail in [11], and [12] and has been developed in several studies [104–107]. In this chapter, a review of its mathematical formulation will be carried out, subsequently based on a circular ring, each of the parameters that emerge from the analysis of the TCM will be described, and its application in antennas design.

2.2 Mathematical Formulation of the TCM

Consider an arbitrary Perfect Electric Conductor (PEC) that is illuminated with an incident plane wave $\mathbf{E}^i$ as shown in Fig. 2.1, the incident plane wave induces a surface current $\mathbf{J}$ on the PEC body, the induced surface current $\mathbf{J}$ generates a field scattering $\mathbf{E}^s$.

Through the boundary condition the tangential electric field can be described, which satisfies the equation:

$$(\mathbf{E}^s(\mathbf{r}) + \mathbf{E}^i(\mathbf{r}))_{\tan} = 0, \mathbf{r} \in S \tag{2.1}$$

where index s represents the scattered field and index i the incident field respectively. Since the electric field $\mathbf{E}^s$ is in function of the induced current $\mathbf{J}$, the integral operator L can be defined as:

$$L(\mathbf{J}) = -\mathbf{E}^s_{\tan}(\mathbf{r}), \tag{2.2}$$

In order to formulate the Theory of Characteristics Modes for conductive bodies, the Electric Field Integral Equation (EFIE) has been described after the combination the Eq. (2.1) and Eq. (2.2) [11].

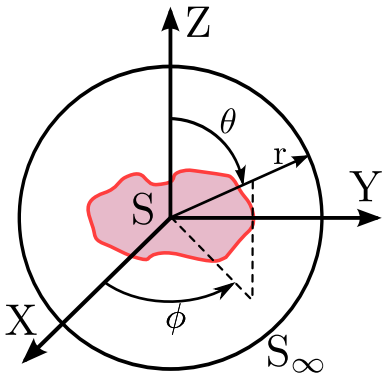

Figure 2.2: Classic scenario to the computation of characteristic modes, and the spherical coordinates systems.

$$[L(\mathbf{J}) - \mathbf{E}^i(\mathbf{r})]_{\tan} = 0, \tag{2.3}$$

Where the subscript "tan" depict the tangential components of the electric field on the surface S.

In Fig. 2.2, the classic scenario to the computation of characteristic modes is shown, and the corresponding spherical coordinates systems.

The integral operator L has a linear behavior and it is defined by:

$$L(\mathbf{J}) = j\omega\mathbf{A}(\mathbf{r}) + \nabla\phi(\mathbf{r}) \tag{2.4}$$

$$\mathbf{A}(\mathbf{r}) = \mu_0 \oiint_s J(\mathbf{r}')\psi(\mathbf{r},\mathbf{r}')dS' \tag{2.5}$$

$$\phi(\mathbf{r}) = \frac{j}{\omega\epsilon_0} \oiint_s \nabla'.J(\mathbf{r}')\psi(\mathbf{r},\mathbf{r}')dS' \tag{2.6}$$

Where $\mathbf{r}$ describe a field point, $\mathbf{r}'$ is a source point, and ϵ_0, μ_0, k represent the permittivity, permeability, and wave number, respectively, of the free space. Operator ∇' denotes divergence with respect to $\mathbf{r}'$. The Green's function of the free space has a well-know form:

$$G(\mathbf{r},\mathbf{r}') = \frac{e^{-jk|\mathbf{r},\mathbf{r}'|}}{4\pi|\mathbf{r},\mathbf{r}'|} = \psi(\mathbf{r},\mathbf{r}') \tag{2.7}$$

Applying the boundary condition 2.1 and in 2.4, the EFIE formulation can be described by:

$$L(\mathbf{J}) = j\omega\mu_0 \iint_s J(\mathbf{r}')\frac{e^{-jk|\mathbf{r},\mathbf{r}'|}}{4\pi|\mathbf{r},\mathbf{r}'|}ds' + \nabla\left(\frac{j}{\omega\epsilon_0}\iint_s \nabla'.J(\mathbf{r}')\frac{e^{-jk|\mathbf{r},\mathbf{r}'|}}{4\pi|\mathbf{r},\mathbf{r}'|}ds'\right) \quad (2.8)$$

Physically, the expression $-L(\mathbf{J})$ provides the electrical intensity at any point in space due to the current $\mathbf{J}$ on the surface S, as the operator L is related to the field and the current quantities, it has an impedance character:

$$Z(\mathbf{J}) = [L(\mathbf{J})]_{tan} \quad (2.9)$$

the Eq. (2.9) in its discrete form is also known as the Method of Moments (MoM) complex impedance matrix [11, 108].

2.2.1 Method of Moments

There are several numerical methods that are used for the analysis and design of antennas, among the main ones we have the finite difference of time domain (FDTD) method and the finite element method (FEM), which transform the differential equations of electromagnetic into difference equations. On the other hand, the integral equations methods, which transform the differential equations of electromagnetic through the use of a Green's function into integral equations that can be solved using the method of moments (MoM) [109].

In this thesis, for the analysis of the behavior of the several structures that will be presented, the method of moments has been used. The MoM was described at the first time in 1967 by Harrington [109], and in 1993 was re-edited in his book [13], this numerical method is particularly well suited to open problems such as the radiation and scattering problems [11, 13, 102, 110, 111].

The main objective of the MoM is to represent in a matrix form of an integral operator through the expansion and approximation of the unknown currents in terms of a finite set of basis functions. To achieve this purpose, three steps can be adopted in a general way and these are described as follow.

Firstly, 3D reference structure must be superficially modeled in several small elements, the triangular shapes are the most popular to model 3-D arbitrary shape. In Fig. 2.3 the triangular elements mesh are shown, there are several electromagnetic simulators capable of generating a triangular mesh such as the PATRAN [112], ANSYS [113], Altair HyperWorks [114], CST Studio Suite [115].

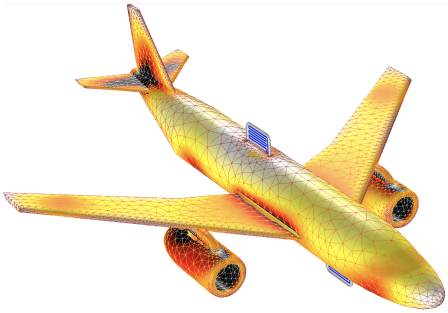

Figure 2.3: Triangular element mesh of an airplane [1]

In general, to obtain precious radiation and dispersion results, a $\lambda/10$ mesh is usually sufficient [116], where λ corresponds to the wavelength at the resonance frequency in the free space. On the other hand, to obtain the distribution of modal currents through the theory of characteristic modes, this mesh is optimal to obtain results of the fundamental modes, however, for modes of higher order, the mesh value at $\lambda/10$ is insufficient, because the modal currents of higher order modes vary drastically, so it has been suggested to model the PEC surface with a relatively dense mesh in excess of $\lambda/15$ [116].

Secondly, the appropriate basis functions should be assigned to each one of the previously described elements such that the unknown currents in the integral equation are expanded. In the method of moments, the most popular basis functions for PEC arbitrary surfaces is Rao-Wilton-Glisson (RWG) basis function [117] and this is based through geometrical modelling using a meshing

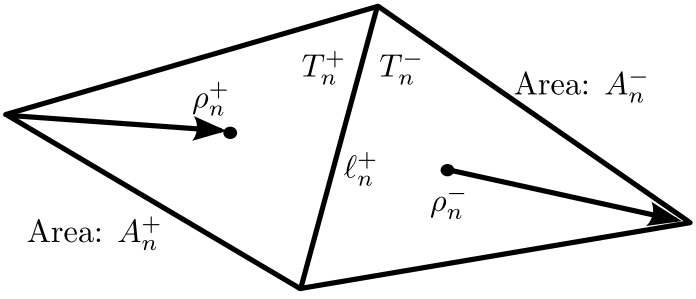

Figure 2.4: RWG basis function depicted over a pair of triangular elements with a common side.

with triangular patches. As shown in Fig. 2.4, the RWG basis function is defined such a vector function $\mathbf{f}_n$ over a pair of triangles elements that share a common edge and it is depicted by the following equation:

$$\mathbf{f}_n(\mathbf{r}) = \begin{cases} \frac{\ell_n}{2A_n^+}\rho_n^+ & \text{if } \mathbf{r} \in T_n^+ \\ \frac{\ell_n}{2A_n^-}\rho_n^- & \text{if } \mathbf{r} \in T_n^- \\ 0 & \text{else} \end{cases} \tag{2.10}$$

where T_n^+ and T_n^- are the contiguous triangles that have a common edge with a length ℓ_n, A_n^+ and A_n^- corresponds to the area that covers each of the triangles considered for the analysis, ρ_n^+ and ρ_n^- are called the charge density, these represent the direction of the vectors that are defined with respect to the vertex free and can be defined with:

$$\rho_n = \frac{1}{j\omega}\nabla.\mathbf{f}_n(\mathbf{r}) \tag{2.11}$$

On the other hand, J component normal to value ℓ_n is assigned a positive when it flows from T_n^+ to T_n^-. The vector function $\mathbf{f}_n(\mathbf{r})$ has no normal components through the outer edge between the pair of triangles T_n^+ and T_n^-. The normal component through the inner edge ℓ_n is equal to 1, constant and continuous along the entire side. Then, the total current can be approximated to:

$$J(\mathbf{r}) = \sum_{n=1}^{N} J_n \mathbf{f}_n(\mathbf{r}) \tag{2.12}$$

Where J_n is the unknown weighting coefficient for the n_{th} RWG basis function i.e. the current that is flowing the side ℓ_n and N depicts the number of common edges in the pair of considering triangles. The surface charge density can be approximated by the Eq. (2.13), it shows that the total charge density associated with the triangle pairs equals to zero.

$$\nabla_s.\mathbf{f}_n = \begin{cases} \frac{\ell_n}{A_n^+} & \text{if } \mathbf{r} \in T_n^+ \\ -\frac{\ell_n}{A_n^-} & \text{if } \mathbf{r} \in T_n^- \\ 0 & \text{else} \end{cases} \tag{2.13}$$

Finally, the last step in discretizing an integral equation into a matrix equation is to test the integral equation with expanded current representation. Then, the Eq. (2.12) has been substituted into the EFIE such as depicted follow:

$$\mathbf{E}^i_{\tan}(\mathbf{r}) = \left(jk_0\eta_0 \sum_{n=1}^{N} J_n \oiint_s \mathbf{f}_n(\mathbf{r}')G(\mathbf{r},\mathbf{r}')dS' \right)_{\tan} + \left(\frac{j\eta_0}{k_0} \sum_{n=1}^{N} J_n \nabla \oiint_s \nabla'.\mathbf{f}_n(\mathbf{r}')G(\mathbf{r},\mathbf{r}')dS' \right)_{\tan} \tag{2.14}$$

Using the RWG basis function $\mathbf{f}_m(\mathbf{r})$ as the testing function and using the vector identity $\nabla.(\phi\mathbf{A}) = \mathbf{A}.(\nabla\phi) + \phi(\nabla.\mathbf{A})$, the following matrix equation can be generated:

$$[Z_{mn}][J_n] = [V_m] \tag{2.15}$$

where,

$$Z_{mn} = jk_0\eta_0 \left(A_{mn} - \frac{1}{k_0^2} B_{mn} \right) \tag{2.16}$$

$$A_{mn} = \oiint_s \mathbf{f}_m(\mathbf{r}). \oiint_s \mathbf{f}_n(\mathbf{r}')G(\mathbf{r},\mathbf{r}')dS'dS \tag{2.17}$$

$$B_{mn} = \oiint_s \nabla_s.\mathbf{f}_m(\mathbf{r}) \oiint_s \nabla'_s.\mathbf{f}_n(\mathbf{r}')G(\mathbf{r},\mathbf{r}')dS'dS \tag{2.18}$$

$$V_m = \oiint_s \mathbf{f}_m(\mathbf{r}).\mathbf{E}^i(\mathbf{r})dS \tag{2.19}$$

Therefore, for the CM analysis, the generalized eigenvalues equation of the impedance matrix $[Z_{mn}]$ has been derived. The generalized eigenvalue equation is independent and not dependent on a specific excitation.

2.2.2 Characteristic currents

Theory of characteristic modes was expanded when Harrington and Mautz demonstrated that the solution for the modes could be found using an eigenvalue problem and could be solved using the method of moments [11]. The method of moments impedance matrix Z used to demonstrate the theory can be decomposed into its real and imaginary parts such as shown below:

$$Z(\mathbf{J}) = R(\mathbf{J}) + jX(\mathbf{J}) \tag{2.20}$$

For purposes of modal decomposition of the TCM, the matrix Z has symmetry with its real and imaginary Hermitian parts [118].

Hence, based on the Harrington and Mautz proposed [10], the characteristics currents modes are the solution of generalized eigenvalue equation over an arbitrary structure.

$$\mathbf{X}(\mathbf{J}_n) = \lambda_n \mathbf{R}(\mathbf{J}_n) \tag{2.21}$$

where λ_n corresponds at the eigenvalues, $\mathbf{J}_n$ represents the eigenfunctions or eigencurrents, and the variables $\mathbf{X}$ and $\mathbf{R}$ depict the imaginary and the real part of the MoM $\mathbf{Z}$ matrix of the analyzed arbitrary structure.

The operators $\mathbf{R}$ and $\mathbf{X}$ of the generalized eigenvalue equation are both real symmetric operators when the reciprocity theorem in a linear symmetric operator is applied, causing the eigenvalues λ_n real with the eigenvectors $\mathbf{J}_n$ real or equiphase [11]. Moreover, the properties of the matrix $\mathbf{R}$ and $\mathbf{X}$ ensure the real eigenvectors $\mathbf{J}_n$ be orthogonal with $\mathbf{R}$ and $\mathbf{X}$. Mathematically, these orthogonality properties can be described as:

$$\langle \mathbf{J}_m^*, R(\mathbf{J}_n) \rangle = \delta_{mn} \tag{2.22}$$

$$\langle \mathbf{J}_m^*, X(\mathbf{J}_n) \rangle = \lambda_n \delta_{mn} \tag{2.23}$$

$$\langle \mathbf{J}_m^*, Z(\mathbf{J}_n) \rangle = (1 + j\lambda_n)\delta_{mn} \tag{2.24}$$

The balance of power between the reactive and active power of the characteristic modes are described through the equations 2.22 to 2.24. Where δ_{mn}, is the Kronecker Delta function defined as:

$$\delta_{mn} = \begin{cases} 1 & m = n \\ \\ 0 & m \neq n \end{cases} \tag{2.25}$$

Given that all eigenvectors $\mathbf{J}_n$ are real, the conjugate operation in equations (2.22), (2.23), and (2.24) can be omitted.

Analyzing the Eq. (2.21), the characteristic modes defined such $\mathbf{J}_n$ can be represented as the real currents that are on the surface of a conductive body, and these currents only depend on the shape and size of the structure and these are independent of any specific source or excitation.

In general, the characteristic currents show two types of orthogonality properties: the current polarizations are orthogonal with each other, and the current magnitudes are orthogonal with each other. In the second property, if

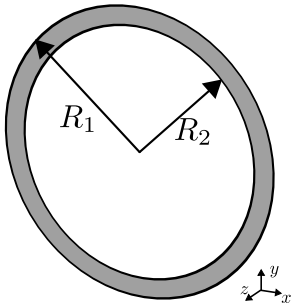

Figure 2.5: Reference structure to represent the parameters generated by the theory of Characteristics Modes.

a mode has a very strong currents at a specific point on the PEC surface, then the orthogonal mode must have a very weak modal current at the same point. Taking advantage of the orthogonality property described above, antennas with circular polarization can be designed by exciting two orthogonal modes simultaneously, for example the typical rectangular patch excited on its adjacent edges as shown in [46]. In addition, using the orthogonality property also obtains important information on how to properly design antennas with multiple ports, helping improve the isolation performance between feeding ports, this concept will be used for some of the designs that will be presented in the following chapters.

In practice, to compute characteristic modes in an arbitrary conductive structure, equation 2.21 needs to be reduced to matrix form as explained in [11], using the Galerkin formulation [13]:

$$[X](\mathbf{J}_n) = \lambda_n[R](\mathbf{J}_n) \tag{2.26}$$

To illustrate and describe the parameters that are generated by the Theory of Characteristic Modes, a metallic circular ring as shown in Fig. 2.5 has been analyzed, the structure is supposed to be a perfect conductor without losses, its dimensions are: outer radius $R_1 = 30$ mm, internal radius $R_2 = 26$ mm and the thickness $t = 0.035$ mm. To compute the modes, hundred triangular functions have been used to calculate the modes for expansion and testing when applying the method of moments.

In Fig. 2.6, the characteristic currents of the first three modes have been represented. Figs. 2.6(a) and 2.6(d) represent mode J_1 and its orthogonal mode or also known as degenerate mode (J_1'), these modes have been obtained at a resonance frequency of 1.87 GHz. In Fig. 2.6(b) and 2.6(e), the mode J_2

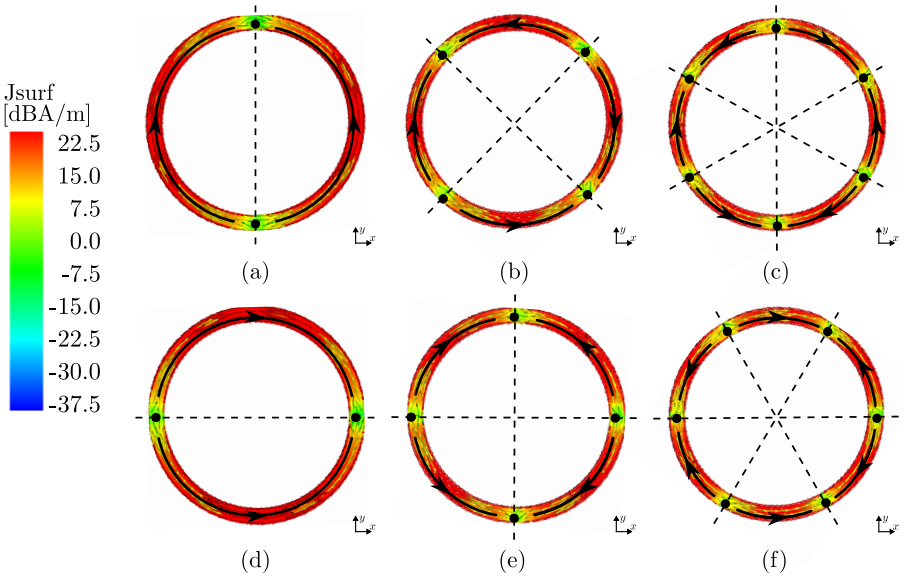

Figure 2.6: Characteristic current distribution. a)Mode J_1 and d) Mode J_1' at 1.87 GHz; b) Mode J_2 and e) Mode J_2' at 3.65 GHz; c)Mode J_3 and f) Mode J_3' at 5.42 GHz

and its degenerate mode (J_2') are depicted, these last modes are obtained at the frequency of 3.65 GHz. Meanwhile, at 5.42 GHz it was obtained at mode J_3 and it's degenerated mode J_3' such as exhibited in Fig. 2.6(c) and 2.6(f).

The denomination of the degree of each of the modes presented in a structure is given by the number of pairs of current nulls. For the metal ring shown in Fig. 2.5, it can be seen that for the mode J_1 and the J_1' there is a pair of current nulls, for the case of the mode J_2 and J_2' there are 2 pairs, while for the case of the mode J_3 and J_3' there are 3 pairs, each case has been illustrated in Fig. 2.6.

However, there is another method to interpret the degree of the modes in a structure. First, the symmetry axes should be placed in the structure: in the case of common modes (J_n) the vertical axis (X-axis) will be used and for degenerate modes (J_n') the horizontal axis (Y-axis). Next, for the analysis, only one of the planes is considered, if it is for the common-mode the part of the left or right of the structure, or else top or bottom in the case of degenerate modes. Finally, in the simplified structure, the maximums of currents must be count, the number of maximums of currents represents the degree of the mode.

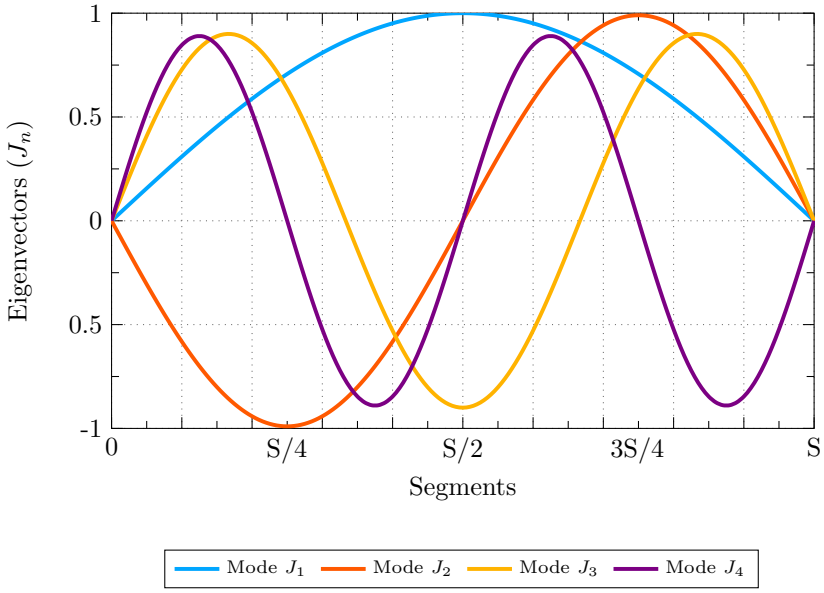

Figure 2.7: Normalized current distribution at 1.87 GHz (1st resonance) for the first four eigencurrents of simplified structure (half circular ring sketched in Fig. 2.5).

To facilitate a comparison between each of the modes that appear in a structure, it will be assumed that the values of the internal radius and the external radius of the analysis structure are approximately equal, the solution for this case is similar to that obtained when a conductive wire is analyzed, i.e. the characteristic currents can be normalized in a graph plotted in cartesian coordinates using the maximum values of the currents versus the number of segments (S) used for the computation of the modes. Then, starting from the distribution of currents shown in the structure of Fig. 2.6, the normalized values of the eigencurrents can be plotted in two ways: the first form is linked to the currents when analyzing the complete structure that it finally can be described as the result of placed two dipoles in parallel, each one of the dipoles have been slightly deformed in order to obtain a semi-circle and that when these are integrated a circular ring has been gotten. Meanwhile, the second can be plotted using the simplified structure obtained by symmetry.

In Fig. 2.7 shows the eigencurrents generated by the simplified structure, it can be observed that eigencurrents have sinusoidal form with nulls at the end points of the dipole (half of the structure). As the order of the mode increases,

the function that depicted the eigencurrents is increasingly oscillatory. It should highlight that by varying the frequency of analysis, the representation of each of the normalized currents will be subject to variation [26].

First current mode presents one cycle, second current mode two cycles, and so on. Furthermore, depending on the symmetry of their current distribution the modes can be classified in even modes (J_1 and J_3) or odd modes (J_2 and J_4).

According to the information provided by the eigenvalues, the fundamental mode will resonate when its physical length of half the structure is approximately $L = \lambda/2$. On the other hand, for higher-order modes, the length value of the fundamental mode ($\lambda/2$) can be multiplied with the order of mode to find. For example, for mode J_2 it should be $\lambda/2 * 2 = \lambda$, in case of mode J_3 it will be $\lambda/2 * 3 = 3\lambda / 2$, respectively to each mode.

Is important to highlight that there are two ways in which the currents flow within a structure, in a first way, the currents flow to around the current nulls either right or left, these are known as a magnetic mode. In the second case, the currents enter or leave of the current nulls generating a source or drain effect, at these kinds is called such an electric mode.

2.2.3 Characteristic fields

The so-called characteristic fields are those generated by the far-field or electric fields E_n that have been produced by the characteristic currents or also known as modal currents J_n on the surface of a conductive body [11]. Characteristic fields can be expressed from Eq. (2.21), as detail below:

$$E_n(\mathbf{J}_n) = Z(\mathbf{J}_n) = R(\mathbf{J}_n) + jX(\mathbf{J}_n) = R(\mathbf{J}_n)(1 + j\lambda_n) \tag{2.27}$$

Then, from the Eq. 2.27 it is extracted that characteristic fields are equiphasal, since they are (1+ jλ_n) times a real quantity. The orthogonality relation for the characteristic fields can be obtained from the characteristic currents of the Eq. (2.24) through the complex Pointing theorem, and after to omit the common coefficients, the relation can be written as:

$$\begin{aligned} P(J_m, J_n) &= \langle J_m^*, ZJ_n \rangle = \langle J_m^*, RJ_n \rangle + j\langle J_m^*, XJ_n \rangle \\ &= \oiint_{S'} (\mathbf{E}_m \times \mathbf{H}_n^*) dS + j\omega \iiint_{V'} (\mu \mathbf{H}_m \cdot \mathbf{H}_n^* - \varepsilon \mathbf{E}_m \cdot \mathbf{E}_n^*) dV \\ &= (1 + j\lambda_n)\delta_{mn} \end{aligned} \tag{2.28}$$

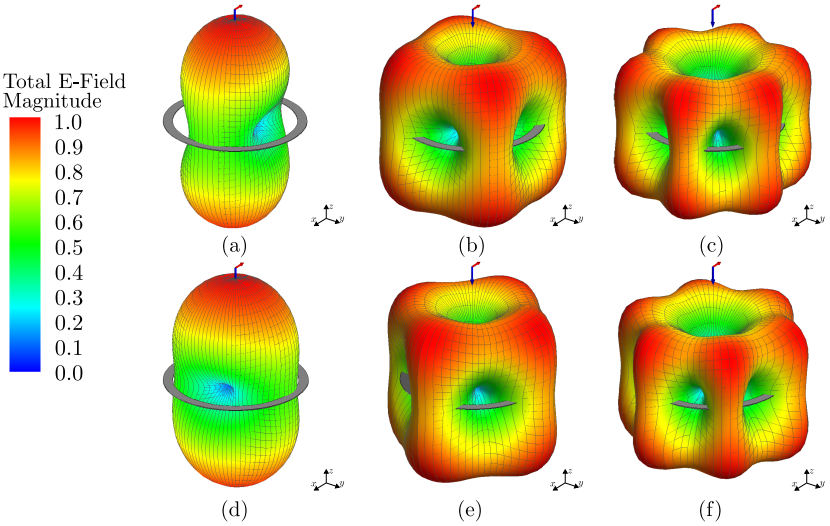

Figure 2.8: 3D Characteristic radiation patterns of the modal electric field $E_{\phi,n}$ caused by the current modes J_n. a)Mode J_1 and d) Mode J_1' at 1.87 GHz; b) Mode J_2 and e) Mode J_2' at 3.65 GHz; c)Mode J_3 and f) Mode J_3' at 5.42 GHz

If a structure with a surface of finite size is considered and the fields on the sphere at infinity (S_∞) are evaluated, as shown in Fig. 2.2, it can be demonstrate that

$$\frac{1}{\eta} \oiint_{S_\infty} \mathbf{E}_n \times \mathbf{E}_m^* dS = \delta_{mn} \tag{2.29}$$

hence, the equation above shows that characteristic electric fields form an orthogonal set in the far field.

In the same way as in the characteristic currents, the characteristic fields also exhibit orthogonality properties, the polarization and the magnitudes of the characteristic fields are orthogonal with each other. It is clear that there is a very close relationship between the orthogonality properties of the characteristic currents with the characteristic field.

There are several applications where the orthogonality properties of the characteristic fields are applied, among the most popular are used to design antennas for MIMO (Multiple Input Multiple Output) technology or when the far field polarization performance is of great importance [74, 119].

In 2.8, the 3D modal electrical field of the two first modes generated by the currents modes of the metallic circular ring illustrated in Fig. 2.5 are expressed. The Fundamental mode J_1 and its degenerated J_1' have been obtained at 1.87 GHz, at 3.65 GHz for the mode J_2 and its degenerate and finally mode J_3 and J_3' at 5.42 GHz.

It is evident that the number of radiating lobes depends on the order of the mode i.e. if the mode increases its order the number of modes grows as well. By comparing the characteristic currents with the characteristic fields, it can be concluded that a radiation is null in one direction when the value of the current in the same direction is null also.

2.2.4 Modal Solutions

Owing to the already mentioned orthogonality properties defined in the characteristic modes, either the characteristic currents or the radiated fields can be extended using the CM. The total currents that appear over the surface of a conductive body can be written as a combination or linear superposition of the characteristic currents.

$$\mathbf{J} = \sum_n a_n \mathbf{J}_n \tag{2.30}$$

where, a_n are the weight for currents as well for radiation patterns and it can be computed using the MoM procedure, derived using linearity of the impedance operator and orthogonality of characteristic modes as

$$\mathbf{J} = \sum_n \frac{\langle \mathbf{J}_n, \mathbf{E}_i \rangle}{1 + j\lambda_n} \mathbf{J}_n = \sum_n \frac{V_n^i}{1 + j\lambda_n} \mathbf{J}_n \tag{2.31}$$

the term V_n^i is called modal excitation coefficient, as it indicates the degree of coupling between the excitation and the characteristic mode [27], and it determines if a particular mode is excited by the antenna feed or incident field.

In addition, interpreting the Eq. (2.31), the total current also depends on the λ_n eigenvalues, which is linked to the nth characteristic current mode, this parameter is very important because it provides important information on the resonant frequency and the radiating properties of the different current modes. Next section, a detailed description will be made of how the maximum advantage can be taken over the information provided by the eigenvalues

2.3 Physical interpretation of CM

Previously it has been described that through the use of the Theory of Characteristic Modes, important information can be obtained that will serve to design antennas or that allows us to describe their behavior. The information that can be obtained through physical interpretation is related to the properties of an arbitrary structure that are: the resonance frequency, the bandwidth and the quality factor. Each of these features described can be obtained through modal significance or characteristic angles values, the latter two are directly linked to the eigenvalues that were previously formulated.

2.3.1 Physical interpretation of eigenvalues

The eigenvalues not only give us information about the characteristic fields and the characteristic currents but also about the resonance frequency of the arbitrary structure as detailed in [11], the relationship that exists between the magnitude of the eigenvalues with the radiation of the modes can be interpreted using Eq. (2.28). The eigenvalues can acquire a value that is between $-\infty$ to $+\infty$, and according to the magnitude of the eigenvalue, the behavior of the structure can be described in three cases as detailed below:

1. when $\lambda_n = 0$ depicts that $\iiint_{V'} \mu \mathbf{H}_n \cdot \mathbf{H}_n^* dV = \iiint_{V'} \varepsilon \mathbf{E}_m \cdot \mathbf{E}_n^* dV$
2. when $\lambda_n > 0$ depicts that $\iiint_{V'} \mu \mathbf{H}_n \cdot \mathbf{H}_n^* dV > \iiint_{V'} \varepsilon \mathbf{E}_m \cdot \mathbf{E}_n^* dV$
3. when $\lambda_n < 0$ depicts that $\iiint_{V'} \mu \mathbf{H}_n \cdot \mathbf{H}_n^* dV < \iiint_{V'} \varepsilon \mathbf{E}_m \cdot \mathbf{E}_n^* dV$

The first corresponds to the case of resonance when the eigenvalues of the modes that are equal to 0, the mode of the structure is in resonant at that frequency. On the other hand, for the following cases, it can be seen that the eigenvalue is different from 0, that is the eigenvalue can be a positive or negative value, the λ_n sign will indicate the type of energy stored associated with the mode. If the sign of λ_n is positive, it is known as inductive modes because the stored magnetic field energy dominates the stored electric field energy. Otherwise, it will be considered as a capacitive mode, storing electric field energy.

In Fig. 2.9 plots the eigenvalues versus frequency of the four current modes with their degenerates of the metallic circular ring depicted in Fig. 2.5. Is seen that there are 4 eigenvalues (mode J_1 to Mode J_4) start being negative,

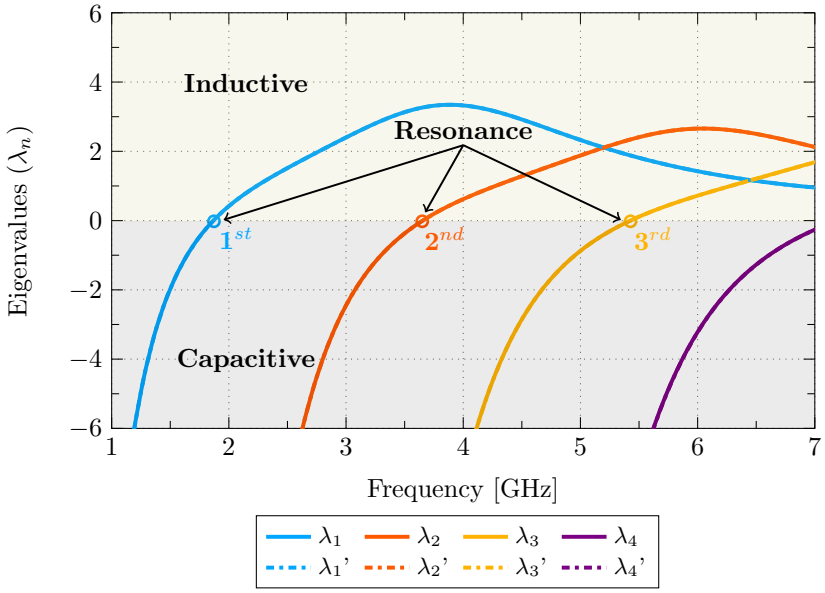

Figure 2.9: Eigenvalue λ_n associated to the current modes J_n of the circular metal ring sketched in Fig. 2.5.

next they resonate (λ_n =0), and at the end, they keep in a positive value, this behavior is known as electric mode such as described in the previous section. Mode J_1 resonates at 1.9 GHz, mode J_1 at 3.63 GHz, mode J_1 at 5.45 GHz, and mode J_1 resonate out of the analyzed frequency band.

2.3.2 Physical interpretation of Modal Significance

Previously it has been commented that the characteristic modes provide important information for antennas design, in the previous section the eigenvalues have been analyzed, offering information about the resonance frequency of modes. However, eigenvalues are not very used, there are other alternatives that are preferred to obtain information such is the case of the Modal Significance.

The modal significance is a representation of the eigenvalues in a normalized way and describes how well the mode radiates, the normalized amplitude will simply depend on the dimensions and shapes of the structure, without considering the excitation. When the value of modal significance MS_n is equal to the unit the mode is in resonance and it is radiating more energy, otherwise when

modal significance MS_n approaches 0, these mode stores more energy instead of radiating. Modal significance is expressed by:

$$\mathrm{MS}_n = \left| \frac{1}{1 + j\lambda_n} \right| \tag{2.32}$$

The modal significance with respect to the frequency of the first four modes of the circular ring analyzed in the previous sections has been drawn in Fig. 2.10. The resonant frequency of each of the modes is described when the value of the modal significance is equal to 1. This means that as soon as the maximum value of the curve is close to the unit, the mode will contribute much more to the radiation.

In addition to offering information about the resonant frequency, modal significance provides a very simple alternative to obtain the bandwidth (BW_n) of each of the characteristic modes. To obtain the frequency range where the structure can work, half-power of the modal significance will be used, it representation can be defined by:

$$\mathrm{MS}_n = \left| \frac{1}{1 + j\lambda_n} \right| = \frac{1}{\sqrt{2}} = 0.707 \tag{2.33}$$

The bandwidth of the characteristic modes according to half-power can be expressed as:

$$BW_n = \frac{f_H - f_L}{f_{res}} \tag{2.34}$$

where f_{res} is the resonance frequency of the mode, f_H and f_L are the upper and lower band frequency. The color-shaded areas in Fig. 2.10 represent the bandwidth available for each of the first 4 modes of the circular metal ring.

As additional information, modal significance is also used to identify modes that are more or less significant, the mode is considered more significant when the value of modal significance is greater than half-power, obviously for values less than half-power it is considered as less significant.

Using the inverse bandwidth value as described in Eq. (2.35), the quality factor of each resonant mode can be evaluated.

$$Q_{rad,n} = \frac{1}{BW_n} \tag{2.35}$$

The concept of quality factor allows quantifying how sharp the resonance of the mode is. If the quality factor is high, the bandwidth will be narrow and the sharper the resonance of the mode is. In Table 2.1 a summary has been made

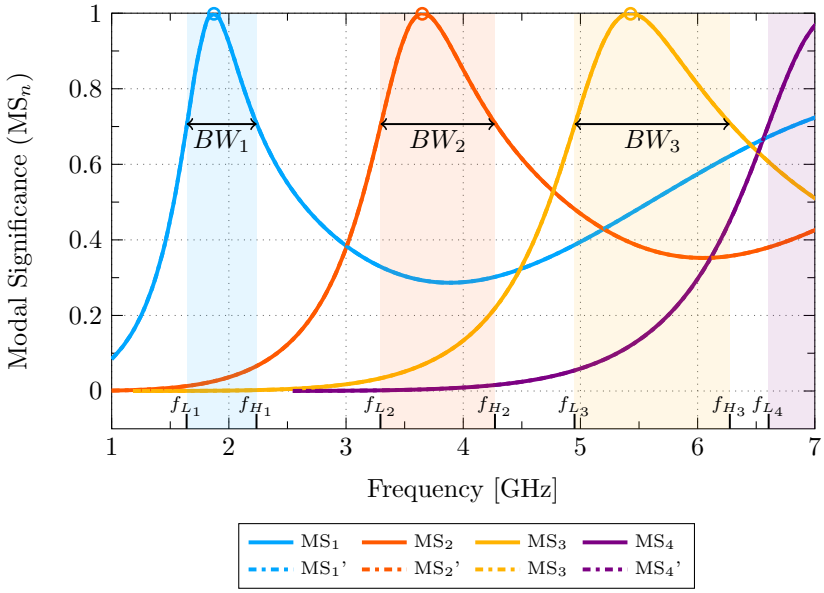

Figure 2.10: Modal significance MS$_n$ associated to the current modes J_n of the circular metal ring sketched in Fig. 2.5.

Table 2.1: Resonance frequency, bandwidth and quality factor of the first three modes of the Fig.2.5

	f_{res} [GHz]	f_L [GHz]	f_H [GHz]	$BW_n(\%)$	$Q_{rad,n}$
Mode J_1	1.9	1.6	2.2	31.57	3.16
Mode J_2	3.8	3.3	4.3	26.31	3.8
Mode J_3	5.67	4.95	6.4	25.5	3.91

with the parameters obtained through the information provided in Fig. 2.10 such as resonance frequency, bandwidth and quality factor of the first three modes of the Fig. 2.5.

With Eq. (2.33) the quality factor has been very simple to calculate, however, it should be considered as simply an approximation. In [26], a compar-

ative analysis is performed using some models to calculate the quality factor and determine the degree of approximation. Among the models considered are those based on Foster's reactance theorem [120, 121] and on the other hand, they approximated the quality factor of a current described by Harrington and Mautz [122]. Coming to the conclusion of the quality factor calculated by Eq. (2.35) is equivalent to that of the mentioned models.

2.3.3 Physical interpretation of Characteristic angle

From the theory of characteristic modes discussed in the previous sections, a set of characteristic currents J_n has been defined on the surface of a conductive body, these currents induce characteristic fields in free space. A characteristic angle models the phase angle between a characteristic current J_n and the associated characteristic field E_n. The characteristic angle can be represented as [123]:

$$\alpha_n = 180^\circ - tan^{-1}(\lambda_n) \tag{2.36}$$

In the same way that modal significance was obtained, characteristic angles can be calculated from the eigenvalues. In Fig. 2.11, the characteristic angles of the first four modes of a metallic circular ring have been shown, each of the characteristic angles can vary between 90° and 270°.

Making an analogy with the graph of modal significance (see Fig. 2.10), the resonance frequencies obtained through the maximums of each of the functions, match when the value of the characteristic angle takes the value of 180°. Therefore, while the characteristic angle slope is closer to 180 degrees, the mode will be considered as a good radiator, on the other hand, the mode stores energy when the values of α_n are close to 90° or 270°.

The bandwidth can be calculated using the values of the slope of the characteristic angles through Eq. (2.34), for this it is required to determine the value of the characteristic angle that corresponds to one half the power radiating. To clearing the eigenvalues of the formula of the modal significance (Eq. (2.34)), the eigenvalues acquire the value of $\lambda_n = 1$ and λ_n = -1 at half-power. Now, if the values found in Eq. (2.34) are substituted, the characteristic angles that are used to calculate the bandwidth are obtained. The lower band corresponds to $f_L = 135^\circ$, while the upper band is $f_H = 225^\circ$.

In Table 2.2 summarizes the behavior of an arbitrary structure using all physical interpretations (eigenvalues, modal significance, and characteristic angles) of the characteristic modes. Hence, to have very good characteristics in

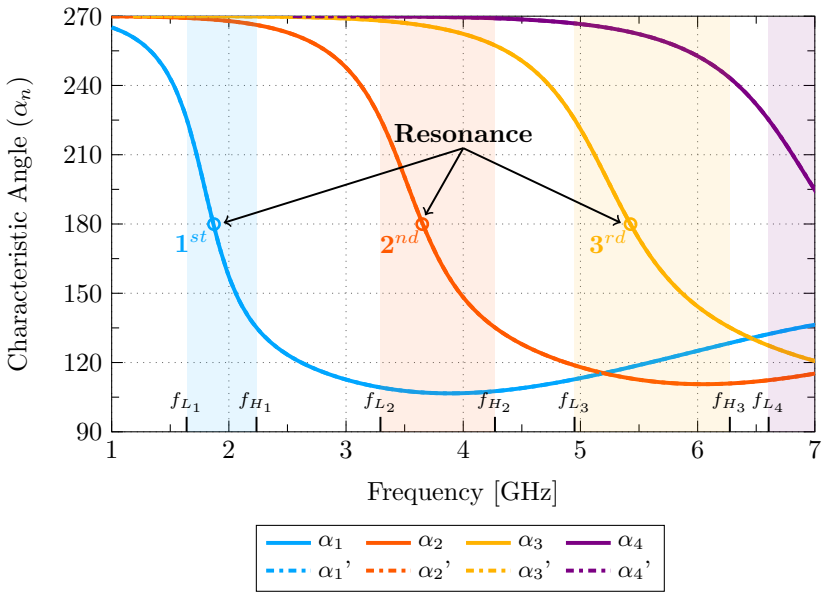

Figure 2.11: Characteristics angles α_n associated to the current modes J_n of the circular metal ring sketched in Fig. 2.5.

Table 2.2: Summary of the physical interpretation of Characteristic Modes

Behaviour	Eigenvalue λ_n	Modal Significance MS_n	Characteristic angle α_n
Inductive	$\lambda_n > 0$	$0 < MS_n > 0$	$90° < \alpha_n > 180°$
Resonance	$\lambda_n = 0$	$MS_n = 1$	$\alpha_n = 180°$
Capacitive	$\lambda_n < 0$	$0 < MS_n > 0$	$180° < \alpha_n > 270°$

an antenna is important that the greatest number of values of the consecutive eigenvalues is approximated to zero.

2.3.4 Excitation of CM

So far, it has been seen that the characteristic modes are obtained through the integral solution of the impedance matrix of an arbitrary structure when it is excited by a plane wave. The resonance frequency, bandwidth, quality factor have been some of the parameters that can be obtained using the TCM. However, it is necessary to determine which modes are excited and what the power contribution is when the structure is excited with a feeding port, for this the structure that has been considered is the same that has been analyzed throughout the chapter including a feeding point.

Then, the method to determine the power contribution of each of the modes that contribute to the bandwidth in which the structure works can be performed based on the impedance Z_{in} or in turn of the input admittance Y_{in} of the antenna [124], and can be calculated through the current J_n when the antenna is excited with a voltage of 1V at the point of feed P as presented below.

$$Y_{in} = \frac{J(P)}{1V} = \sum_n \frac{V_n^i . J_n(P)}{1 + j\lambda} \tag{2.37}$$

The inductance parameter or also called modal admittances can be expressed in phasors or complex terms.

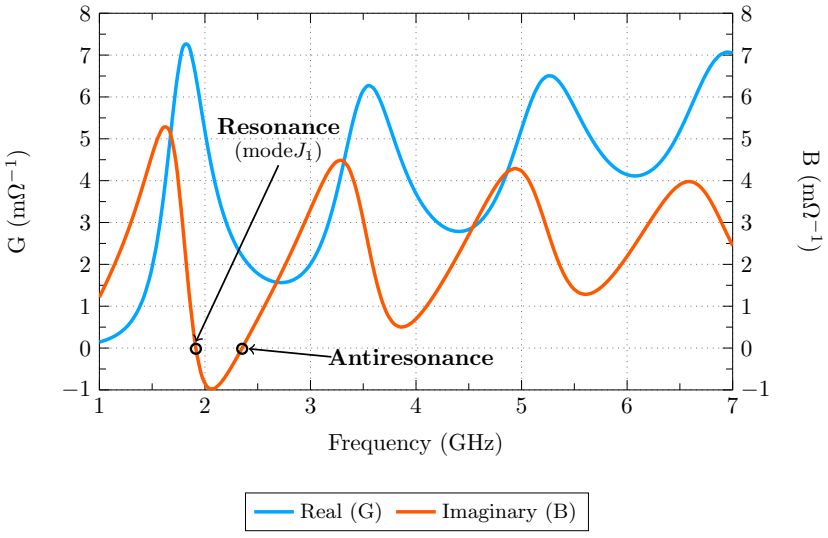

Figure 2.12: Representation of the input admittance Y_{in} of a metallic circular ring with feeding point (a) Real part (G), and (b) Imaginary part (B).

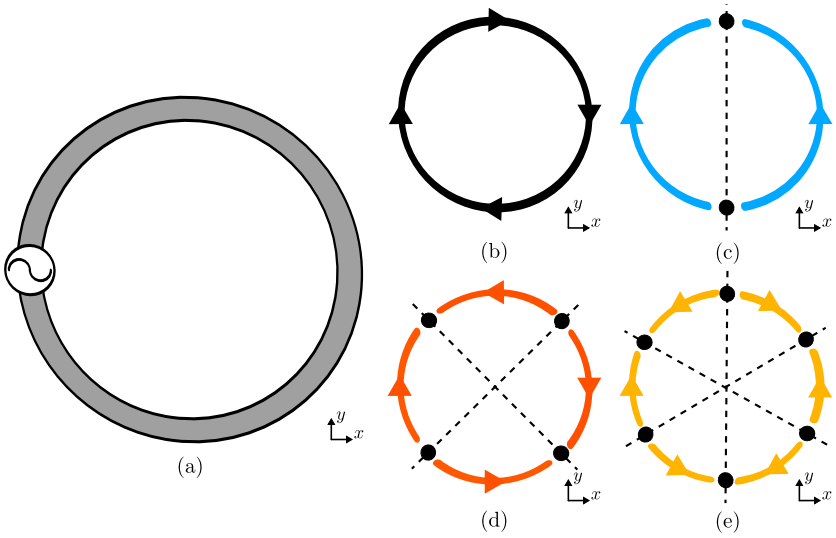

Figure 2.13: Possible first modes that can be excited when a metallic circular ring have an inductive feeding point. b) Mode J_0, c) Mode J_1, d) Mode J_2, e) Mode J_3.

The admittance plot in its real and imaginary part ($Y_n = G_n + jB_n$) associated with the currents that flow surround the structure when it is excited in the left (X-axis) has been represented in Fig. 2.12. The resonances of the structure are described when the imaginary value B is equal to 0, as long as the slope that describes the curve begins in the positive zone and ends in the negative, otherwise it will be considered as an antiresonance.

At the moment when a feeding point is inserted into the structure, the modes that have been previously referred to as degenerate modes (J_n') will not be excited because the current nulls of each mode match with the feeding point in the Y-axis, then, the possible modes that can will be excited with this kind of configuration are shown in Fig. 2.13.

Each one of resonances in the structure are associated with the radiating modes, however, to the case of the circular ring the fundamental mode (J_1) is the mode that it attributes the resonation, it's working frequency is 1.90 GHz, the other modes (see Fig. 2.13) are not been excited because is impedance coupling between the feeding point and the structure is not appropriate, therefore, to excite the higher-order modes, the admittance must be change until to obtain a smooth graph around to 0. On the other hand, the antiresonance that ap-

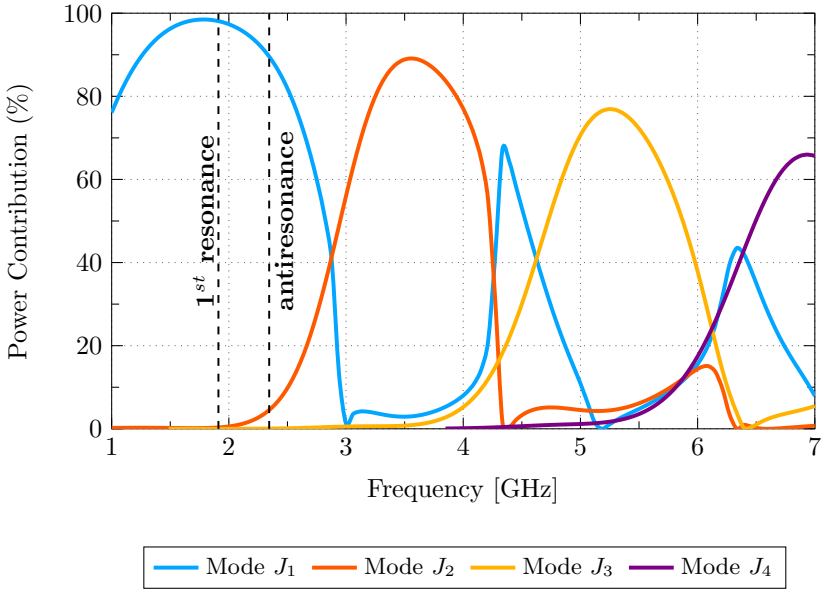

Figure 2.14: Power contribution of the modes in a metallic circular ring with a feeding point

pears at 2.25 GHz according to Fig. 2.12 is generated through the combination of two or several modes.

One of the methods to describe which modes contribute to radiation and the percentage of participation is to use the power contribution of each mode versus the frequency variation graph.

To obtain the power contribution values in terms of percentage, each of the powers generated by the modes must be normalized through the total radiated power. Using the contribution of powers it can be determined in a simple way which modes participate in the resonance, it can be corroborated that for the frequency of 1.9 GHz the mode that is in resonance is the fundamental mode (J_1) and its potential contribution is of 97 % as seen in Fig. 2.14 while anti-resonance appears when there is a combination of modes, the mode with the greatest contribution is still J_1 and with lower power the higher order modes are presented.

Chapter 3

TCM in planar structures

"Design is not just what you see, it is discovering how it works"

— Steve Jobs

3.1 Introduction

In this chapter, a detailed study of several planar structures is carried out using the concepts on the Theory of Characteristic Modes that have been described in the previous chapter.

There are several works in which countless shapes have been studied, among the most popular are: metallic circular plates, metallic rectangular plates, metallic triangles plates, etc [25–27,116]. Therefore, the intention in this chapter is not to be redundant in the studies that have been done previously, but to collect some of these mentioned structures and use them as reference elements in order to generate new structures in which very good characteristics can be obtained such as bandwidth, radiation patterns, polarization, and efficiency.

Then, in Fig. 3.1 a summary has been detailed with the characteristic currents of the first 4 vertical modes (J_0 to J_3) of some structures that will be taken into account as a starting point, the structures that have considered the to development of this chapter are: the circular ring, the circular plate, the square ring, the square plate, and the elliptical plate. Each of the results of the characteristic currents of each of the structures have been organized horizontally, so it is much easier to perform a comparative analysis.

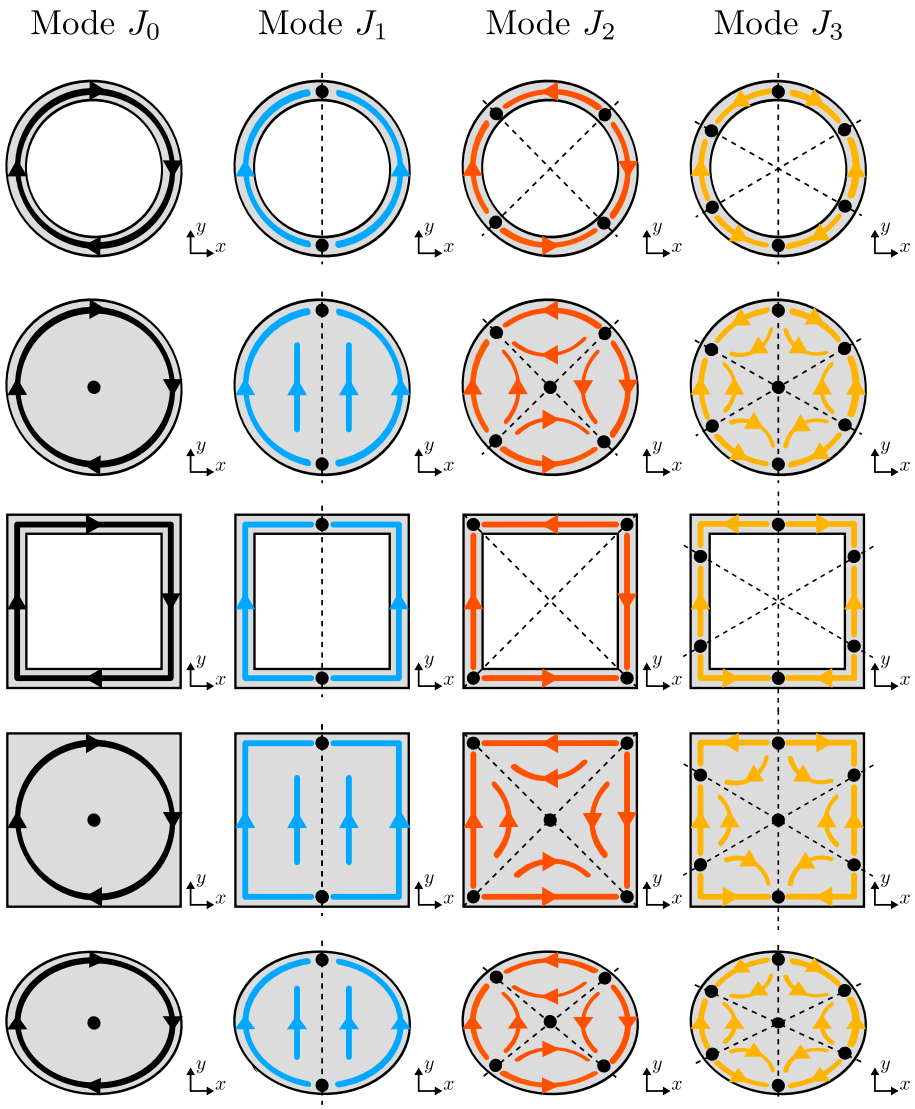

Figure 3.1: Current distribution at 1.9 GHz of the 4 first vertical eigenvectors of several planar geometries

Interpreting each of the columns that are part of Fig. 3.1, it can be seen that, for the fundamental mode or for the higher-order modes, a pattern that repeats for each of them is presented.

In the case of J_0 mode, the currents rotate continuously surround the structure regardless of its shape, and will be present when the value of contour is approximately at 2λ, for J_1 mode as in the previous case, the currents flow along the contour until reaching a pair of nulls, these currents will enter or exit the nulls, the resonance of the structure will be generated when the distance of the contour between each current null is equal to λ; and for the following cases of higher-order modes such as J_2 and J_3 the current nulls will be at a distance of $\lambda/2$ and $\lambda/3$.

In the section below, the analysis of various designs is presented that will be the result of a combination of some structures with the shapes that have been presented in Fig. 3.1. This combination can be integrated by structures with the same or different shape.

3.2 Coupled circular structures

From the mathematical formulation described previously, it has been shown that it is possible to obtain the characteristic modes of any conductive body with arbitrary geometry using Eq. (2.26). The resolution of the equation provides a set of eigencurrents that only depend on the geometry of the body. The eigenvalues obtained with the resolution of this problem provide information on the physical behavior of each mode.

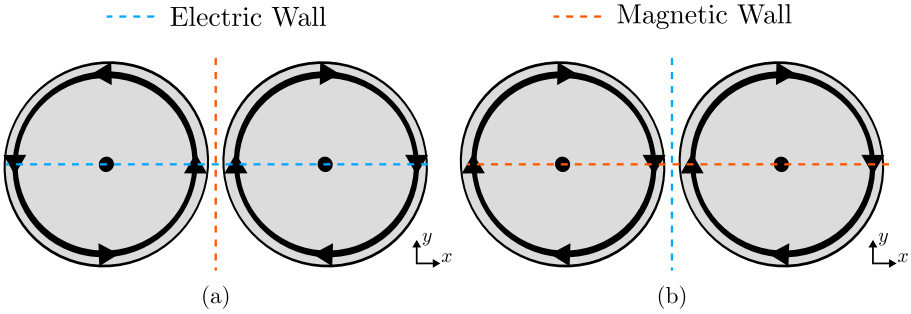

Figure 3.2: The characteristics current of two circular isolated discs applying electric and magnetic wall. (a) Antenna mode J_{00}, and (b) Transmission line mode J_{10}.

When the study structure is composed of two or more elements that have the same or different shape, a set of characteristic currents will be generated by each of the elements that composed the structure. In Fig. 3.2 the characteristic currents of the J_0 mode of two isolated metal rings having the same properties and are separated by an air gap are shown.

It can clearly be seen that a phenomenon is generated between the two elements which in [26] has been described as the antenna mode and the transmission line mode.

This phenomenon can be described very simply by applying an electric or magnetic plane of symmetry between the two isolated elements, placing the structure in front of an electric conductor plane (see Fig. 3.2(a)), the currents must flow in the same direction and be perpendicular to the electric conductor plane to be called an antenna mode, on the other hand, by applying the structure in front of a magnetic conductor plane such as depicted in Fig. 3.2 (b), the currents parallel to the plane must be flowing in the opposite direction, in this case, the modes will be called transmission line modes. It should be a highlight that this phenomenon will be present in each of the modes that are produced in the structure.

To identify the so-called transmission line modes or the antenna modes that appear in the structure when 2 elements are coupled, the nomenclature J_{nm} has been used, where n can acquire the value of 0 or 1, 0 being the antenna mode or 1 the transmission line mode, whereas, sub index m can acquire any real value as long as it is greater than equal to 0.

Analyzing structures that are isolated as in the example shown in Fig. 3.2 does not make much practical sense because an antenna must have one or more excitation points, therefore, inserting a short circuit between them as it can be seen in Fig. 3.3 it is possible to emulate an excitation point without having to change the plane wave as a mean of illumination.

The dimensions of the discs that will analyze are $R = 14.5$ mm, the width of the short circuit strip is $l = 2$ mm and its air gap $g = 1$ mm.

In Fig. 3.4, the characteristic currents that are flowing over the structure composed of two interconnected elements in the central area have been represented. These currents have been plotted according to each of the resonance frequencies, or in the case that the structure does not enter resonance, the currents are represented at a value closer to the characteristic angle $\alpha_{mn} = 180°$. The information about the resonance frequencies has been obtained from the

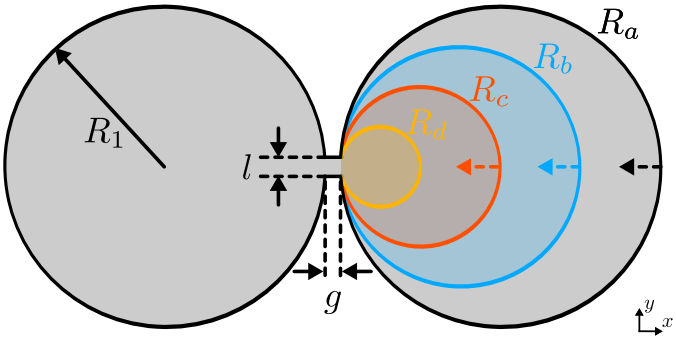

Figure 3.3: Two interconnected nearby circular metal discs.

Table 3.1: Analysis and plot frequencies of two coupled circular discs short-circuited in the middle

Antenna Mode		Transmission line mode		Full structure	
Mode	Frequency	Mode	Frequency	Mode	Frequency
J_{00}	7 GHz	J_{10}	7 GHz	J_1	1.98 GHz
J_{01} or J_{01}'	7 GHz	J_{11}	7 GHz	J_3	7 GHz
J_{02} or J_{02}'	7 GHz	J_{12}	7 GHz	-	-

characteristic angles represented in Fig. 3.4. In Table 3.1 can see a summary detailing the values in which each mode has been plotted.

As expected, the families of the antenna modes J_{0m} and the transmission line modes J_{1m} are present (see Fig. 3.4(a) and 3.4(b)), however, at the moment in which a short circuit is made between the elements that are part of the structure, the currents can flow continuously between them, these types of modes that have this distribution will use the nomenclature J_m, where m can be any integer value. For the short-circuited structure, only the J_1 and J_3 mode has been represented as can be seen in Fig. 3.4 (c), the J_2 mode has not been plotted because its current distribution matches with that of the J_{01}, it is not so easy to be able to make this analogy, so later an analysis of the structure

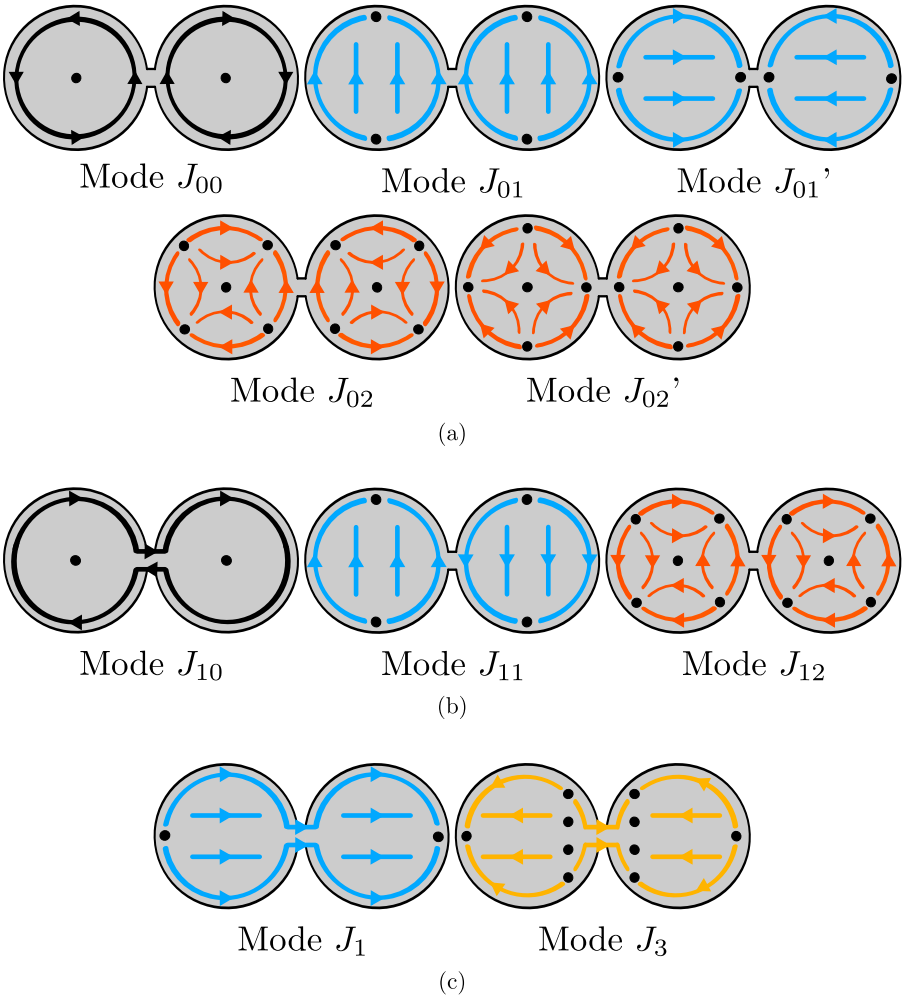

Figure 3.4: The characteristic current distribution of the two interconnected circular metal discs. (a) Analysis using the electric wall, (b) using a magnetic wall, and (c) current distribution on the full structure.

will be carried out breaking the symmetry in the vertical axis to clarify this criterion.

Then, for the frequency range of 1 to 7 GHz in which the structure has been analyzed as described in Fig. 3.5, only mode J_1 is in resonance with a bandwidth

of 53 %, the other modes are storing capacitive energy or inductive energy, for example by its behavior in the case of the J_{00} and J_{10} modes describe an inductive storage. Due to the way in which the currents flow in the analyzed structure, the modes J_1 and J_3 are the modes that could be excited in the event that the power point is located in the short-circuit area, these modes will become at the point of interest and study.

The mode J_1 will be present when the total perimeter of the structure has a value 2λ of the resonant frequency, if there is a variation of one of the elements that are part of the structure, the frequency will also be shifted, to verify this argues, has performed a parametric analysis of the structure according to what is represented in Fig. 3.3 by varying one of the 2 discs, the moment the structure's perimeter value is reduced ($R_a = 30$ mm, $R_b = 3/4\ R_a$, $R_c = 1/2\ R_a$, $R_d = 1/4\ R_a$), it will resonate at a higher frequency each time as the radius of one of the disks decreases. On the other hand, as previously mentioned, at the time of breaking the symmetry in the case of J_2 mode, its distribution can be seen in a much simpler way because the current nulls do not coincide with the

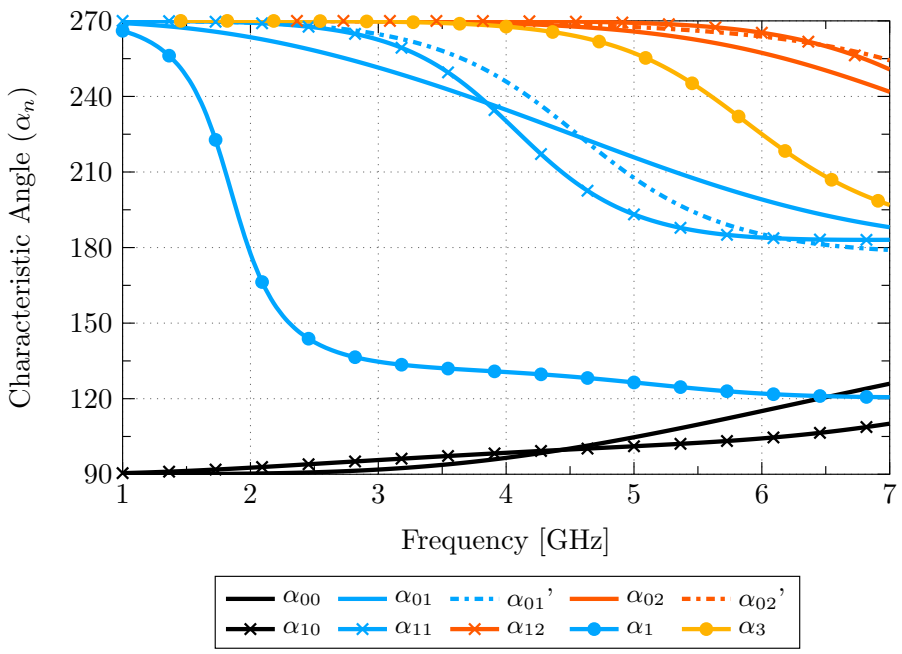

Figure 3.5: The characteristic angle of the two symmetrical interconnected discs.

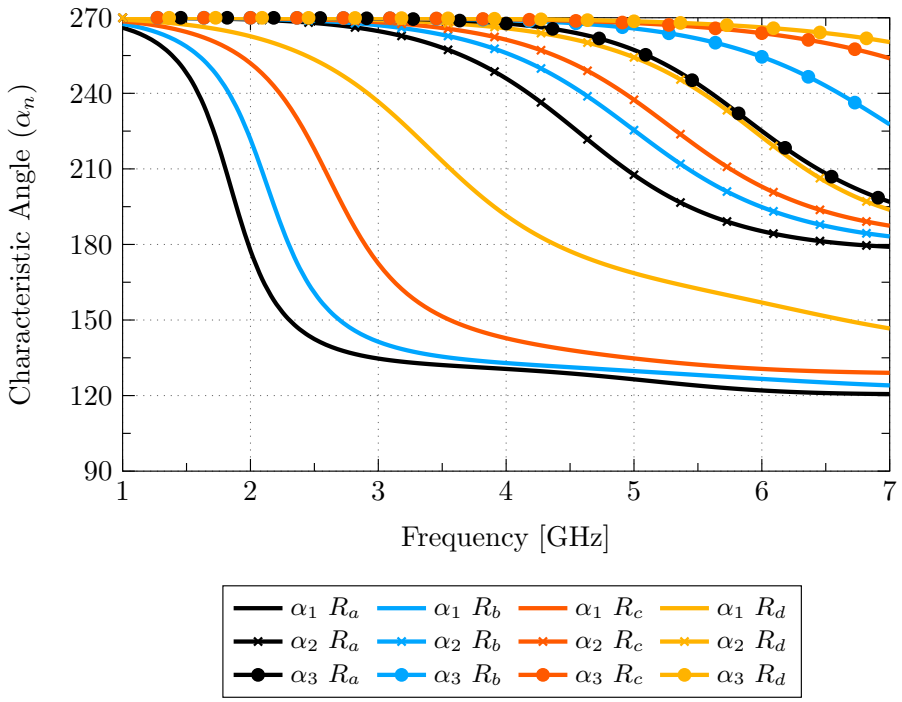

Figure 3.6: The characteristic angle comparison of the two interconnected discs when the radius of one of them is variating (R_a = 30 mm, R_b = 3/4 R_a, R_c = 1/2 R_a, R_d = 1/4 R_a)

area of the short circuit, so if a feeding point is inserted, not only odd modes can be excited but also even modes.

In the structure analyzed, the element with a larger radius can be replaced by one with different shape, and that can be coupled by one or multiple resonant elements, in the next section, a sample will be analyzed.

3.3 Monopoles coupled a metallic ring

It has seen that by short-circuiting 2 elements, three families of modes can be generated: the transmission line modes, the antenna modes and the modes that flow throughout the structure, the latter being those of interest, in this section it is intended to show the behaviour of the modes of a structure composed of three coupled elements. The proposal is given by a circular ring that is

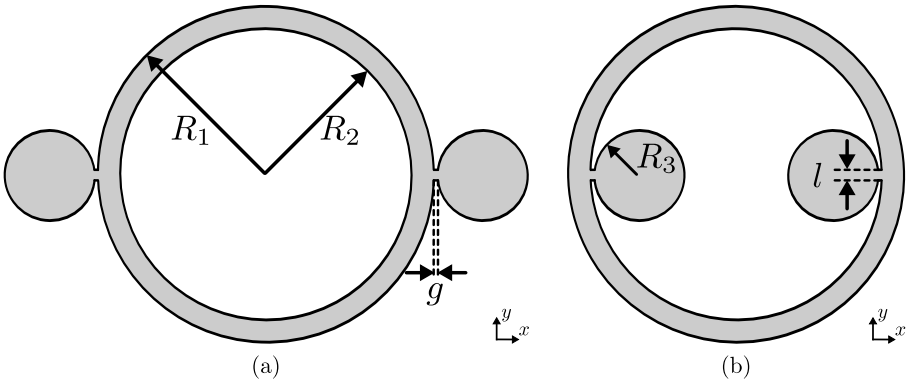

Figure 3.7: Circular ring coupled two circular monopoles. (a) External coupled, and (b) Internal coupled.

externally and internally coupled to two small circular monopoles. The first option will be called structure A and the second as structure B

The dimensions of the proposed structure according to Fig. 3.7 are: external radius $R_1 = 30$ mm, internal radius $R_2 = 26$ mm, gap $g = 0.5$ mm, coupling elements $R_3 = 8$ mm and the transmission line $l = 1$ mm.

The distribution of the characteristic currents analyzed for the two types of proposed configurations, the first with external coupling and the second with internal coupling have been described in Fig. 3.7. As expected, the flow of the currents of the first 4 modes in both cases describes a very similar behaviour. However, if a comparison is made with the characteristic angles (see Fig. 3.9), it can be seen that there is a great difference between the two configurations. The slopes that represent the characteristic angles of the structure that the internal couplers have are much smoother when they pass from the capacitive to the inductive part, this means that with internally coupled elements, modes with greater bandwidth can be generated than structures with coupling internal. Therefore, to design antennas with a large bandwidth, elements that have an internal coupling should be used.

A summary of the resonant frequencies at which the characteristic currents have been plotted of Fig. 3.8 and their available bandwidths for the two configurations analyzed has been made in Table 3.2.

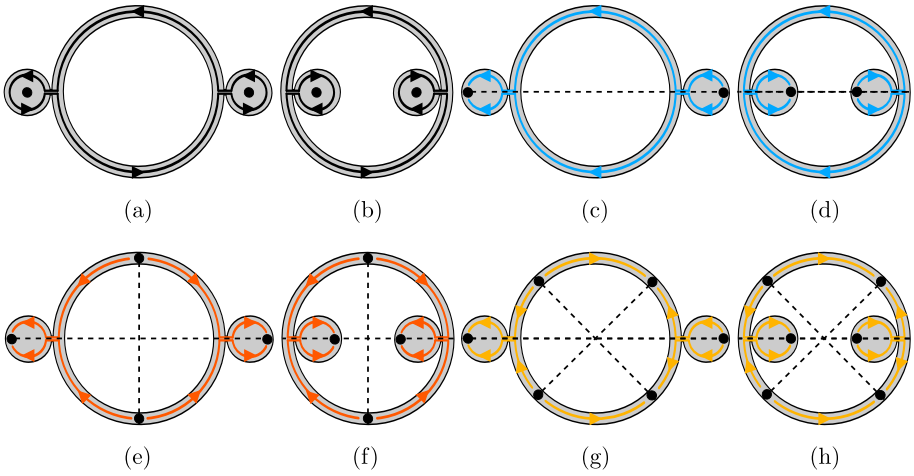

Figure 3.8: The Characteristic current distribution comparison analyzed in horizontal polarization of the three first modes of the metallic ring coupled external and internal form by two monopoles. (a) (b) Mode J_0, (c) (d) Mode J_1, (e) (f) Mode J_2 and (g) (h) Mode J_3

On the other hand, at the same frequency in which the characteristic currents were analyzed, the radiation patterns have been generated for the first 4 modes of the two structures studied, the comparative analysis of the two structures are illustrated in Fig. 3.10. It is shown that for both mode J_0 and mode J_1, the radiation patterns are very similar, however, modes J_2 and J_3 there is a big difference and this is due to the way in which the coupled elements are located in the structure.

At the moment in which the resonant elements were placed inside the structure, the currents that flow over the monopoles and the circular ring are in the opposite direction, causing a cancellation of the currents and that can be interpreted as a virtual current null such as seen in Fig. 3.11. This configuration is very helpful because it allows generating radiation patterns with very good characteristics even when working in higher-order modes, for example in the case of J_3 mode in the Fig. 3.10, the radiation pattern that is generated is in the broadside direction. With this type of behavior is possible to design antennas with a very good bandwidth and radiation pattern stability as the structure is excited.

In addition to the capacitive coupling through the circular monopole that has been studied previously, there are some alternative shapes that can be used to excite the circular ring, among them there are: the ellipse, the triangle that is very similar to a piece of cheese and the square as shown in Fig. 3.12.

To realize a comparative analysis and be able to describe which of the forms that have been proposed generate the best characteristic, optimization of each of them has been carried out until their resonance frequencies corresponding to the fundamental mode matches with the resonant frequency of the structure excited through the circular shape. Therefore, in Fig. 3.13 the first 4 characteristic angles of each of the proposed shapes have been represented compared to the circular feed.

Hence, in Fig. 3.13 a comparative plot of the first 4 characteristic angles in horizontal polarization of each of the forms proposed in Fig. 3.12 has been made together with the excitation using a circular coupling. Each of the structures have been classified through a particular color as described by the legend that is located inside the graph.

As expected, each of the modes from mode J_1 to mode J_4 that have been shown, have very similar behavior and a resonant frequency that is very close

Table 3.2: Analysis and plot frequencies of two coupled circular discs short-circuited in the center

	External coupling		Internal coupling	
Mode	Freq. [GHz]	BW [%]	Freq. [GHz]	BW [%]
J_0	5.4	-	5.4	-
J_1	1.39	12.21	1.49	13.68
J_2	2.47	19.25	2.72	4.03
J_3	3.48	12.69	3.94	22.67
J_4	4.71	9.46	5.14	36.06

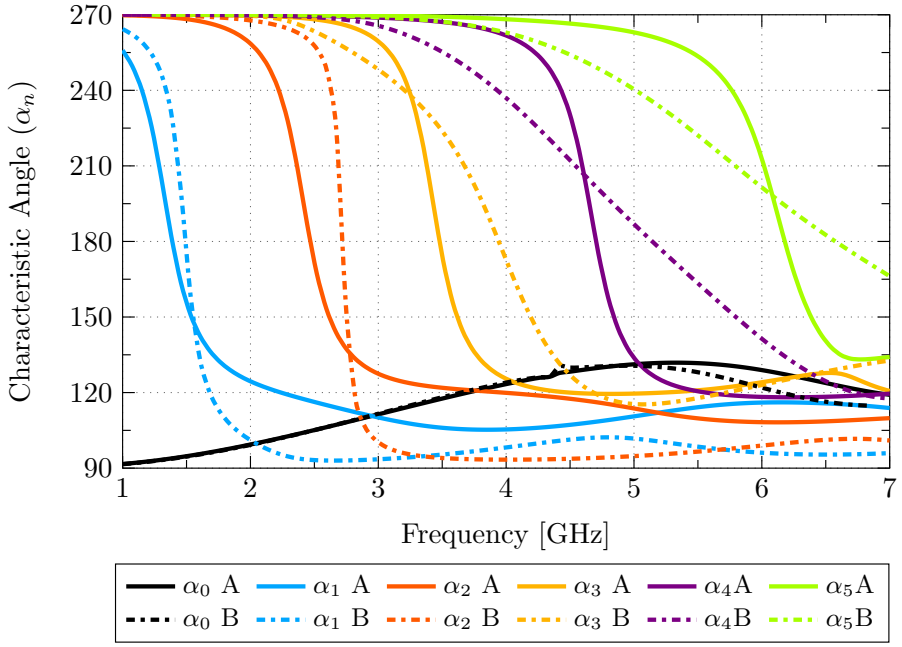

Figure 3.9: The characteristic angles of the metallic ring coupled external and internal form by two monopoles, drawn only in the horizontal polarization.

to each other, however, despite their proximity, there is a minimum variation. In order to determine this variation and describe which of the shapes has better behavior, a summary of the bandwidth has been made in Table 3.3 using the Eq. (2.32) and taking as reference the characteristic angles between 135° to 225°

Analyzing each of the terms that are part of the table in which the bandwidth of each of the modes are depicted (J_1 to J_4), it can be described that for J_1 mode, the best bandwidth is obtained when triangular feeding is used, for J_2 and J_4 when the circular ring is being excited by the circle, whereas, in the case of J_3 mode, the best bandwidth is obtained when the feeding form has the square shape. Thus, performing an evaluation in general, the method that allows generating the best bandwidth is when the circular ring is fed by a circle. Obviously, the results obtained corresponding to the distribution of characteristic currents and the characteristic radiation patterns of each of the shapes that have been proposed, describe the same behavior of the capacitive coupling case using the circular monopole, as presented in Fig. 3.8 and 3.10.

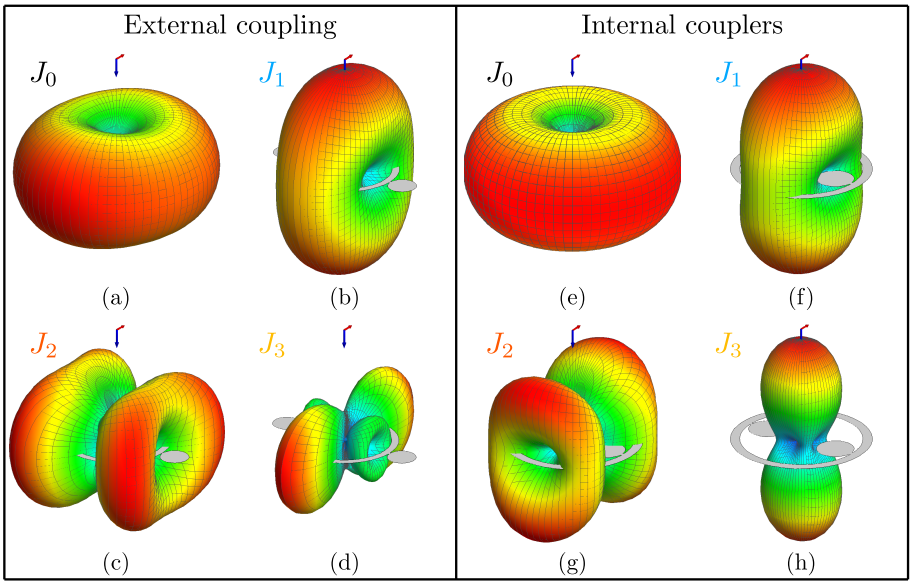

Figure 3.10: 3D Radiation pattern of the structures with external and internal coupling

On the other hand, by modifying in a certain way the geometry of the analyzed model, a new structure with similar behavior and characteristics can be generated, whether in bandwidth, current distribution or radiation patterns. This proposal alternative or denominated model B as well has been obtained

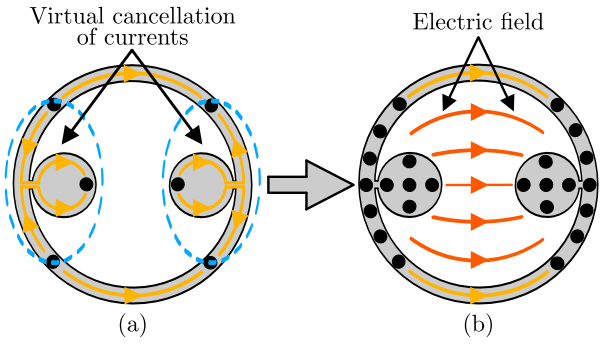

Figure 3.11: Virtual current null described in J_3 mode in the structure with internal coupling

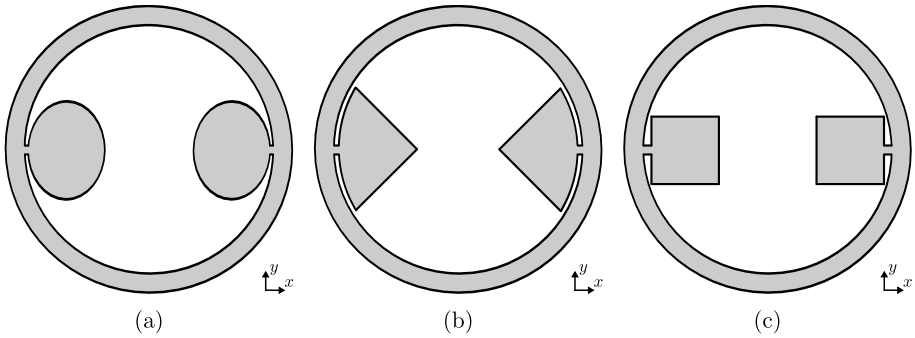

Figure 3.12: Alternative shapes to excite a circular ring.

through elongation and deformation of the reference structure (model A) until it has the shape of a square ring, creating a square ring circumscribed to a circular ring as seen in Fig. 3.14 (a) and (b). The optimized parameters of this new proposal are $L = 2 * R_1 = 60$ mm, $W = 2 * R_3 = 16$ mm, $w = 4$ mm and $l = 1$ mm.

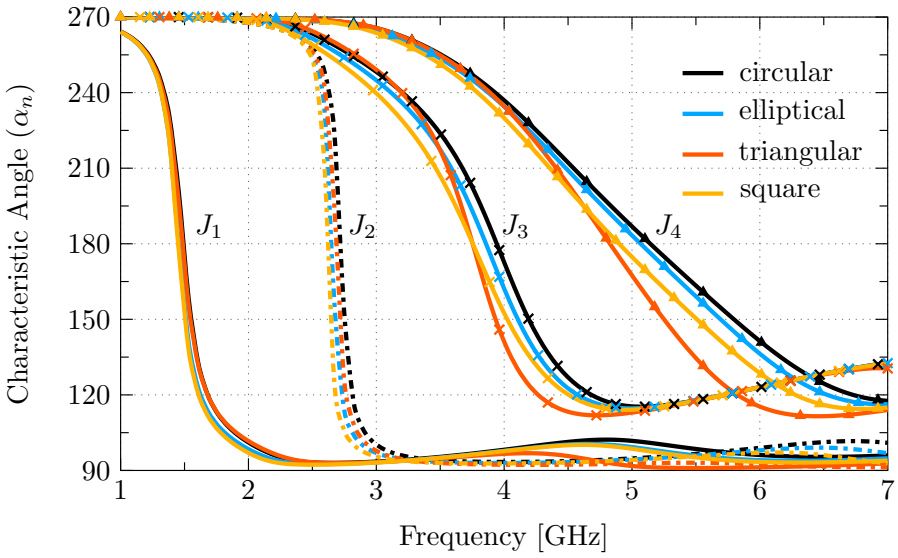

Figure 3.13: Comparative plot of the characteristic angles using different shapes to excite the circular ring with capacitive coupling.

Table 3.3: Comparative summary of the bandwidths of the different shapes to excite the circular ring with capacitive coupling.

Mode	Circle	Elliptical	Triangular	Square
J_1	13.33	11.52	14.04	11.68
J_2	4.25	4.14	4.11	3.55
J_3	22.67	23.20	17.11	24.89
J_4	36.7	35.77	27.32	35.25

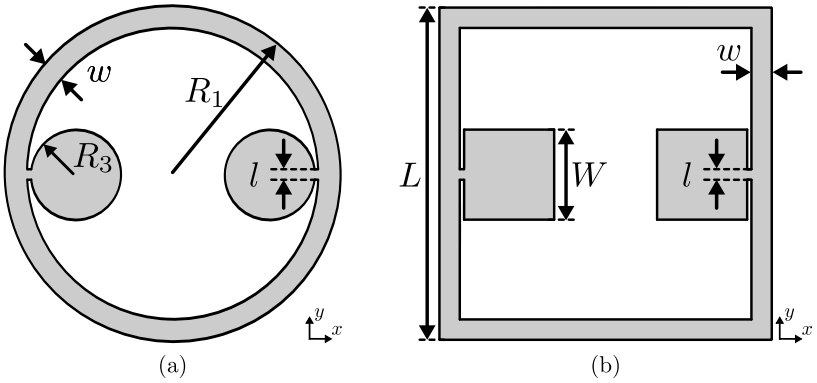

Figure 3.14: Physical set up of the proposed structures. (a) Model A and (b) Model B

The first 5 characteristic angles obtained in vertical polarization that emerge from the modal analysis performed on each of the 2 structures (model A and model B) have been contrasted between them in Fig. 3.15. Although its edges physically matched, the variation in frequency of the structure called model B with respect to model A is very clear, which means that the effective length surrounding model B is greater than the perimeter of model A, therefore, if the values of the square ring are re-optimized i.e. the size is reduced, resonances can be achieved at approximate frequencies for each of the analysis modes of the circular shape.

Taking the results of Fig. 3.14 it can be seen that the bandwidths of the circular ring structure (model A) are slightly larger than those of the square ring (model B), this is due to the coupling form that is generated between the circular ring and the monopole, then, it can be said that the currents flow better and very subtle form in structures that are circular shape rather than in a square, because in the square the coupling that is generated between in the zones of the ring and the monopole is lower, further the losses due to dispersion at the edge of the square structure.

At this point, using the theory of characteristic modes, it has been seen that the combination of a circular ring fed with a circular monopole is capable of generating very good characteristics in bandwidth and also in radiation patterns, it should be emphasized that these have been calculated in the absence of any specific source or excitation. However, we must not only stay in the modal analysis, but use it as a structure to work in transmission mode, therefore, the next step is to decide how to feed the structure in order to excite the modes that provide a desired behavior such as the type of polarization, pattern

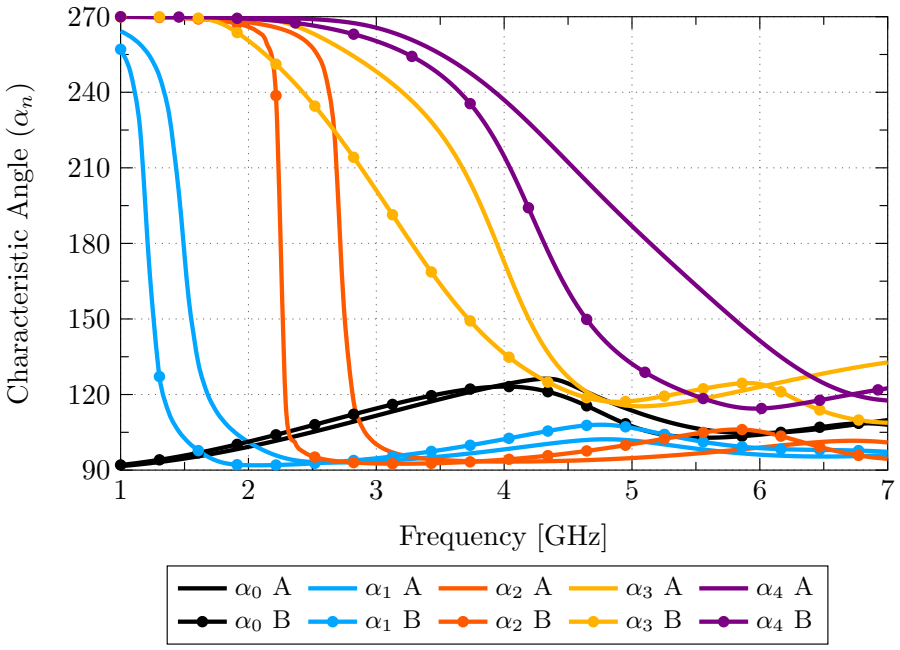

Figure 3.15: Comparison of characteristic angles of the proposed structures. Where A represents the circular model and B depict the square model

diversity, etc. So for the structure to work in transmission mode it must be stimulated, and one or more feeding points can be used [52] [23].

Hence, in order to describe the behavior of the structure shown in Fig. 3.14 (a), the modal analysis of the metallic circular ring that has been presented in Fig. 3.1 will be used. There are 2 types of mechanisms in which a structure can be fed, through a capacitive coupling or an inductive coupling, as has been proposed in previous works that were applied in mobile terminals [125] [126].

For example, to excite the J_1 or J_1' mode of the circular ring through an inductive coupling, the source or feeding point must be placed in the area where the characteristic current of the mode has the greatest intensity, so that, to insert the source a air gap must be made in the structure. Otherwise, for the alternative feed through the capacitive coupling, the source must be inserted in the areas where the characteristic currents of the surface are nulls, for this case, it is not necessary to make an air gap into the structure but simply it can mount a feeder of any shape over the circular ring, thus generating a multi-layer model

It should be taken into account that the polarization of the feeding points is critical, for example in the case of inductive sources polarized vertically at points with maximum current, the Characteristic Modes with maximum current distribution for horizontal polarization at this point will not excite. Consequently, the magnitude, polarization, and the symmetries exhibited by the modal current distributions are important for the excitation of the Characteristic Modes.

Considering the odd and even symmetries that describe the characteristic currents in the circular ring (see Fig. 3.1), an excitation of certain modes can be achieved and even the excitation of unwanted modes can be avoided. This characteristic could only get if multiple feeding points are used to excite the radiant structure, establishing its magnitude and phase value according to the desired symmetry condition for the modes in the structure.

Then, using symmetries the modes represented in the structure can be classified as odd and even modes, therefore, based on the above, the structure is shown in Fig. 3.16 proposes 2 alternatives to capacitive feed the structure and achieve the symmetries previously mentioned, the first is commonly, where the amplitude and phase for each of the ports is the same (+1, +1), on the other hand, the differentially, that although the amplitude has the same value, the phase will have a 180° variation for each of the ports (+1, -1). The ports (Port1, Port2) are placed along the vertical axis of symmetry of the structure.

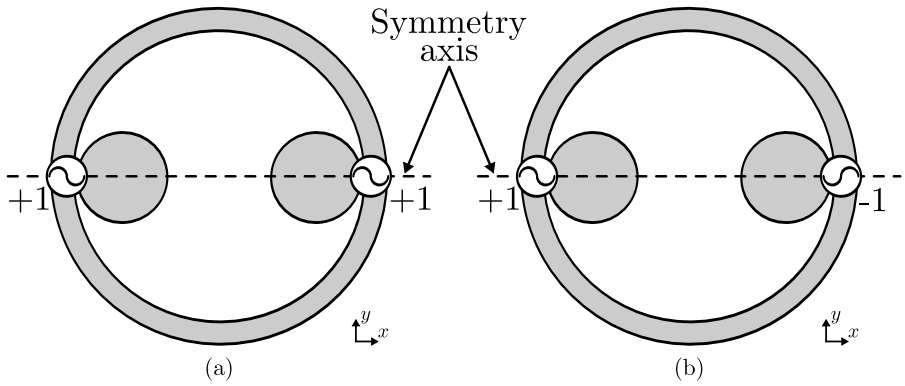

Figure 3.16: Vertical symmetry conditions imposed for the feeding set up. (a) Common feed (sources with the same magnitude and phase). (b) Differential feed (sources with the same magnitude but opposite phase)

Using the first configuration shown in Fig. 3.16 (a) where the ports are being fed in common or also called balanced feed (+1, +1), the modes that can be excited are the modes with even symmetry, among these are the J_2, J_4, J_6, etc, thus discriminating the modes with odd symmetry. Otherwise, the differential feed configuration should be used such as shown in Fig. 3.16 (b), thus exciting only the modes that converge with the odd symmetry J_1, J_3, J_5, etc. This last configuration being the most optimal for various applications that will be detailed later.

In Fig. 3.17, the characteristic angles generated of each one of the 2 proposed configurations have been represented, in the left image, the modes that are excited when the ports are fed differentially have been described, meantime, on the right side the modes generated by common or balanced feeding. These two graphs finally become a decomposition of all vertical polarization modes present when the structure is being illuminated by a plane wave.

Now, once information on the behaviour of the model has been obtained through the characteristic modes, it must be evaluated using a full-wave analysis in order to know its resonance frequency when the antenna works like a radiator, as it mentioned in the previous chapter, some of the ways to obtain the value of the resonant frequency in a structure is through its scattering parameters or the complex impedance values. In Fig. 3.18, the real and imaginary parts of the impedance have been plotted versus the frequency of the proposed structure excited with differential feeding ports (+1, -1).

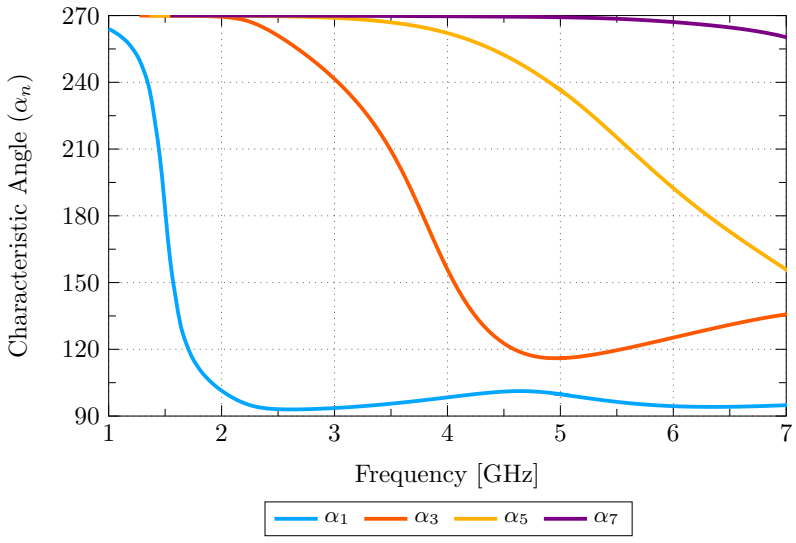

(a)

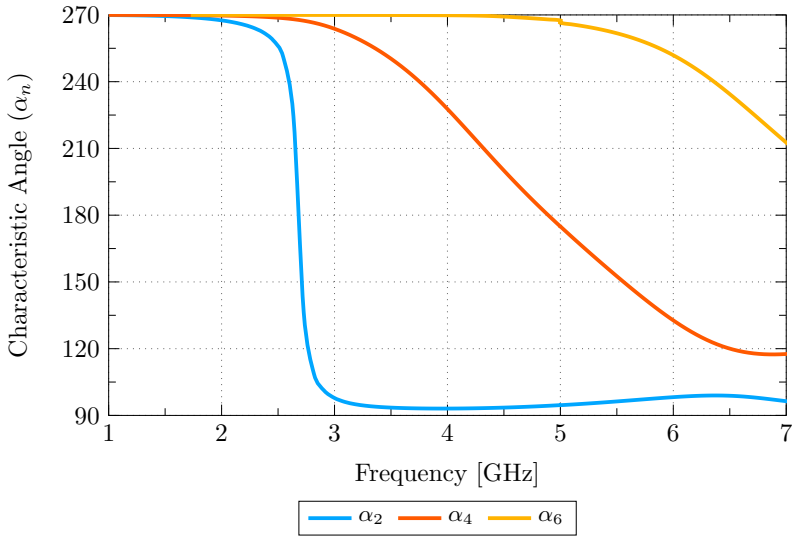

(b)

Figure 3.17: Characteristic angles of the circular metallic ring structure capacitively coupled by a circular monopole. (a) Differential feeding, (b) balanced feeding.

It is said that a structure is in resonance when the imaginary part of the impedance is equal to 0 Ω in its upward slope, on the other hand, if this slope has a downward behaviour and acquires the value of 0 Ω it is known as an anti-resonance. The first frequency in which the antenna is in resonance is approximately at 1.6 GHz, it can be seen that at this frequency the imaginary part does not cross by 0 Ω but it is very close to this value, generating a very limited bandwidth when the antenna is coupled to 50 Ω. Whereas, at the frequency of 3.87 GHz where the second resonance is available, the antenna is very well coupled and generates a bandwidth greater than the previous one because the slope is not very pronounced when passing from the negative to the positive part.

Using the Fig. 3.19, it is possible to know which modes are those that participate in each of the resonant frequencies, in addition to their contribution percentage. So, for the first resonance frequency (at 1.6 GHz), the predominant is the mode J_1 with a contribution of 100 %, it has this contribution percentage because precisely the resonance frequency of the characteristic mode J_1 of Fig. 3.19(a) coincides with the resonance obtained through the full-wave anal-

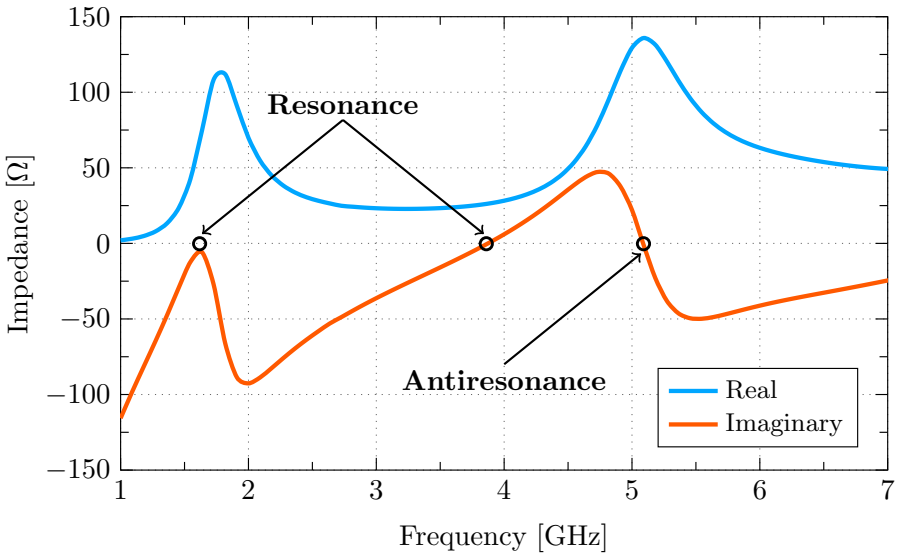

Figure 3.18: Real and imaginary part of the characteristic impedance of a circular ring excited by two circular capacitive couplings with differential feeding (+1, -1).

ysis of Fig. 3.18 (imaginary part), this should be mentioned because it does not always happen that the 2 frequencies coincide and there is a contribution of 100 %, generally for the resonances, there is a combination of multiple modes, for example, in the case of the second resonance at 3.87 GHz, according to Fig. 3.19, it is necessary to combine 2 modes in order to generate resonance, the mode J_3 that is predominant with a contribution of 97 % and the mode J_1 that despite entering resonance at low frequencies is contributing with a 2.68 %.

Indirectly, by saying that there is a combination of modes to generate a resonance, allusions are being made that both the radiation pattern and the current distribution on the surface are also the product of the same combination. Therefore, according to the Eq. (2.30), to describe the total radiation patterns or the total current distributions that appear in the structure, the superposition of the characteristic currents or characteristic fields is used, such as depicted below:

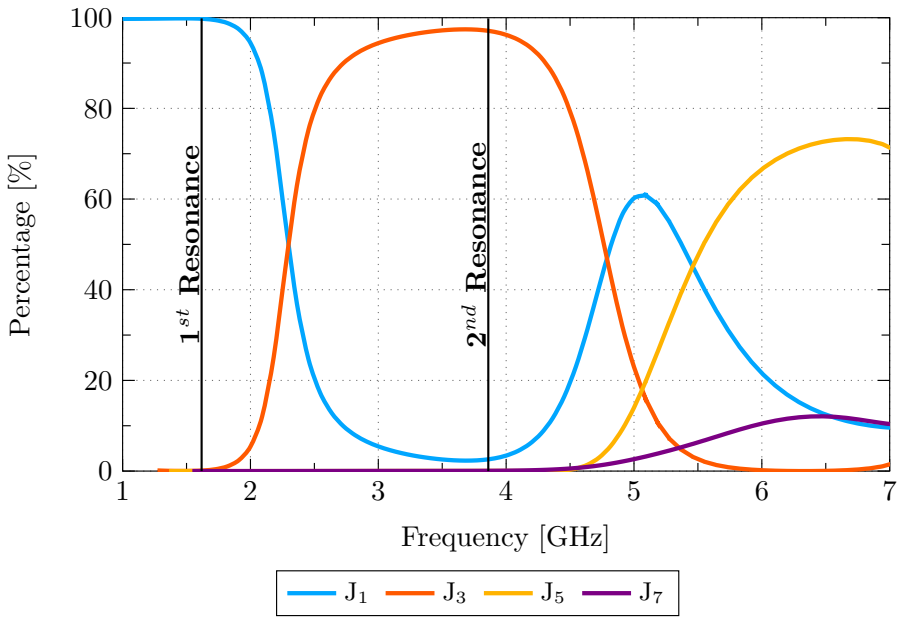

Figure 3.19: Power contribution versus frequency of a circular ring excited by two circular capacitive couplings with differential feeding (+1, -1)

$$\mathbf{J} = \sum_n a_n \mathbf{J}_n \qquad \text{or} \qquad \mathbf{E} = \sum_n a_n \mathbf{E}_n$$

For either case, through the mathematical formulation presented, it is being dependent on the a_n variable, which is referred to as the modal weight coefficient, these values have been represented in Fig. 3.20.

At each of the frequencies in which the antenna is in resonance, the modal weight coefficient acquires a value, at the frequency of 1.55 GHz in which only mode J_1 intervenes, the value of $a_1 = 0.204$, whereas, at 3.85 GHz, the 2 modes that contribute to resonance take the value of $a_1 = 0.004$ and $a_3 = 0.2718$. These values multiplied by the modal current matrix or characteristic field matrix, allow obtaining the total current and the total field at each resonance frequencies [127], [128], such as described in Fig.3.21.

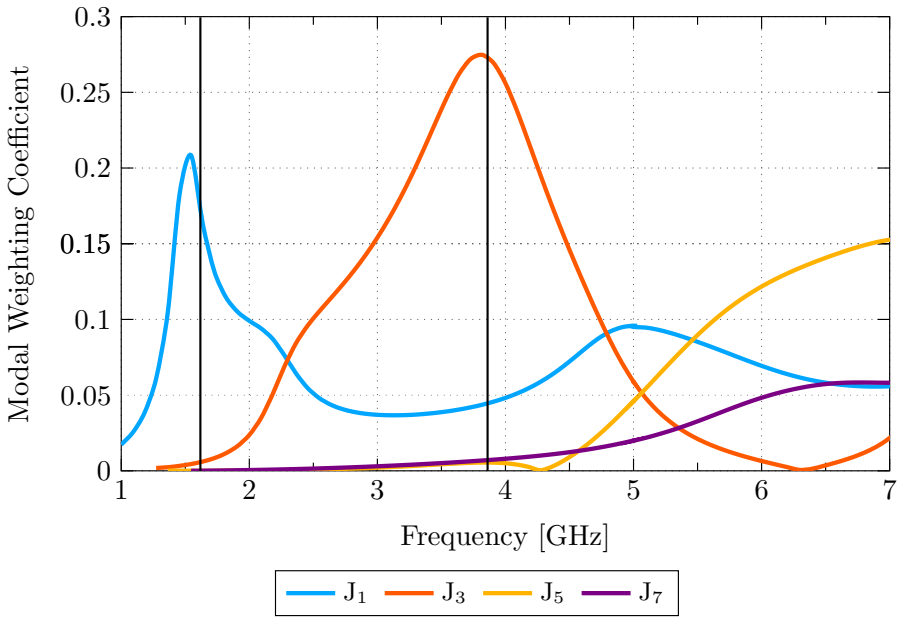

Figure 3.20: Modal Weighting Coefficient of a circular ring excited by two circular capacitive couplings with differential feeding (+1, -1)

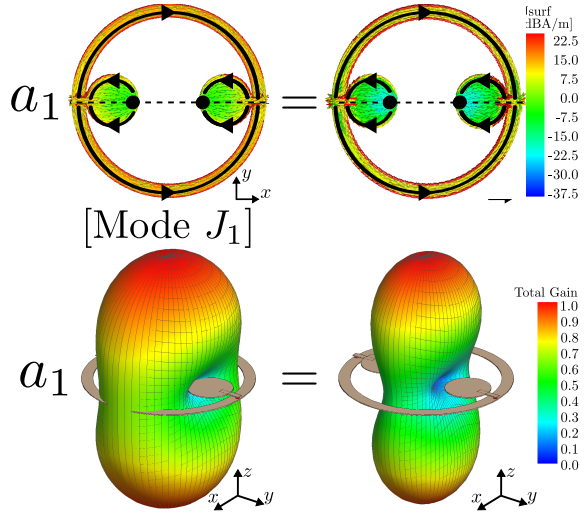

(a)

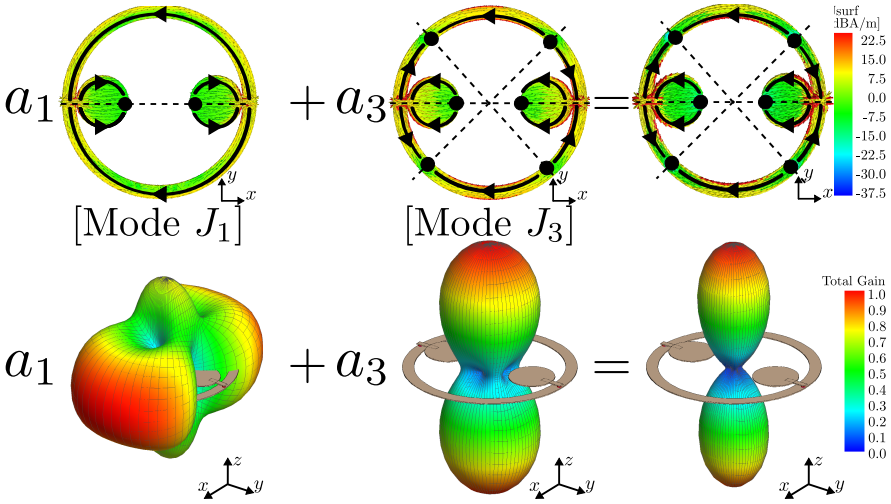

(b)

Figure 3.21: Total current and total field of a circular ring excited by two circular capacitive couplings with differential feeding (+1, -1). (a) At 1.55 GHz and, (b) at 3.85 GHz.

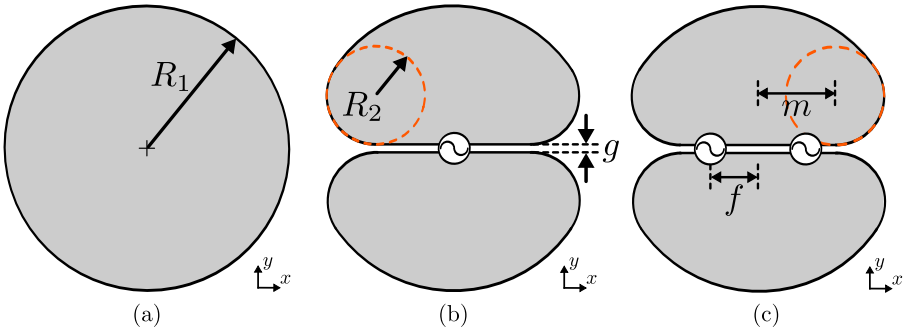

Figure 3.22: Evolution of the coupled semi-circular structures. (a) First step: circular disk, (b) second step: two semi-circular shapes with a feeding port and, (c) third step: two semi-circular shapes with two feeding ports in parallel.

3.4 Coupled semi-circular structures with parallel feed

Another alternative structure that is going to be analyzed in this section, follows from the circular metal disk that was previously described in Fig. 3.1. While it is true, the modes of this structure are well known, so, taking advantage of this preliminary knowledge, an antenna will be designed that will have a large bandwidth with a very stable radiation pattern in the broadside direction.

One of the simplest ways that can be used to excite this type of structure is inserting a horizontal slot in it, the feeding point is located in the middle as shown in Fig. 3.22(b), in addition, to somehow avoid the singularities that occur at the edges where the slot was made, and so that the currents flow very smoothly over the surface, a deformation has been made that is linked to a circle of radius R_2. The coefficient of reflection of the structure with a feeding point has been shown with a light blue line in Fig. 3.23, it can see clearly be that it is very well matched to -6 dB and that it has a large bandwidth.

However, the main goal with this structure is to achieve a great bandwidth, that it is coupled below at -10 dB, in order to fulfill this purpose another extra feeding point to the existing one has been inserted as suggested in [53] and, further, the optimization of each parameter has been optimized. The final dimensions for this proposed structure are greater radius $R_1 = 30$ mm, air gap $g = 1.5$ mm, internal deformation radius $R_2 = 10.46$ mm and its shift from the center of the structure $m = 16$ mm, location of the feeding points $f = 10$ mm.

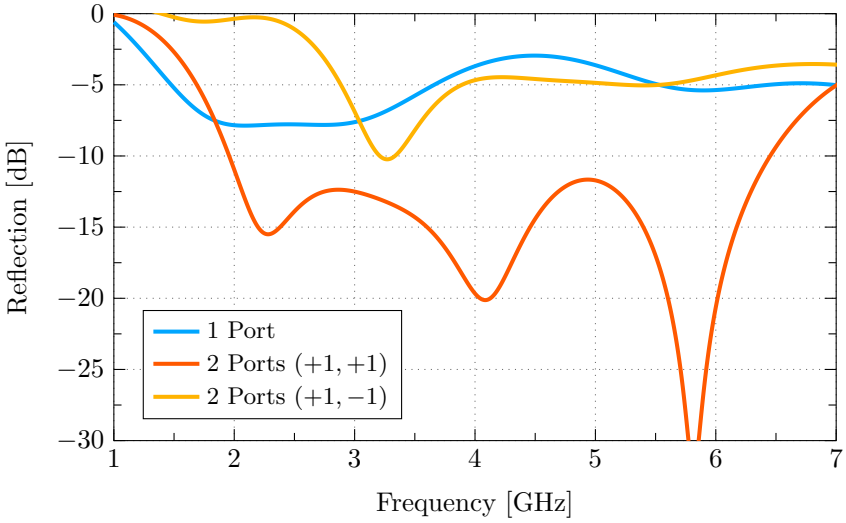

Figure 3.23: Reflection coefficients of the two semi-circular structures using one and two feeding ports (odd and even feed).

With the location of the two excitation points, two feeding alternatives are generated, the balanced and the differential or also known as even and odd feeding, the scattering parameters corresponding to these two forms of feeding can be obtained through the combination of the S-Parameters generated in each port through a full-wave analysis, and those are linked to the following mathematical formulation [129], [130], [131]:

$$\Gamma_{odd} = \frac{1}{2}(S_{11} - S_{21} + S_{22} - S_{12}) \tag{3.1}$$

$$\Gamma_{even} = \frac{1}{2}(S_{11} + S_{21} + S_{22} + S_{12}) \tag{3.2}$$

for cases where the parameters are completely symmetric and balanced (i.e. $S_{11} = S_{22}$ and $S_{21} = S_{12}$), the equation can be reduced and written as follows:

$$\Gamma_{odd} = \frac{1}{2}(S_{11} - S_{21}) \tag{3.3}$$

$$\Gamma_{even} = \frac{1}{2}(S_{11} + S_{21}) \tag{3.4}$$

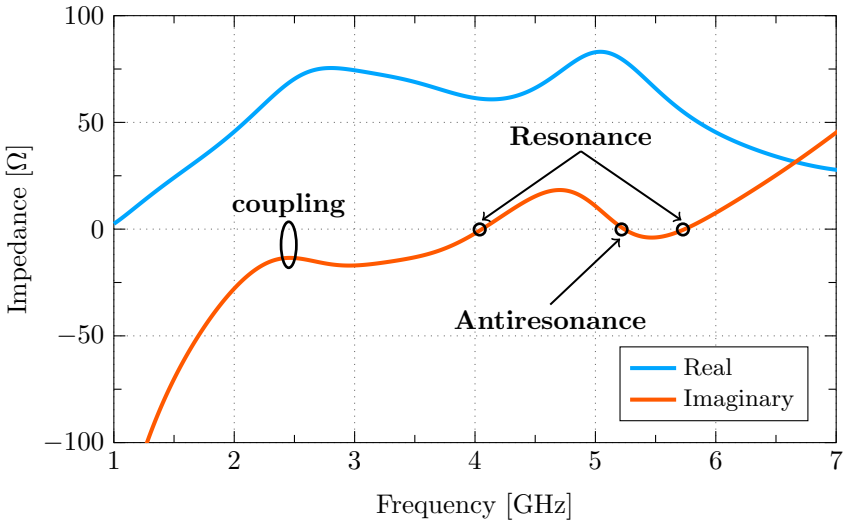

Figure 3.24: Real and Imaginary part of the two semi-circular shapes with two feeding ports (+1, +1).

The reflection coefficients for both the common and differential mode have been depicted in Fig. 3.23. It can clearly be seen that using the even excitation (+1, +1), the antenna is capable of generating a very good bandwidth if it is used as a radiator, the frequencies range for this structure is from 1.95 GHz to 6.45 GHz which represents 107.14 %. It is very noticeable that there are 3 frequencies in which there is a very good coupling, approximately the first resonance is around 2.27 GHz, the second at 4.07 GHz and the third at 5.81 GHz.

By contrasting these frequencies with those that can be generated in Fig. 3.24 when the impedance in its imaginary part is equal to 0, we can see that its values for both the second and third resonance (4.07 GHz and 5.81 GHz) matching exactly, however, for the first resonance, there is no relationship because in none case, the impedance values acquire the value of 0, nevertheless, there is a strong coupling that allows generating a resonance.

Once the full-wave analysis has been carried out, it is appropriate to describe how many and which are the modes involved in the generation of each of the resonances previously described, in addition, of the contribution of each mode through their power percentages. Therefore, in Fig. 3.25, the modes that are involved in the frequency range of 1 to 7 GHz have been specified, for each of the resonances marked with the black vertical line, it is appreciated that the

mode J_1 is the most important because it is involved in the three resonances, for example for resonance at 2.46 GHz, there is a contribution of 99.8 %, while the other 0.2 % is the product of the combination of the other modes. In the case of the second resonance at 4.05 GHz, the mode J_1 is still the mode that provides the highest power with a 77.8 % that is being combined with the mode called J_{11} with a 17.3 %, the rest modes have a contribution with a lower percentage but that although they are very small should be considered.

Finally, the last resonance has been possible thanks to the combination of various modes, the mode J_1 that has been the most important for its presence in the 3 resonances with a 28.6 % with the mode that has been generated by the slot formed between the feeding points and the structures with a 56.1 % and the J_{11} with a 7.93 %, the other modes contribute with minimal quantities. A detailed summary of the power percentages provided by each of the modes in each of the resonances (f_c) has been presented in Table 3.4.

After knowing the modes that participate in each of the resonances generated by the structure analyzed, it will proceed to describe their physical

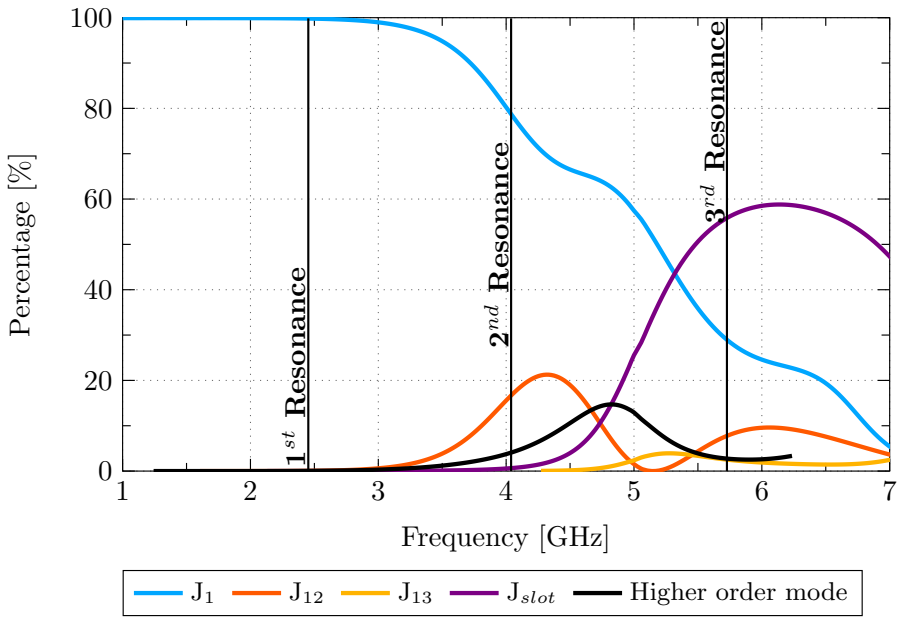

Figure 3.25: Power contribution of the two semi-circular structures with two feeding ports (+1, +1).

Table 3.4: Comparative summary of power contributions and modal weighting coefficient of the two semi-circular structures with two feeding ports (+1, +1).

	Power Contribution [%]			MWC [a_n]		
f_c [GHz] / Modes	2.46	4.06	5.74	2.46	4.06	5.74
J_1	99.8	77.8	28.6	0.168	0.15	0.09
J_{12}	0.06	17.3	7.93	0.004	0.07	0.049
J_{13}	-	-	2.18	-	-	0.028
J_{slot}	0.003	0.59	56.1	0.0009	0.0141	0.133
Higher order mode	0.047	4.31	2.71	0.0036	0.035	0.029
Others	0.09	-	2.18	-	-	-

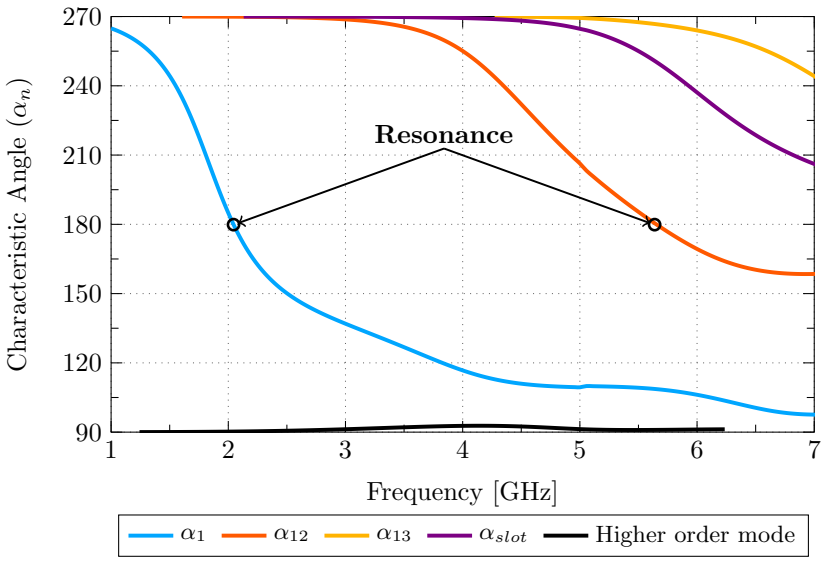

Figure 3.26: Characteristic angles of the two semi-circular structures with two feeding ports (+1, +1).

behaviour using the characteristic angles that have been obtained through the TCM, for this, the feeding ports will be replaced by short circuits and it will be illuminated by a plane wave. The characteristic angles that have been plotted in Fig. 3.26 represent the modes that participate in the resonance, only two of them are in resonance ($a_n = 180°$) for the range of frequencies analyzed, the mode J_1 at 2.06 GHz describing the fundamental mode (see Fig. 3.27(a)), its characteristic currents are zero at the edges and across the entire structure vertically. The mode J_{12} at 5.65 GHz is described by applying an electric wall on the horizontal symmetry axis, the currents in the upper plate flow inversely to the currents in the lower plate, in addition, that in each plate there is a variation in the direction of the currents such is depicted in Fig. 3.27(b). The other modes in none case come into resonance, for J_{13} and J_{slot} the modes store capacitive energy and for the mode that has been described as higher-order mode (HOM) inductive energy storage (their current distribution have been represented in Fig. 3.27(c), (d), (e)). However, although these modes are not in resonance, they are still participating so that the antenna works within the described bandwidth.

The total fields of the structure obtained through the full-wave analysis for each of the resonance frequencies have been represented in Fig. 3.29, in the same way that was done in the previous section, modal weights coefficients will be used together with the current matrices of each mode obtained at the resonant frequencies as assumed by Eq. (2.30). The modal weight coefficients for this case can be taken from Fig. 3.28 or turn in Table 3.4, comparing the modal coefficient weights of each of the analyzes resonances with the power contribution of Fig. 3.25, it is easy to conclude that their proportionality percentage for both cases are equal. Therefore, using a balanced feed in parallel allows obtaining a radiating element with very good characteristics in bandwidth and

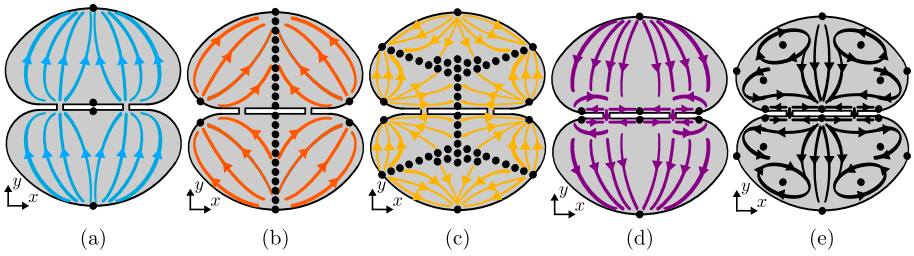

Figure 3.27: Characteristic current distributions of the proposed structure. (a) Mode J_1 at 2.048 GHz, (b) Mode J_{12} at 5.65 GHz, (c) Mode J_{13} at 7 GHz, (d) Mode J_{slot} at 7 GHz and, (d) Higher-order mode at 7 GHz.

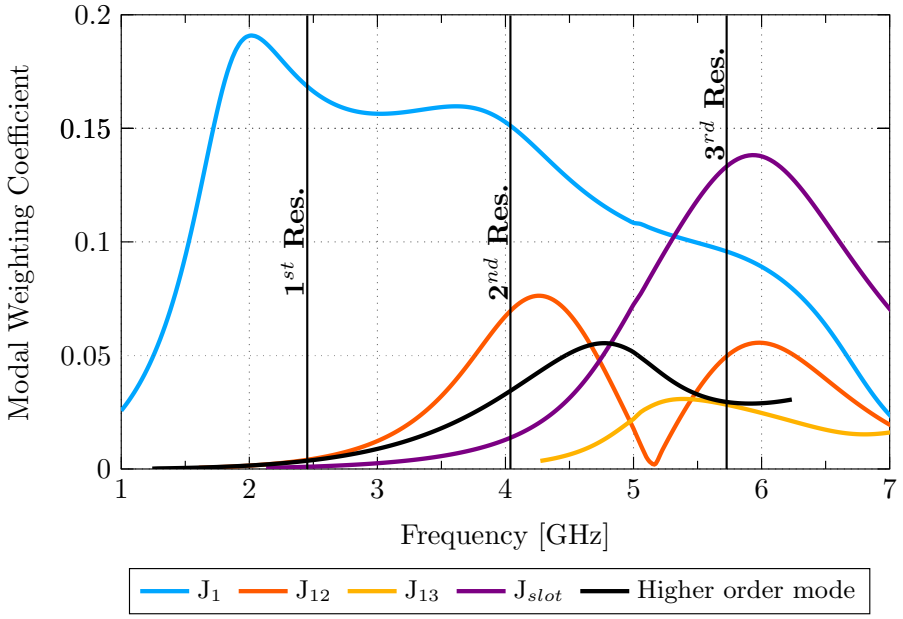

Figure 3.28: Modal Weighting Coefficient of the two semi-circular structures with two feeding ports (+1, +1).

radiation patterns, nevertheless, the parallel feeding is not the only alternative to excite it, another way is to use the serially feeding points as well, which will be described below.

3.5 Coupled rectangular structure with serial feed

After the operation of several structures with multiple feeding in parallel that has been described in the previous sections, this part aims to describe the behaviour of an antenna using one feed and with multiple feeds in serial, in addition to demonstrating through mathematical formulation the generation of the multiple resonances in the structure as a radiator element. To achieve the objective, a rectangular metal plate of dimensions $W = 20$ mm and $L = 52$ mm will be taken as a reference element as shown in Fig. 3.30(a).

The definition of the principle of operation of the rectangular metal plate has been made through the use of the theory of characteristic modes, in Fig. 3.31

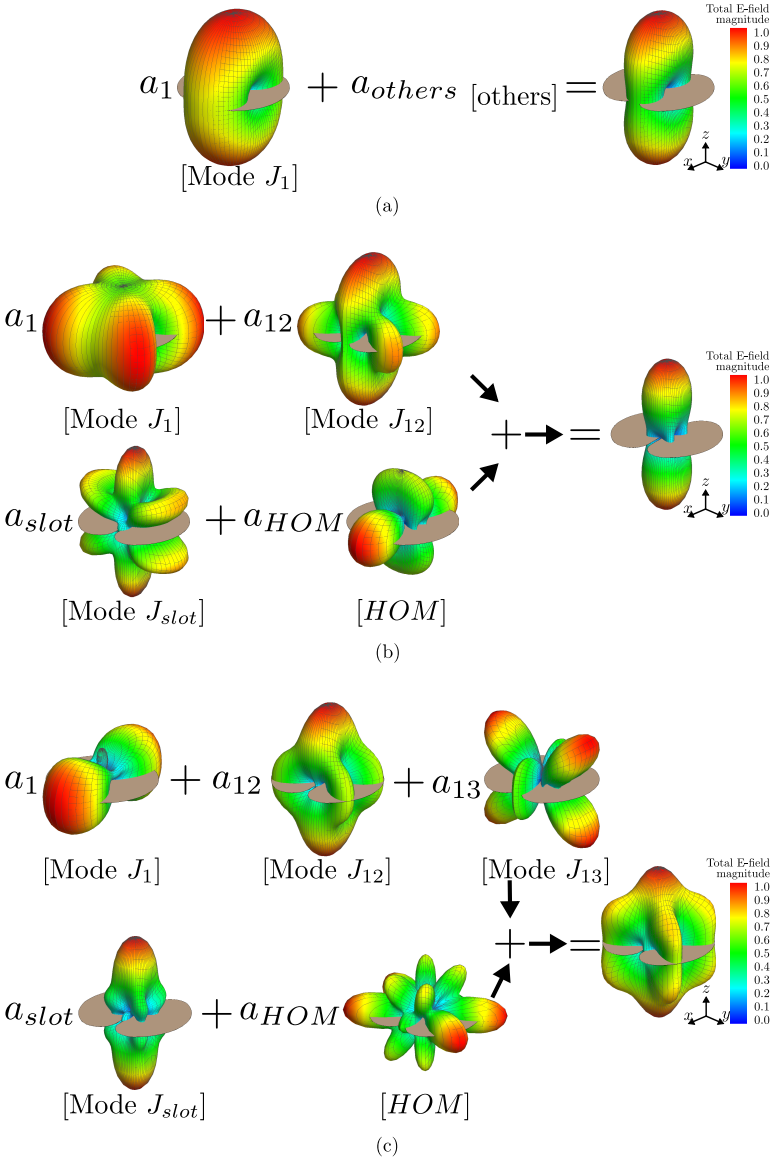

Figure 3.29: Total radiation patterns generated by the combination of the modal weighting coefficients and matrices of the electric field for each resonance. (a) At 2.46 GHz, (b) at 4.058 GHz and, (b) at 5.74 GHz.

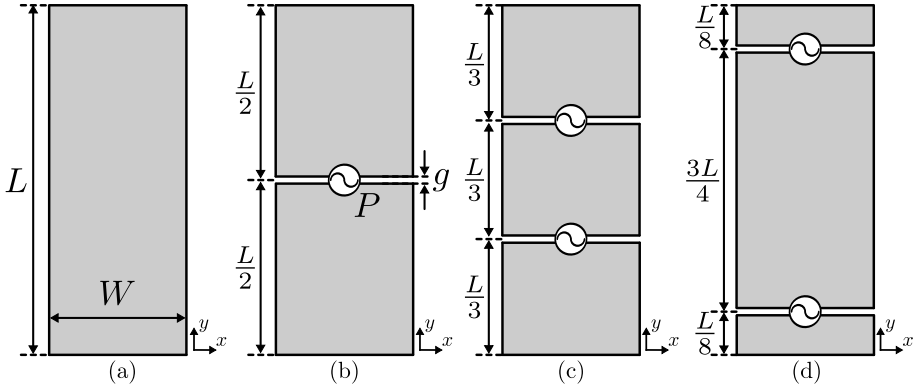

Figure 3.30: Evolution of proposed coupled rectangular structures analyzed. (a) Metallic rectangular plate, (b) rectangular plate with a feeding port in the middle (c) and (d) rectangular plate with two feeding ports in serial +1 +1 (symmetric and asymmetric areas).

the characteristic angles of the first 4 modes corresponding to the vertical polarization have been represented, the current distributions are very clear for each of the modes.

The currents of the fundamental mode (J_1) flow through the surface from each of the edges of the structure, it is in resonance that is presented when the length of the structure in its vertical section is equal to $\lambda/2$, by increasing the order number of the mode, the currents will change their direction of flow, for example, in the case of mode J_2, on the surface, the currents are moving in 2 directions, for mode J_3 there will be 3 directions, so, generalizing the concept, for mode J_n, n senses of flow will be generated. Obviously, these will not be the only modes that appear in the modal analysis, however, they are the ones that have the greatest interest for our study.

On the other hand, this type of structure is one of many that have a very good bandwidth, it should be emphasized that for the type of modes that have been described in Fig. 3.31, it has a limited bandwidth at the time it stores capacitive energy ($\alpha_n > 180°$) from 2.1 GHz to 2.58 GHz, whereas for inductive storage ($\alpha_n < 180°$) from 2.58 GHz wants to exceed the 8 GHz.

In order for the structure to work as a radiator, it is necessary to insert one or several feeding points, in Fig. 3.30 (b), (c) and (d) three excitation alternatives have been represented. In the first one, a port has been used that

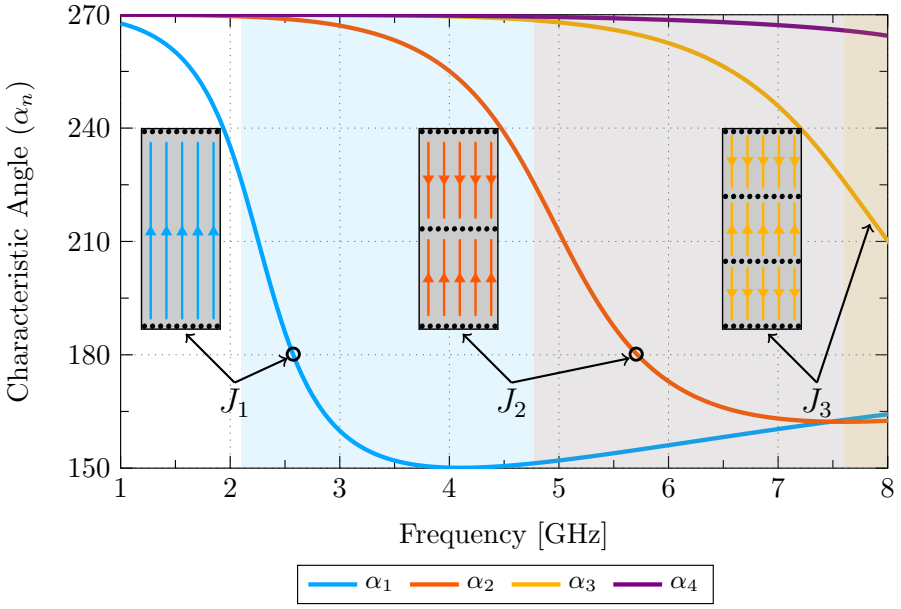

Figure 3.31: Four first characteristic angles in vertical polarization and the corresponding current distributions for each α_n. Mode J_1 at 2.58 GHz, mode J_2 at 5.71 GHz and J_3 at 8 GHz.

has been located in the middle of the structure making a cut through a gap of dimension $g = 2$ mm, its reflection coefficient (S_{11} parameter) has been shown in Fig. 3.32, with this kind of set up the structure, has been able to generate two well-marked resonances (at 2.4 GHz and 4.7 GHz), producing a very good bandwidth that covers from 2.1 GHz to 5.5 GHz for values below -10 dB.

Then, that one may increase the bandwidth, two serially excitation ports with balanced supply (+1, +1) have been placed, each of the ports are symmetrically located and separated 1/3 of the total length of structure L. Following the previous case, the simulated results of the reflection coefficient have been added in the same graph of Fig. 3.32; It can clearly be seen that with this type of feed the bandwidth obtained in the previous case could be improved, however, the coupling of impedances required in the resonance marked at low frequencies (approximately 2.4 GHz) is not enough.

Another option has been to slightly change the aspect ratio of the structure, e.i., break the symmetry of the location of the feeding points as shown

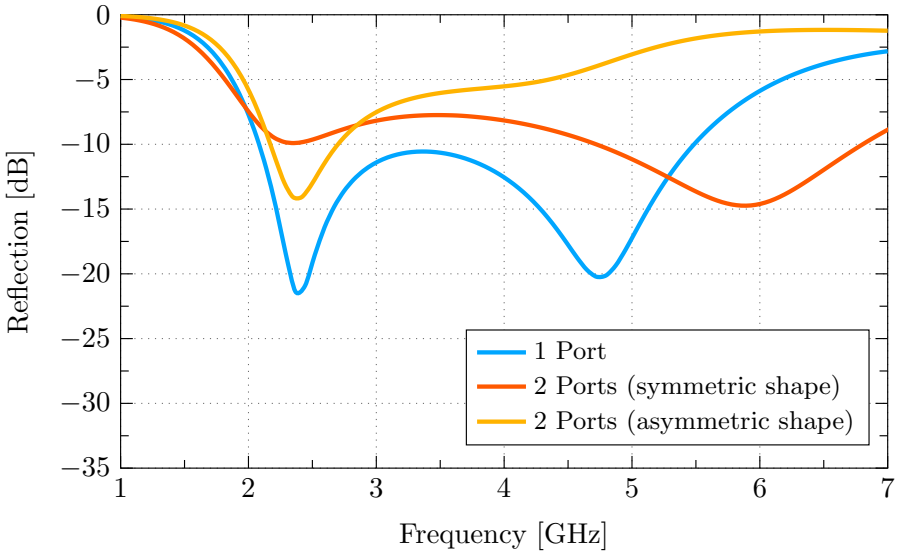

Figure 3.32: Reflection coefficient of the 3 proposed structures including a feeding points according the models in Fig.3.30 (b), (c), (d).

in Fig. 3.30 (d), the results of the S_{11} parameters have been integrated into Fig. 3.32. Using this form of excitation has allowed solving the problem of coupling impedance in resonance at 2.4 GHz, but unfortunately, the second resonance has been completely lost.

Once these three scenarios have been analyzed, it can be concluded that using one or multiple feeding points in a balanced way, one or multiple resonances can be generated, what is clear is that the first resonance obtained through a full-wave analysis is linked at fundamental mode J_1 of the structure obtained by the TCM (see Fig. 3.32), the other resonances will be the result of a combination of multiple modes, to substantiate this argument a complete analysis will be performed using the TCM of the rectangular plate with feed in the middle.

Using the values of the real and imaginary part of the input impedance Z_{in} (see Fig. 3.33), it is possible to know exactly the values where the proposed structure is in resonance, the first one is presented at 2.27 GHz and the second at 4.97 GHz, the impedance in both cases will be $Z = 38 + \mathrm{j}\ 0\ \Omega$. In Fig. 3.33, has included the current graphs and total radiation diagrams for each of the resonances as well.

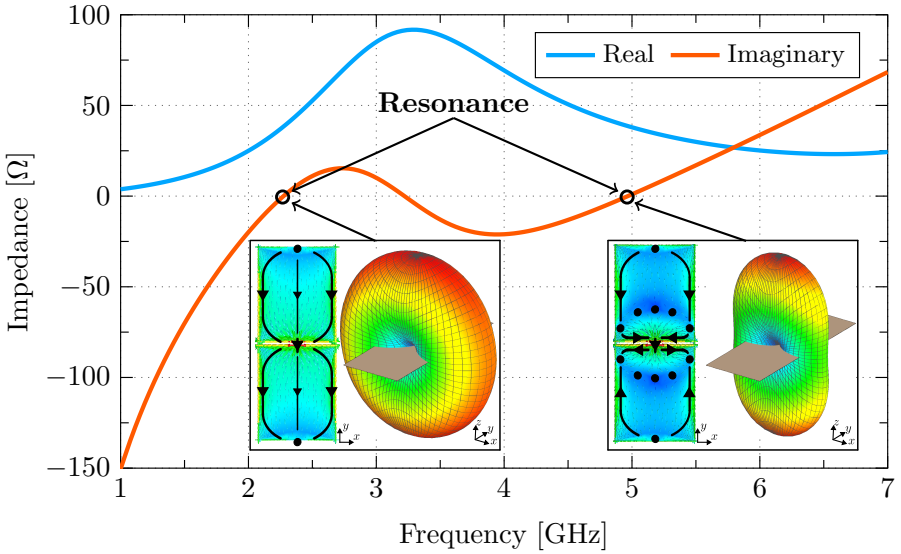

Figure 3.33: Real and Imaginary part of the input impedance of the rectangular plate with centre-fed, including the total radiation pattern and total current distribution at their resonance frequencies.

By associating the even modal currents (J_2, J_4, J_6, etc.) with the fed structure, the currents of the even modes generate a zero current value at the feeding point, causing these modes to not be excited in any way, therefore, the only modes that can appear with this type of configuration are the odd modes. According to the results shown in Fig. 3.34, at the first resonant frequency (2.27 GHz), the fundamental mode contributes with 99.9% of the total radiation power, the remaining 0.01% is a contribution of the other higher-order modes. For the frequency at 4.59 GHz, the concept is different, however, is such as expected, the resonance has been generated by the combination of several modes, among the main modes there is mode J_1 with a power contribution of 49.2% and the mode J_3 with a 50.4%, the power contribution between the two modes becoming almost balanced, the remaining 0.4% to complete the 100% will be distributed in a contribution of various higher-order modes.

The first resonance frequency generated by the full-wave analysis (at 2.25 GHz) is approximately the resonance value obtained by the characteristic angles through the theory of characteristic modes (2.1 GHz) as seen in Fig. 3.35, thus, it is confirmed that the first resonance is generated by the fundamental mode although the frequencies for both cases do not match, on the other hand, in

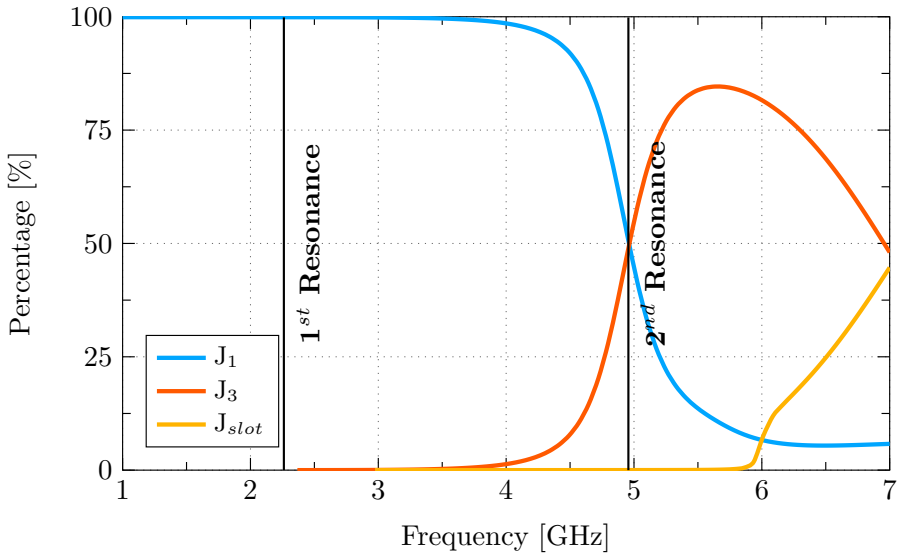

Figure 3.34: Power contribution for the centre-fed rectangular metallic plate.

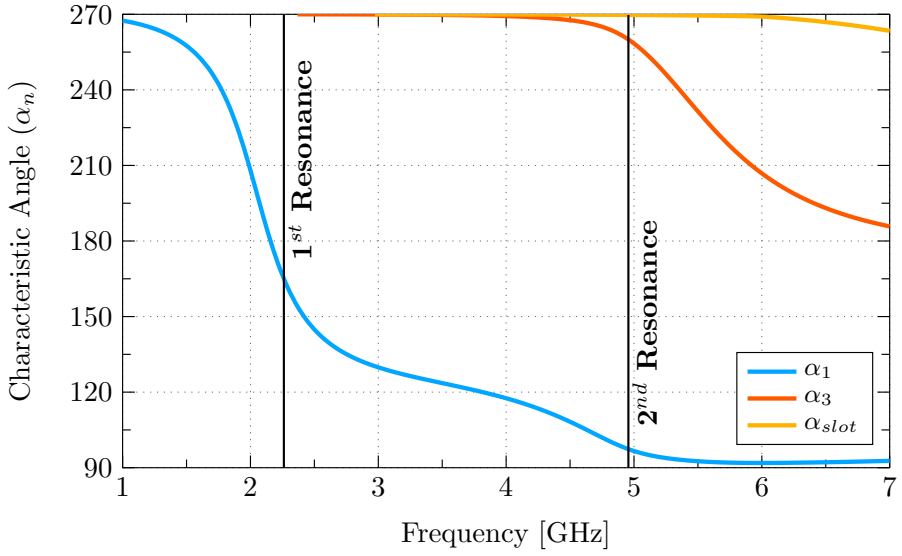

Figure 3.35: Characteristic angles for the centre-fed rectangular metallic plate.

the case of the second frequency there are not modes in resonance, the mode J_1 has already resonated, then, the mode contributes with storing inductive energy; whereas, mode J_3 mode does not yet resonate and will be providing capacitive energy storage, remaining between the modes an angular variation of approximately 180°.

Another form to quantify the contribution of each mode in the total power is through the input admittance Y_{in} of the antenna. The input admittance can be very easy to compute if it is assumed that the voltage input is a 1 V, with this in mind that the total current is given by equation (3.5) sampled at the feeding point P [26]:

$$Y_{in} = \frac{J(P)}{1} = \sum_n \frac{V_n^i}{1 + j\lambda_n} J_n(P) \tag{3.5}$$

The input admittance can be expressed in terms of the complex admittance of each mode (Y_n), as follow [26]:

$$Y_{in} = \sum_n Y_n = \sum_n G_n + jB_n = \sum_n \frac{V_n^i . J_n(P)}{1 + \lambda_n^2} - j\frac{V_n^i . J_n(P) . \lambda_n}{1 + \lambda_n^2} \tag{3.6}$$

In Fig. 3.35 shows the complex values of the Y_{in} input admittance associated with the metallic rectangular metal plate fed at the center (see Fig. 3.30(b)), together with the complex modal admittance $Y_n = G_n + jB_n$ for mode J_1, mode J_3 and, the mode called J_m, this mode J_m corresponds to all higher-order modes that have contributed less to the resonance.

Then, the total admittance for the 2.25 GHz frequency knowing that the admittance of mode J_1 (Y_1 = 25.7 - j 8.3 mS) and higher-order modes (Y_m = 0.1 + j 8 mS) is:

$$\begin{aligned} Y_{in} &= Y_1 + Y_m \\ Y_{in} &= (25.7 - j8.3) + (0.1 + j8) = 25.8 \text{ [mS]} \end{aligned}$$

where the total current can be computed as:

$$\begin{aligned} I_T &= (V).(Y_1) + (V).(Y_m) \\ I_T &= (1).(25.7 - j8.3) + (1).(0.1 + j8) = 25.8 \text{ [mA]} \end{aligned}$$

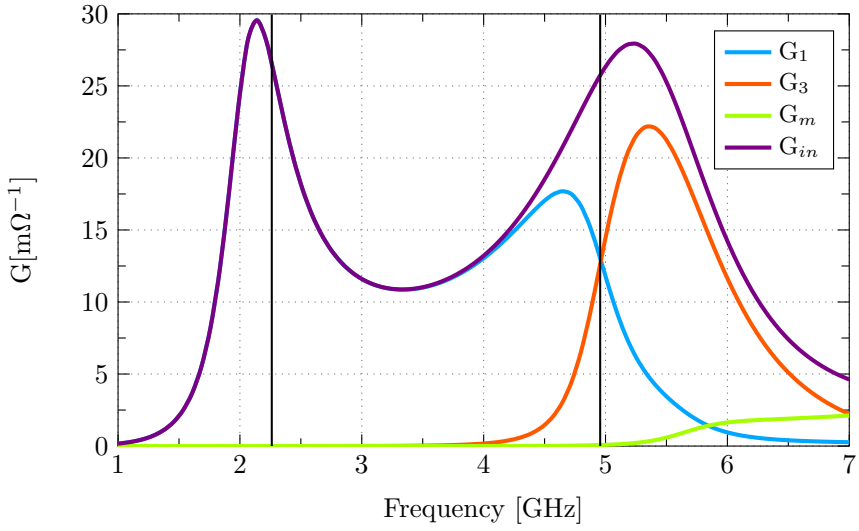

(a)

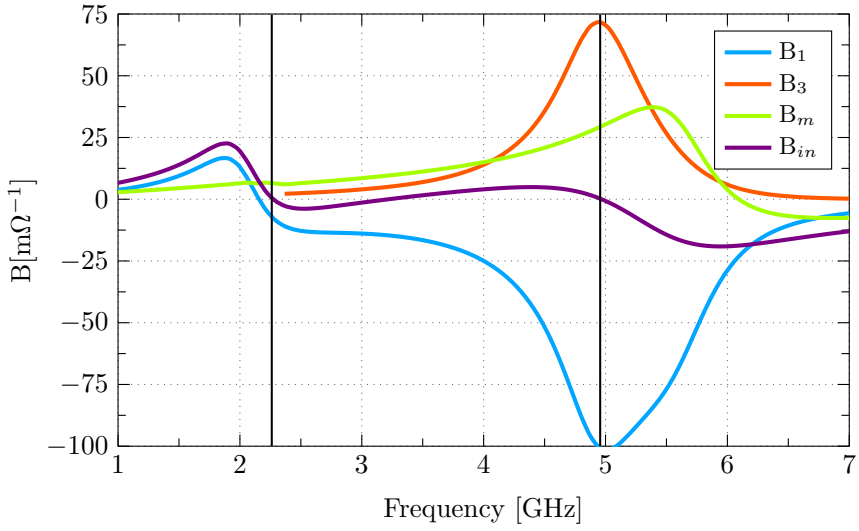

(b)

Figure 3.36: Representation of the input admittance Y_{in} and modal admittances Y_n of a centre-fed rectangular metallic plate: (a) Real part (G), and (b) Imaginary part (B).

The total active power is the real part of the so-called apparent total power and can be calculated as:

$$P_T = (\Re(I_1^2)/\Re(Y_1)) + (\Re(I_m^2)/\Re(Y_m)) = 25.8 \text{ [mW]}$$

Relating the total active power with the real power of each of the modes, it can know the contribution percentages of each of them:

$$\% \text{ Mode } J_1 = (P_1 * 100\ \%)/P_T = 99.6\ \%$$
$$\% \text{ Mode } J_m = (P_m * 100\ \%)/P_T = 0.4\ \%$$

Using the same formulation described previously, the contribution rates for the second resonance (4.97 GHz) can be calculated. In this case, the complex values of the admittance of the modes J_1 (Y_1 = 12.5 - j 101 mS), J_3 (Y_3 = 13.3 + j 71 mS) and the higher-order modes J_m (Y_m = 0 + j 30 mS).

$$\% \text{ Mode } J_1 = (P_1 * 100\ \%)/P_T = 48.44\ \%$$
$$\% \text{ Mode } J_3 = (P_3 * 100\ \%)/P_T = 51.55\ \%$$
$$\% \text{ Mode } J_m = (P_m * 100\ \%)/P_T = 0.01\ \%$$

Each of the resonances present in the analyzed structure can be represented through an equivalent parallel circuit as shown in Fig. 3.37. The values of resistance R, capacitor C, and inductor L can be calculated very easily through the capacitive and inductive reactance:

$$X_l = j\omega L \tag{3.7}$$

$$X_c = \frac{-j}{\omega C} \tag{3.8}$$

On the other hand, analyzing the area in which the excitation point has been inserted as shown in Fig. 3.38, it can be seen that a slotted transmission line is generated on the left and right side of the power supply, it's input reactance can be calculated from the formulation of a transmission line terminated in open circuit as presented in Eq. (3.9) [2] [132]:

$$jX_i = -j\ Z_0\ cot(\beta l) \tag{3.9}$$

where, l corresponds to the length of the transmission line $l = W/2$, Z_0 describes the load impedance and, β is the imaginary part of the propagation

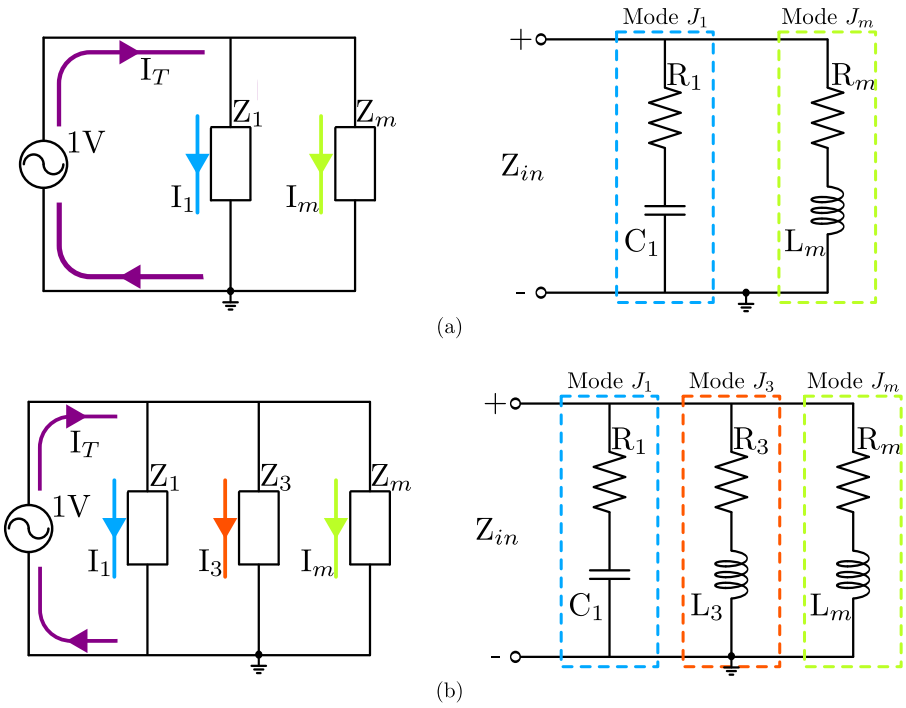

Figure 3.37: Equivalent circuit based on the modal expansion of the input impedance, for the centre-fed rectangular metallic plate at the two resonance frequencies. (a) At 2.27 GHz and, (b) at 4.97 GHz.

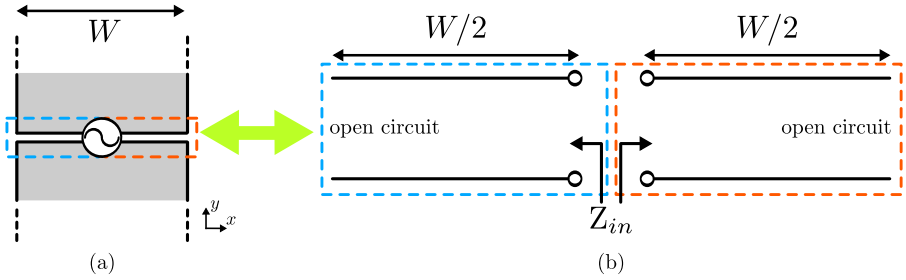

Figure 3.38: Slotted transmission lines generated in a rectangular plate with central feed, and their solution with transmission line terminated in open circuit.

constant. β represents the rate at which the waves oscillate as a function of position on the line. In general, β can be determined from:

$$\beta = \omega\sqrt{\mu\epsilon} = \frac{2\pi}{\lambda} \tag{3.10}$$

According to Fig. 3.38, to obtain the total reactance calculation must be taken into account the two circuits that are in parallel, the result of the input impedance will be purely reactive, which can be inductive or capacitive, this will depend on the values that are generated from βl, due to the function $cot(\beta l)$ can take positive or negative values.

3.6 Interaction between planar structures

The interaction between arbitrary structures that are located in the x or y directions has been presented in the previous sections of this chapter, however,

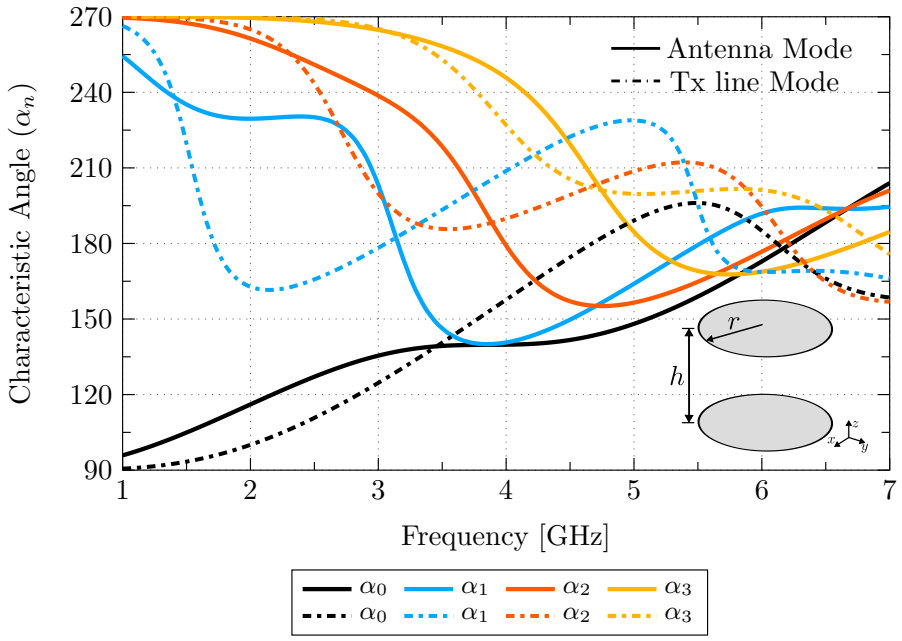

Figure 3.39: Characteristic angle of two parallel disks of radius r= 38.20 mm and, height h= 60 mm.

it is also important to analyze the structures when they are located along the $z-$ axis. The reference elements considered for this analysis are the metallic circular discs as shown in the graph inside the Fig. 3.39. Due to the revolution symmetry of the structure, the characteristic modes present will be the same for both polarizations (vertical and horizontal), therefore, it would be enough to only analyze one of the 2 polarizations.

The characteristic angles of the first 4 modes of two disks separated by a height $\lambda/2$ at the frequency of 2.5 GHz, and illuminated with a plane wave have been shown in Fig. 3.39. In the same way as in the analysis of the cases in the previous sections, when two or more elements interact, 2 types of modes are generated by the direction in which the currents flow, the transmission line mode (the currents in the upper element flow in the direction opposite to that of the lower element) and, the antenna mode in which the currents of the two elements flow in the same direction.

Analyzing the resonances of each of the modes through the characteristic angles, the electric modes (those that change from 270° downwards) of the

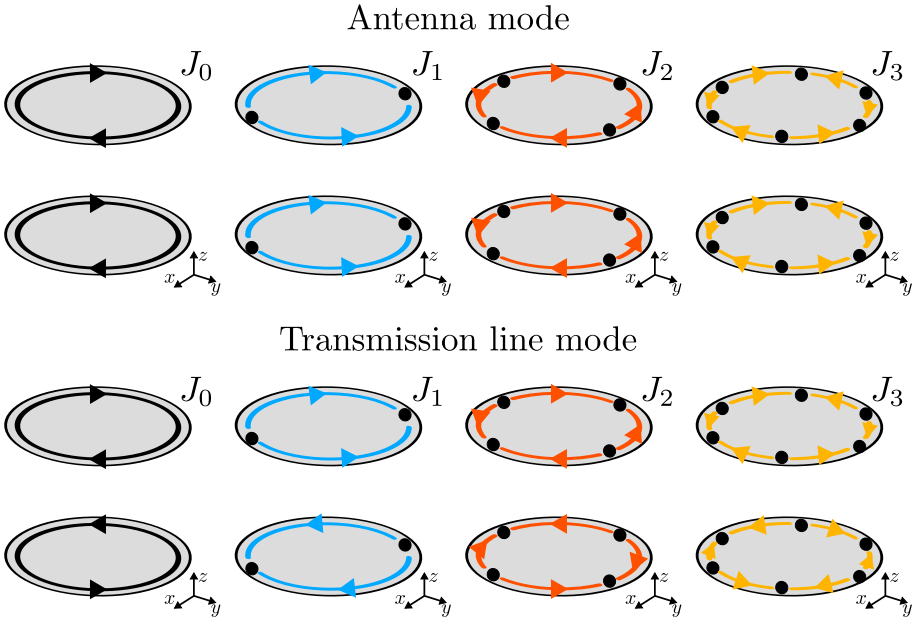

Figure 3.40: Characteristic current distributions of the 4 first modes presents in a two parallel disks.

transmission line type are much more inductive than the antenna modes, for example, in the case of the fundamental mode, once it enters resonance it quickly goes from being inductive store to being capacitive store.

As the order of the mode is raised, the first resonance is not reached, however, they are very close to $\alpha = 180°$ but they do not enter in resonance, making the mode more inductive, obviously, it will then enter resonance at a higher frequency, but the current distributions and radiation patterns will be slightly different from those seen at the first resonance.

On the other hand, the electric antenna modes are very clearer in their resonance at least in the analyzed frequency range, they have a rather interesting bandwidth and at higher frequencies, they resonate again. In Fig. 3.40, the currents distributions at the first resonance frequency can be seen for each of the modes seen in Fig. 3.39. As expected, depending on the kind of mode, the currents flow in the same or opposite direction, in addition, as the order of the

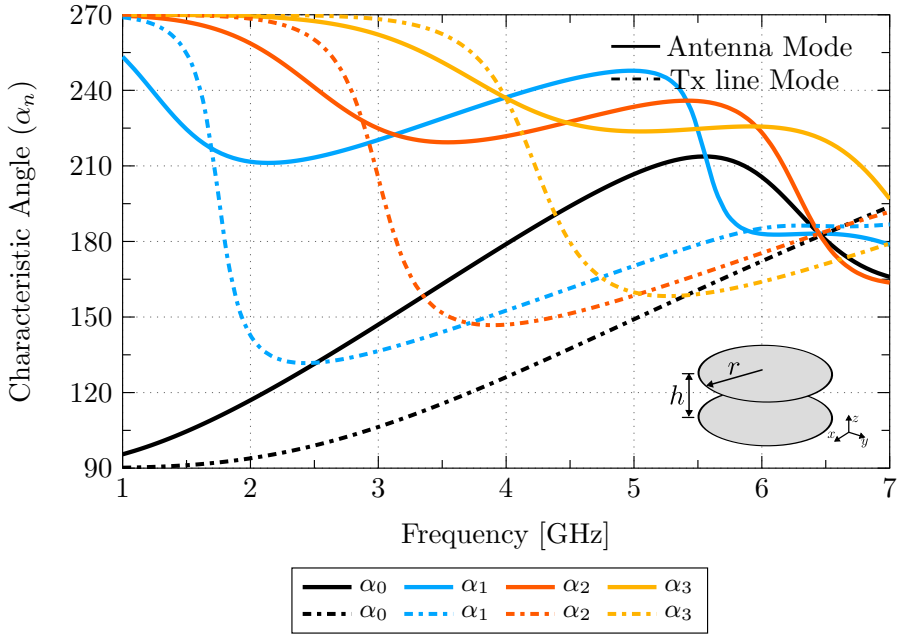

Figure 3.41: Characteristic angle of two parallel disks of radius r= 38.20 mm and, height h= 30 mm.

mode increases, the number of current nulls and variations in the direction of the current will increase.

By reducing the height of the two parallel disks by half, i.e. changing from $\lambda/2$ to $\lambda/4$ at the 2.5 GHz frequency. The characteristic angles of the structure undergo a great variation as can be seen in Fig. 3.41. The electric transmission line modes went from being very inductive to capacitive, the resonances are well marked and generate a very limited bandwidth. Whereas, the electrical antenna modes lost their first resonance, and frequencies below 5 GHz are purely inductive.

Therefore, when we have two elements separated by a very short distance and in order to take advantage of the dimensions of the structure at low frequencies, only the modes that are linked to the transmission line modes should be excited.

3.7 Conclusions

In this chapter some structures with single or multiple feeding with a very good bandwidth have been designed and analyzed, taking advantage of some results of preliminary works on planar structures that have been obtained through the analysis of the TCM.

It has been possible to demonstrate that by placing two isolated structures very close to each other, two types of modes have been generated, the antenna mode and the transmission line mode. To describe these modes, electric walls and magnetic walls have been used. The antenna mode has a large bandwidth and its currents are parallel to the magnetic wall and flowing in the same direction, whereas, the transmission line mode has a limited bandwidth and its currents are flowing in the opposite directions, parallel of the electric wall. The nomenclature used for coupled elements to represent each of the modes is J_{nm}, where n is 0 for the antenna mode and 1 for the transmission line mode, on the other hand, m responds to the order of the mode.

The TCM provides important information for the antennas design because of some parameters such as resonance frequency, currents flow on the surface, bandwidth, etc. can be known in the absence of any external sources. In order to analyze the antenna in reception, it can be illuminated by a plane wave. When the antenna works as a transmitter, it requires the inclusion of an excitation port. When the excitation port connects two parallel structures, it creates an electrical connection between them, so the two elements behave as

a single folded structure, modifying the current distribution of the modes and its resonance frequency.

To discriminate or enhance the excitation of certain modes, multiple feeding ports have been employed. In several structures of this chapter differential feeding (+1, −1) and balanced feeding (+1, +1) have been used. In the case of a circular ring and in order to excite it, capacitive elements have been inserted in the inner part of the ring. The use of the differential feed only allows the odd modes to appear ($J_1, J_3, J_5, ..., J_{2n+1}$), while with the balanced feed, only the even modes ($J_0, J_2, J_4, ..., J_{2n}$) are present.

The metal ring with differential capacitive fed is capable of generating a large bandwidth and stability in the radiation pattern for all available frequencies. The modes with minimum current at the position of the excitation are excited. Thus, the resonances are generated by modes J_1 and J_3, due to the physical configuration and the type of excitation. The cancellation of currents in the feeding zone, makes the radiation pattern of J_3 mode unidirectional as in J_1 mode.

Subsequently, structures have been analyzed in which several modes are combined to generate a resonance. In force the resonance, the imaginary part $\Im(Z)$ of the input impedance must be cancelled by the sum of different modes, i.e. some modes will contribute with capacitive energy and others with inductive, leaving only the real part of the impedance as result. Analyzing the modal power contributions, it has been possible to determine which are the modes that generate the resonance and their percentage of contribution.

Finally, in the last section, the interaction of 2 metallic parallel plates has been analyzed using the TCM. If the parallel plates have a very large separation, the usable modes are those of the antenna type, which would finally be like working with a single element, in other words, there is no considerable contribution to having 2 parallel plates. However, if the height between the elements is very small, transmission line modes appear that can be easily excited.

Chapter 4

Folded structures

"Nothing in life is to be feared, it is only to be understood. Now is the time to understand more, so that we may fear less."

— Marie Curie

4.1 Introduction

With the imminent development of technology in wireless communications, it has become increasingly desirable for modern communication devices to integrate multiple communication standards into a single system as is the goal of 5G technology. Within the great diversity of applications that host fifth-generation networks such as applications in the field of biomedicine [133, 134], Internet of things IoT [135], indoor base stations [136], they require a type of antenna with some specific characteristics such as a large bandwidth, stable radiation patterns in broadside direction.

Many of the devices that work under 5G technology have limited space, they need unidirectional radiation patterns, compact and with low profile characteristics, such as the antennas used for the human body [137–139].

One of the valid alternatives to obtain this behavior is to place a ground plane at a certain distance at the back of the antenna. In this chapter it is proposed to fold simple structures on itself, with this the required radiation pattern can be generated and in addition to obtaining compact antennas, to

achieve this objective, it will be based on the information obtained through the modes of some of the structures analyzed in the previous one.

4.2 Rectangular folded structure

In Chapter 3, the characteristic modes of some planar symmetric structures such as the circular disk, the square plate, a circular and square ring in the $x-y$ plane were represented. It has been possible to show that due to the symmetry of the structure, the distribution of currents and the radiation patterns generated for each of the modes in both polarizations are orthogonal, that is, the fundamental mode J_1 and it's degenerate J_1' are rotated 90°. Therefore, the resonance frequencies of the mode J_1 and J_1' are the same, as well as the behaviour of the characteristic angles.

Thus, if the structure is deformed, going from a square to a rectangular shape, it allows generating a phase shift of the resonance frequencies between the polarizations of each mode, the cross section with the longest length will resonate at a low frequency, and the one with the shortest length at a higher frequency. In Fig. 4.1, the five first characteristic angles of the rectangular

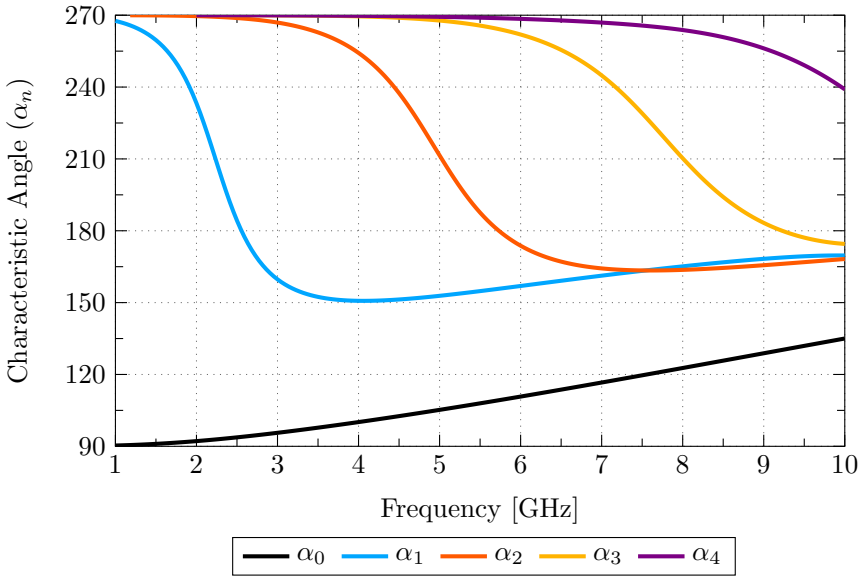

Figure 4.1: Characteristic angles of the first modes presented in a rectangular plate of dimension W = 20 mm and L= 51 mm.

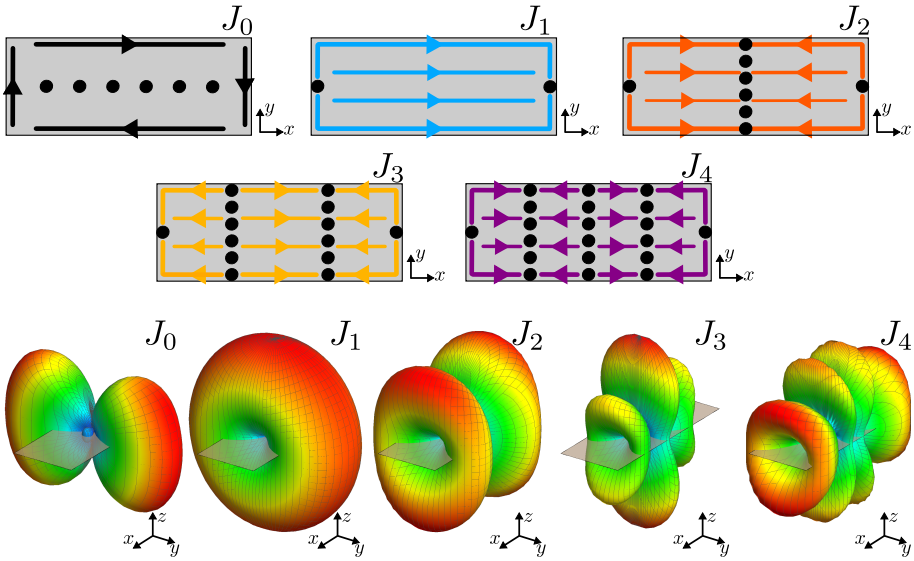

Figure 4.2: Characteristic current distributions and radiation patterns of the 5 first horizontal modes presented on a rectangular plate.

plate have been shown, the bandwidth of each of the represented modes J_1, J_2, J_3 are very good, but in most frequencies it stores capacitive energy after having entered into resonance.

The radiation patterns and the characteristic current distributions corresponding to the rectangular plate at each of its resonance frequencies are shown in Fig. 4.2. It can be clearly seen that in the distribution of currents it complies with a pattern for the case of the electrical modes obtained in the frequency range, in the mode J_1 a pair of current nulls is generated at the edges of the plate, and according to the order of mode, current nulls are generated in the form of vertical walls organized in an orderly way, this organization of the currents allows obtaining radiation diagrams that generate multiple beams according to the order of the mode, that is, for the mode J_1 Because it has only one direction of the currents, it has a bidirectional beam, the J_2 mode has 2 variations of the direction of the current, therefore, 2 bidirectional beams are generated.

Being able to excite the modes generated in the rectangular plate becomes a little bit complicated, for this it would need external elements to feed capacitively, or make some cuts in the structure to be able to excite inductively.

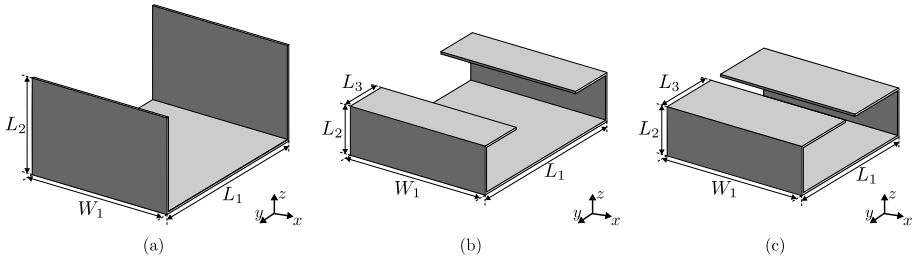

Figure 4.3: Progressive analysis of a folded structure on itself from a rectangular plate. (a) Structure 1, (b) Structure 2 and, (c) Structure 3.

Table 4.1: Summary of variables used for the design of the structures folded on themselves.

Structure 1		Structure 2		Structure 3	
Variable	Dim. [mm]	Variable	Dim. [mm]	Variable	Dim. [mm]
W_1	20	W_1	20	W_1	20
L_1	25.5	L_1	25.86	L_1	20
L_2	12.75	L_2	6	L_2	6
-	-	L_3	6.57	L_3	9.5

However, if the entire transverse length of the rectangular plate is taken advantage of and is folded on itself to the point that the two edges of the plate almost come together, a very compact structure with a unidirectional radiation pattern can be achieved.

Then, to understand the behavior of this bent structure, an analysis is performed using the Theory of Modes characteristic of a progressive bending starting from the information obtained in the rectangular plate to the final structure described above, such as is represent in Fig. 4.3. The parameters with which each of the analyzed structures described in Fig. 4.3 were designed have been summarized in table Table 4.1.

In Fig. 4.4, a comparative graph of the first 4 characteristic angles obtained in each of the structures proposed in Fig. 4.3 has been made. The behavior of the characteristic angles for each of the modes shown are very similar for the 3 structures, the resonances are very coincident, however, the bandwidth depends a lot on the height at which the edges of the ground plane are located. With this structure it has been possible to demonstrate the concept described

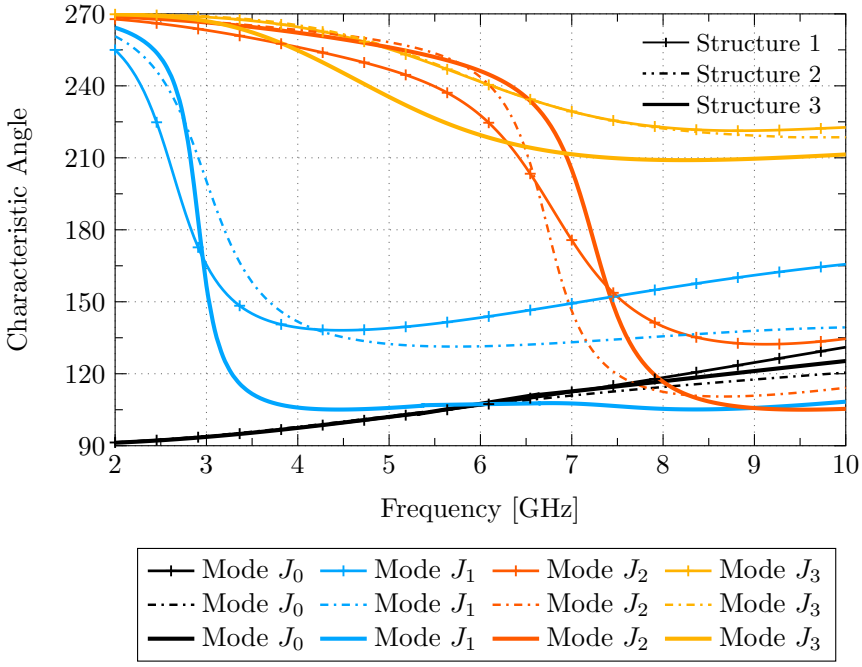

Figure 4.4: Comparison of characteristic angles present in three structures proposed in Fig. 4.3

in the Chapter 3 that deals with the interaction of two parallel elements. Then, as the height of the structure is reduced more, the more capacitive the mode tends to be for the case of the electric modes, whereas for the magnetic modes the angle will tend to be less capacitive, at high frequencies it will start to store inductive energy after going into resonance.

The current distribution and the radiation pattenrs of the J_1 to J_3 modes of each of the proposed structures have been represented in Fig. 4.5, for the J_1 and J_2 modes they have been plotted at resonance frequencies, while for the J_3 mode, the results have been plotted for a frequency of 10 GHz (approximately when the angle is very close to 180 °).

Analyzing the current distribution corresponding to the fundamental modes of each of the structures, it can be seen that as the plate is folded, the null of the currents moved to the side walls, generating a continuous flow on the upper layer, this current flux helps improve directivity in the radiation pattern.

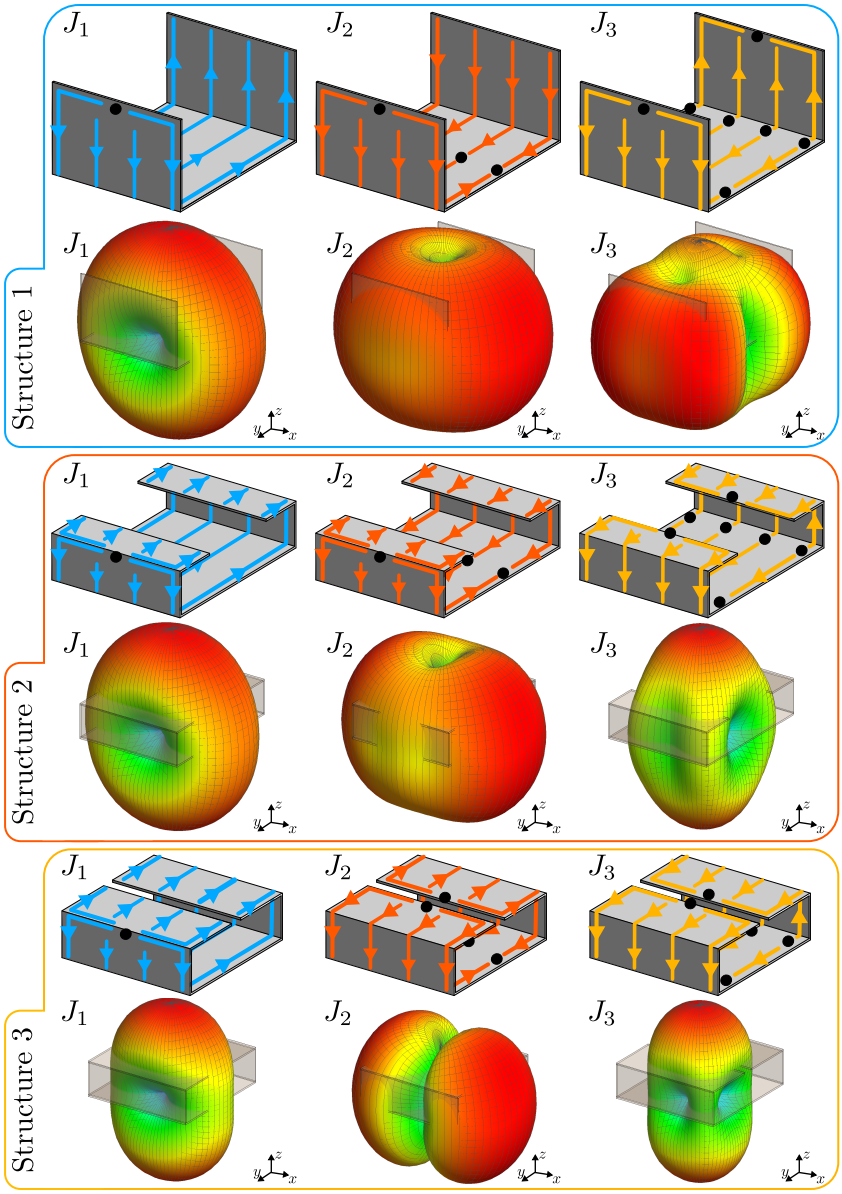

Figure 4.5: Characteristic current distributions and radiation pattern of the folded structures depicted in Fig. 4.3.

A very important characteristic in the folded structures that can be taken advantage of is the J_3 mode radiation pattern, if it compare the J_3 mode radiation patterns for a rectangular plate and the folded structure on itself, we have that the maximum radiation power is in the broadside direction for both cases, but in the structure folded on itself, the two secondary lobes that were generated in the rectangular plate have been cancelled.

Thus, with the structure already completely folded and with a small air gap between the two flaps, it is very easy to insert the power point inductively between the 2 ends of the antenna, this configuration can be appreciated with the structure framed with a blue line inside the Fig. 4.6. The matching in the antenna is very good, below the -10 dB the reflection coefficient a bandwidth of 32% has been generated.

However, if the edge of the structure is slightly modified from linear to curved, the bandwidth of the antenna improves by 3%, obviously the central operating frequency has moved to a higher frequency, This really is understandable since the length where the currents flow has been reduced; in the case of these structures, currents will always flow along the edges.

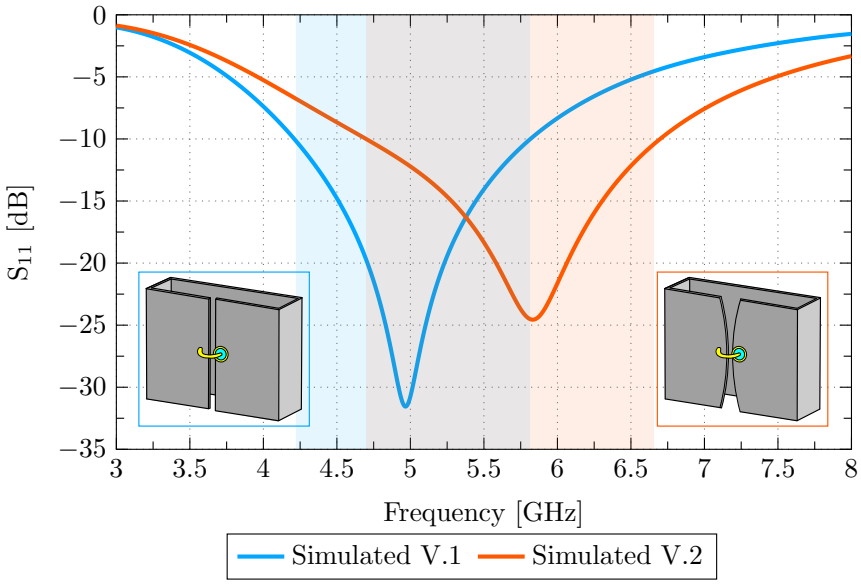

Figure 4.6: Reflection coefficient of the antenna designed from the rectangular plate folded over itself, varying the shape at the edges.

4.3 Elliptical folded structure

The small deformation that was made to the edges of the rectangular plate in the previous section, and that has allowed to improve the coupling conditions when an inductive feeding port is inserted between the two ends, has not been accidental. To reach this point of deformation, it is started from a study and analysis of an elliptical structure with dimensions $R_1 = 40$ mm and $R_2 = 19.5$ mm, as shown in Fig. 4.7(a).

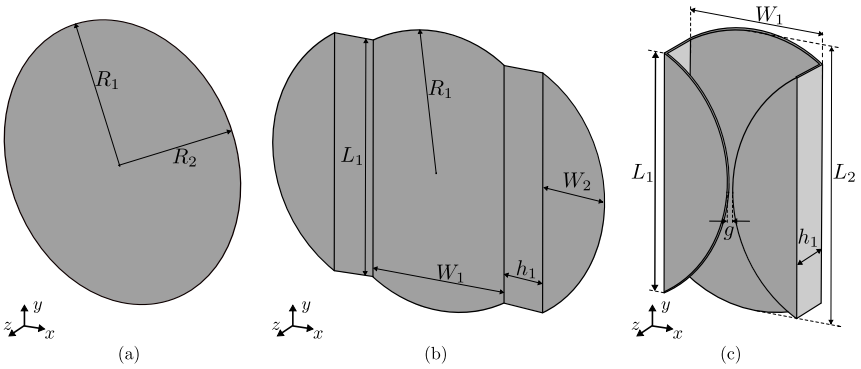

Figure 4.7: The progressive design of an Elliptical structure folded itself.

Describing the physical characteristics of an ellipse, it is easy to see that one of the axes will be greater than the other, so if an analysis is carried out with the Theory of Characteristic Modes, it can easily say that the modes of the two polarizations will be shifted each others. Making a summary of the modes found in the ellipse (check Fig. 3.1) [140], it is well known that there are vertical and horizontal modes in a planar structure. For example, in the case of the fundamental modes (J_1, J_1') present in the ellipse, the vertical resonance frequency is shifted from the horizontal, the diameter of the semi-major axis will resonate at a lower frequency, on the other hand, the diameter of the semi-minor axis will resonate at a higher frequency.

Then, depending on the frequency at which you want to work, the designer will be able to fold the ellipse in any of the 2 polarizations, for the case under study the ellipse will be folded on its minor axis, i.e, the physical dimensions will be used to generate the highest possible frequency. However, to reduce the difficulty in designing the sidewalls in the structure folded on itself, the ellipse has been cut into 3 sections; the main section will be the central one with a width of $W_1 = 20$ mm, the two lateral sections will be integrated again

to the central part through two rectangular plates of dimensions $h_1 = 6$ mm and $L_1 = 34.5$ mm according to the configuration shown in Fig. 4.7(b). By inserting the two metal pieces, the horizontal section now becomes the major axis, so the ellipse fold will be made to achieve the lowest possible frequency, finally leaving the structure as shown in Fig. 4.7(c).

In Fig. 4.8, the characteristic angles of these two proposed structures have been represented, the results are very similar for the J_1 and J_2 modes, while the J_3 modes are very different, the J_3 mode of the larger structure it is much more inductive than that of the small structure. For all modes, the resonant frequencies will be offset due to the difference in sizes of the structures. However, the case of structure 1 (full ellipse structure) is very curious, because according to its dimensions in the vertical section it resonates at a higher frequency than the frequency of structure 2, when it should be the opposite.

As mentioned above, the frequency shift can be explained using the characteristic current distribution generated in each of the structures. Thus, if it compare the fundamental modes J_1 of Fig. 4.9(a) and Fig. 4.9(b), it see that

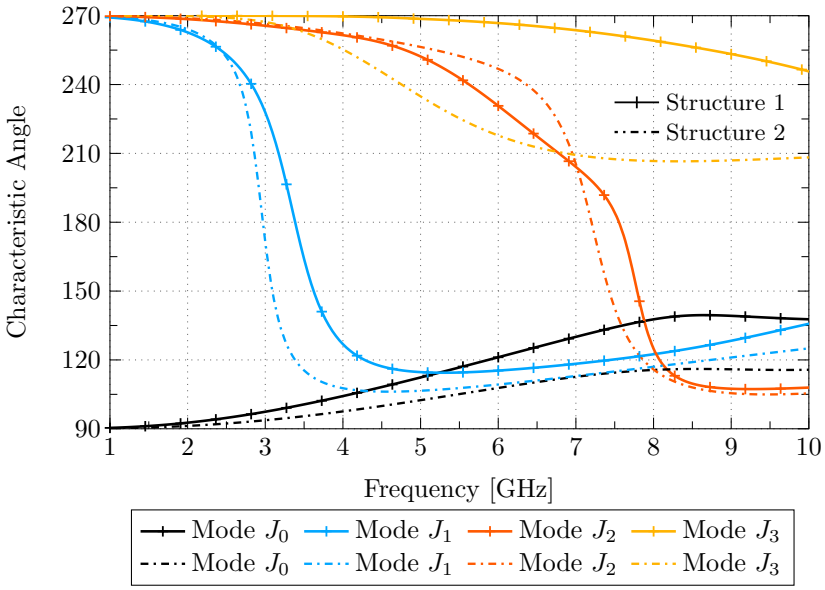

Figure 4.8: The first four characteristic angles in vertical polarization of the structures folded on themselves. The elliptical folded on itself is called Structure 1 and, rectangular plate folded on itself such Structure 2.

the currents found in the central part are very more intense than in the edges. Then, considering that currents follow the shortest path and travel where there is least opposition, resonance is associated to the shortest length in the structure. On the other hand, in the structure of the rectangular plate folded on itself, the most intense currents flow along the edges, making the path through which the currents flow larger that the first structure.

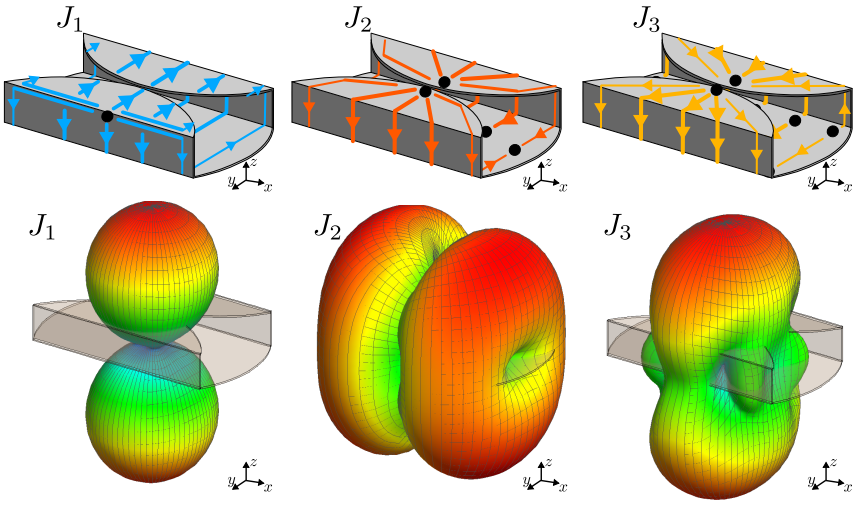

(a)

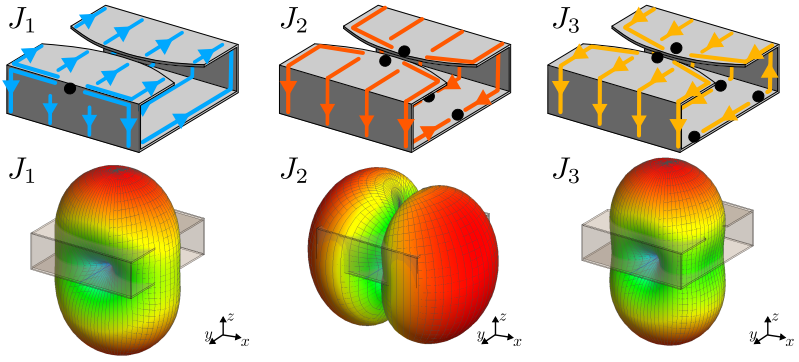

(b)

Figure 4.9: Characteristic current distribution and radiation patterns. (a) Elliptical structure folded on itself, and (b) Rectangular structure folded on itself.

This concept, which starts from the analysis of the characteristic currents, can be used to describe the resonances of each of the modes represented in Fig. 4.8. In fact, seeing the radiation patterns of Fig. 4.9 are slightly different, the maximum in the radiation pattern of the J_1 mode of structure 1 is a little more spherical than that of structure 2, showing that the radiation pattern is generated by the currents that flow in the central zone.

4.4 Application of a Folded Antenna

The proposed antenna in this section [141] is based on the information obtained in the structures analyzed in the Chapter 3 and the previous section, specifically the modal analysis of the ellipse shown in Fig. 3.1.

Then, taking advantage characteristics current distribution generated in the direction of propagation of semi-minor axis in the ellipse in Fig. 3.1. Folding on itself, the structure will be able to be compacted and keep it resonance such as describe in the previous section; from the ground plane to top layer, the feeding port has been inserted between the two end of lapels in the ellipse as shown in Fig. 4.10(a) and Fig. 4.10(b).

Carrying out a full wave analysis, the reflection coefficient of the structure has been obtained, showing that a resonance in the elliptical structure folded itself is generated at 6.7 GHz. The total currents for this frequency that have been shown in Fig. 4.11(a), the currents are flowing from left to right through

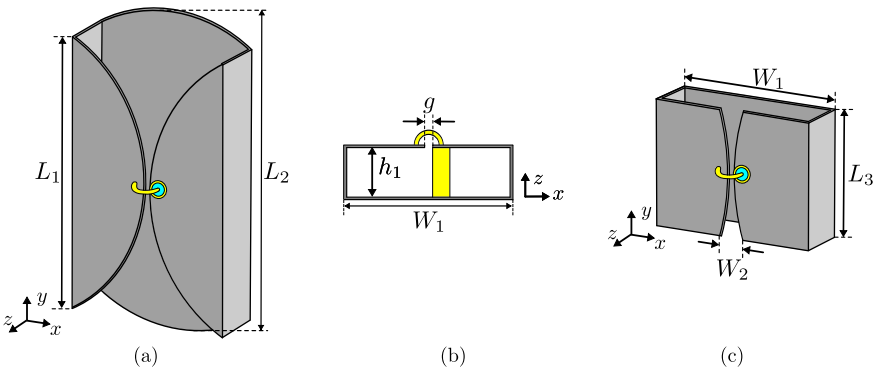

Figure 4.10: Elliptical proposed antenna. (a) 3D view of structure V.1, and (b) 3D view of structure V.2

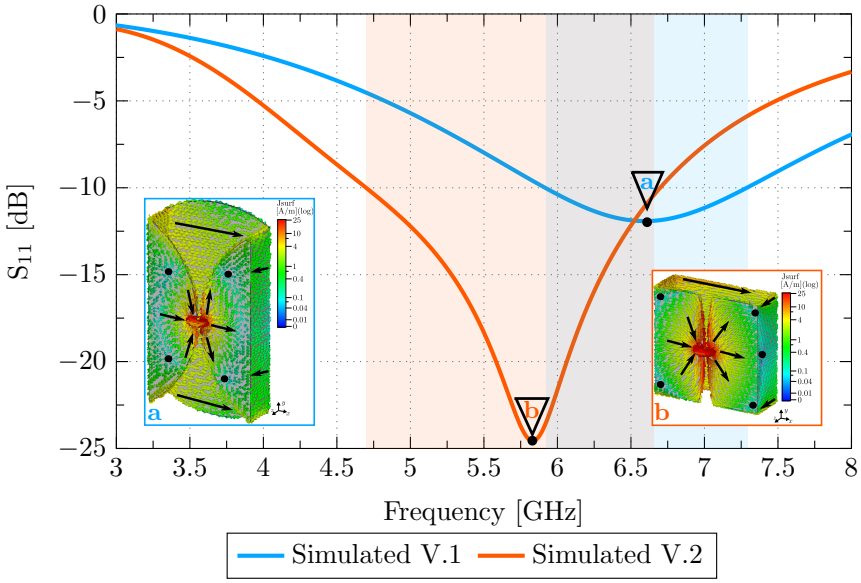

Figure 4.11: Simulated reflection coefficient results and total current distributions of the proposed antenna.

the feed point, however, a pair of current nulls are generated in each of the lapels causing the currents to change direction.

Thus, considering to the current distribution generated, the antenna can be further optimized and compacted even more. Therefore, in the current null direction, and parallel to the feeding point a cut in the device has been made, remaining a shape equal to shown in Fig. 4.6). In this way, the physical modification of the air gap that was made at the edges of the rectangular plate folded over itself is justified, remaining the proposed antenna parameters depicted in Fig. 4.10(b) and, Fig. 4.10(c) as: $L_3 = 20$ mm, $h_1 = 6.07$ mm, $W_1 = 20$ mm, $W_2 = 3.02$ mm, and $g = 1$ mm.

The proposed V.2 antenna generates a better bandwidth that the elliptical structure, even a better impedance matching (see orange line in Fig. 4.11), a frequency shifted is generated toward a lower frequency due to the small decrease of the air gap between to lapels in the top layer, causing a decrease in the matching. Additionally, it should be remembered that the bandwidth can be improved or worsen if the height between the top and bottom layers is changed. If the height is increased the bandwidth will increase as well, it

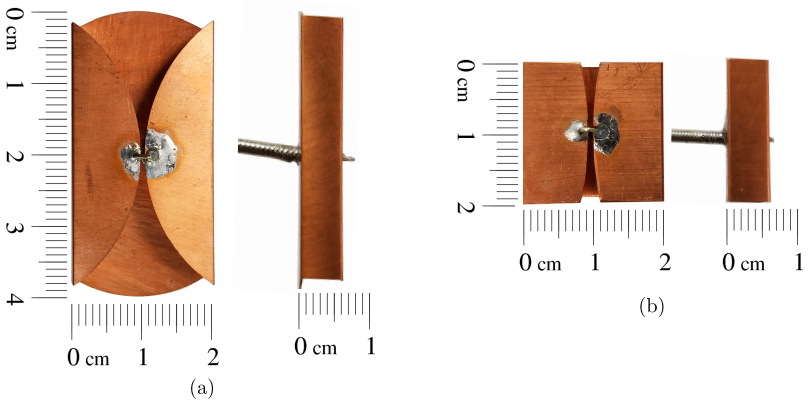

Figure 4.12: Manufactured folded antenna. (a) Structure V.1, and (b) Structure V.2.

is possible because the slope of the characteristic angle isn't very vertical. On the contrary case, the bandwidth is limited by reducing the height, because the slope is closer to the vertical axis.

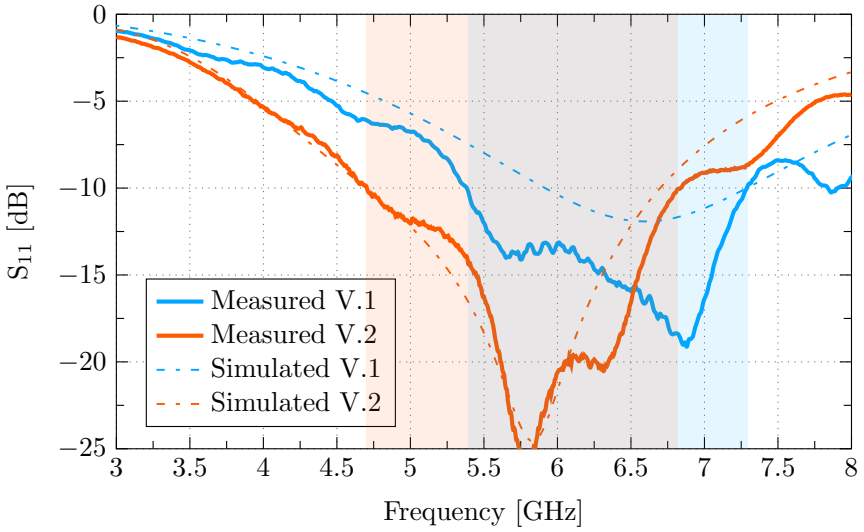

Figure 4.13: Measured scattering parameters of the folded proposed antenna. (a) Structure V.1, and (b) Structure V.2.

In Fig. 4.12, the frontal and side view of the proposed manufactured structure have been represented, each one of them have been manufactured with on the air. From the bottom towards the 2 ends of the structure, a coaxial cable has been inserted in order to excite it.

The measured results obtained are plotted in Fig. 4.13, the results are very similar to those simulated. The impedance matching under -10 dB of the folded antenna is working in range frequency from 4.4 GHz to 6.65 GHz, representing 40% of bandwidth. The final dimension of the structure in terms of wavelength at center frequency are: 0.35 λ_0 x 0.35 λ_0 x 0.1 λ_0.

In order to complement the study of the proposed antenna realized with the theory of characteristic modes, in the Fig. 4.14, the modes that contribute the resonance in the available range frequencies have been plotted. The fundamental mode J_1 contributes the highest power at the center frequency with 70%, while the sum of the powers of the J_3 and J_0 modes contribute a 30% approximately.

The combination of the radiation patterns of the J_1 and J_0 modes and J_3 with a minimum quantity allows generating a unidirectional radiation pattern in broadside direction at 5.8 GHz as represented in Fig. 4.15. Using this type of structure proposed in this section, reconfigurable antennas can be designed us-

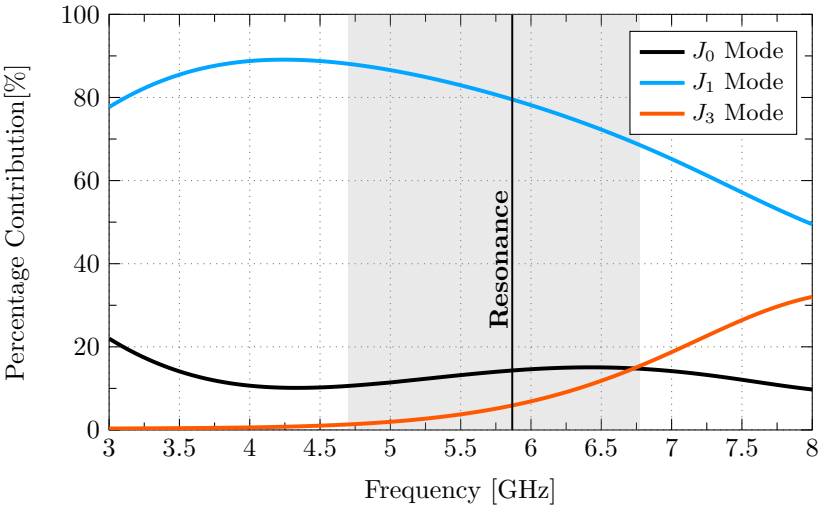

Figure 4.14: Power contribution of the folded proposed antenna.

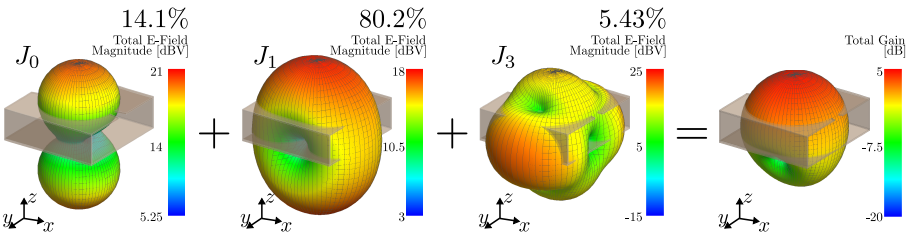

Figure 4.15: Unidirectional radiation pattern at 5.8 GHz as a result of the combination of the radiation patterns of modes J_0, J_1, J_3.

ing electronic devices such as pin diodes [142], however, these kinds of antennas are not within the scope of this thesis.

4.5 Array antenna using a folded structure

An array antenna is the result of the orderly integration of multiple identical radiators, which allows improving the radiation patterns considerably, the array antenna is very important because it allows managing the amplitude of the currents and the excitation phase of each single radiator element, in this sense, the radiation patterns can be modified according to the designer's application.

In this section, it is intended to design an array antenna that has the possibility of generating multiple beams through the combination of amplitude and

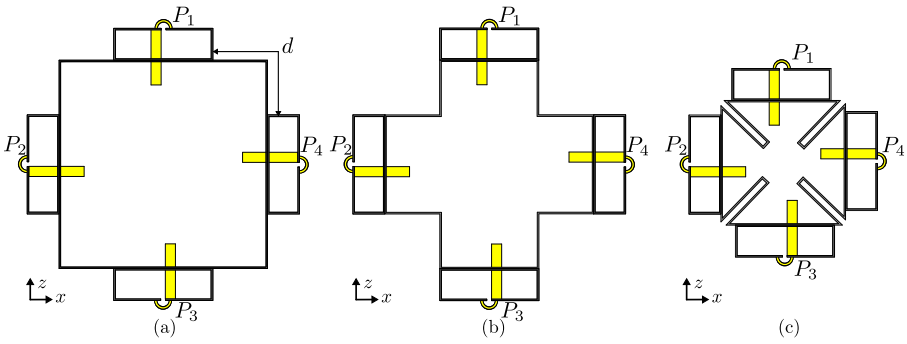

Figure 4.16: Setup of proposed array antenna . (a) Option 1, (b) option 2, and (c) option 3.

phase in the feeding ports, the rectangular structure folded over it detailed in Section 3.4 has been used such reference radiator element. In Fig. 4.16, some alternatives of antenna arrays have been shown.

The four elements have been mounted on each sidewalls of a piece of a rectangular waveguide opened in the two edges. The distance between the each element correspond to $0.5\lambda_0$ at the resonance frequency ($d = 25.5$ mm). Using a full-wave analysis, the scattering parameters of the three proposals array antennas have been obtained and depicted in Fig. 4.17, all of them have a good matching under -10 dB.

However, the third option would be the best for three things: the first because it generates a very good bandwidth, the second one because, in order to ensure that the radiation is produced only by each bent element, the edges of the waveguide have been deformed towards the center of the structure, with this design method a virtual cancellation of currents will be generated in the edges and, third because with this kind of configuration it has been possible to compact the structure to the maximum.

In Fig. 4.18, the 3D and top view of the manufacturing array antenna are shown, the material used to manufacture this prototype is copper and brass,

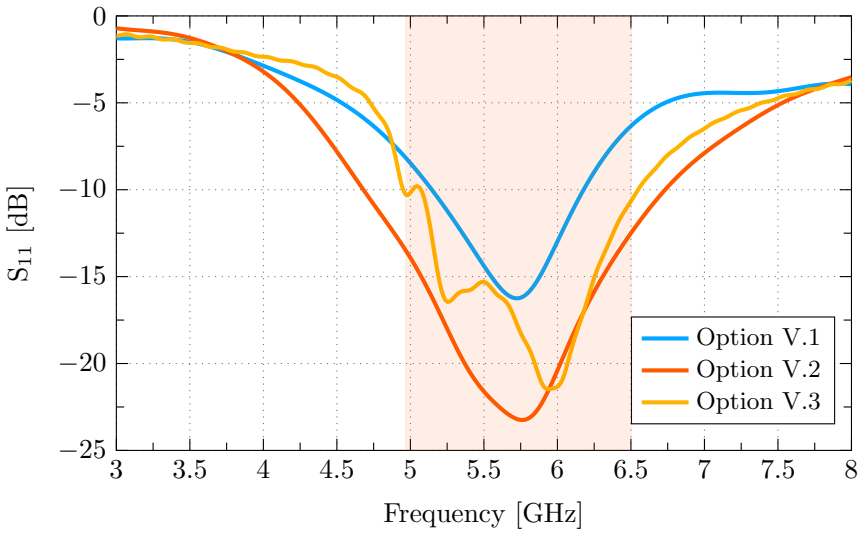

Figure 4.17: Simulated reflection coefficients of the different proposed array antenna.

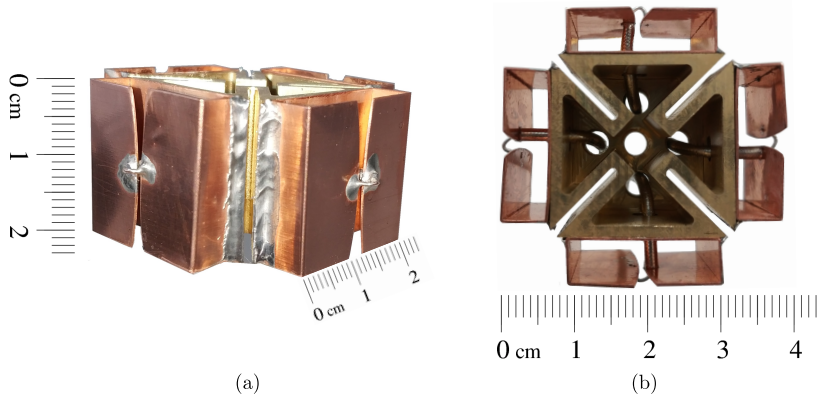

Figure 4.18: Array manufactured antenna proposed. (a) 3D view, and (b) top view.

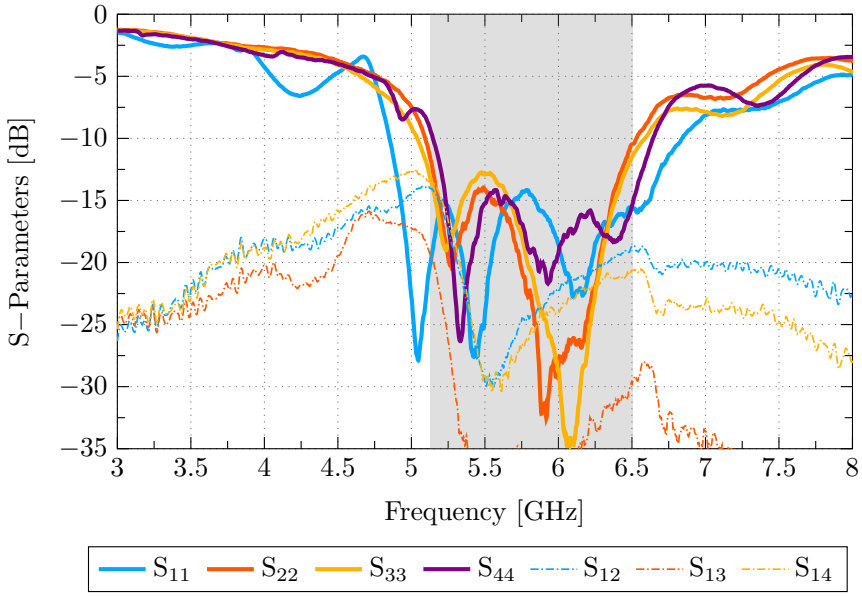

Figure 4.19: Measured Scattering parameters of the folded array antenna.

copper has been used for the manufacture of each radiator element, on the other hand, the brass is used for the chassis that is shaped like a waveguide with its edges bent inwards.

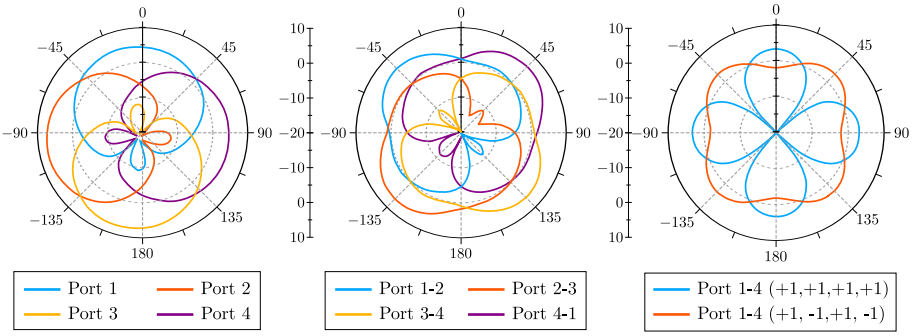

(a) (b) (c)

Figure 4.20: Radiation pattern of the folded array antenna. (a) Excitation of an isolated element, (b) Balanced feeding (+1, +1, +1, +1) and, (c) Differentially feeding (+1, -1, +1, -1).

The measured scattering parameters of the proposed array antenna have been plotted in Fig. 4.19. As anticipated, the bandwidth of this structure is the same as that of the simple element, in addition, the mutual coupling is very good that they are under -15 dB for the frequency range in which the antenna works optimally.

Depending to the feed of the array antenna, some radiation patterns with diverse directions can be generated. Exciting each of the elements in isolation, orthogonally radiation patterns are generated as seen in Fig. 4.20(a). Whereas, exciting at the same time two pairs of contiguous antennas, the radiation patterns in the vertices direction are generated such as shown in Fig. 4.20(b)). Finally, using simultaneously and balanced feeding (+1, +1, +1, +1), radiation patterns normal direction to each element that integrates the array antenna are obtained at the same time. However, by making a combination in the feeding, e.i, change the phases of the ports (+1, -1, +1, -1), the direction of maximum propagation can be shifted in 45° according at orange line in Fig. 4.20(c).

4.6 Conclusion

In this chapter a detailed study has been carried out of a structure folded on itself starting from a rectangular plate and an ellipse. In section 4.2, these structures have been analyzed using the Theory of Characteristic Modes and the effect of the folding on the modal resonances and on the modal current dis-

tributions has been modeled. The analysis has been focused on the longitudinal modes of the folded structure

Bent structures operate with several characteristic modes simultaneously. Modes are achieved with capacitive or inductive character over a large bandwidth. The combination of several modes yields a reactance close to 0 over a large range frequency. By bending the structures there is an additional advantage, the two ends of the structure can be easily connected to a transmission line or a voltage generator. Another interpretation of the folding is that between the feed points there is a slot in parallel with a shorted half-wavelength resonator.

Another very important thing that must be highlighted is the variation that occurs in the radiation pattern of J_3 mode. In planar plates J_3 modes has maximum radiation in the broadside direction and 2 lateral lobes, however, when the structure is folded, the secondary lobes disappear, leaving only a radiation lobe in broadside direction.

By folding the structure on itself, a resonance can be generated at low frequencies, achieving compactness of the antenna and allowing the generation of a unidirectional radiation pattern. In section 4.3, a planar ellipse is folded. The edges have a curved shape in the upper layer that help to improve the impedance matching since they behave as an impedance transformer.

In the last section of this chapter, several antennas based on the bending principle have been developed. A compact antenna with 4 independent radiation beams pointing in the directions 0°, 90°, 180° and, 270° has been proposed. Moreover, making use of the design considerations obtained from the modal analysis, several antenna prototypes for practical applications have been manufactured and measured.

Chapter 5

TCM in 3D structures

> "*The scientific man does not aim at an immediate result. He does not expect that his advanced ideas will be readily taken up. His work is like that of the planter - for the future. His duty is to lay the foundation for those who are to come, and point the way.*"
>
> — Nikola Tesla

5.1 Introduction

Over the years, it has been seen that waveguides have become one of the most important elements for the transport of microwave signals, being widely used for the design of multiple components such as couplers, power dividers, filters, resonators, etc [2, 143]. However, the vast majority of studies have focused on the analysis of the electric and magnetic fields inside the guide, leaving a gap in the study of the behavior of currents on the surface. The Theory of Characteristic Modes is a tool that will allow us to describe this behavior.

This chapter aims to study what is the relationship between the theory of characteristic modes and the electric transverse modes TE_{mn} and magnetic transverse TM_{mn} in a rectangular waveguide and a circular waveguide. To do this, a description and analysis will be carried out independently of the TE_{mn}, TM_{mn} modes and the characteristic modes of the two proposed waveguides.

Subsequently, the results obtained in each of the analyzes will be checked to describe what is the relationship between them.

5.2 Rectangular Waveguide Analysis

The hollow rectangular waveguides or rectangular tubes, inside it, are capable of propagating TE and TM modes after a cutoff frequency, while TEM modes will not propagate because at least two conductors are required. In order to understand how each of these modes is obtained and propagated inside the waveguide, the analysis of the waveguide using mathematical formulation have been used.

In Fig. 5.1, it is considered a 3-dimensional small section of the rectangular waveguide with dimensions a x b x h (where $a = b = h = 60$ mm), surrounded with perfect electric conductor and filling of a homogeneous material with ϵ permittivity and permeability μ.

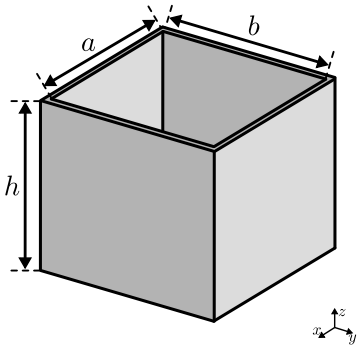

Figure 5.1: 3D view of waveguide section of a rectangular waveguide

5.2.1 TE and TM modes

The TE_{mn} and TM_{mn} modes have a very similar mathematical resolution, the only difference for each of the 2 cases is the condition of fields that are imposed, for the TE_{mn} mode you must satisfy $E_z = 0$ and $H_z \neq 0$, whereas, for TM_{mn} modes it will be $H_z = 0$ and $E_z \neq 0$. In both cases it is begun by solving the Helmholtz equation or also known as the wave equation [2, 143].

$$\nabla^2 A_z + k_c^2 A_z = 0 \tag{5.1}$$

where A_z is an arbitrary amplitude and can be replaced by H_z field in the case of TE_{mn} modes and the E_z field for TM_{mn} modes. Applying the aforementioned boundary conditions, the wave equation can be reduced to the following form:

$$\left(\frac{\partial^2}{\partial_x^2}+\frac{\partial^2}{\partial_y^2}+k_c^2\right)h_z(x,y)=0 \qquad \text{for } \mathrm{TE}_{mn} \text{ modes,} \tag{5.2a}$$

$$\left(\frac{\partial^2}{\partial_x^2}+\frac{\partial^2}{\partial_y^2}+k_c^2\right)e_z(x,y)=0 \qquad \text{for } \mathrm{TM}_{mn} \text{ modes,} \tag{5.2b}$$

with $H_z(x,y,z) = h_z(x,y)e^{-j\beta z}$, and $E_z(x,y,z) = e_z(x,y)e^{-j\beta z}$, where $k_c^2 = k^2 - \beta^2$ is called cutoff wave number and $k = \omega\sqrt{\mu\epsilon}$. A common procedure to solve this type of the partial differential equation is through the method of separation of variables, where each dependent term of x and y must be equal to a constant called separation constant k_x or k_y depending case.

$$\frac{1}{\mathrm{X}}\frac{\mathrm{d}^2\mathrm{X}}{\mathrm{d}x^2} = cte = -k_x^2 \tag{5.3a}$$

$$\frac{1}{\mathrm{Y}}\frac{\mathrm{d}^2\mathrm{Y}}{\mathrm{d}y^2} = cte = -k_y^2 \tag{5.3b}$$

and

$$k_x^2 + k_y^2 = k_c^2 \tag{5.4}$$

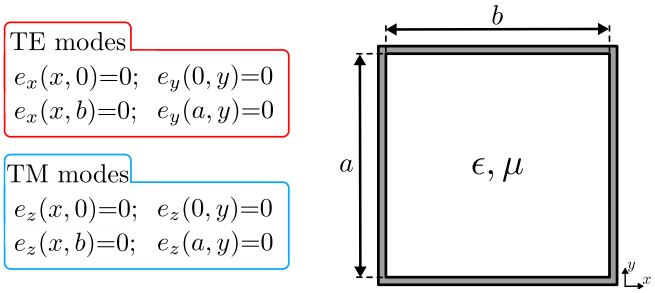

Figure 5.2: Boundary conditions on the electric field components tangential to the waveguide walls.

Then, the general solution for h_z and e_z can then be written as:

$$h_z(x,y) = (A\cos k_x x + B\sin k_x x)\,(C\cos k_y y + D\sin k_y y) \tag{5.5a}$$

$$e_z(x,y) = (A\cos k_x x + B\sin k_x x)\,(C\cos k_y y + D\sin k_y y) \tag{5.5b}$$

To obtain $h_z(x,y)$, the boundary conditions on the electric field tangential components must be applied in the walls of the rectangular waveguide according to the Fig. 5.2. However, that value cannot be obtained directly, the values of e_x and e_y must first be found.

$$e_x = \frac{-j\omega\mu}{k_c^2} k_y\,(A\cos k_x x + B\sin k_x x)\,(-C\sin k_y y + D\cos k_y y) \tag{5.6a}$$

$$e_y = \frac{j\omega\mu}{k_c^2} k_y\,(-A\sin k_x x + B\cos k_x x)\,(C\cos k_y y + D\sin k_y y) \tag{5.6b}$$

Applying the boundary conditions of Fig. 5.2 in e_x and e_y equations, we have the values D=0 and $k_y = n\pi/b$ for $n = 1, 2, 3, ...$, while for e_y, B=0 and $k_x = m\pi/a$ when $m = 1, 2, 3....$ Thus, the final solution for H_z is then

$$H_z(x,y,z) = A_{mn}\cos\frac{m\pi x}{a}\cos\frac{n\pi y}{b}e^{-j\beta_z} \tag{5.7}$$

On the other hand, for TM_{mn} modes, the conditions shown in Fig. 5.2 are applied directly over the equation of e_x, leaving A=0 and $k_y = n\pi/b$ for $n = 1, 2, 3, ...$, and in e_y shows that C=0 and $k_x = m\pi/a$ for $m = 1, 2, 3, ...$ Then, the solution for E_z can be expressed as

$$E_z(x,y,z) = B_{mn}\sin\frac{m\pi x}{a}\sin\frac{n\pi y}{b}e^{-j\beta_z} \tag{5.8}$$

where A_{mn} and B_{mn} are arbitrary amplitude constant. The transverse field components for the TE_{mn} and TM_{mn} modes, have been depicted in Table 5.1.

In addition to the components of the cross fields in the rectangular waveguide, the cutoff frequency can also be expressed through the equation Eq. (5.9). It is important to highlight that this expression can be used for both TE and TM modes.

$$f_{c_{nm}} = \frac{1}{2\pi a\sqrt{\mu\epsilon}}\sqrt{\left(\frac{n\pi}{a}\right)^2 + \left(\frac{m\pi}{b}\right)^2} \tag{5.9}$$

According to equations of the **E** and **H** fields shown in Table 5.1, the TE_{00} mode cannot exist because the expressions will be cancelled if the values n and

Table 5.1: Summary of equations for Rectangular Waveguide [2]

Quantity	TE_{mn} Mode	TM_{mn} Mode
k	$\omega\sqrt{\mu\epsilon}$	$\omega\sqrt{\mu\epsilon}$
k_c	$\sqrt{(m\pi/a)^2+(n\pi/b)^2}$	$\sqrt{(m\pi/a)^2+(n\pi/b)^2}$
β	$\sqrt{k^2-k_c^2}$	$\sqrt{k^2-k_c^2}$
λ_c	$\frac{2\pi}{k_c}$	$\frac{2\pi}{k_c}$
λ_g	$\frac{2\pi}{\beta}$	$\frac{2\pi}{\beta}$
E_x	$\frac{j\omega\mu n\pi}{k_c^2 b}A\cos\frac{m\pi x}{a}\sin\frac{n\pi y}{b}e^{-j\beta_z}$	$\frac{-j\beta m\pi}{k_c^2 a}B\cos\frac{m\pi x}{a}\sin\frac{n\pi y}{b}e^{-j\beta_z}$
E_y	$\frac{-j\omega\mu m\pi}{k_c^2 a}A\sin\frac{m\pi x}{a}\cos\frac{n\pi y}{b}e^{-j\beta_z}$	$\frac{-j\beta n\pi}{k_c^2 b}B\sin\frac{m\pi x}{a}\cos\frac{n\pi y}{b}e^{-j\beta_z}$
E_z	0	$B\sin\frac{m\pi x}{a}\sin\frac{n\pi y}{b}e^{-j\beta_z}$
H_x	$\frac{j\beta m\pi}{k_c^2 a}A\sin\frac{m\pi x}{a}\cos\frac{n\pi y}{b}e^{-j\beta_z}$	$\frac{j\omega\epsilon n\pi}{k_c^2 b}B\sin\frac{m\pi x}{a}\cos\frac{n\pi y}{b}e^{-j\beta_z}$
H_y	$\frac{j\beta n\pi}{k_c^2 b}A\cos\frac{m\pi x}{a}\sin\frac{n\pi y}{b}e^{-j\beta_z}$	$\frac{-j\omega\epsilon m\pi}{k_c^2 a}B\cos\frac{m\pi x}{a}\sin\frac{n\pi y}{b}e^{-j\beta_z}$
H_z	$A\cos\frac{m\pi x}{a}\cos\frac{n\pi y}{b}e^{-j\beta_z}$	0

m are taken the value of 0. Therefore, keeping in mind that their sides are equals, the TE_{10}, and TE_{01} modes will be considered such as dominant modes, whereas, the lowest order magnetic transverse mode that can be transmitted an electromagnetic wave in is TM_{11} mode. Using Eq. (5.9), in Table 5.2 the cutoff frequencies for several TE and TM modes have been computed for the rectangular waveguide of dimensions 60 mm x 60 mm x 60 mm.

To determine if the waveguide works correctly, it is necessary to check whether the cutoff frequency is as expected, and second that the wave propagates without attenuation, i.e., no energy escapes through the four conductive walls. Therefore, to know if the cutoff frequency is as expected, we must analyze the propagation constant inside the guide.

Table 5.2: Calculated cut-off frequencies in GHz of TE_{mn} and TM_{mn} first modals fields for a rectangular waveguide.

	TE_{mn} modes			TM_{mn} modes		
m	f_{m0}	f_{m1}	f_{m2}	f_{m0}	f_{m1}	f_{m2}
0	-	2,498	4,996	-	-	-
1	2,498	3,533	5,586	-	3,533	5,586
2	4,996	5,586	7,066	-	5,586	7,066
3	7,494	7,900	9,007	-	7,900	9,007

$$\gamma = \alpha - j\beta \tag{5.10}$$

where γ is the propagation constant, α is the wave attenuation constant, is the real part of the propagation constant, and represents the attenuation of the waveguide along the guide, β is the phase constant, is the imaginary part of the propagation constant and represents the phase change of the wave along the waveguide.

In order for the waveguide to work properly, it is expected to obtain an attenuation constant that tends to zero after the cutoff frequency and a phase constant that increases from the cutoff frequency.

Fig. 5.3 shows that from the cutoff frequency, the attenuation constant (α) begins to decrease until it stabilises at practically zero. Therefore, higher frequencies will become less attenuated. On the other hand, in Fig. 5.4 it shows the phase constant (β) versus the frequency, as expected, depending on the mode order for a range of frequency lower than the cutoff frequency the propagation constant is equal to 0, therefore, in the rectangular waveguide nothing can be propagated for frequencies lower than the cutoff. Therefore, it has been possible to verify that the cutoff frequencies obtained through mathematical formulation represented in Table 5.2 coincide exactly with the simulated results.

Once the cutoff frequency has been exceeded, the waveguide is capable of propagating the electric or magnetic field within it, the increase in the phase constant will depend directly on the frequency. As you can see, each of the modes will have different behavior for an analysis frequency, not only in the value of the phase constant but also in the distribution of the electric and magnetic field.

In Fig. 5.5, the frontal view (X-Y axis) of a rectangular waveguide section has been depicted, inside it the electric and the magnetic field (**E**, **H**) of some TE and TM modes have been plotted, the continuous lines will represent the electric field, whereas the dash-dotted lines the magnetic field. Other higher order modes can be seen in the article [144].

The electric and magnetic fields of the TE and TM modes at each of their cutoff frequencies have been represented in Fig. 5.5, the cutoff frequencies are a function of the dimensions of the waveguide in its cross section a and b, this is expressed in the equations of H_x, H_y, E_x, E_y of Table 5.1.

However, each of them depends on a propagation constant ($e^{-j\beta_z}$) in the z-direction, the distribution of the electric and magnetic fields has been represented in Fig. 5.6. As it can see, there is one or more phase variations throughout the guide, in order to explain this behavior, the resonant cavities will be analyzed.

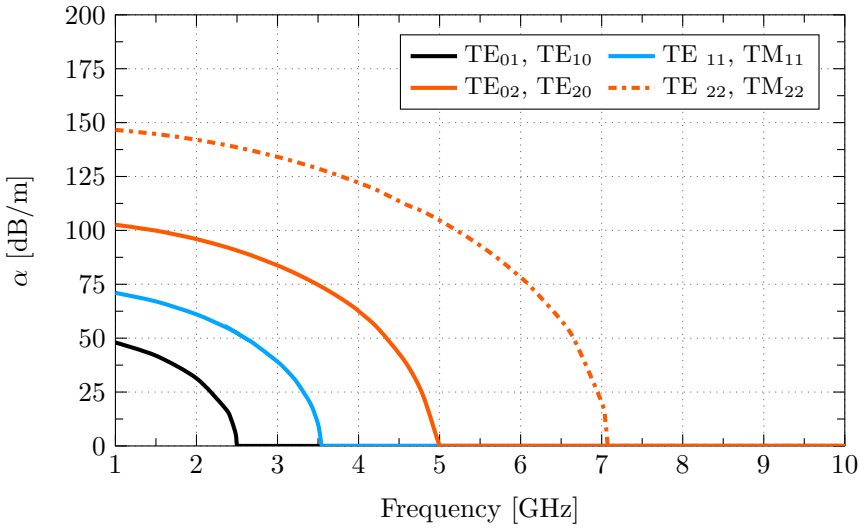

Figure 5.3: Attenuation constant of TE and TM first modals fields for a rectangular waveguide.

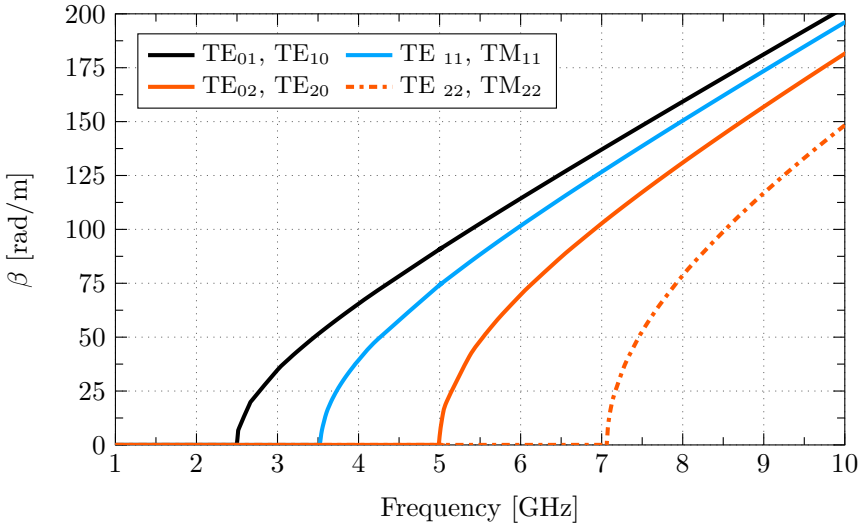

Figure 5.4: Phase constant of TE and TM first modals fields for a rectangular waveguide.

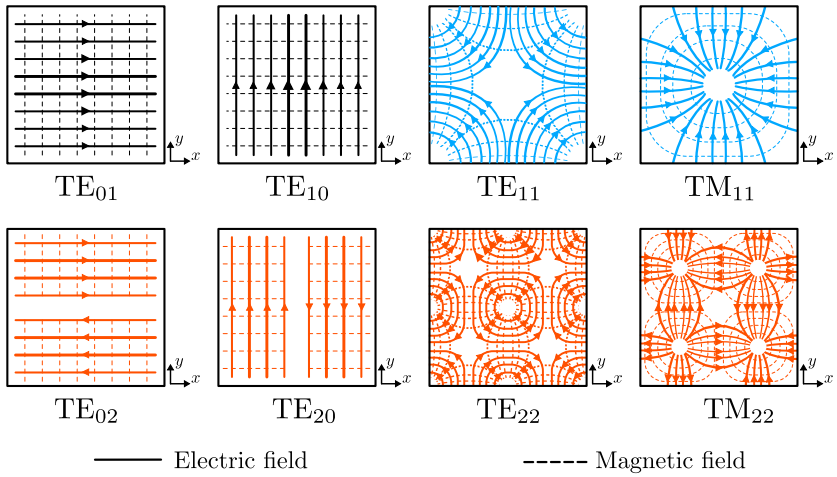

Figure 5.5: Front view of TE and TM modal field distribution for a rectangular waveguide of dimensions *axb*.

5.2.2 Rectangular waveguide cavity resonator analysis

Along the axis z of a waveguide, boundary conditions can be imposed, that is, electric or magnetic walls can be applied to it, these will be called resonant

cavities. This type of structures will no longer have a cutoff frequency but a resonance frequency, so, to find the resonances of the modes when the waves propagate along the axis z, therefore, not only the lateral dimensions a and b but also the length h, as can be seen in Fig. 5.7.

The electric and magnetic fields of the TE or TM modes can be calculated from the solution of the Helmholtz equation (5.1) through the separation of variables method applying the boundary conditions for the cavities, generating the separation constants:

$$k^2 = k_x^2 + k_y^2 + k_z^2 = \omega^2 \mu \epsilon \tag{5.11}$$

Considering the solutions depicted in Table 5.1, which already satisfy the boundary conditions on the side walls (x= 0, a and y= 0, b) of the cavity, it will only be necessary to impose the boundary conditions for $E_x = E_y = 0$ on the end walls at z= 0, d. Therefore, the transverse electric fields (E_x, E_y) of the TE_{mn} or TM_{mn} rectangular waveguide mode can be written through the transverse mode $\overline{e}(x, y)$, and arbitrary amplitudes of standing wave (A^+, A^-).

$$\mathrm{E}_t(x, y, z) = \overline{e}(x, y) \left(A^+ e^{-j\beta_{mn} z} + A^- e^{-j\beta_{mn} z} \right) \tag{5.12}$$

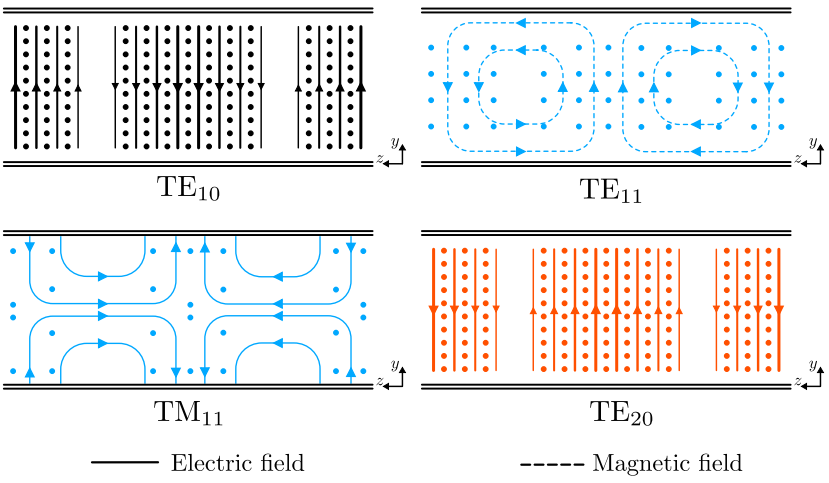

Figure 5.6: Lateral view of TE and TM modal field distribution for a rectangular waveguide.

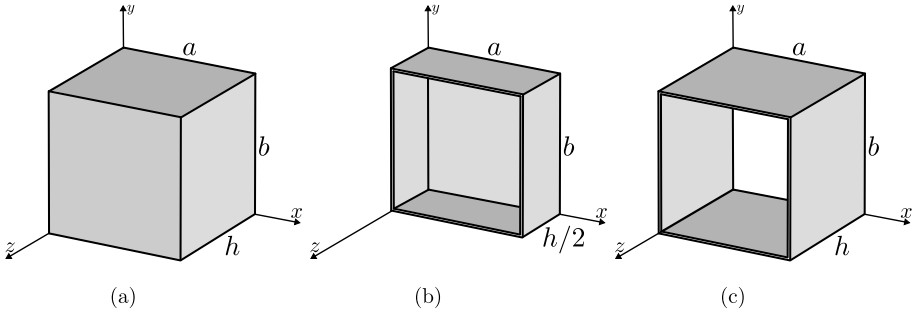

Figure 5.7: 3D views of resonant cavities configurations with dimension $a = b = h = 60$ mm. (a) Shorted at both ends, (b) shorted at one end and opened at the other, (c) opened at both ends.

The propagation constant of the m, n th TE or TM mode can be compute using Eq. (5.13), and should be consider the electric and magnetic properties of the material filling the cavity.

$$\beta_{mn} = \sqrt{k^2 - \left(\frac{m\pi}{a}\right)^2 - \left(\frac{n\pi}{b}\right)^2} \tag{5.13}$$

The expression of resonance frequency for $\text{TE}_{mn\ell}$ or $\text{TM}_{mn\ell}$ can be describe using the Eq. (5.14), where $k_x = (m\pi/a)$, $k_y = (n\pi/b)$, $k_z = (\ell\pi/h)$.

$$f_{mn\ell} = \frac{k_{mn\ell}}{2\pi\sqrt{\mu\epsilon}} = \frac{ck_{mn\ell}}{2\pi\sqrt{\mu_r\epsilon_r}} = \frac{c}{2\pi\sqrt{\mu_r\epsilon_r}}\sqrt{\left(\frac{m\pi}{a}\right)^2 + \left(\frac{n\pi}{b}\right)^2 + \left(\frac{\ell\pi}{h}\right)^2} \tag{5.14}$$

The resonance frequencies of the structures in Fig. 5.7 can be calculated under the equation (5.14), in Table 5.3 shows the resonance frequencies calculated for the first 2 modes TE and TM, however, the distribution of fields **E** and **H** are different for each case, then a detailed analysis will be carried out below.

5.2.2.1 Case shorted at both ends

Applying the field condition $\mathbf{E}_t = 0$ (short circuit) for $z = 0$ in Eq. (5.12), implies that the arbitrary amplitudes A^+ and A^- are equal (i.e. total reflection from a conductive wall), while the equation obtained for the condition $\mathbf{E}_t = 0$ at $z = h$ would be

Table 5.3: Calculated resonant frequencies in GHz of $TE_{mn\ell}$ and $TM_{mn\ell}$ first modals fields for a rectangular cavity resonator.

	TE_{mn1} modes			TM_{mn1} modes			TE_{mn2} modes			TM_{mn2} modes		
m	f_{m01}	f_{m11}	f_{m21}	f_{m01}	f_{m11}	f_{m21}	f_{m02}	f_{m12}	f_{m22}	f_{m02}	f_{m12}	f_{m22}
0	-	3,53	5,58	-	-	-	-	5,58	7,06	-	-	-
1	3,53	4,32	6,12	-	4,32	6,12	5,58	6,12	7,49	-	6,12	7,49
2	5,58	6,12	7,49	-	6,12	7,49	7,06	7,49	8,65	-	7,49	8,65
3	7,90	8,28	9,34	-	8,28	9,34	9,00	9,34	10,3	-	9,34	10,3

$$\mathbf{E}_t(x,y,h) = -\bar{e}(x,y)A^+ 2j \sin\beta_{mn}h = 0 \tag{5.15}$$

Remaining as one of solutions ($A^+ \neq 0$) when

$$\beta_{mn}h = \ell\pi, \qquad \ell = 1,2,3,..., \tag{5.16}$$

that is, the length of the cavity must be an integer multiple of one half the wavelength at the resonant frequency. Keeping in mind the values of the Table 5.1 and applying the Eq. (5.12), and considering the fact that $A^+ = A^-$, the total fields for the resonance of the modes $TE_{mn\ell}$ can be written as:

$$E_x = -A^+ \cos\frac{m\pi x}{a}\sin\frac{n\pi y}{b}\left(e^{-j\beta z} - e^{j\beta z}\right) \tag{5.17a}$$

$$E_y = A^+ \sin\frac{m\pi x}{a}\cos\frac{n\pi y}{b}\left(e^{-j\beta z} - e^{j\beta z}\right) \tag{5.17b}$$

$$E_z = 0 \tag{5.17c}$$

$$H_x = \frac{-A^+\beta}{k\eta}\sin\frac{m\pi x}{a}\cos\frac{n\pi y}{b}\left(e^{-j\beta z} + e^{j\beta z}\right) \tag{5.17d}$$

$$H_y = \frac{-A^+\beta}{k\eta}\cos\frac{m\pi x}{a}\sin\frac{n\pi y}{b}\left(e^{-j\beta z} + e^{j\beta z}\right) \tag{5.17e}$$

$$H_z = \frac{j\pi A^+}{k\eta a}\cos\frac{m\pi x}{a}\cos\frac{n\pi y}{b}\left(e^{-j\beta z} - e^{j\beta z}\right) \tag{5.17f}$$

Letting $E_0 = -2jA^+$, using the Eq. (5.16) and applying the Euler relation $e^{-j\beta_z} = \cos(\beta_z) - j\sin(\beta_z)$, the field equations can be simplified to

$$E_x = -E_0 \cos\frac{m\pi x}{a} \sin\frac{n\pi y}{b} \sin\frac{\ell\pi z}{h} \tag{5.18a}$$

$$E_y = E_0 \sin\frac{m\pi x}{a} \cos\frac{n\pi y}{b} \sin\frac{\ell\pi z}{h} \tag{5.18b}$$

$$E_z = 0 \tag{5.18c}$$

$$H_x = \frac{-jE_0\beta}{k\eta} \sin\frac{m\pi x}{a} \cos\frac{n\pi y}{b} \cos\frac{\ell\pi z}{h} \tag{5.18d}$$

$$H_y = \frac{-jE_0\beta}{k\eta} \cos\frac{m\pi x}{a} \sin\frac{n\pi y}{b} \cos\frac{\ell\pi z}{h} \tag{5.18e}$$

$$H_z = \frac{j\pi E_0}{k\eta a} \cos\frac{m\pi x}{a} \cos\frac{n\pi y}{b} \sin\frac{\ell\pi z}{h} \tag{5.18f}$$

5.2.2.2 Case of shorted and open circuit

For the analysis of a structure that has a short circuit and an open circuit at the ends, it can be carried out based on the analysis previously carried out. Then, the closed cavity shown in Fig. 5.7a, will be divided into 2 equal semi-structures, leaving as dimensions a x b x $h/2$, the method to represent the fields will be performed using the same mathematical formulation that was described for a closed cavity, to In this case the resonance frequency can be obtained using Eq. (5.14), however, the resonance will not be as in the previous case at $\lambda_g/2$ but at $\lambda_g/4$.

5.2.2.3 Case of opened at both ends

For this case, the tangential field condition that will be applied will be $E_t = \max$ (open circuit) for $z = 0$ in the Eq. (5.14), the procedure to solve the fields in the different directions are the same that the shorted at both ends case, the only component that is changed is the equation for the H_z field, such as shown below

$$H_z = \frac{j\pi E_0}{k\eta a} \cos\frac{m\pi x}{a} \cos\frac{n\pi y}{b} \cos\frac{\ell\pi z}{h} \tag{5.19}$$

In Fig. 5.8, the electric field and its variation have been represented for the modes TE_{101} and TE_{102} of each of the structures shown in Fig. 5.7. The representation of the frontal, lateral and top views of the electric field within the cavities has been performed, the front view has been taken at a distance

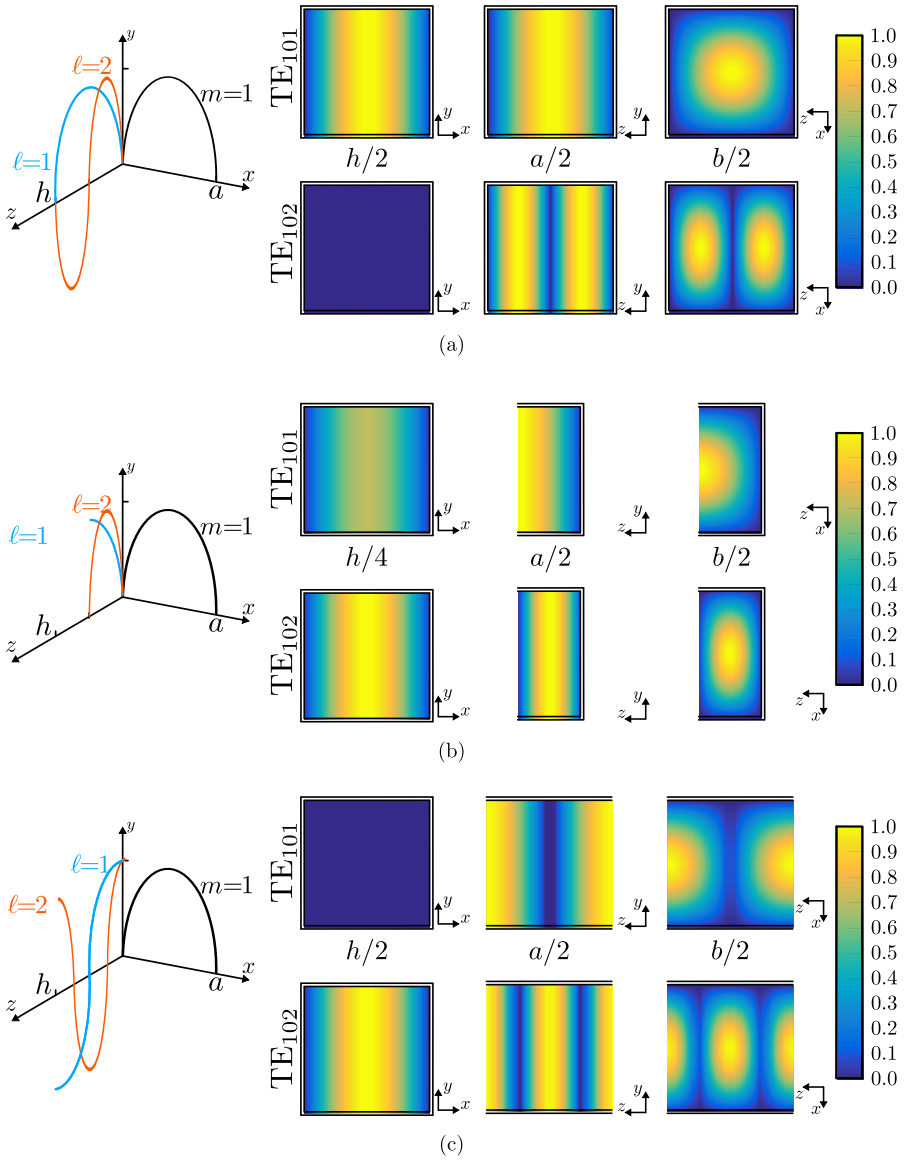

Figure 5.8: Absolute electric field variation for the TE_{101} and TE_{102} modes in rectangular cavities and their frontal, lateral and top view. (a) Shorted at both ends, (b) shorted at one end and opened at the other, (c) opened at both ends.

$a/2$ for Fig. 5.8(a) and (c), while for Fig. 5.8(b) at $h/4$, the side view at a distance $a/2$ and the top view at $b/2$.

Depending on each of the structures in Fig. 5.7, the variation of the electric field is different for each of the structures. In the cavity short-circuited on both sides, the electric field represents a sine function for the x-y and y-z axes for a wavelength $h = \lambda_g/2$ at the resonance frequency. On the other hand, for the structure with an open circuit at its ends, the function that represents the electric field is the sine for the x-y axis and cosine for the y-z axis.

In both cases, the variation of the electric field on the axis y-z depends on the order of the subscript ℓ. Finally, for the configuration of a waveguide with short circuit and open circuit at the ends with length $\lambda_g/4 = h/2$, the field will be $E_z = 0$ at $h = 0$ and $E_z = \max$ for the other end.

5.2.3 TCM in Rectangular Waveguide

Once the behavior of the electromagnetic waves and modes that exist in the rectangular waveguides has been described, through their longitudinal magnetic and electric field components. In this section will describe the behavior of rectangular waveguides using the Theory of Characteristic Modes. Therefore, in order to achieve this objective, the entire mathematical formulation described in Chapter 2 of this document will be applied, through the use of electromagnetic simulators.

The geometry of the rectangular waveguide used for the analysis in this section has been presented in Fig. 5.1, the dimensions of the structure are symmetrical; the width, the height and the depth have a value of $\lambda/2$ at the frequency of 2.5 GHz.

Similar to the planar structures, the electrical and magnetic modes are generated in 3D structures as well, in addition to the antenna and transmission line modes. Therefore, the nomenclature that will allow distinguishing them somehow will be linked to the coefficients m and n, where the m coefficient describes the azimuthal variation and n the axial variation.

Some of the first characteristic angles ($\alpha = 180°$) of the section of rectangular waveguide in the range frequency from 1 to 7 GHz have been represented in Fig. 5.9. As can be seen in the graph, there are some modes in resonance at the mentioned frequency range, such as J_{00}H, J_{10}E, J_{20}E, J_{30}E, J_{01}E, J_{11}E, J_{11}H; whereas others of them have a value close to the resonance.

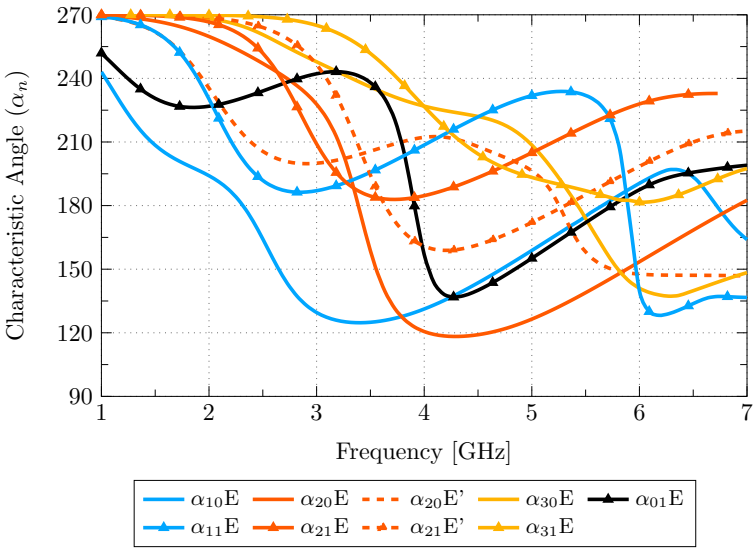

(a)

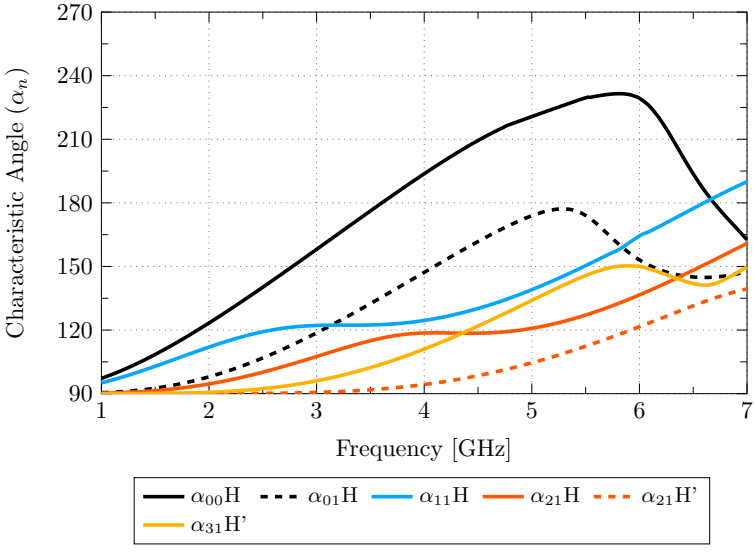

(b)

Figure 5.9: Characteristic angle of a rectangular waveguide.(a)Electric modes and, (b) Magnetic modes.

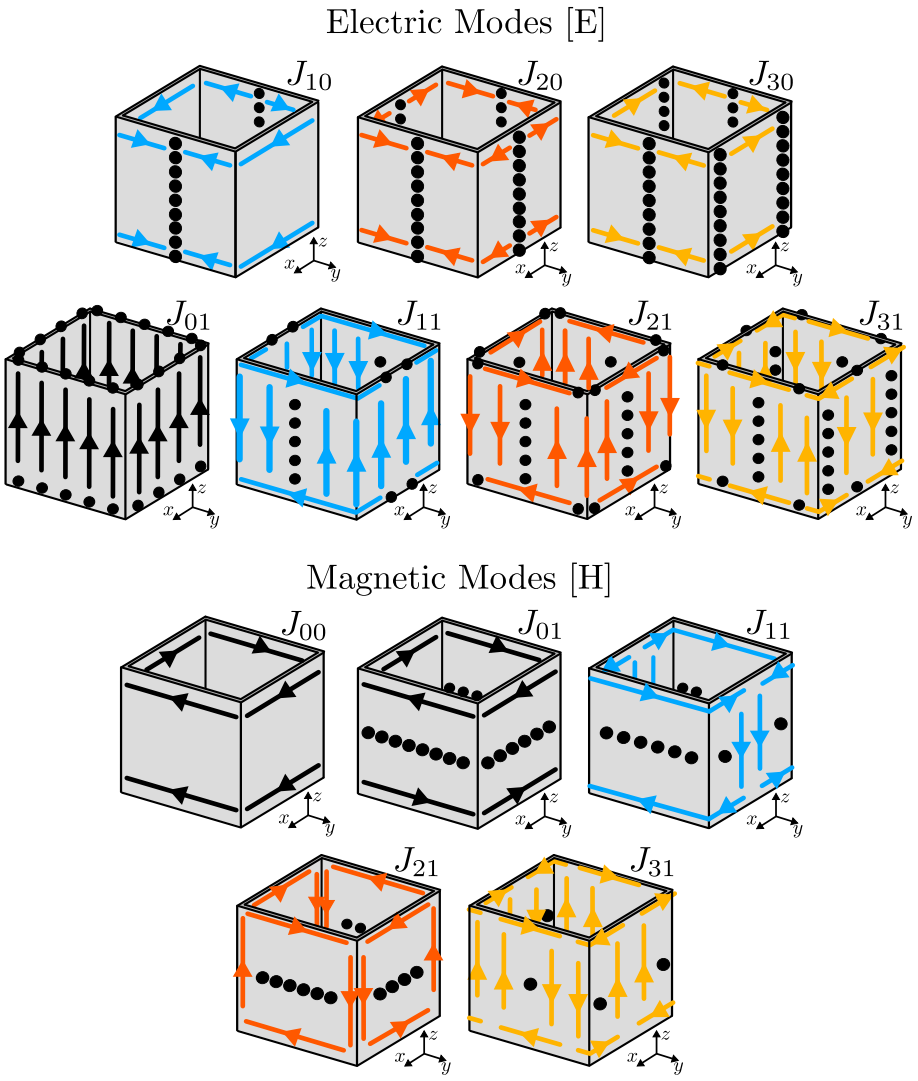

Figure 5.10: Modal current distribution of a rectangular waveguide

Each of the odd modes (J_{10}, J_{30}, ..., $J_{(2n-1)}$) and their degenerates are resonating at the same frequency, for example the fundamental mode J_{01}E and J'_{01}E are resonating at the 2.31 GHz frequency. On the other hand, the even modes (J_{20}, J_{40}, ..., $J_{(2n+1)0}$) have a different behavior, the common modes

and their degenerate modes are resonating at different frequencies, so in the case of the J_{20} mode the resonance is at 3.39 GHz and the J_{20}' at 5.25 GHz.

In Fig. 5.10, the distribution of modal currents at the resonance frequency of each of the characteristic angles plotted in Fig. 5.9 has been presented. For the electric antenna modes corresponding to those represented in the first row of Fig. 5.10, the currents have an azimuth direction, it can clearly be seen that the odd modes have the current nulls vertically on the face parallel to the $y-z$ axis. The electric transmission line modes are represented in the second row, the currents flow from top to bottom according to the order of the mode, this order is given by the number of current null pairs generating in the edges of the waveguide.

Then, the main concept in this type of modes is that the direction of the currents between two axial edges in the waveguide should be opposites. Finally, in the third row, the currents of the magnetic modes have been shown, it can clearly be seen that the currents are rotating around the current nulls.

The coincidence in the resonances of each odd modes (common and degenerate) in Fig. 5.9 is due to the symmetry with which the currents flow on the surface of the waveguide, shifting the current nulls from the front wall ($y-z$ plane) in common modes towards the side-wall ($x-z$ plane) for degenerated modes, with polarization being the only difference between them.

The frequency shift that is generated between the common even modes and their degenerates in a rectangular waveguide section (see Fig. 5.11(a)) can be demonstrated through their characteristic currents. Comparing the modal current distribution of the J_{20}E and J_{02}'E mode in Fig. 5.11(b), it can be seen that the current nulls for J_{02}E mode are presented vertically in the middle of the walls of the waveguide; while for the J_{02}'E mode, the current nulls have been shifted towards the azimuth edges of the structure, producing an imminent reduction of the path to flow the current, even forming 4 elements array as well.

On the other hand, in Fig. 5.12 the modal radiation patterns of some TE and TM modes in a rectangular waveguide have been shown, these radiation patterns have been plotted at the same frequency of the modal characteristic currents of Fig. 5.10. One of the most important radiation patterns generated in the piece of rectangular waveguide piece is mode J_1, its unique broadside direction of propagation makes it highly desirable for applications that require directional radiation patterns.

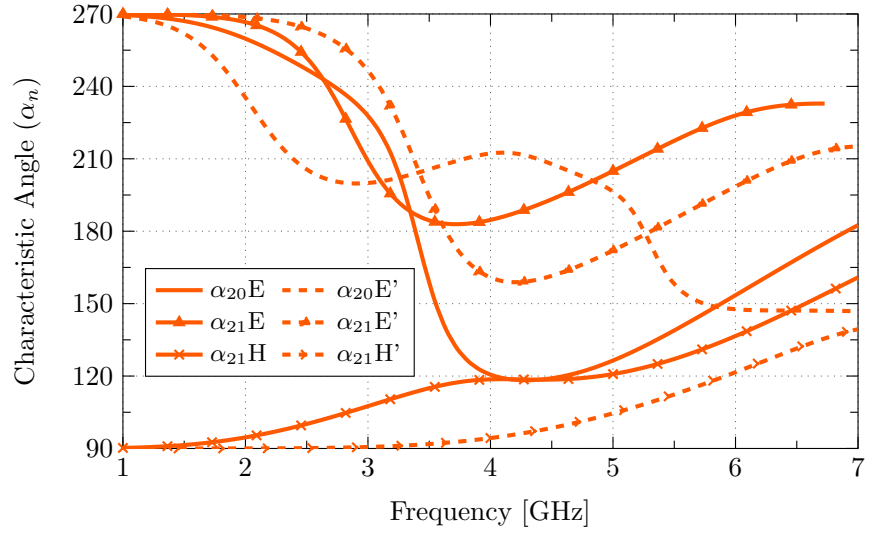

(a)

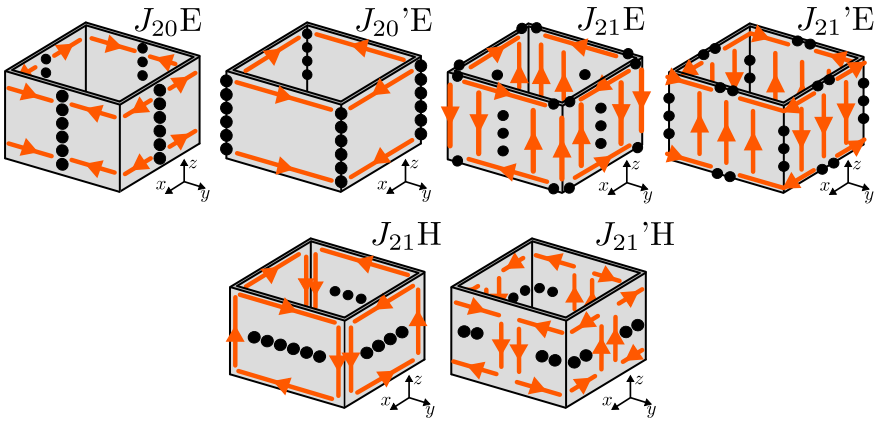

(b)

Figure 5.11: Main and degenerate even modes of a rectangular waveguide section. (a) Characteristic angles (b) Modal current distributions.

Once the modes that appear in the frequency range from 1 to 7 GHz have been described. It is necessary to determine which modes can be excited, and how much they can contribute to the total radiated power when a plane wave impinging the rectangular waveguide.

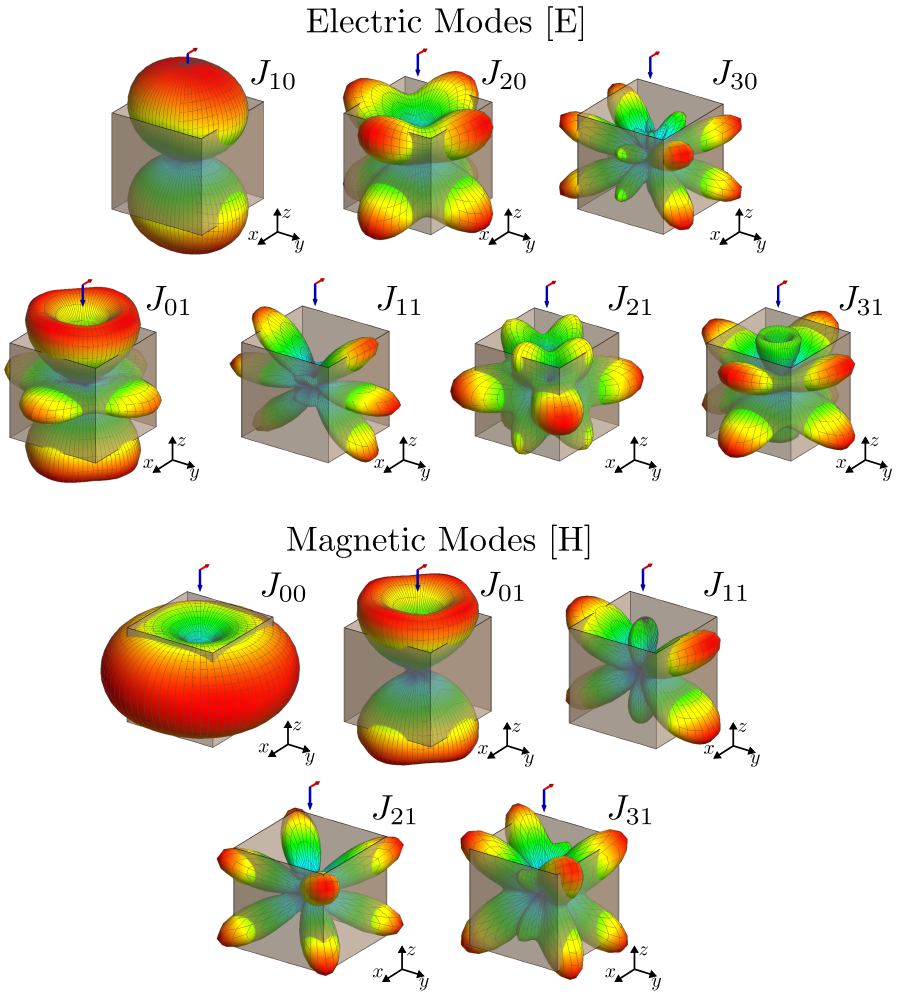

Figure 5.12: Modal radiation pattern of a rectangular waveguide

By illuminating a rectangular waveguide with a plane wave in vertical polarization, it can be seen that in the analyzed frequency range, some modes contribute more power than others as is depicted in Fig. 5.13, this contribution is different at the frequency. At 2 GHz, the J_{10}E mode is the most important because it contributes approximately 65%, followed by the J_{11}'E mode with 30%, and the J_{11}' magnetic mode with 14%, the other modes contribute with minimum powers.

Table 5.4: Power contribution percentage of modes that participating in the range frequency from 1 to 7 GHz, when the structure is illuminated with plane wave in vertical polarization.

Mode	1 GHz	2 GHz	3 GHz	4 GHz	5 GHz	6 GHz	7 GHz
J_{10}E	95,7%	60,2%	33%	14,9%	0,69%	0%	0%
J'_{11}E	0%	26,3%	20,4%	4,36%	3,83%	0%	0%
J_{31}E	0%	0%	0%	9,31%	7,8%	0,9%	0,8%
J_{52}E	0%	0%	1,82%	10,5%	8,13%	22,3%	3,42%
J'_{11}H	4,08%	13,5%	44,2%	43,1%	29,4%	8,4%	0,9%
J_{12}H	0%	0%	0%	14,9%	40%	49,1%	35,6%
Others	0,22%	0%	0,58%	2,93%	10,15%	19,3%	59,28%

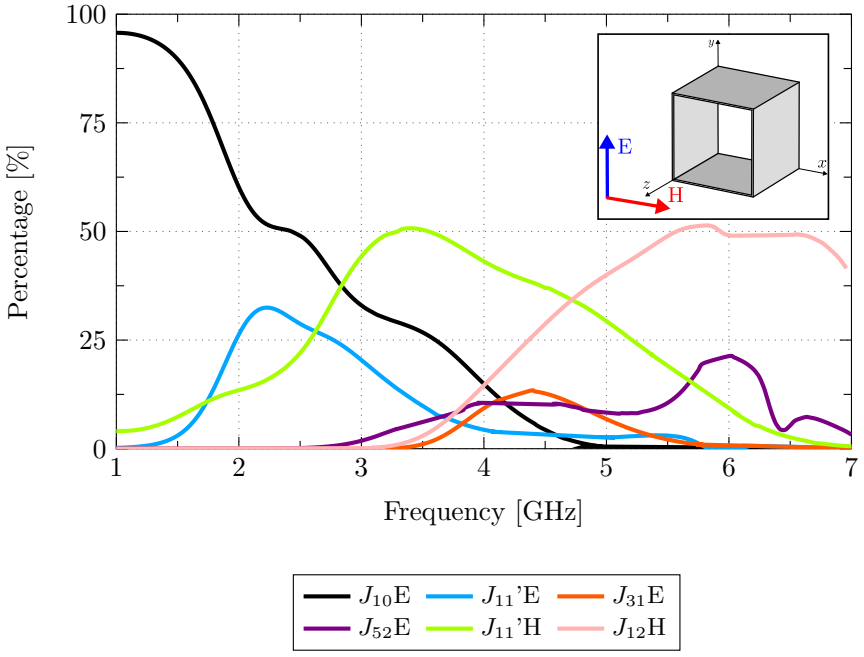

Figure 5.13: Power contribution of modes that participating in the range frequency from 1 to 7 GHz, when the structure is illuminated with plane wave in vertical polarization.

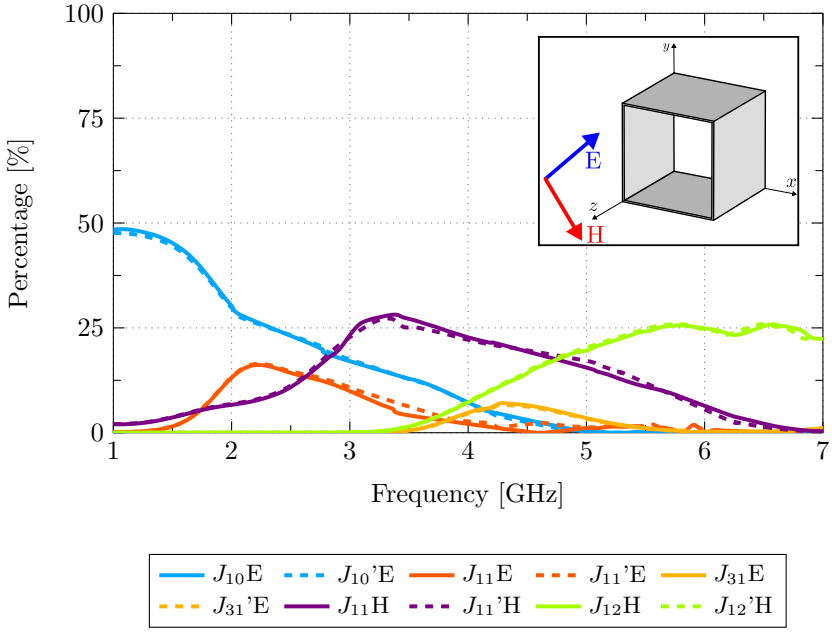

Figure 5.14: Power contribution of modes that participating in the range frequency from 1 to 7 GHz, when the structure is illuminated with plane wave rotated -45°.

Table 5.5: Power contribution percentage of modes that participating in the range frequency from 1 to 7 GHz, when the structure is illuminated with plane wave rotated -45°.

Mode	1 GHz	2 GHz	3 GHz	4 GHz	5 GHz	6 GHz	7 GHz
J_{10}E	48,5%	30,2%	17,4%	7,4%	0%	0%	0%
J_{10}'E	47,7%	29,7%	16,7%	7,3%	0%	0%	0%
J_{11}E	0%	13,3%	10,8%	0%	1,1%	7,8%	0%
J_{11}'E	0%	13,2%	9,93%	0%	1,2%	7,6%	0%
J_{31}E	0%	0%	0%	4,72%	4,32%	0%	0%
J_{31}'E	0%	0%	0%	4,54%	4,26%	0%	0%
J_{11}H	2,02%	6,87%	22,8%	22,8%	17,6%	0%	0%
J_{11}'H	2,0%	6,87%	21,2%	22,2%	17,4%	0%	0%
J_{12}H	0%	0%	0%	7,8%	22,8%	24,6%	23%
J_{12}'H	0%	0%	0%	7,6%	22,6%	24,4%	23%
Others	0%	0%	1,17%	15,64%	8,72%	35,6%	54%

In general form, for the range frequencies, the modes that have the most prominence are J_{10}E, J_{11}'E, J_{11}'H, J_{12}H, respectively. Table 5.4 has provided a complete summary of the contribution of powers for frequencies from 1 to 7 GHz.

Rotating the illumination source (plane wave) in 45° from the vertical polarization as shown in Fig. 5.13, it can clearly be seen that there are 5 modes and their degenerates contribute the greatest percentage of power in the range frequency analyzed. Each normal mode and its orthogonal provide the same percentage contribution. Then, a summary of the contribution percentage of each of the modes in the frequency range from 1 to 7 GHz has been shown in Table 5.5.

Reducing the waveguide to the half and placing a short circuit at one of its ends, the characteristic angles shown in Fig. 5.15 are very different behavior from those generated in the rectangular waveguide rectangular that were depicted in Fig. 5.9. Due to the reduction of height in the structure, the res-

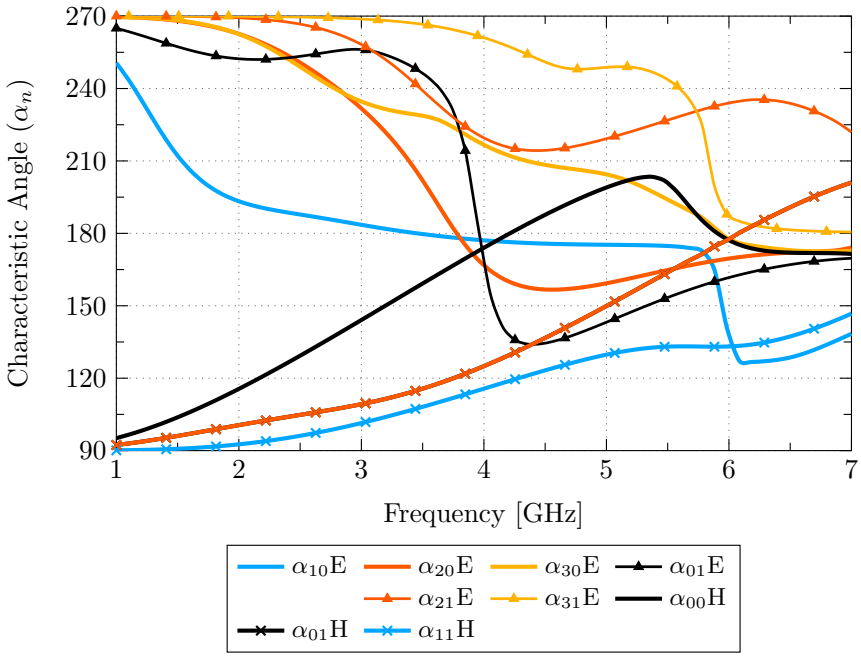

Figure 5.15: Characteristic angles of a rectangular waveguide with short circuit and an open circuit at the ends.

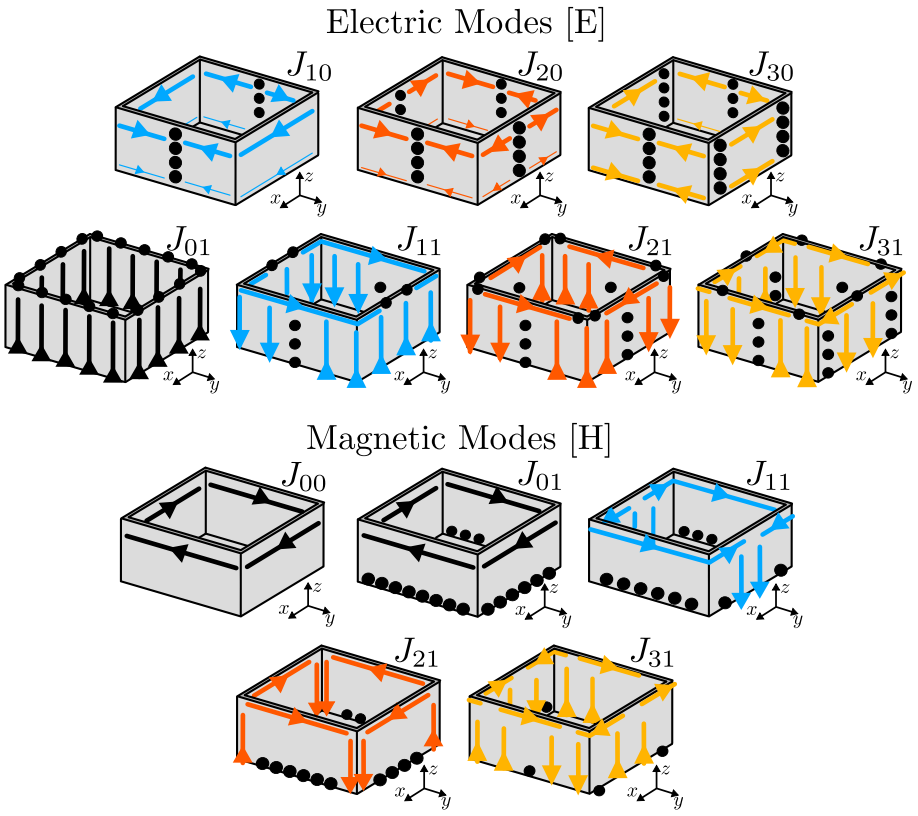

Figure 5.16: Modal current distribution of a rectangular waveguide with short circuit and an open circuit at the ends.

onance frequencies have shifted from lower frequency to higher frequency, the characteristic angles of the electrical modes J_{10}, J_{20}, and, J_{30}, before and after having resonated are keeping stable and very closed to 180° in a wide range of frequencies, this stability represent that each mode on the structure is broadband.

The behavior of the mode J_{01} remains the same as presented in the rectangular waveguide, the modes that are affected with a considerable variation in it's characteristic angle are the J_{21} and J_{31} modes, these modes become more inductive than those of the waveguide. If the mode J_{21} of the double-height waveguide open on both sides is taken as an example, it is very close to enter-

ing resonance at 3.7 GHz, this being the first minimum with purely inductive storage, while in the half-short-circuited structure at one end, the resonance would be outside the range of analysis, but with a minimum at a frequency of approximately 4.2 GHz with purely inductive storage. For both cases, the form in which the characteristic angles change is very similar, but due to the short circuit at one end, the characteristic angles are more inductive.

A very significant advantage that is obtained when the height of the structure is reduced by half and it is short-circuited at one of its ends, is that it is possible to avoid half of the currents that flow in the side walls in the direction of axial propagation i.e. on the z−axis. In Fig. 5.15, the characteristic currents of the modes present in the structure have been shown. These currents have been graphed at each of their resonance frequencies. In the case that an electrical mode has a value of a minimum below 225° before resonance, and a magnetic mode has a maximum above 135° before resonance, the characteristic currents will be plotted at that minimum or maximum value respectively. In this way, it is guaranteed that the graph of the mode is correct, because if it is plotted at the resonance frequency after a minimum or maximum, the currents and radiation patterns will be completely different from those of the analysis mode.

5.2.4 Square Cavity Backed Antenna

In this section, the main objective is to design an antenna starting from a square cavity. In order for the structure to be resonant, one or multiple feeding ports must be inserted in a specific place, therefore, we will ask ourselves, what will be the appropriate place to insert the feeding ports? To answer this question, the information shown in Fig. 5.16 has been used.

We remembered that there are two methods to excite a structure, the capacitive feeding port, and inductively, for this specific application the capacitive power supply will be used, therefore, it is required to insert external elements in the areas where the characteristics currents are null. The elements that will be used are a pair of rectangular patches (it can be any arbitrary structure), and the optimized parameter to the proposed antenna design are: $L = 64$ mm, $l_p = 20$ mm, $w_p = 9$ mm, $w_1 = 6$ mm, $w_2 = 1.9$ mm, $h_1 = 15$ mm, $h_2 = 0.6$ mm and, $t = 0.035$ mm.

In Fig. 5.18, the simulated results of the scattering parameters of the proposed antenna obtained through a full wave analysis have been represented, due to the symmetry of the structure in the x − axis, it will be enough to repre-

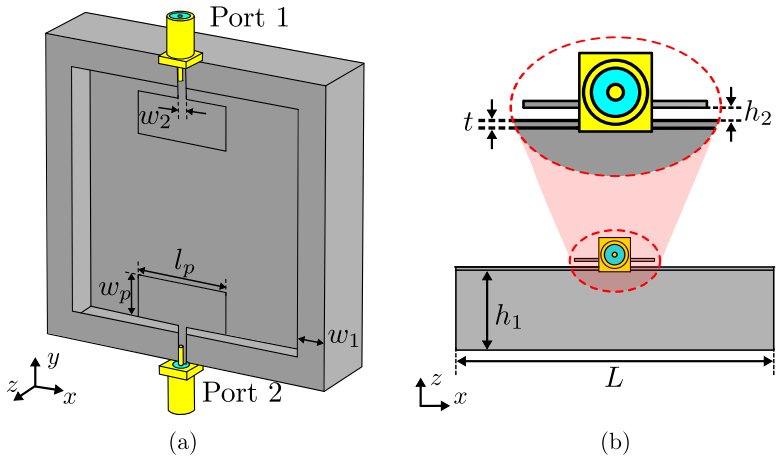

Figure 5.17: Square cavity antenna excited with two rectangular capacitive patches.

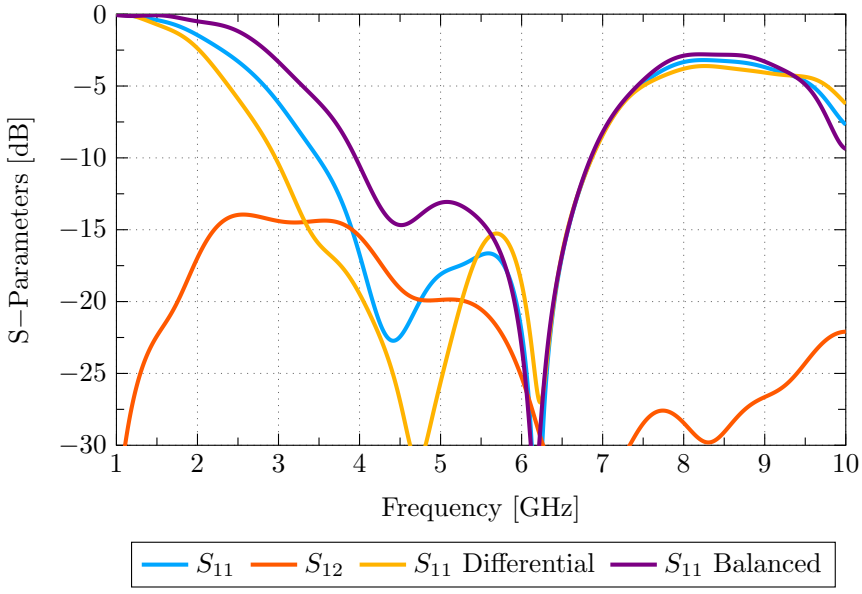

Figure 5.18: Simulated reflection coefficient of square cavity antenna.

sent the reflection and transmission coefficient of a single port. There is a very good matching of the ports when they are working as an individual element, in addition, the isolation between ports is optimal for the available bandwidth, the isolation port values will be below −14 dB. However, despite having a large bandwidth, the maximum direction of propagation will not be orthogonal to the structure, the maximum will be inclined in the opposite direction to the feeding point.

An alternative to achieve a radiation pattern in the broadside direction is to force some modes will be excited, for this, it will be necessary to excite 2 ports simultaneously. Using the explanation described in the Chapter 3 and in previous works [129, 130], a structure of these characteristics can be excited with a differential capacitive feed or balanced capacitive feed. Using the balanced option, a good bandwidth will be generated, and all even modes have been forced to excite, however, the radiation patterns will be the result of a combination of the patterns when the ports work as an isolated element, i.e. a radiation pattern with two main lobes.

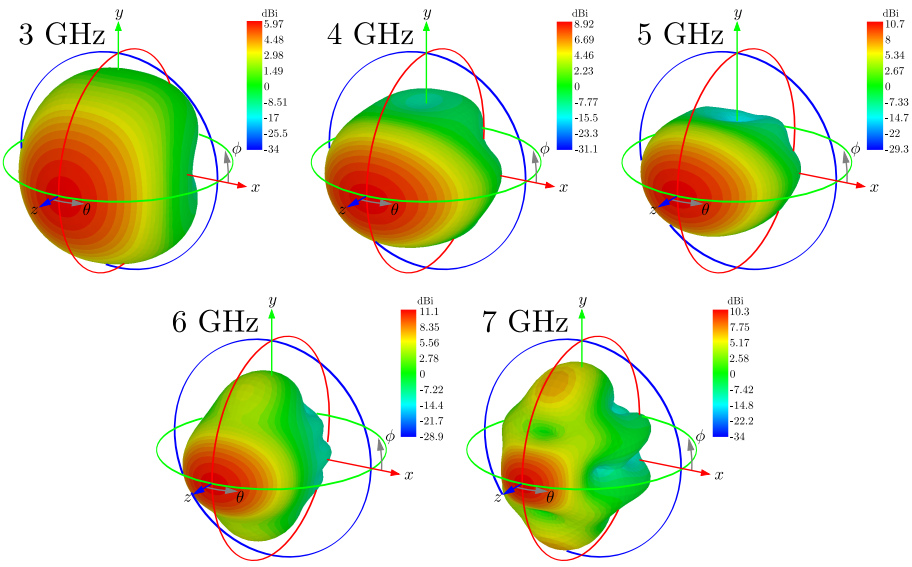

Figure 5.19: Unidirectional total radiation patterns of square cavity antenna from 3 GHz to 7 GHz using differentially capacitive coupling.

Therefore, the next option will be to use a differential capacitive feed, with this form of feeding it is possible to excite the odd modes, and it allows generating a good bandwidth that will be approximately 86 %, and the advantage of using this kind of excitation is that the radiation patterns generated are in the broadside direction. In Fig. 5.19, the total radiation patterns have been represented for the frequency range where the antenna works in optimal conditions. At the lowest operating frequency, the radiation pattern is nearly symmetrical in the theta and phi directions, whereas, at the highest frequency, secondary radiation lobes have been generated.

In any case, depending on the application that the designer establishes, multiple beams can be generated through the phase and amplitude combinations in the feeding ports, without this becoming a problem when generating a good bandwidth and an unidirectional radiation pattern.

5.3 Circular waveguide analysis

A circular waveguide is a hollow cylinder piece that supports TE and TM waveguide modes. In 5.20 the geometry with inner radius a has been shows. Therefore, unlike the coordinates used for a rectangular waveguide, the cylindrical coordinates will be used because this is the best suited to the surface.

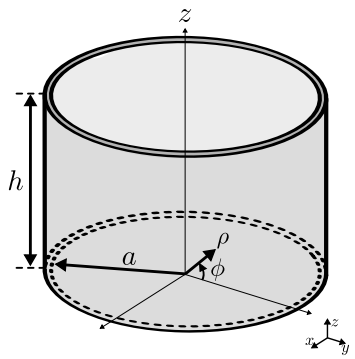

Figure 5.20: 3D view of waveguide section of a circular waveguide

5.3.1 TE y TM modes

The method to find the transverse fields in cylindrical coordinates is made from the components of the E_z or H_z fields of the TE and TM modes, as was developed in the case of the rectangular waveguide. Then, solving the wave

equation (5.1) in terms of H_z for the TE and E_z modes for TM modes, we will find the values of the components of the electric and magnetic field as a function of ρ and ϕ

$$E_\rho = \frac{-j}{k_c^2}\left(\beta\frac{\partial E_z}{\partial_\rho} + \frac{w\mu}{\rho}\frac{\partial H_z}{\partial\phi}\right), \tag{5.20a}$$

$$E_\phi = \frac{-j}{k_c^2}\left(\frac{\beta}{\rho}\frac{\partial E_z}{\partial_\phi} - w\mu\frac{\partial H_z}{\partial\rho}\right), \tag{5.20b}$$

$$H_\rho = \frac{j}{k_c^2}\left(\frac{w\epsilon}{\rho}\frac{\partial E_z}{\partial_\phi} - \beta\frac{\partial H_z}{\partial\rho}\right), \tag{5.20c}$$

$$H_\phi = \frac{-j}{k_c^2}\left(w\epsilon\frac{\partial E_z}{\partial_\rho} + \frac{\beta}{\rho}\frac{\partial H_z}{\partial\phi}\right), \tag{5.20d}$$

where $k_c^2 = k^2 - \beta^2$, and $e^{j\beta z}$ propagation has been assumed. For $e^{+j\beta z}$ propagation, replace β with $-\beta$ in all expressions. The mathematical solution of

the E_ρ, E_ϕ, H_ρ, H_ϕ components for the TE and TM modes are very similar, the difference between both is the initial conditions, for the TE mode the E_z component is equal to 0, while for TM is $H_z = 0$.

Knowing that $H_z(\phi,\rho,z) = h_z(\phi,\rho)e^{-j\beta z}$ and $E_z(\phi,\rho,z) = e_z(\phi,\rho)e^{-j\beta z}$, the wave equation ($\nabla^2 A_z + k_c^2 A_z = 0$) for H_z and E_z would be

$$\left(\frac{\partial^2}{\partial_\rho^2} + \frac{1}{\rho}\frac{\partial}{\partial\rho} + \frac{1}{\rho^2}\frac{\partial^2}{\partial\phi^2} + k_c^2\right)h_z(\rho,\phi) = 0 \qquad \text{for TE}_{mn}\text{ modes,} \tag{5.21a}$$

$$\left(\frac{\partial^2}{\partial_\rho^2} + \frac{1}{\rho}\frac{\partial}{\partial\rho} + \frac{1}{\rho^2}\frac{\partial^2}{\partial\phi^2} + k_c^2\right)e_z(\rho,\phi) = 0 \qquad \text{for TM}_{mn}\text{ modes.} \tag{5.21b}$$

As in the case of rectangular waveguides, the variable separation method is the best option to solve this type of differential equations.

$$h_z(\rho,\phi)) = R(\rho)P(\phi) \tag{5.22}$$

substituting in Eq. (5.21a) and multiplying by the term ρ^2

$$\frac{-1}{P}\frac{d^2P}{d\phi^2} = \frac{\rho^2}{R}\frac{d^2R}{d_\rho^2} + \frac{\rho}{R}\frac{dR}{d\rho} + \rho^2 k_c^2 \tag{5.23}$$

clearly it can see that the left side of the equation depends only on the term ϕ, while the right side depends on the variable ρ. Thus, each side must be equal to a constant denominate k_ϕ^2, remaining then

$$\frac{d^2P}{d\phi^2} + k_\phi^2 P = 0 \tag{5.24a}$$

$$\rho^2 \frac{d^2R}{d\rho^2} + \rho \frac{dR}{d_\rho} + \left(\rho^2 k_c^2 - k_\phi^2\right) R = 0 \tag{5.24b}$$

these two equations have a different form of solution, the first is of the type $P(\phi) = A \sin k_\phi \phi + B \cos k_\phi \phi$, however, this is slightly modified because the solution to h_z must be periodic in ϕ, so that k_ϕ must be an integer value for n

$$P(\phi) = A \sin n\phi + B \cos n\phi \tag{5.25}$$

On the other hand, the Ec.5.24b which is known as Bessel′s differential equation, the solution is $R(\rho) = CJ_n(k_c\rho) + DY_n(k_c\rho)$. Because $Y_n(k_c\rho)$ becomes infinite at $\rho = 0$, this term is physically unacceptable for a circular waveguide, so $D = 0$. Therefore, the solution for h_z can then be simplified to

$$h_z(\rho, \phi) = (A \sin n\phi + B \cos n\phi)\, J_n(k_c\rho), \tag{5.26}$$

The cutoff wave number k_c can be obtained using the boundary condition that $E_{tan} = 0$ on the waveguide wall. Because $E_z = 0$, E_ϕ should be

$$E_\phi(\rho, \phi) = 0 \quad at \quad \rho = a. \tag{5.27}$$

Remaining E_ϕ from H_z as

$$E_\phi(\rho, \phi, z) = \frac{j\omega\mu}{k_c}(A \sin n\phi + B \cos n\phi) J_n'(k_c\rho) e^{-j\beta_z} \tag{5.28}$$

Term $J_n'(k_c\rho)$ refers to the derivative of J_n, the only way for this to happen is by choosing a suitable cutoff wave number that will that the derivative of the Bessel function is always null, that is, that there is a zero of the function when $\rho = a$.

$$J_n'(k_c a) = 0 \tag{5.29}$$

Table 5.6: mth roots of the Bessel function J_n and J'_n

n	$\mathbf{TE}_{mn}$ **modes**			$\mathbf{TM}_{mn}$ **modes**		
	p'_{n1}	p'_{n2}	p'_{n3}	p_{n1}	p_{n2}	p_{n3}
0	3.832	7.016	10.174	2.405	5.520	8.654
1	1.841	5.331	8.536	3.832	7.016	10.174
2	3.054	6.706	9.970	5.135	8.417	11.620
3	4.201	8.015	11.345	6.380	9.761	-

Then it can find the cut off wave number of the circular waveguide starting from the knowledge of the radius of the cylindrical structure.

$$k_{c_{mn}} = \frac{p'_{nm}}{a} \tag{5.30}$$

The roots of the Bessel function $J'_n(x)$ are defined as p'_{nm}, so that $J'_n\,(p'_{nm}) = 0$, values of p'_{nm} are given in mathematical tables, the first few values are listed in Table 5.6. TE modes propagate along the waveguide in the z-direction after a certain cutoff frequency, the equation is described as

$$f_{c_{nm}} = \frac{p'_{nm}}{2\pi a\sqrt{\mu\epsilon}}, \tag{5.31}$$

The mathematical formulation for the TM propagation mode in circular waveguides is much easier, since it is done in a similar way to the TE mode. The wave equation has been described in Eq. (5.21b), using the variable separation method the longitudinal electric field is obtained

$$e_z(\rho,\phi) = (A\sin n\phi + B\cos n\phi)\, J_n(k_c\rho) \tag{5.32}$$

Boundary conditions apply directly to this longitudinal electric field, where the field must be annulled when it is tangential to the surface of the conductive walls of the waveguide.

$$E_z(\rho,\phi) = 0 \quad at \quad \rho = a. \tag{5.33}$$

For the electric field to cancel using the specified boundary conditions, the only option is to generate a zero in the function in a distance i.e. $J'_n(k_c a) = 0$. Then the cutoff wave number of the circular waveguide can be obtained using

$$k_{c_{mn}} = \frac{p_{nm}}{a} \tag{5.34}$$

where p_{mn} describes the mth roots of the Bessel function J_n, thus, $J_n(p_{nm}) = 0$. Consequently, the Bessel functions values for the TM modes have been shown in Table 5.6. The cutoff frequency is given by:

Table 5.7: Summary of equations for Circular Waveguide, where $q = (k_c\rho)\, e^{-j\beta_z}$

Quantity	**TE$_{mn}$ Mode**	**TM$_{mn}$ Mode**
k	$\omega\sqrt{\mu\epsilon}$	$\omega\sqrt{\mu\epsilon}$
k_c	$\frac{p'_{nm}}{a}$	$\frac{p_{nm}}{a}$
β	$\sqrt{k^2 - k_c^2}$	$\sqrt{k^2 - k_c^2}$
λ_c	$\frac{2\pi}{k_c}$	$\frac{2\pi}{k_c}$
λ_g	$\frac{2\pi}{\beta}$	$\frac{2\pi}{\beta}$
E_ρ	$\frac{-j\omega\mu n}{k_c^2\rho}\left(A\cos n\phi - B\sin n\phi\right) J_n q$	$\frac{-j\beta}{k_c}\left(A\sin n\phi + B\cos n\phi\right) J'_n q$
E_ϕ	$\frac{j\omega\mu}{k_c}\left(A\sin n\phi + B\cos n\phi\right) J'_n q$	$\frac{-j\beta n}{k_c^2\rho}\left(A\cos n\phi - B\sin n\phi\right) J_n q$
E_z	0	$\left(A\sin n\phi + B\cos n\phi\right) J_n q$
H_ρ	$\frac{-j\beta}{k_c}\left(A\sin n\phi + B\cos n\phi\right) J'_n q$	$\frac{j\omega\epsilon n}{k_c^2\rho}\left(A\cos n\phi - B\sin n\phi\right) J_n q$
H_ϕ	$\frac{-j\beta n}{k_c^2\rho}\left(A\cos n\phi - B\sin n\phi\right) J_n q$	$\frac{-j\omega\epsilon}{k_c}\left(A\sin n\phi + B\cos n\phi\right) J'_n q$
H_z	$\left(A\sin n\phi + B\cos n\phi\right) J_n q$	0

Table 5.8: Calculated cut-off frequencies in GHz of TE and TM first modals fields for a circular waveguide.

n	**TE modes**			**TM modes**		
	f_{n1}	f_{n2}	f_{n3}	f_{n1}	f_{n2}	f_{n3}
0	4.787	8.766	12.711	3.004	6.896	10.812
1	2.300	6.660	10.665	4.787	8.766	12.711
2	3.815	8.378	12.456	6.415	10.516	14.518
3	5.248	10.01	14.174	7.971	12.195	-

$$f_{c_{nm}} = \frac{p_{nm}}{2\pi a\sqrt{\mu\epsilon}} \tag{5.35}$$

Once the longitudinal fields for the TE and TM modes have been found, the transverse components for the electric and magnetic field have been written in Table 5.7. In addition a summary with equations has been included, which will be very useful to describe the TE and TM modes.

For both cases (TE or TM modes), the values of the roots of the Bessel functions in Table 5.8 will be taken into account. Therefore, the resonance frequencies of the first modes for the electric and magnetic transversal modes corresponding to the circular waveguide of aspect relation a x h (where the radius $a = 38.20$ mm and height $h = 60$ mm) have been calculated and shown in Table 5.8.

The imaginary part of the propagation constant β for some TE and TM modes of the circular waveguide has been plotted in Fig. 5.21. As expected, the propagation constant of each mode behaves exponentially from the frequency cut, this is in accordance with the results shown in Table 5.8. Therefore, this graph allows confirming the mathematical part with the simulation.

In Fig. 5.22, the frontal cross section (ρ - ϕ axis) of the circular waveguide at their cut-off frequencies (see table 5.8) has been shown, each of the variations of the fields according to the order of the mode will have a specific colour, the continuous line representing the electric field, and the dashed line describes the magnetic field. TE modes have zero electric fields in the walls of the guides,

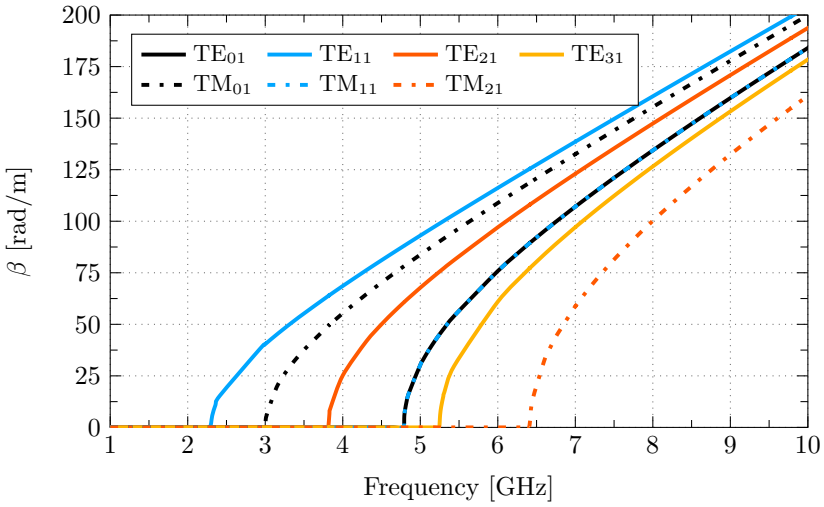

Figure 5.21: Cut-off frequencies of TE and TM first modals fields for a circular waveguide.

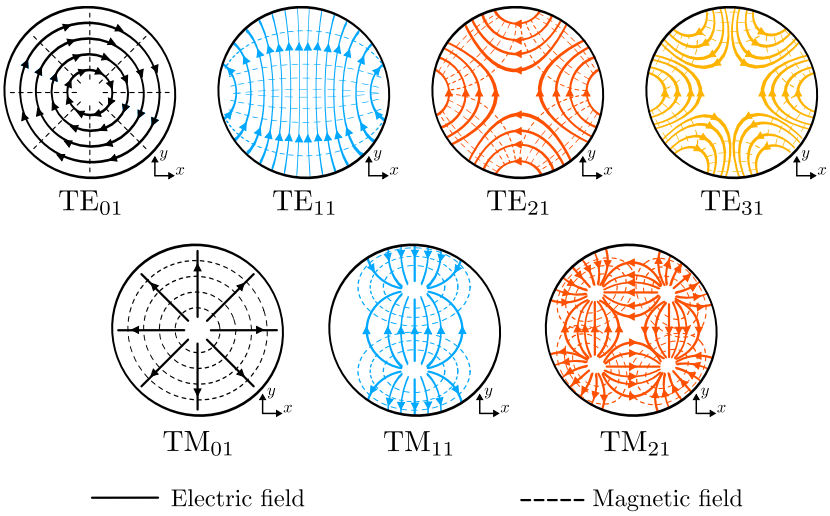

Figure 5.22: TE and TM modal field distribution for a circular waveguide in front view.

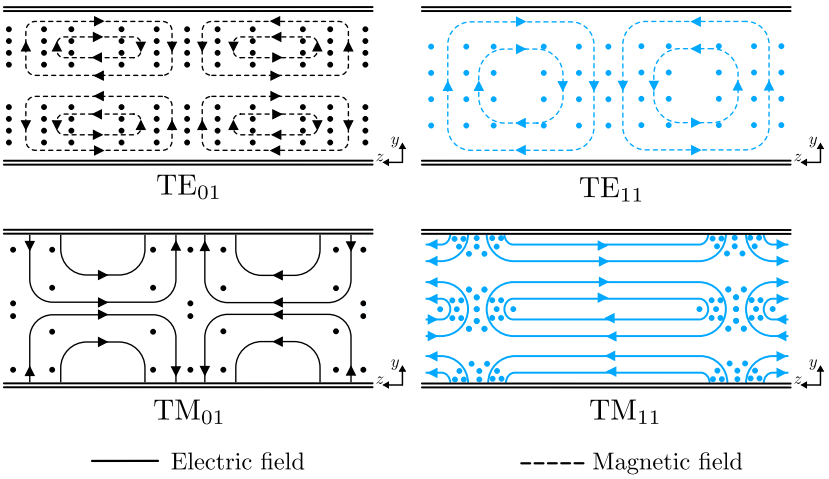

Figure 5.23: TE and TM modal field distribution for a circular waveguide in lateral view.

that is, an azimuth variation, while for TM modes the electric field will be null in the central zone, the variation being azimuth or radial depending on the order of the mode.

By making a cross section of the circular guide, the electric and magnetic field distribution for the first TE and TM modes along the propagation axis ($z-$ axis) has been shown in Fig. 5.23. Here, as in the case of the rectangular waveguide, magnetic or electrical walls can be placed to obtain a resonator, this structure will be analyzed below.

5.3.2 Circular waveguide cavity resonator analysis

The geometry of a cylindrical cavity is shown in Fig. 5.24, this represents a section of a circular waveguide closed by short-circuit surfaces at the two ends. The mathematical formulation is very similar to the rectangular cavity, beginning from the solutions obtained from the guide, in this case from the circular waveguide, because these satisfy the boundary conditions on the walls. Then, using the information depicted in Table 5.7, the transverse electric fields (E_ϕ, E_θ) for the TE and TM modes of a circular waveguide can be expressed as:

$$\overline{E}_t(\rho,\phi,z) = \overline{e}(\rho,\phi)\left(A^+e^{-j\beta_{nm}z} + A^-e^{j\beta_{nm}z}\right) \tag{5.36}$$

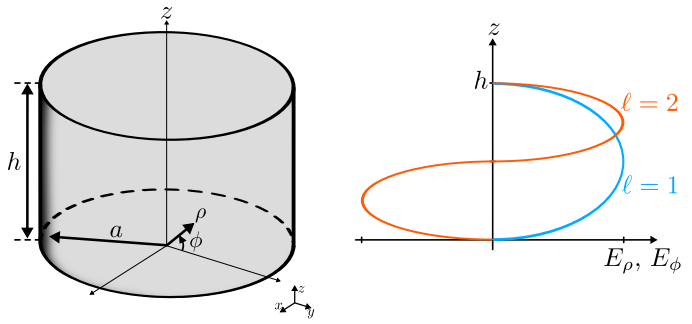

Figure 5.24: Circular cavity resonator and electric field distribution for resonant modes with $\ell = 1$ and $\ell = 2$.

where the term $\overline{e}(\rho, \phi)$ describes the electric transverse variation, and the arbitrary amplitudes of the forward and backward travelling waves is represented by A^+ and A^-.

The propagation constants for either TE or TM modes will be obtained in the same way as the circular waveguide, then according to Table 5.7 it will be:

$$\beta_{nm} = \sqrt{k^2 - \left(\frac{p'_{nm}}{a}\right)} \qquad \text{for TE}_{nm} \text{ modes,} \tag{5.37a}$$

$$\beta_{nm} = \sqrt{k^2 - \left(\frac{p_{nm}}{a}\right)} \qquad \text{for TM}_{nm} \text{ modes.} \tag{5.37b}$$

with $k = \omega\sqrt{\mu\epsilon}$, for the E_t to be 0 at the ends of the waveguide (in z-axis), the arbitrary amplitudes A^+ and A^- must be equal and A^+ sin $\beta_{nmd} = 0$, therefore, the wavelength must be an integer value of a half waveguide. Then the resonance frequency for each of them can be found using:

$$f_{nm\ell} = \frac{c}{2\pi\sqrt{\mu_r\epsilon_r}}\sqrt{\left(\frac{X_{nm}}{a}\right)^2 + \left(\frac{\ell\pi}{d}\right)^2} \tag{5.38}$$

$$\text{or} \qquad (2af_{nm\ell})^2 = \left(\frac{cX_{nm}}{\pi}\right)^2 + \left(\frac{c\ell}{2}\right)^2\left(\frac{2a}{d}\right)^2 \tag{5.39}$$

where $X_{nm} = p'_{nm}$ for the TE modes and p'_{nm} for TM modes. Taking into account the dimensions $a = 38.20$ mm, and $h = 60$ mm of a circular waveguide

Table 5.9: Calculated resonant frequencies in GHz of $TE_{mn\ell}$ and $TM_{mn\ell}$ first modals fields for a circular cavity resonator.

	TE_{mn0} modes			TM_{mn0} modes			TE_{mn1} modes			TM_{mn1} modes		
n	f_{n10}	f_{n20}	f_{n30}	f_{n10}	f_{n20}	f_{n30}	f_{n11}	f_{n21}	f_{n31}	f_{n11}	f_{n21}	f_{n31}
0	4.8	8.8	12.7	3.0	6.9	10.8	5.4	9.1	13.0	3.9	7.3	11.1
1	2.3	6.7	10.7	4.8	8.8	12.7	3.4	7.1	11.0	5.4	9.1	13
2	3.8	8.4	12.5	6.4	10.5	14.5	4.6	8.7	12.7	6.9	10.8	14.7
3	5.3	10	14.2	8.0	12.2	-	5.8	10.3	14.4	8.4	12.5	2.5

cavity resonator, according to the Fig. 5.24, the resonance frequencies for some TE and TM modes have been calculated and these have been summarized in Table 5.9.

It is important to note that the TE dominant mode is TE_{111} when the length is larger than the diameter, i.e., a slim cavity, while for the dominant mode is TM_{010} when the length is smaller than the diameter, i.e., a wide cavity [143, 145], as it can see in Fig. 5.25.

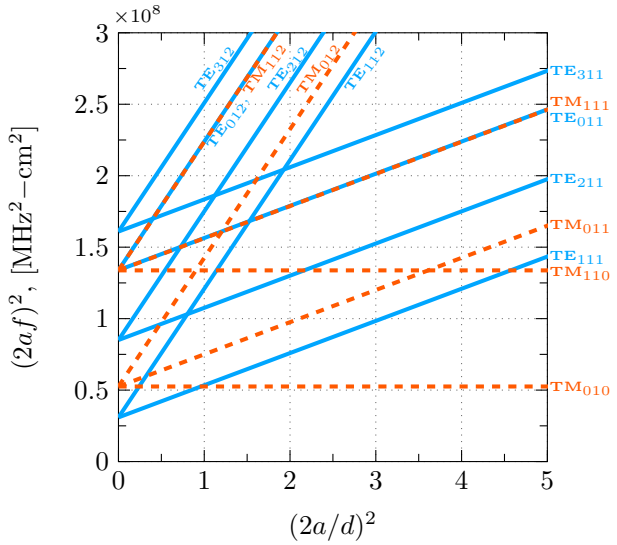

Figure 5.25: Mode-distribution diagram of a circular cylindrical cavity.

The electric and magnetic fields distributions for the TE and TM modes of the circular waveguide closed by short-circuit surfaces at the two ends can be computed using the equations below:

$$H_z = H_0 J_n\left(\frac{p'_{nm}\rho}{a}\right)\cos(n\phi)\cos\left(\frac{\ell\pi z}{d}\right) \tag{5.40a}$$

$$H_\rho = \frac{\beta a H_0}{p'_{nm}} J'_n\left(\frac{p'_{nm}\rho}{a}\right)\cos(n\phi)\sin\left(\frac{\ell\pi z}{d}\right) \tag{5.40b}$$

$$H_\phi = \frac{-\beta a^2 n H_0}{(p'_{nm})^2\rho} J_n\left(\frac{p'_{nm}\rho}{a}\right)\sin(n\phi)\sin\left(\frac{\ell\pi z}{d}\right) \tag{5.40c}$$

$$E_\rho = \frac{jk\eta a^2 n H_0}{(p'_{nm})^2\rho} J_n\left(\frac{p'_{nm}\rho}{a}\right)\sin(n\phi)\cos\left(\frac{\ell\pi z}{d}\right) \tag{5.40d}$$

$$E_\phi = \frac{jk\eta a H_0}{p'_{nm}} J'_n\left(\frac{p'_{nm}\rho}{a}\right)\cos(n\phi)\cos\left(\frac{\ell\pi z}{d}\right) \tag{5.40e}$$

$$E_z = 0, \tag{5.40f}$$

On the other hand, a circular waveguide can not only be in resonance when electrical walls are imposed at the ends (short circuits), but can also be generated when magnetic walls are imposed on the structure (open circuit). To demonstrate this concept, an example has been represented using the TE_{01} and TM_{01} modes of a circular waveguide as shown in Fig. 5.26, the orange arrows represent the location where the short circuits can be placed, while the sky blue arrows the open circuits. Therefore, in the place where the tangent electric field $E_t = 0$ can be imposed the electric walls and, where the normal electric field $E_n =$ maximum could be imposed a magnetic wall.

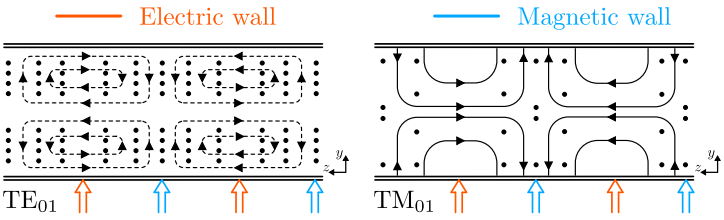

Figure 5.26: Open circuit and short circuit setup in order to design a resonator

Using the Eqs. (5.40a) to (5.40f), in Fig. 5.27(a) some of the lower order modes TE and TM of a short-circuited circular waveguide at the ends have

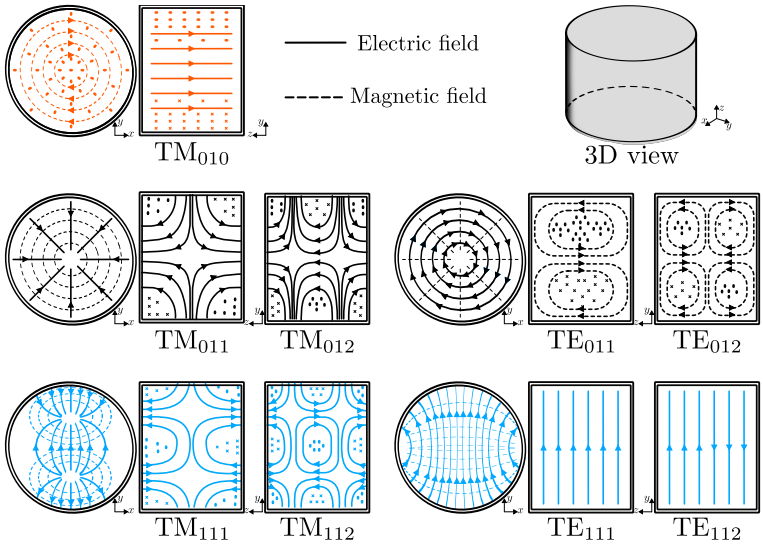

(a)

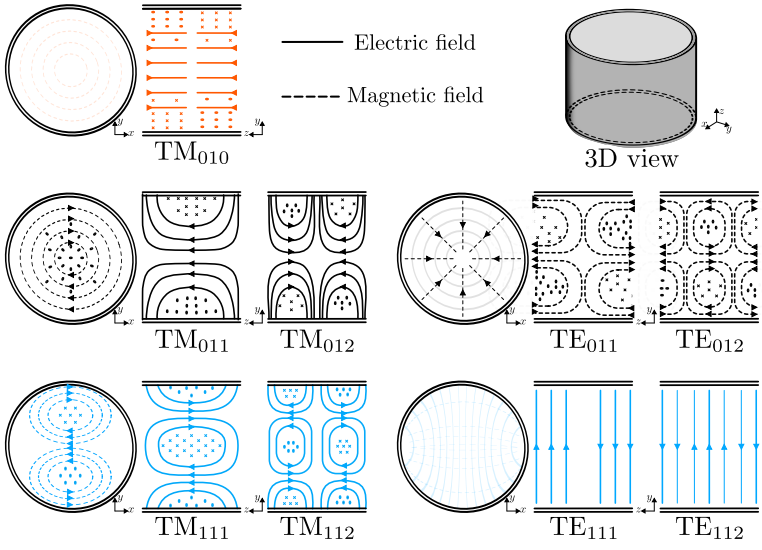

(b)

Figure 5.27: Electric and magnetic fields distributions of some lower modes. (a) In a short-circuited circular cylindrical cavity at the ends, (b) In a open-circuited circular cylindrical cavity at the ends.

been represented, each of them has been plotted at their resonance frequencies that were calculated in Table 5.9. The fields are represented from their front view ($x-y$ axis) at a height of $h/2$, while the side view ($z-y$ axis) is shown at the middle of the structure.

For the other part of Fig. 5.27, the electric and magnetic fields have been plotted through equations (5.40a) to (5.40f), the resonance frequencies of each mode will be the same as the case of the closed cavity. The difference between the two configurations is marked by a shift of 90°.

$$H_z = H_0 J_n\left(\frac{p'_{nm}\rho}{a}\right)\cos(n\phi)\sin\left(\frac{\ell\pi z}{d}\right) \tag{5.41a}$$

$$H_\rho = \frac{\beta a H_0}{p'_{nm}} J'_n\left(\frac{p'_{nm}\rho}{a}\right)\cos(n\phi)\cos\left(\frac{\ell\pi z}{d}\right) \tag{5.41b}$$

$$H_\phi = \frac{-\beta a^2 n H_0}{(p'_{nm})^2\rho} J_n\left(\frac{p'_{nm}\rho}{a}\right)\sin(n\phi)\cos\left(\frac{\ell\pi z}{d}\right) \tag{5.41c}$$

$$E_\rho = \frac{jk\eta a^2 n H_0}{(p'_{nm})^2\rho} J_n\left(\frac{p'_{nm}\rho}{a}\right)\sin(n\phi)\sin\left(\frac{\ell\pi z}{d}\right) \tag{5.41d}$$

$$E_\phi = \frac{jk\eta a H_0}{p'_{nm}} J'_n\left(\frac{p'_{nm}\rho}{a}\right)\cos(n\phi)\sin\left(\frac{\ell\pi z}{d}\right) \tag{5.41e}$$

$$E_z = 0, \tag{5.41f}$$

5.3.3 TCM in circular waveguide

At the moment, the information obtained through the electrical and magnetic transversal components of the circular waveguide has been shown, allowing us to know the cutoff frequencies for each transversal propagation mode (TE and TM). However, the resonances of the guide can be determined using the distribution of currents on the surface, therefore, the Theory of Characteristic Modes will be used as a tool to achieve the objective.

The circular waveguide used for this analysis has a diameter of λ at the center frequency of 2.5 GHz and a height of $h = \lambda/2$. In this type of structure and according to the behavior of the currents; the modes that appear have been classified into electrical or capacitive modes and magnetic or inductive modes. In the electrical modes, the currents enter or leave the current nulls as described in Gaussian law for the electric field. On the other hand, Gauss's law for the magnetic field allows us to describe the behavior of magnetic modes.

In addition, according to the direction in which the currents flow on the surface of the structure, the order of the Mode (J_{nm}) in its n or m components can be increased, the subscript m will change according to the number of times the currents change direction in the direction azimuthal, on the other hand, the variation of the currents change in axial direction determine the order of the coefficient n.

Due to the symmetry of the structure in the x and y axis, in Fig. 5.28, only the first four characteristic angles of one of the generated polarizations have been represented. The electrical modes with azimuthal variation (J_{10}, J_{20}, J_{30}, ..., J_{n0}) generate a bandwidth of approximately 1 GHz (when α_n is between 135 ° and 225° as mentioned in the Chapter 2). This structure is curious because the modes, after having resonated, will again resonate at a higher frequency than the first, going from storing inductive to capacitive energy, for example, the mode J_{10} has it's first resonance at 2.1 GHz and the second at 5.2 GHz. The difference between the two resonances is that at 5 GHz, the characteristic properties of the mode at the first resonance have been lost, that is, the distribution of characteristic currents and radiation patterns are different.

On the other hand, the other electrical modes (J_{01}, J_{11}, J_{21}, J_{31}) have a particular behavior before entering in resonance, generating a variation in the characteristic angle that approaches $\alpha_n = 180°$ while increasing the order of the mode. Furthermore, in this type of structure, it is striking that apart from capacitive modes, inductive modes can also be resonant, this will depend on the height of the waveguide [146].

In 5.29, the distribution of currents in the circular waveguide at each of the resonance frequencies has been represented (in some cases the value of the approximate characteristic angle has been taken at $\alpha_n = 180°$), the modes J_{00}H, J_{10}E, J_{20}E, J_{30}E clearly have an azimuthal variation, the maximum intensity of the currents are located at the edges of the structure in the $z-$ direction, that is, when $z = 0$ and $z = h$, and is almost zero in the middle of the structure when $z = h/2$. For the other modes, the distribution of currents will be the result of a mixture between azimuthal and axial variation, just as in the first cases the maximum intensity of the currents is located at the edges as well.

At the same frequencies in which each of the characteristic currents has been plotted, the radiation patterns of the first 4 modes have been depicted as shown in Fig. 5.30. Clearly, perfect symmetry is seen in radiation patterns, whether for the vertical or horizontal plane. If the current distribution and radiation patterns generated are optimally used, antennas for applications with multiple

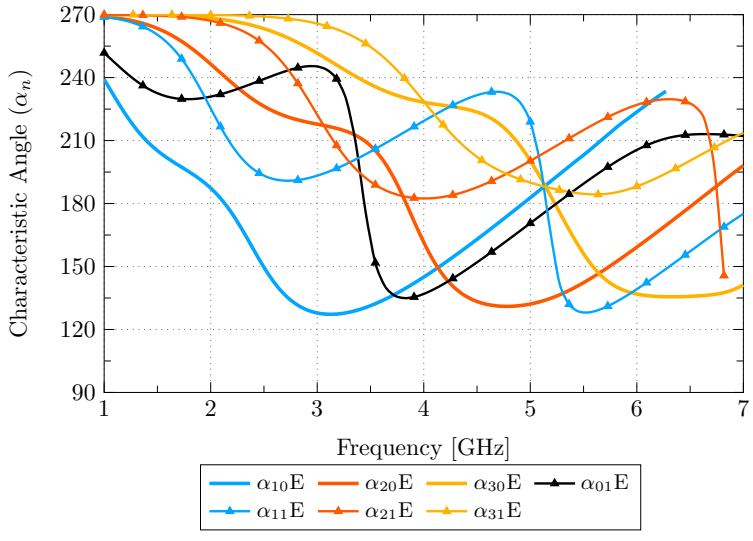

(a)

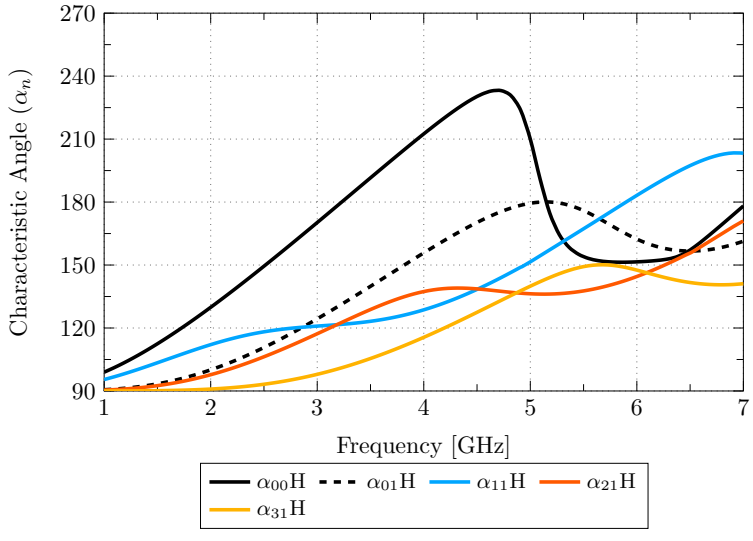

(b)

Figure 5.28: Characteristic angle of the circular waveguide. (a) Electric modes and, (b) Magnetic modes.

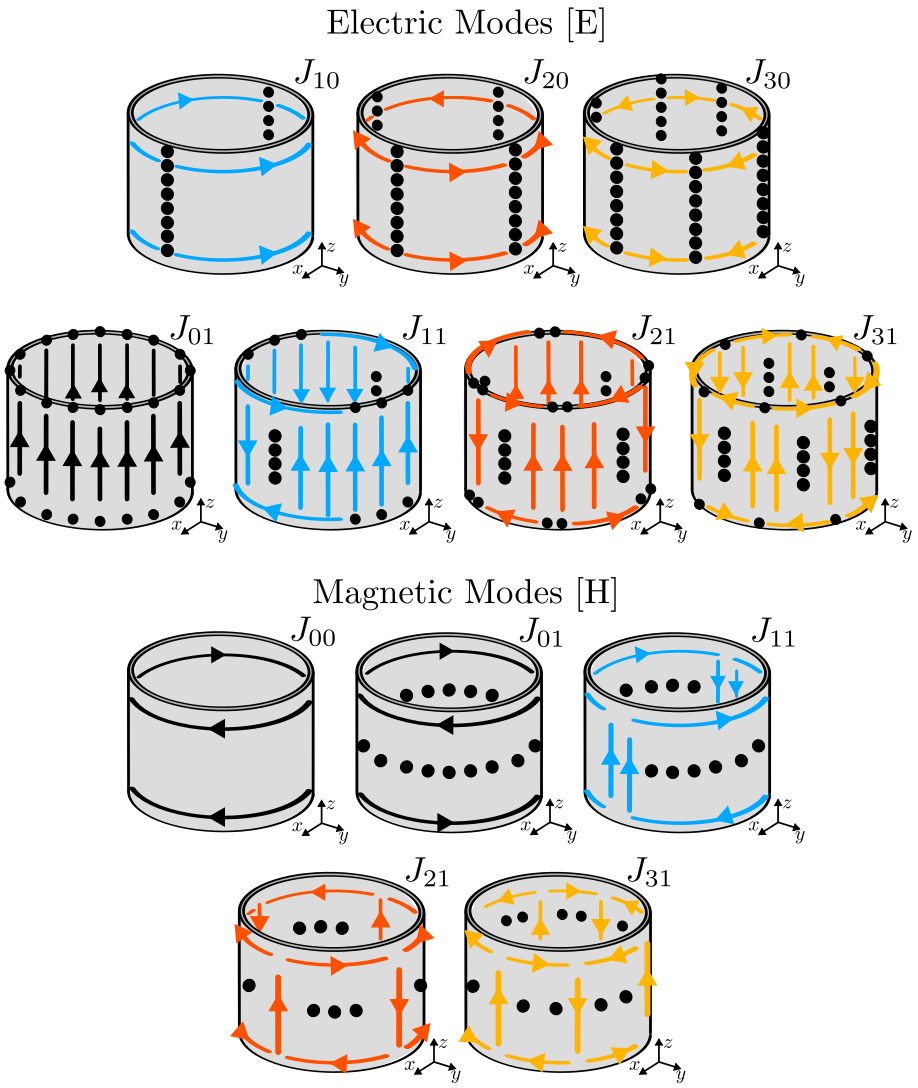

Figure 5.29: Modal current distribution of circular waveguide.

beams can be designed, for this, some capacitive or inductive feeding ports must be inserted according to the criteria and the need of the designer or the application.

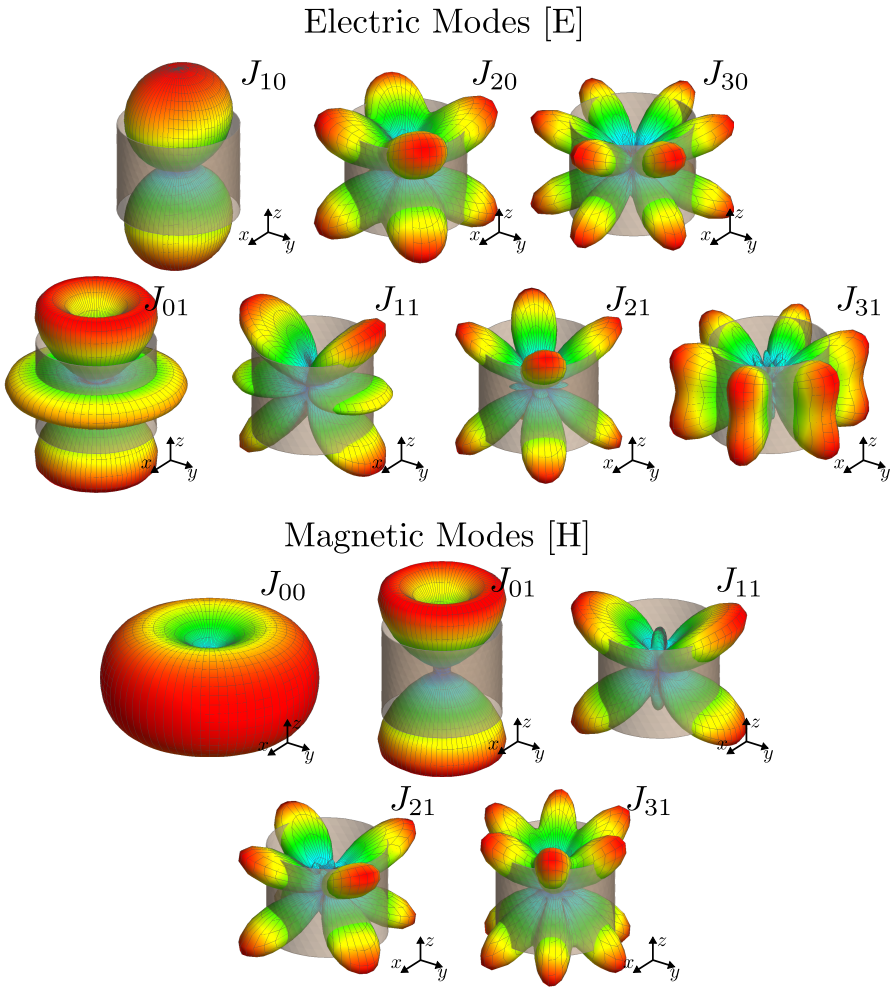

Figure 5.30: Modal radiation pattern of a circular waveguide

The modes that are excited and contribute to radiation in the range frequency from 1 to 7 GHz, have been represented in Fig. 5.31. These contribution percentages can be generated when the structure is illuminated with a plane wave, for the circular waveguide, the polarization of illumination is negligible due to its symmetry. It is evident that for the range from 1 to 7 GHz, three modes are the most important and that contribute more in the total radiated power, the electric mode J_{10} from 1 to 3 GHz, the inductive mode J_{11}' from

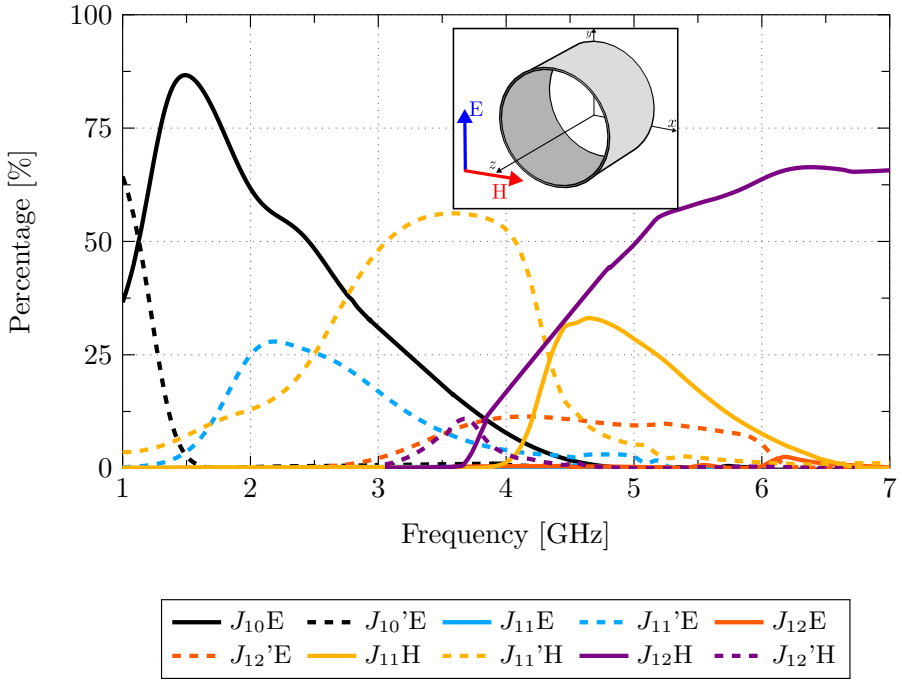

Figure 5.31: Modal current distribution of circular waveguide.

2.5 GHz to 4.5 GHz and, from the 4.5 GHz onwards the inductive mode J_{12}. However, in addition to the three modes mentioned, there are other modes that contribute with minimum power to the total radiation, which although they are minimal must be considered, for this reason, in the Table 5.10 a summary has been made with the percentages of power that contribute each one of them in the frequency range from 1 to 7 GHz.

Then, once a complete analysis of the circular waveguide through the characteristic modes has been carried out, it has been seen that the characteristic currents distribution that flow on the surface of the guide is symmetrical in the direction of propagation z, i.e., the currents that are between $z = 0$ and $z = h/2$ are equal to those between $z = h/2$ and $z = h$. Thus, depending on the order of the mode in the axial variation (subscript n), it will have currents in the opposite direction when n is odd, and currents in the same direction when n is even.

Table 5.10: Power contribution percentage of modes that participating in the range frequency from 1 to 7 GHz in a circular waveguide.

Mode	1 GHz	2 GHz	3 GHz	4 GHz	5 GHz	6 GHz	7 GHz
J_{10}E	36,6%	61.7%	31%	7.8%	0%	0%	0%
J_{10}'E	64,3%	0%	0%	0%	0%	0%	0%
J_{11}'E	0,20%	25%	17%	3.96%	2 .55%	0%	0%
J_{12}'E	0%	0%	2.18%	11.2%	9.42%	5.28%	0%
J_{11}H	0%	0%	0%	3.18%	28.5%	7.6%	0%
J_{11}'H	3,51%	13%	48%	52.6%	5.25%	0%	0%
J_{12}H	0%	0%	0%	17.5%	49.3%	63.7%	65.5%
Others	0%	0.3%	1.82%	3.76%	4.98%	23.42%	35.50%

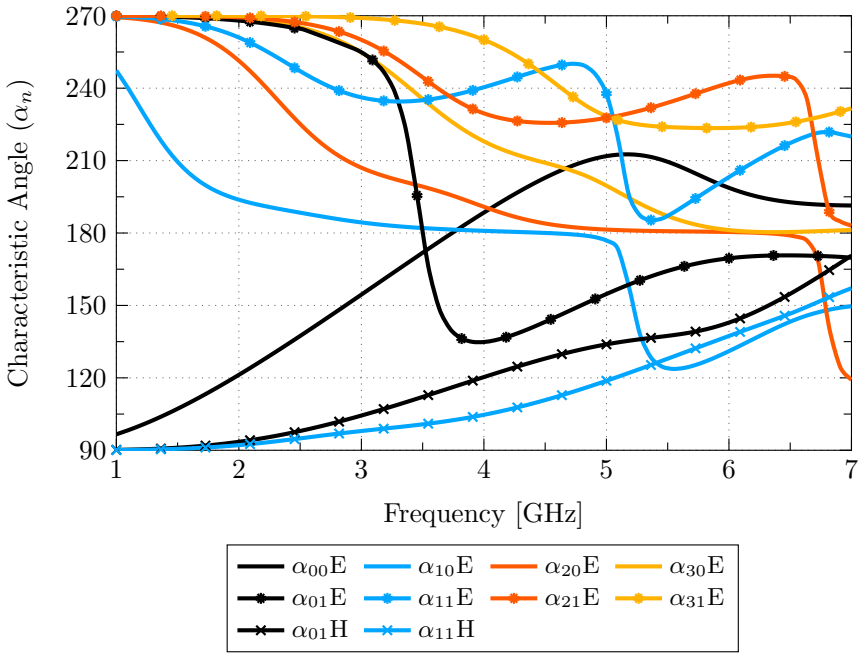

Figure 5.32: Characteristic angle of a circular waveguide with a shorted circuit in the edge.

Then, in the area where the tangential field $E_t = 0$ (when $z = h/2$) for the fundamental mode J_{10}, a metal wall can be generated through a short

circuit and the structure reduced by half, leaving a height of $\lambda/4$, this makes it possible to discriminate a part of the current distributions of the lateral wall. In Fig. 5.32, the characteristic angles of a circular waveguide with a shorted circuit in the edge have been plotted.

Comparing the characteristic angle of the fundamental mode J_{10} between the complete circular waveguide with the piece of circular waveguide short-circuited in one of the ends, it is very evident that the structure divided in half has a better bandwidth for each mode represented, in the first case it is generated a very marked 180° crossing at 2.1 GHz, on the contrary in the second case, in a wide frequency range the characteristic angle is very close to 180°. Suddenly, it goes into resonance and goes from storing capacitive to inductive energy, the large bandwidth is maintained for all the modes represented in the analyzed frequency range. Therefore, the resonance frequencies of the cavity are at a higher frequency than what is generated in a waveguide.

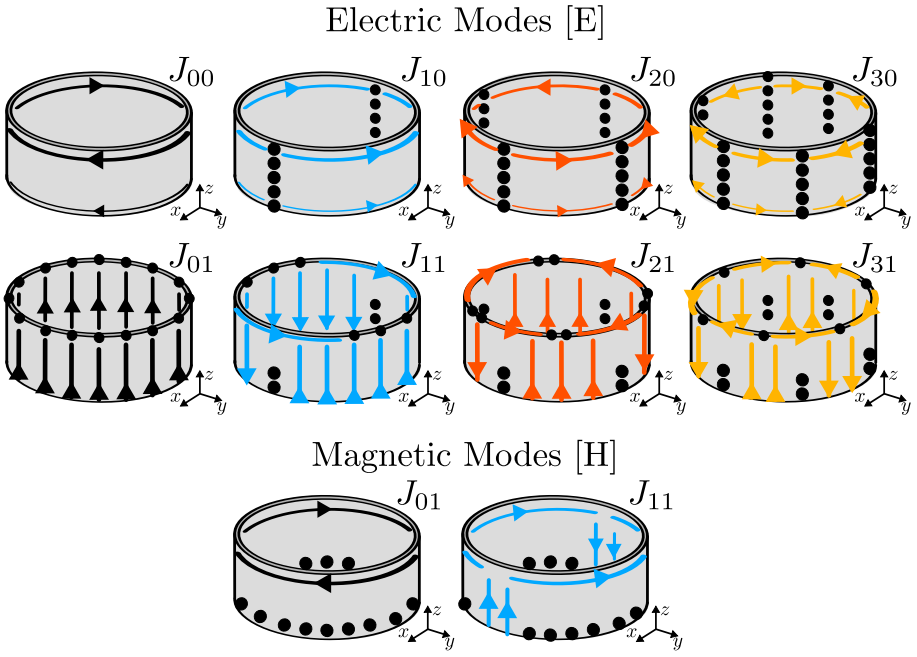

Figure 5.33: Modal current distribution of circular waveguide with a shorted circuit in the edge.

As anticipated, the current distribution that appears in the structure is only half of that obtained in the circular waveguide (see Fig. 5.29), in the open edge of the structure you can see that there are currents with maximum intensity in parallel. On the other hand, in the short-circuited edge, for the electrical and magnetic modes with axial variation, null currents or currents with very low intensity are generated compared to the maximum value of the other extreme, whereas, for modes with azimuthal variation, it will be had in some zones a point of zero current and in other maximum currents in a direction perpendicular to the edge. In any case, with the short-circuited cavity it is possible to achieve the objective of discriminating a part of the currents, in this way, the fields will be concentrated in the central part of the cavity.

5.3.4 UWB Circular Cavity Backed Antenna

Cylindrical or rectangular cavities have become very important elements for the design of UWB antennas, thus allowing the generation of unidirectional radiation patterns and good directivity due to the concentration of fields within

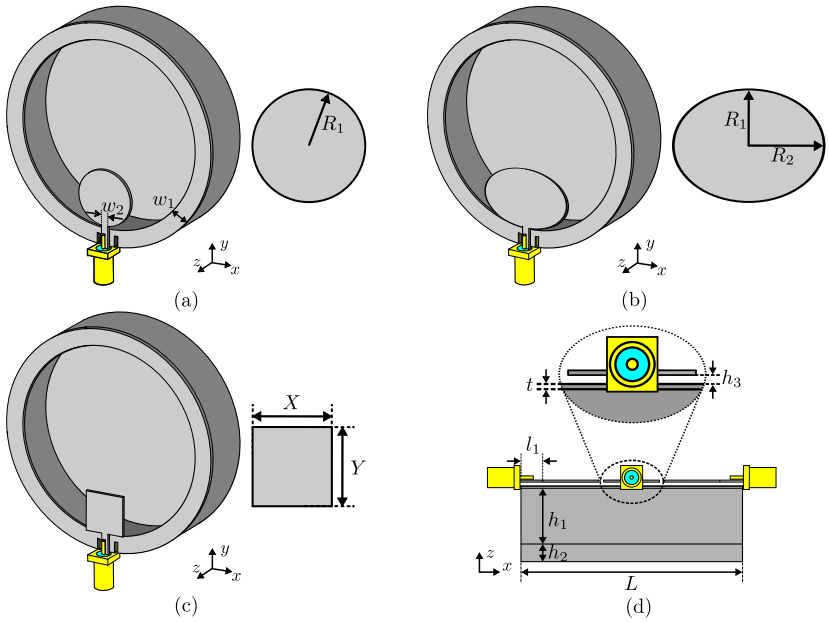

Figure 5.34: Proposed UWB cavity backed antenna with different types of excitation. (a) 3D view antenna with circular patch, (b) Elliptic patch, (c) Square patch, and (d) Cross section view.

the structure. There are different ways to generate the described characteristics such as [147–149], however, to design the proposed structure we will take advantage of the information provided by the Theory of Characteristic Modes.

The cavity begins from the metal ring analysis as seen previously in Chapter Chapter 3, this ring can be excited through a capacitive or inductive feed. To excite a structure of this type through a capacitive form, the feeding port must be placed in the zone where there is a current null [125, 126, 150], on the other hand, where the currents are maximum the capacitive fed can be inserted.

Then, starting from this concept, the structure shown in Fig. 5.34 has been proposed. The antenna is composed of a metal circular ring at the top, it is excited by a capacitively shaped patch, at the rear a piece of a circular waveguide has been inserted in order to close the cavity. The feeder patch can have any arbitrary shape (a circular, elliptical, or square shape, the last has been used for the development in this section) as can be seen in Fig. 5.35.

The optimized parameter to the proposed antenna design are: $L = 64$ mm, $X = Y = 11.31$ mm, $R_1 = 8$ mm, $R_2 = 12$ mm, $l_1 = 6.5$ mm, $w_1 = 6$ mm, $w_2 = 1.9$ mm, $h_1 = 15$ mm, $h_2 = 5$ mm, $h_3 = 0.6$ mm, $t = 0.035$ mm.

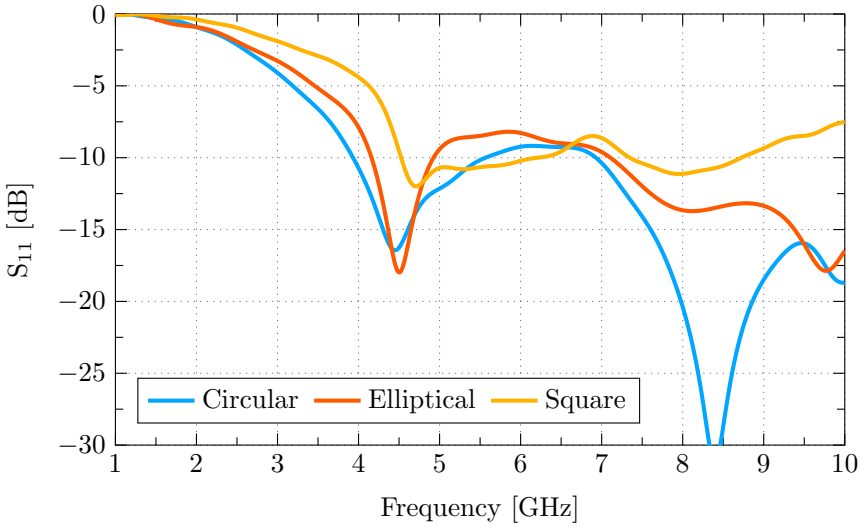

Figure 5.35: Simulated reflection coefficient of the proposed cavity backed antenna with different excitation.

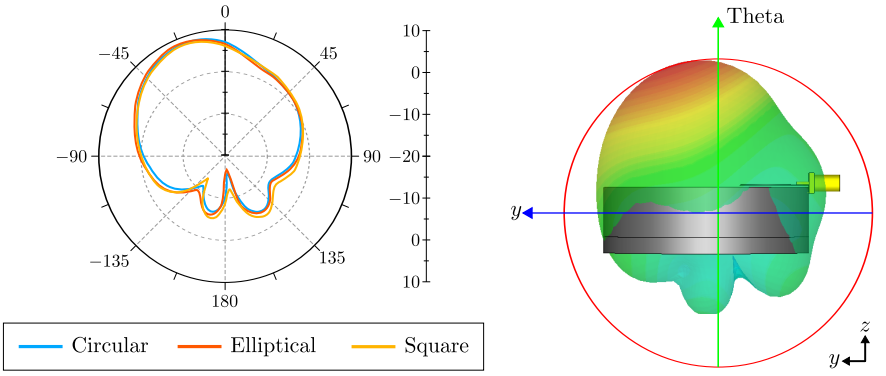

(a) (b)

Figure 5.36: Simulated radiation pattern of the proposed cavity backed antenna with different excitation.

Despite being able to excite the structure with any type of arbitrary shape, under the same conditions, that is to say only by replacing the shape of the feeder without carrying out an additional modification, not all the proposed shapes generate a good matching. In Fig. 5.35, a full-wave analysis of each of the proposed structures with the different types of feeder has been performed, it can clearly be seen that the circular feed structure generates a better bandwidth than the others under the parametric conditions.

Making a virtual cut around the middle of the structure and looking from the $x-y$ plane (Fig. 5.34(a)), an asymmetry is clearly appreciated in the design, this asymmetry generates a shifted problem in the direction of propagation in the radiation pattern at the resonance frequency. The shift is generated in the opposite direction to the place where the feeding port is located, as expressed in Fig. 5.36.

An easy method to correct the offset direction of propagation in the radiation pattern and generate it in the broadside direction is to use a differential feed [23, 52]. Therefore, another additional excitation port must be placed in the opposite direction to the first, the excitation of the structure must have a phase difference between each of them of 180°, to achieve this phase variation a 180° hybrid coupler is required [151, 152]. With this configuration has been forced that the maximum of the currents will be in the orthogonal zone of the feeding ports.

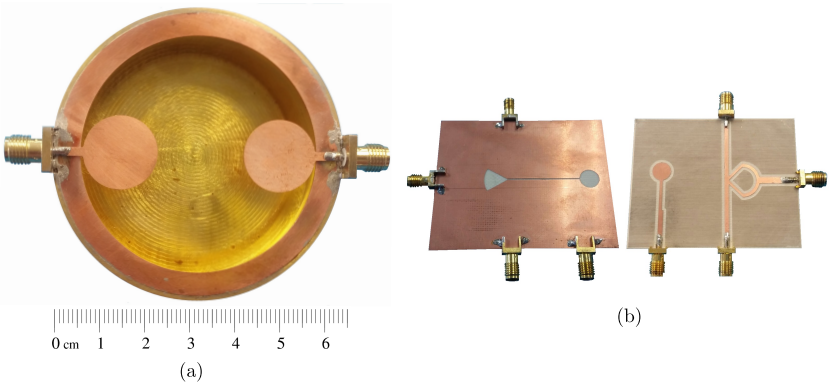

Figure 5.37: Proposed antenna. (a) UWB cavity antenna with differential excitation, and (b) 180° hybrid coupler.

In Fig. 5.37(a), the frontal view of the proposed antenna has been shown. The low-profile UWB cavity backed antenna with 2 ports has been fabricated with two types of materials: copper for the ring, and the two circular patches, and brass for the cylindrical cavity.

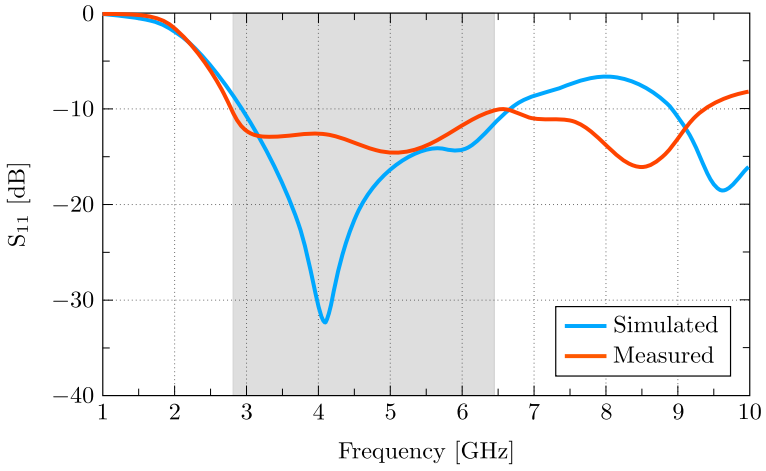

Figure 5.38: Reflection coefficient comparison between simulated and measured results of the proposed antenna with 2 ports using a differential excitation

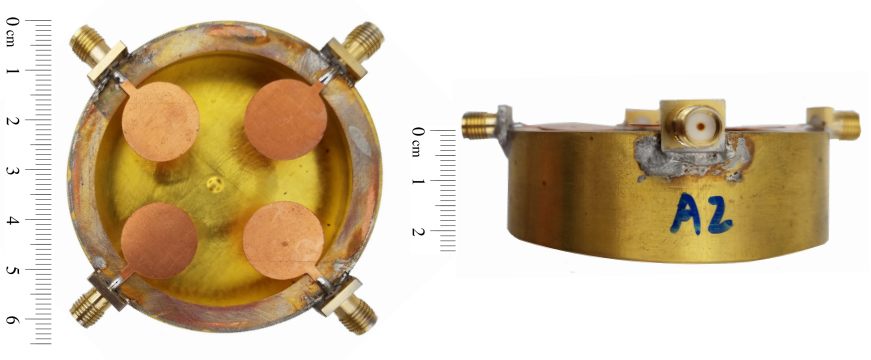

Figure 5.39: Dual-polarized cavity backed antenna

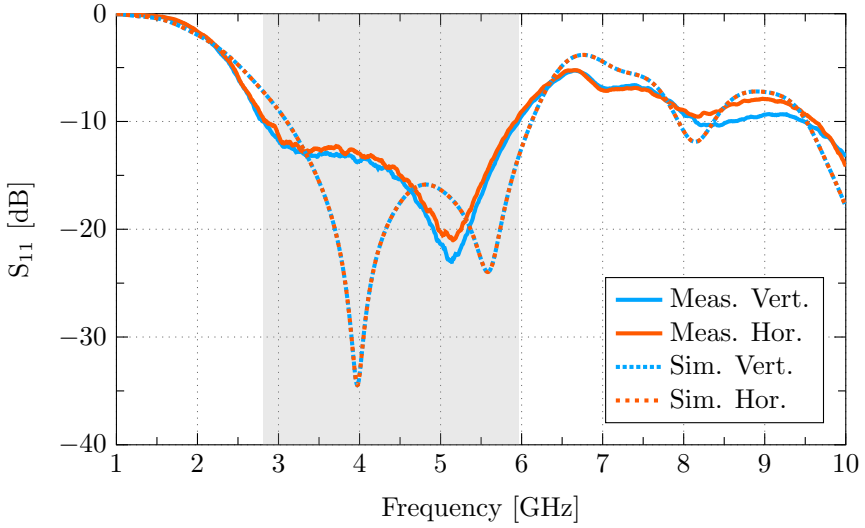

Figure 5.40: Reflection coefficient comparison between simulated and measured results of the dual-polarized cavity antenna

The characterization of the proposed antenna has been carried out using 180° hybrid coupler depicted in Fig. 5.37(b). As can be observed, measured and simulated results are quite similar. The matching band (S11< −10 dB) extends from 2.8 GHz to 6.45 GHz, which corresponds to 79% bandwidth (see Fig. 5.38). The biggest advantage of using a differential feed (+1, -1) is that better bandwidth can be generated compared to using a isolated feed point.

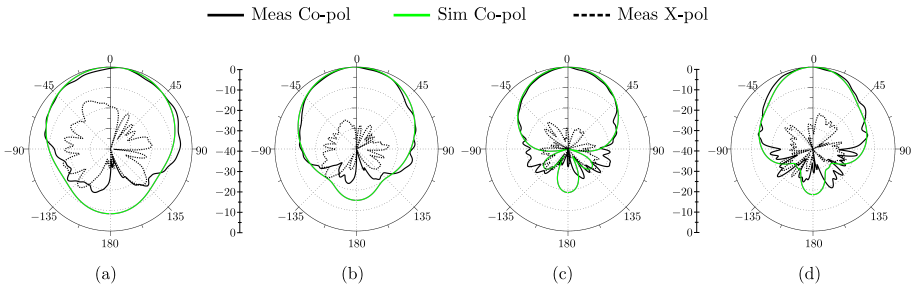

Figure 5.41: XZ−plane normalized E-field radiation pattern of the antenna with horizontal polarization: (a) 3 GHz, (b) 4 GHz, (c) 5 GHz and (d) 6 GHz. Simulated (Sim) and measured (Meas) copolar (Co-pol) and crosspolar (X-pol) components.

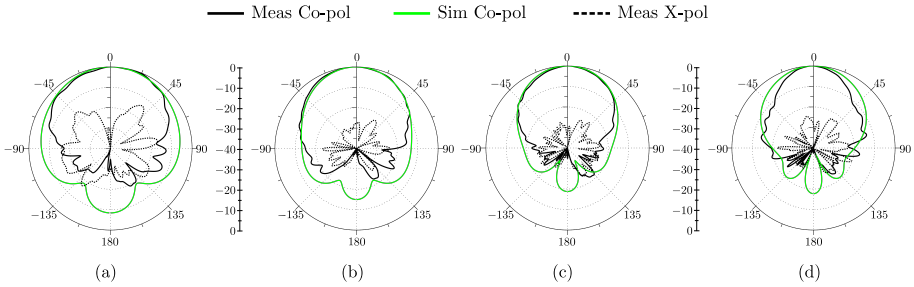

Figure 5.42: XZ−plane normalized E-field radiation pattern of the antenna with vertical polarization: (a) 3 GHz, (b) 4 GHz, (c) 5 GHz and (d) 6 GHz. Simulated(Sim) and measured (Meas) copolar (Co-pol) and crosspolar (X-pol)components

Once the operation and behavior of the proposed structure is clear. Its symmetry can be used to generate an antenna with similar properties in impedance matching but dual in polarization. In Fig. 5.39, the front view and the side view of the circular cavity with 4 ports have been represented. The materials used to make the prototype are the same as those used to make the structure shown in Fig. 5.36.

A comparative graph on the reflection coefficient between the measured and simulated results of the dual polarized antenna has been shown in Fig. 5.40.

The results are very similar in both polarizations, the bandwidth that has been generated is 72%, reaching the frequencies that are between 2.8 GHz to 6 GHz.

In Fig. 5.41 and, Fig. 5.42 show the normalized radiation patterns on the XZ−plane at four frequencies between 3 GHz to 6 GHz, demonstrating that the proposed antenna has a unidirectional radiation pattern for both polarizations. As observed the measured cross-polar radiation pattern is very low in all cases (below −15 dB). The simulated cross-polar component is negligible, so it has not been included.

5.4 Conclusion

The objective of this chapter is to analyze cavity-backed antennas and their extension for multimode feeding. A methodology based on comparing the field modes of canonical waveguides and cavities with characteristic modes has been used.

Rectangular waveguides and circular waveguides have been studied. First, an analysis of the transverse electric TE_{mn} and transverse magnetic TM_{mn} modes has been carried out in a waveguide, to describe the way in which the fields propagate inside the waveguides, and using mathematical formulation, their cutoff frequencies have been calculated.

In microwave analysis, the closed cavities are well known. In this chapter, the analysis has been extended to different cavities with a combination of a PEC (Perfect Electric Conductors), equivalent to short-circuited and PMC (Perfect Magnetic Conductors), equivalent to open circuit, and finally, PMC in both sides.

These cavities with PMC at one end do not take into account the effect of radiation losses at the end, and induced currents outside of the cavity. To perform this study it is necessary to use a full-wave analysis, based on the integral equations of the electromagnetic field, including the sources.

Another alternative, which is an important contribution of this thesis, is the use of 3D characteristic modes, which have been compared with previous results. It has been found that there is a great similarity in the behavior of the currents with the two analysis methodologies, but the characteristic modes allow the analysis of the radiation resistance and the coupling of currents.

In section 5.2, rectangular waveguides and cavities have been analyzed applying this methodology. Based on these results, an square cavity backed an-

tenna with differential feeding has been designed to demonstrate applicability, with impedance bandwidth from 3 GHz to 7 GHz and high stability in the radiation pattern.

In section 5.3, a circular cavity backed antenna with four feeds has been designed. The shape of the feeding elements have been optimized. Feeding elements with circular, elliptical and square geometries have been compared. An impedance bandwidth from 3 to 6 GHz has been obtained.

In order to measure the prototypes in sum or difference mode, a 4-port microwave circuits has been developed. The 4-port microwave circuit exhibits better bandwidth performance that the classical 180° hybrid coupler, providing specific radiation modes in the antenna. The antenna has four independent radiation patterns, allowing it to be used for MIMO systems.

As a final conclusion, the great advantage of analyzing cavity-backed antennas by means of characteristic mode theory has been demonstrated.

Chapter 6

Applications

"*Failure is an option here. If things are not failing you are not innovating.*"

— Elon Musk

6.1 Introduction

In this chapter some of the manufactured prototypes will be presented, each one of them has been designed from the information described in the previous chapters. The prototypes manufactured present very good characteristics in terms of bandwidth, directivity, and low profile. With these structures, it has also been possible to demonstrate the use of the Theory of Characteristic Modes TCM as a great tool to design and to describe the preliminary antenna's behavior, the importance of these devices can be easily integrated into applications of Fifth-generation (5G) and internet of things IoT. The frequencies range in which two of the presented devices are resonating from 2.5 GHz to 6.7 GHz, other prototypes are resonating around 5.8 GHz and 6.2 GHz respectively.

The manufacturing and characterisation process of some devices has been carried out in the Laboratory of the Electromagnetic Radiation Group (GRE) of the Instituto de Telecomunicaciones y Aplicaciones Multimedia (iTEAM) at Universitat Politcnica de Valencia. Another antenna measurement laboratory that has been used is in Antenna and Electromagnetism Research Group at the Queen Mary University of London. Each of these laboratories is very well equipped with the necessary measurement devices to validate the results that

have been generated through electromagnetic simulators such as CTS, and FEKO.

To manufacture the prototypes, the material properties and the physical dimensions must be first considered, these characteristics must be equal to those shown with the design proposed through simulation. The conductive material that will be used for the manufacturing is copper, it has a conductivity $\sigma = 5.8\text{x}10^7$ [S/m], and in some proposed designs, the rohacell material that has a dielectric constant of $\epsilon_r = 1.07$ have been used, this material has similar properties to the air.

The characterization devices are normally given by the measurement of the radiation patterns in an anechoic chamber, and the scattering parameters obtained by a vector network analyzer (VNA). Finally, to validate the behavior a comparative analysis with the simulated and measured results is carried out. Therefore, the operation and the results obtained from the different manufactured devices have been described in the following sections.

6.2 Beamforming Network Excitation

With the rise in the development of intelligent antenna systems, the multibeam and beam-scanning antennas are crucial to modern communication systems such as Direct- Broadcast Satellite (DBS), Multipurpose Radar, multiple beam antenna for mobile communications. Therefore, is necessary to implement multiple antennas in order to create several beams in different directions, either as a beam switch or even forming a continuous beam. The microwave distribution networks are the fundamental element for the design of array antennas, there are some alternatives that are used to achieve this goal.

The most popular microwave distribution networks are divided into three groups as based on transmission lines (Network BFNS), based on quasi-optical lenses (Quasioptical BFNS), and based on digital data processing networks (digital BFN) [153]. All of them are capable of performing multiple beam scanning by making a selection of one or more input ports [154–156]. Within the category of transmission line devices, the Butler matrix is broadly used as it can achieve a large number of switched beams using well-known design algorithms.

The Butler matrix is formed by a passive network with N input ports and N output ports, depending on the port through which the signal accesses the network, the beam that it feeds will be directed towards a space direction. The most common Butler Matrix is the one with 4 input ports and four output

Table 6.1: Theoretical phase value in the outputs ports according to the input port in a 4x4 Butler Matrix.

Ports	P_{out5}	P_{out6}	P_{out7}	P_{out8}	β
P_{in1}	-45°	-90°	-135°	-180°	-45°
P_{in2}	-135°	0°	135°	-90°	135°
P_{in3}	-90°	135°	0°	-135°	-135°
P_{in4}	-180°	-135°	-90°	-45°	45°

ports, the angular variation that is generated according to the input port can be seen in Table 6.1

The physical 4 x 4 Butler matrix structure is designed through a configuration consisting of: 4 hybrid quadrature couplers (90°) at −3dB; 2 crossover couplers at 0 dB and, 2 phase shifters at 45° as is depicted in Fig. 6.1 (a). The fundamental element is the hybrid coupler of 90°, the standard configuration of this element can be seen in Fig. 6.1(b), for its construction it requires transmission lines in microstrip technology of length $\lambda/4$ with impedances of $Z_0 = 50\Omega$ and, $Z_0 = 35{,}35\Omega$ respectively. On the other hand, the crossover turns out to be the combination of two 90° hybrid couplers cascaded as seen in the Fig. 6.1(c).

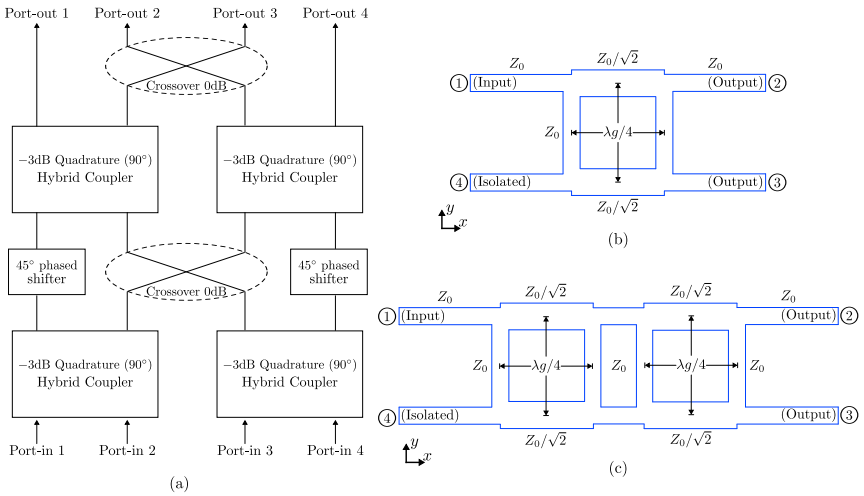

Figure 6.1: Proposed model of −3 dB quadrature (90°) hybrid coupler, and description of the optimized parameters.

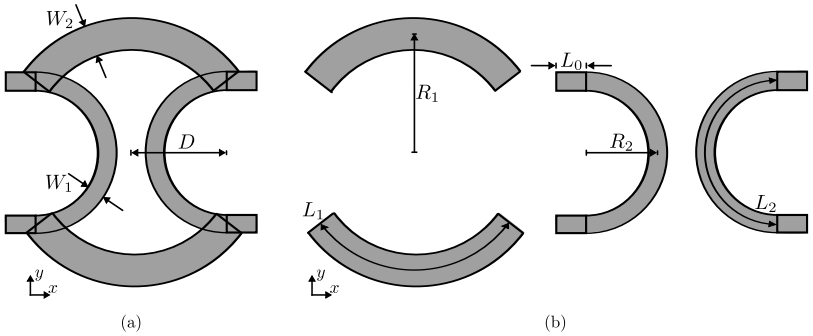

Figure 6.2: Proposed model of −3dB quadrature (90°) hybrid coupler, and description of the optimized parameters.

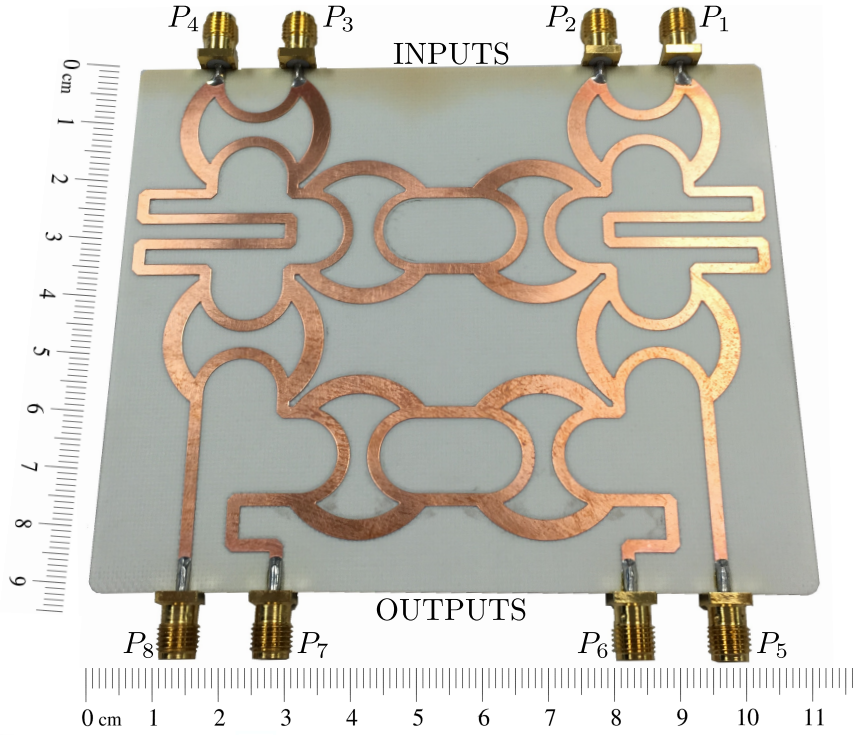

Figure 6.3: Manufactured Butler matrix optimized at 2.45 GHz

The proposed hybrid coupler used to the Butler Matrix design has been has been shown, each of the parameters have been optimized to work at a frequency of 2.45 GHz, where: $W_1 = 1.9$ mm, $W_2 = 3.1$ mm, $D = 9.3$ mm, $R_1 = 6.97$ mm, $R_2 = 11.62$ mm, $L_1 = 21.5$ mm and, $L_2 = 21.9$ mm. The design has been mounted over a Roger 4003C material with dielectric properties $\epsilon_r = 3.55$ and, thickness $h = 0.813$ mm. In Fig. 6.3, a picture of the manufactured Butler Matrix using the referential 90° hybrid coupler is shown, it is necessary to emphasize that due to the dimensions of the coupler, it is impossible to use a 45° phase shifter, what has been done is to insert a piece of transmission line of length 405°.

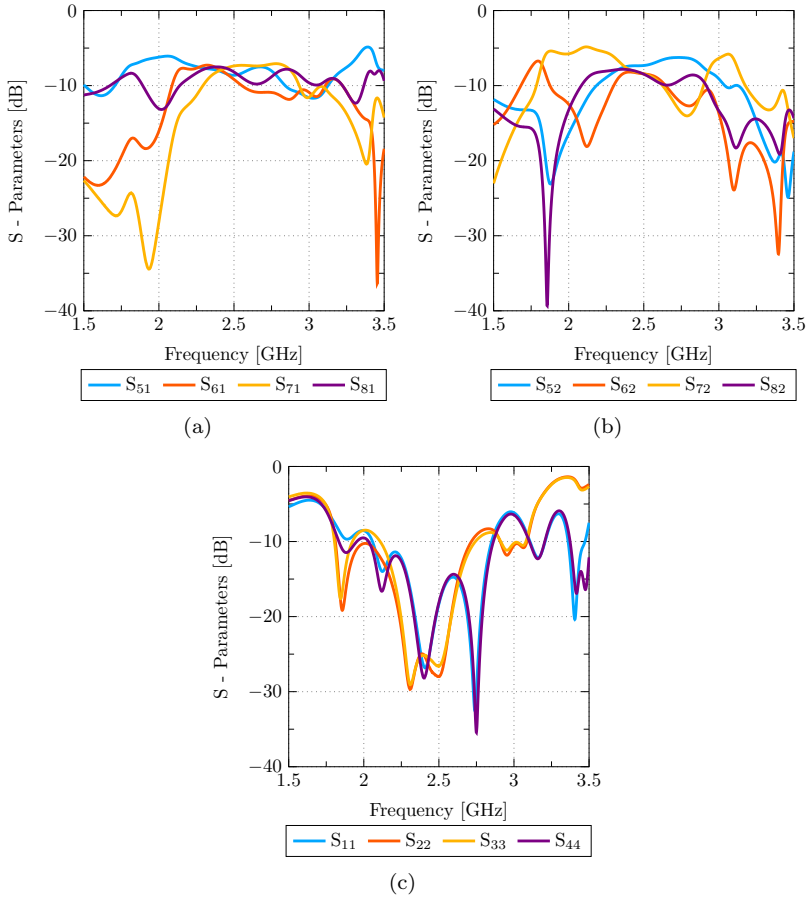

Figure 6.4: Measured Scattering parameters of the Butler Matrix.

The measured scattering parameters of the proposed microwave distribution network have been plotted in Fig. 6.4, the physical symmetry that exists between input ports 1−4 and 2−3 allows the characterization process to be halved, therefore, only the results of input ports 1 and 2 with respect to the outputs have been shown in the said graph. Analyzing the transmission coefficients (Fig. 6.4(a) and Fig. 6.4(b)) at the resonance frequency, the values are between around −6 dB, these results are correct because there are 2 power dividers between an input port and the output ports. In Table 6.2, the phase variation that is generated between the input and output ports is described.

Table 6.2: Measured phase value in the outputs ports according to the input port in a 4x4 Butler Matrix.

Ports	P_{out5}	P_{out6}	P_{out7}	P_{out8}	β
P_{in1}	-134.45°	173.25°	131°	76.68°	-45°
P_{in2}	124.59°	-91.48°	58.65°	168.15°	135°
P_{in3}	168.15°	58.65°	-91.48°	124.59°	-135°
P_{in4}	76.68°	131°	-173.25°	-134.45°	45°

To demonstrate the operation of the manufactured Butler Matrix, it has been integrated into an array of commercial antenna panels under the configuration shown in the photographs of Fig. 6.5, the radiation patterns obtained for a resonance frequency of 2.45 GHz are described in the Fig. 6.5. Depending on the input port is used, the radiation pattern will be displaced towards a specific direction. Using input 1, a variation of −45° in the outputs will be generated between each port, causing the orientation of the maximum power

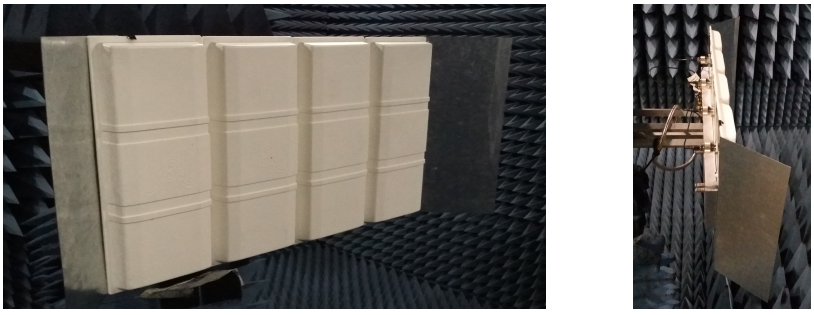

(a) (b)

Figure 6.5: Radiation pattern characterization of the beamforming system inside the anechoic chamber.

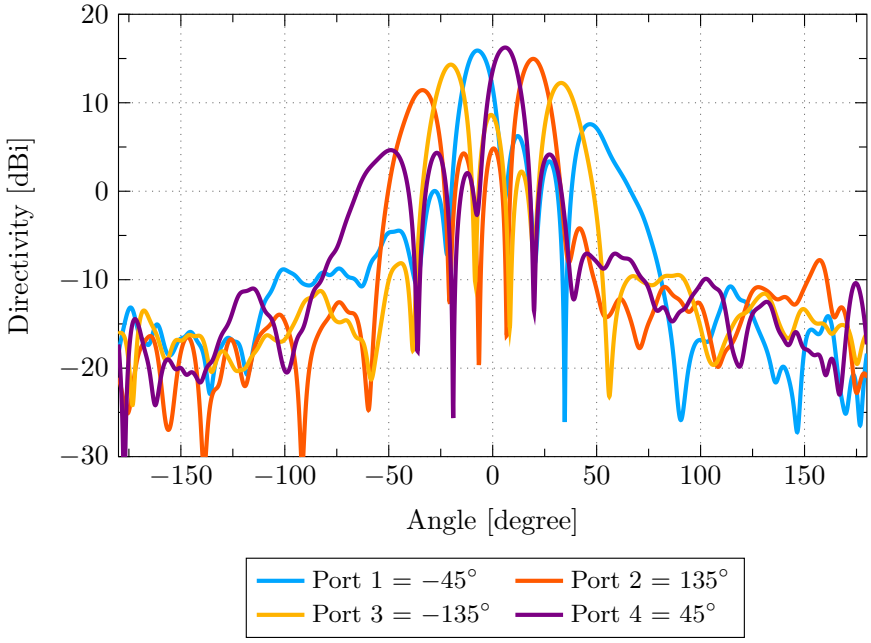

Figure 6.6: Radiation pattern generated by the Butler matrix using a commercial antenna.

of the radiation pattern to be shifted to 6.5°, port 2 generates a radiation pattern with a maximum in −18°, the other 2 ports are reciprocal i.e. 2 radiation pattern at −6.5° and +18°.

6.3 Substrate Integrated Waveguide antenna

Low Profile antennas with a very good bandwidth are very necessary for several types of applications, one of the most used technologies to design this type of antennas is SIW technology, due to its good efficiency, low profile and cost of production [157–159]. The design that has been called Air-Filled Substrate Integrated Waveguide antenna [160] has been inspired by preliminary work [161], which begins from a prototype composed of a square cavity filled with air, the dimensions are 30.64 cm on each side and a very low profile, the cavity consists of 2 orthogonal slots in the upper layer that allow the insertion of the feeding point with vertical polarization through a microstrip line.

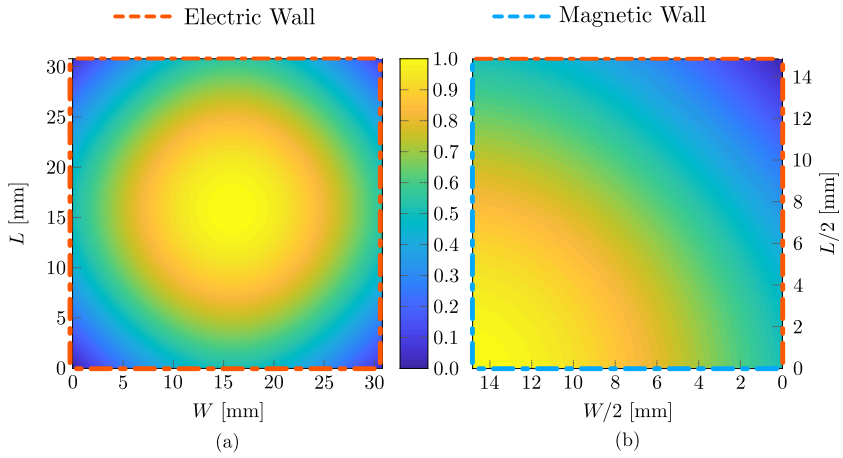

Figure 6.7: Scalar wave equation solution to the E_z. (a) Full rectangular cavity, (b) Semi-closed cavity

Analyzing the current distribution and the total electric fields that are generated in the prototype as shown in Fig. 6.7(a), it can be seen that the maximum fields are in the middle of the structure (represent the magnetic walls) and the minimum fields in the short-circuited side walls (depict the electric walls), this behavior is equal at TM_{110} mode in the resonator, being the solution of the Helmholtz equation 6.1 for the field E_z.

$$\nabla^2 E_z + k^2 E_z = 0 \tag{6.1}$$

With the information described and taking advantage of the vertical and horizontal symmetry axes, it is possible to generate a resonance only with the fourth part of the cavity as can be seen in Fig. 6.7 (b), therefore, now the structure will now consist of 2 electric walls and 2 magnetic walls, remaining $E_z = 0$ for the electric walls and $E_z =$ maximum in the magnetic walls.

Using the excitation mentioned in [162] is the optimal form to feed the structure and to achieve the mentioned characteristics. However, you must be very careful because with a minimum variation in the slot dimension between the structure and the feeding point, the real or imaginary part of the impedance values can be modified as can be seen in the Fig. 6.8(a), generating a greater or lesser capacitive effect between the feed and the structure. In Fig. 6.8 (b), a parametric analysis of the dimensions of the structure can see, thus showing that the dimensions can be tuned to the desired frequency.

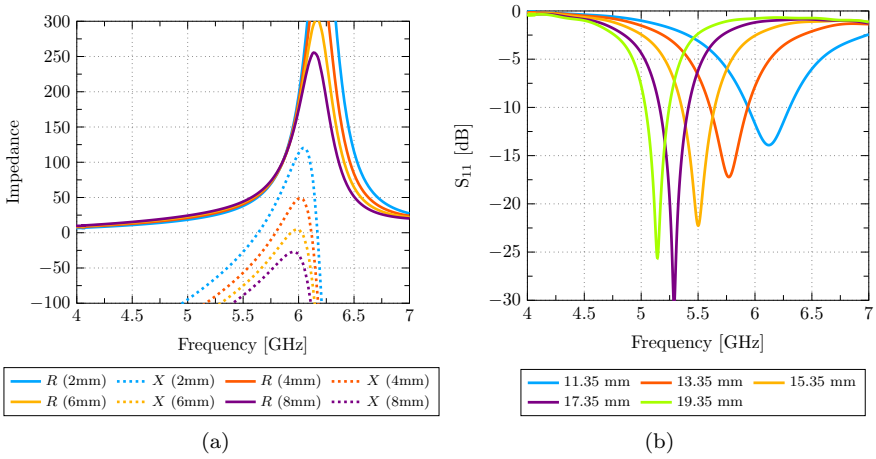

Figure 6.8: (a) Real part R and Imaginary part X of the impedance obtained of the Gap g variation, (b) Symmetrically dimensions parametric analysis W and L.

Therefore, the proposed structure in its first version has been shown in Fig. 6.9(a) and (b), its optimized parameters are: $X_p = Y_p = 15.35$ mm, $L_f = 3.2$ mm, $W_f = 1$ mm, $g = 0.4$ mm, $h_1 = 1.9$ mm, $h_2 = 2.2$ mm, and $W = L = 16.75$ mm.

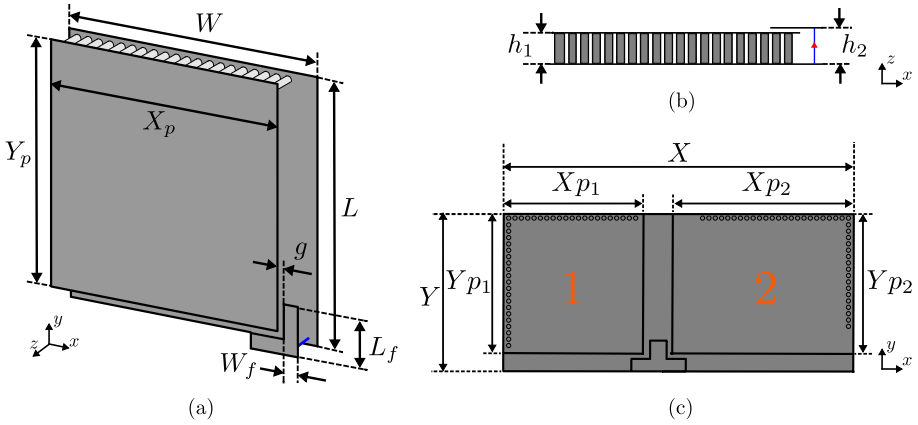

Figure 6.9: Optimised Air-Filled SIW antenna. (a) 3D view of proposed antenna V.1, (b) Lateral view of proposed antenna V.1 and, (c) Front view of proposed antenna V.2

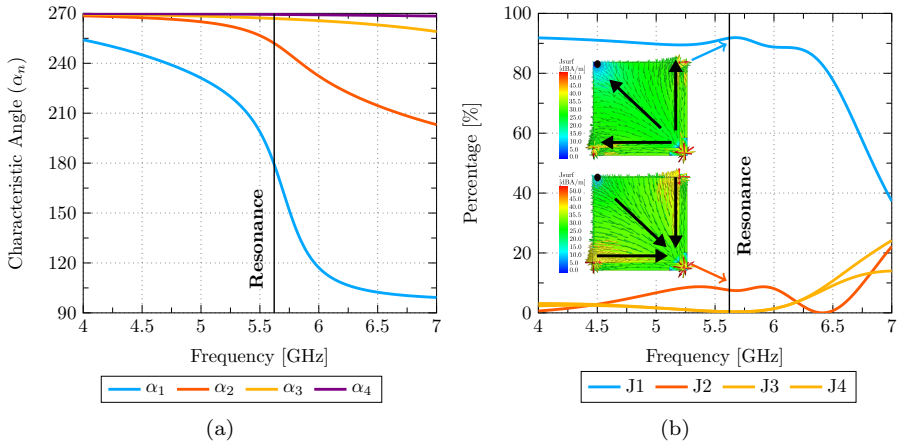

Figure 6.10: Characteristic modes analysis of the Air-filled SIW antenna V.1. (a) Characteristic angle, and (b)Power contribution.

Analysing the structure using the Theory of characteristic modes, it is determined that in the frequency range from 4 to 7 GHz, only one mode is found in resonance at 5.66 GHz, i.e, the characteristic angle acquires a value of 180°, while the other modes that appear in the sweep range are purely inductive as described in Fig. 6.10(a). The power contribution is well defined, the fundamental mode (the current distribution flows through inside the structure in diagonal form) is the more important mode because it is contributing with the 90%, and the remaining 10% are a combination of the higher-order modes (see Fig. 6.10 (b)).

Then, a semi-cavity has been integrated into the V.1 structure, which has a similar characteristic but with a rectangular shape, as can be seen in Fig. 6.9(c). The feeding point must be optimized for each one of the cavities that are part of the V.2 structure, like this, it is possible to increase the bandwidth by generating a resonance by each element of the structure.

Using the characteristic modes, it has been possible to identify that in the structure composed of 2 semi-cavities there are 3 types of modes in the frequency range from 4 to 7 GHz (see Fig. 6.11(a)), the first ones are the fundamental modes J_1 and J_1' that are generated throughout the complete structure (the current flow throughout the lower layer), the mode J_1 mode has resonated at a frequency lower than 4 GHz, and J_1' would resonate at a frequency higher than 7 GHz.

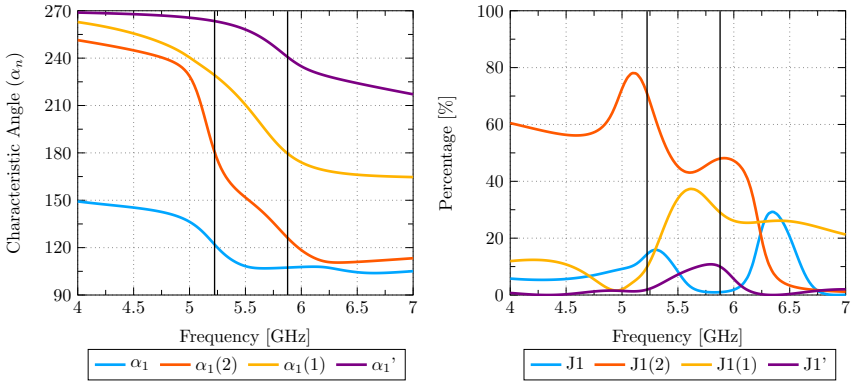

Figure 6.11: Characteristic modes analysis of the Air-filled SIW antenna V.2. (a) Characteristic angle, and (b) Power contribution.

The resonant modes have been generated by each one of the semi cavities, the cavity with the largest area produces a resonance at 5.22 GHz and has been called $J_1(2)$, meanwhile the cavity with the smallest area is resonated at 5.86 GHz represented in mode $J_1(1)$, this can be clearly seen in the characteristic currents distributions of the Fig. 6.12. The percentage of power that contribute in each of the 2 resonances represented in Fig. 6.11(c) have been summarised in table Table 6.3.

Table 6.3: Power contribution percentage of modes that participating in the dual semi-cavity antenna

Mode	5.22 GHz	5.86 GHz
J_1	14.2%	0.97%
$J_1'(2)$	71.4%	47.1%
$J_1(1)$	9.55%	29.6%
J_1'	1.85%	10.3%

Then, once it has been seen that each of the elements of the cavity of the structure generate a resonance, 2 additional cavities have been integrated as can be seen in Fig. 6.13. The gap between the lines of the feeding port and each of the elements does not have symmetry, in fact, for cavity number 4 it has even had to be over-mounted to achieve the impedance coupling necessary

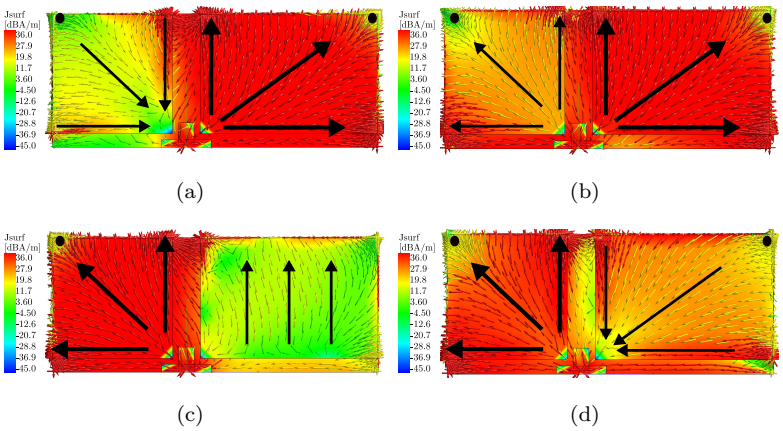

Figure 6.12: Characteristic current distribution of the dual semi-cavity antenna. (a) Mode $J_1(2)$, and (b) Mode J_1 at 5.22 GHz; (c) Mode $J_1(1)$, and (d) Mode J_1 at 5.86 GHz.

for resonance. In the Table 6.4, all the optimized parameters for the proposed design have been described.

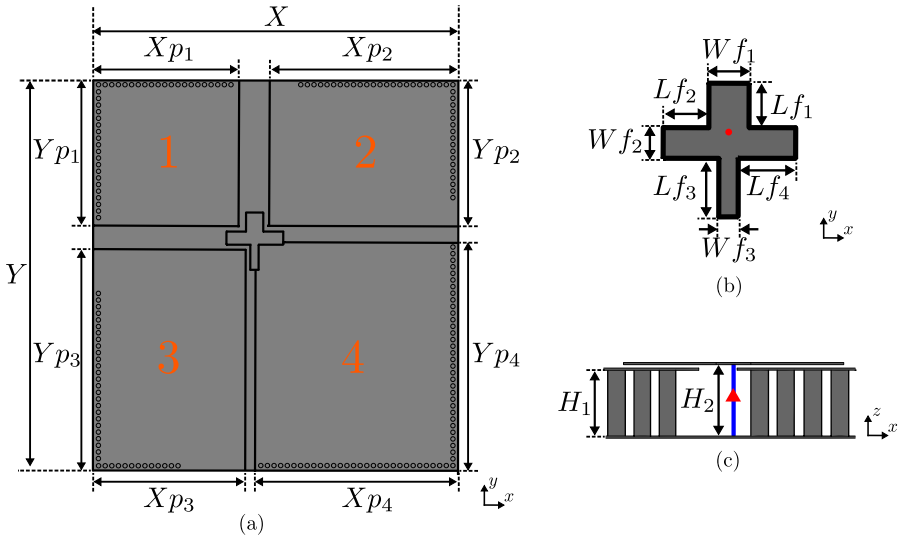

Figure 6.13: Proposed Substrate Integrate Waveguide antenna parameters design.

Table 6.4: Optimized parameters of the proposed antenna.

Par.	Value (mm)	Par.	Value (mm)	Par.	Value (mm)	Par.	Value (mm)
Xp_1	16.50	Xp_2	21.30	Xp_3	17.20	Xp_4	22.90
Yp_1	16.50	Yp_2	16.50	Yp_3	25.0	Yp_4	25.90
Wf_1	2.0	Wf_2	1.5	Wf_3	1.0	Wf_4	1.5
Lf_1	2.2	Lf_2	2.2	Lf_3	2.7	Lf_4	2.7
H_1	1.5	H_2	2.0	X	41.2	Y	44.2

The S-parameters obtained through the full wave analysis of the structure composed of 1 to 4 elements have been shown in Fig. 6.14. As anticipated, it can be verified that each element that makes up the cavity generates a resonance, so with a structure composed of a semi-cavity it has a reduced bandwidth, meanwhile, the complete cavity (4 semicavities) generates a very large bandwidth from 3.3 GHz to 5.7 GHz.

In Fig. 6.15, the photograph of the manufactured propotype in its front and side view have been shown, the rohacell dielectric material has been used as the central element, surround the rohacell the conductive material has been

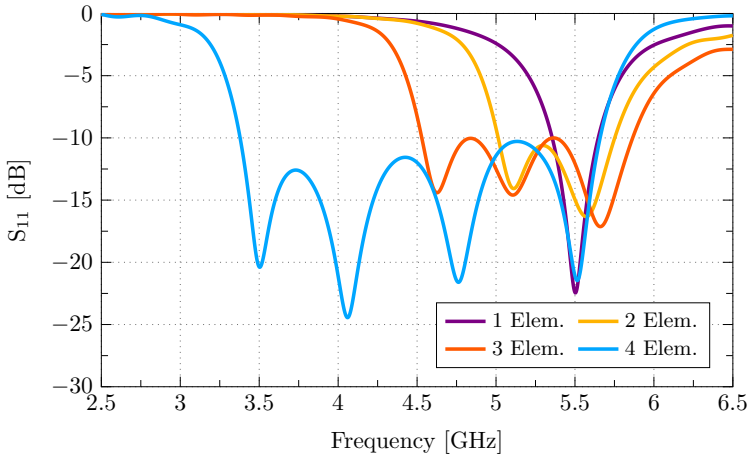

Figure 6.14: Reflection coefficient of the proposed antenna with a progressive increase from 1 to 4 elements.

mounted, the feeding point has been inserted from the bottom to top with a 50 Ohm coaxial cable. A comparative analysis of the measured and simulated results has been plotted in Fig. 6.16, it can clearly be seen that the measurements have shifted towards the low frequencies, the variation has been generated by

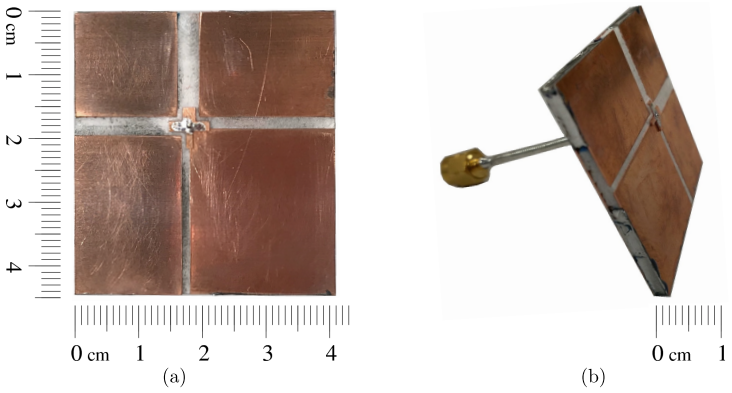

Figure 6.15: Photograph of a Substrate Integrate Waveguide antenna prototype. (a) Frontal view and, (b) lateral view.

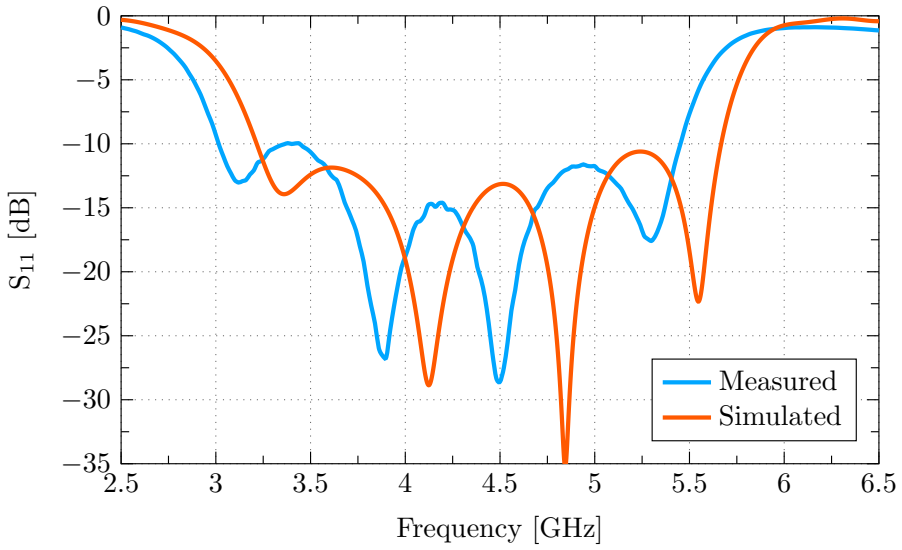

Figure 6.16: Reflection coefficient comparative analysis between simulated and measured results of the SIW antenna.

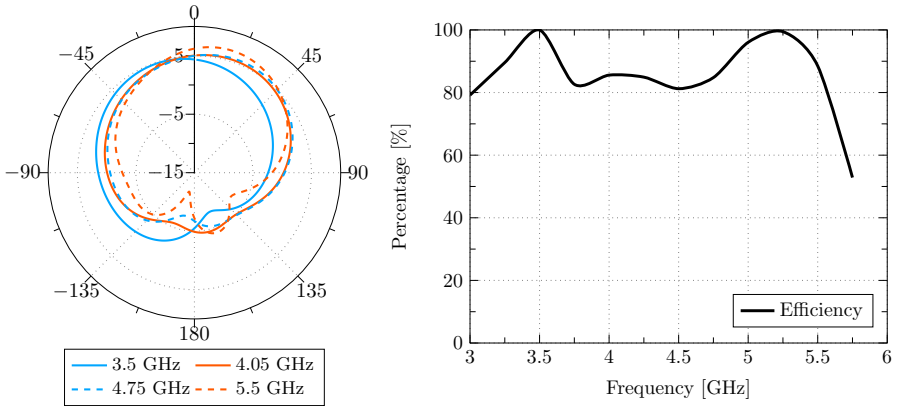

(a) (b)

Figure 6.17: (a) Radiation patterns at different frequencies, and (b) Total efficiency of the proposed SIW antenna.

the precision with which the device and the length of the shorts located on the edges. Remaining the final dimensions of the structure for the lowest frequency as 0.41λ x 0.45λ x 0.02λ, being evident that it is a very low profile antenna.

The radiation patterns for each of the well-marked resonance frequencies in the proposed structure have been represented in Fig. 6.17(a), each of them has a different direction of polarization generated by the sense in which the currents flow in each semi-cavity. Due to the asymmetry of the structure with respect to the feeding point, it causes the maximum propagation direction to deviate slightly from the broadside direction. The antenna efficiency is good in the range frequency analyzed, each of them have been better than the 80% value such as described in Fig. 6.17(b).

An alternative application in which this type of configuration and the characteristics mode can be used is in smart watches [163], because it has limited spaces and require compact devices. The design of this kind antennas will be mounted on a circular plate of radius R. In the same way that the Substrate Integrate Waveguide SIW antenna was designed at the beginning of this section, the dimensions of structures between the upper layer and the lower layer will be used to generate a resonance.

In Fig. 6.18, the configuration of some antennas that can be integrated into a smart watch is shown. The structure consists of 4 antennas, 2 antennas that

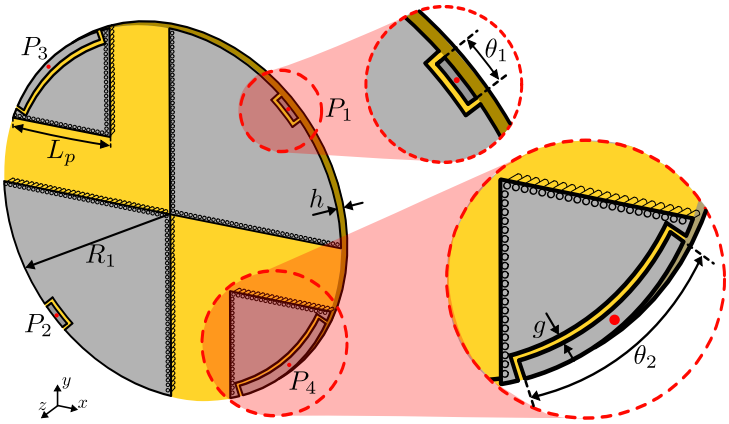

Figure 6.18: Parameters of 4 ports MIMO Antennas with SIW technology for smart watches applications.

work at a frequency of 2.45 GHz and 2 antennas that work at 5.8 GHz. Low-frequency resonance antennas are those that limit the physical dimensions of the complete structure, the shape that these have. Structures are a quarter of a circle, on the line edges 2 electrical walls made with SIW technology have been located. The form of excitation is through capacitive transmission lines separated through an air gap g, the length optimization of the feeding point allows to achieve the necessary coupling so that the antenna is in resonance.

The other 2 pieces that integrate the structure are designed under the same criteria, to resonate at a higher frequency, the dimensions must be reduced as seen in Fig. 6.18, the length of the feeding point will be greater than the used for low frequency antennas. The final dimensions for the proposed antenna are: $R_1 = 29.5$ mm, $L_p = 17.18$ mm, $h = 1.6$ mm, $g = 0.4$ mm, $\theta_1 = 8.45°$, $\theta_2 = 38.85°$. The antenna has been designed over FR-4 material with a dielectric permittivity $\epsilon_r = 4.3$.

Using the full wave analysis, the scattering parameters of the proposed structure have been obtained, the reflection coefficient of ports 1 and 2 are coupled at 2.45 GHz, generating an additional frequency at 5.3 GHz, however, this second resonance is not in our interest. Parameters S_{33} and S_{44} are in resonance at 5.6 GHz, the isolation between the ports is very good, for all cases there are values lower than -30 dB, therefore, in this way it has been possible to meet the objective of generate a MIMO antenna with resonance at 2.45 GHz and 3.6 GHz. Finally, in Fig. 6.20, the radiation patterns for each of

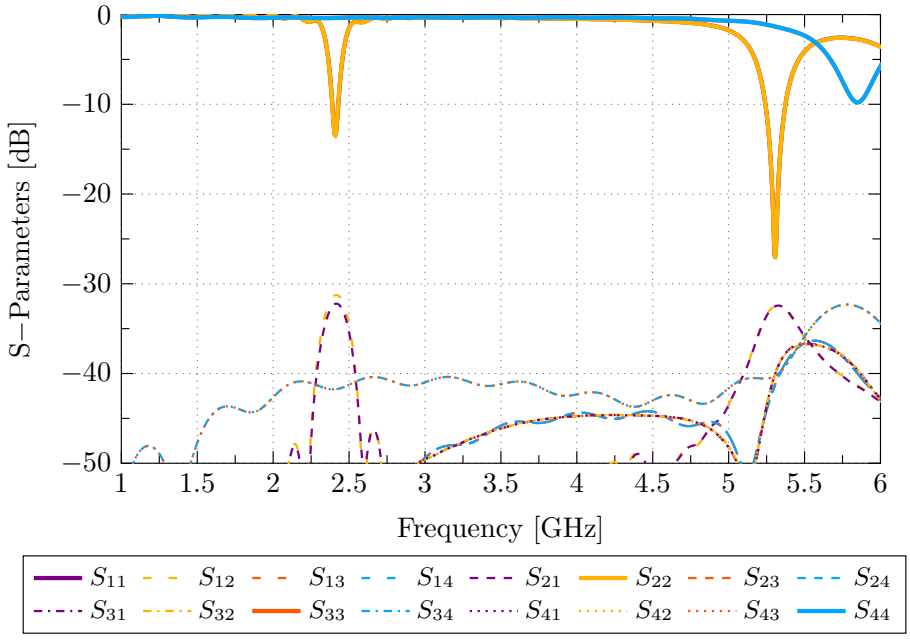

Figure 6.19: Scattering parameters of 4 ports MIMO Antennas with SIW technology for smart watches applications

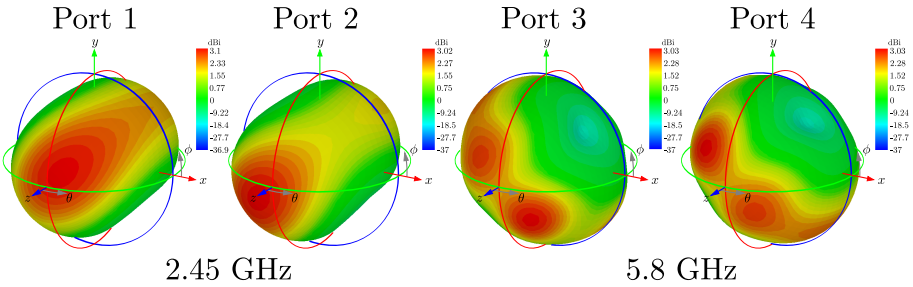

Figure 6.20: Radiation patterns of 4 ports MIMO Antennas with SIW technology for smart watches applications.

the resonance frequencies are shown, each one with a characteristic behavior according to its configuration.

6.4 MIMO antenna for handset applications

Since the appearance of portable mobile phones in 1983 with the launch of the Motorola DynaTAC 8000X, researchers and technology developers from companies that manufacture mobile devices realized that the antenna had a physical limitation [164, 165], understanding this criterion undoubtedly helped the complete elimination of external antennas for mobile telephones and the development of a great variety of telephones with a revolution in their designs, in addition to the integration of new wireless services [166]. Every time mobile devices are scaled-down and compacted, the bandwidth and directivity of the antenna also suffer from reduction [167].

A good solution to mitigate the reduction of these parameters is to consider that the same chassis is part of the antenna [167, 168], then, based on this concept and using the theory of characteristic modes, several types of antennas that after are integrated into the chassis have been designed [169–172].

Then, based on these concepts, a couple of proposals for antennas have been made that are integrated into a mobile device chassis, the reference chassis is a rectangular metallic material with dimensions $W = 75$ mm and $L = 150$ mm. The first option consists of 2 antennas optimized at 2 specific frequencies, the

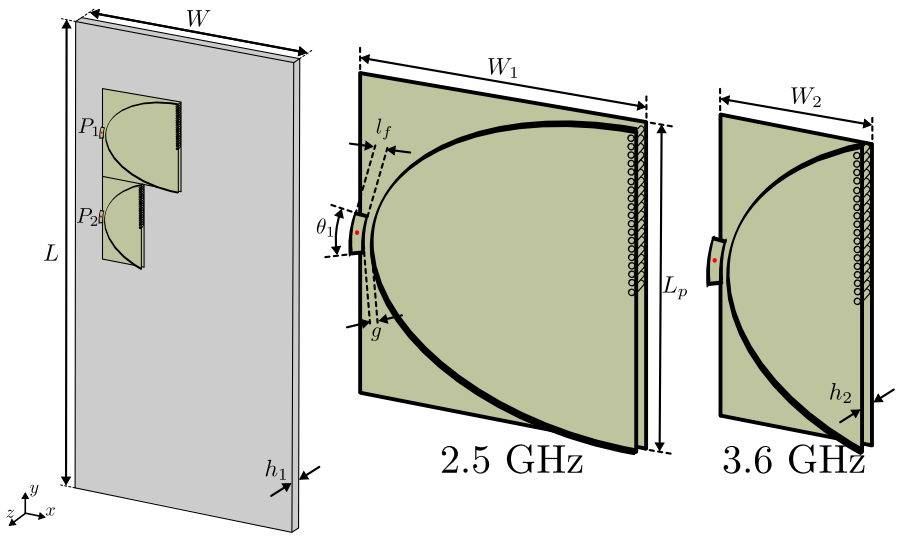

Figure 6.21: Semi-elliptical antennas optimized at 2.5GHz and 3.6GHz for a tablet chassis.

first will resonate at 2.5 GHz and the second at 3.6 GHz. The antenna has been designed based on the information generated in the Chapter 4, basically, the results of an ellipse folded on itself. The folding is carried out in the section of the semi-major axis, in order to reduce the mutual coupling between the antenna ports that will be integrating the MIMO antenna, their electrical wall using SIW technology placed between the upper and lower layer has a limited dimension, It will be a half-length of the semi-minor axis. Later, to achieve the resonance at 3.6 GHz, the structure will be optimized in its horizontal section.

The impedance matching necessary to achieve resonance is directly related to the shape of the excitation, therefore, the feeding point must be treated with great care, in this proposal a capacitive feeding has been used through a piece of the transmission line, this transmission line induces currents to the plate, generating a current distribution that flow from upper plate bordering the sidewall to the lower layer. The length of the feeder and the air gap is the critical matching area, so a lot of emphasis should be placed when designing it. In Fig. 6.21, it can see the configuration of the proposed antennas, their

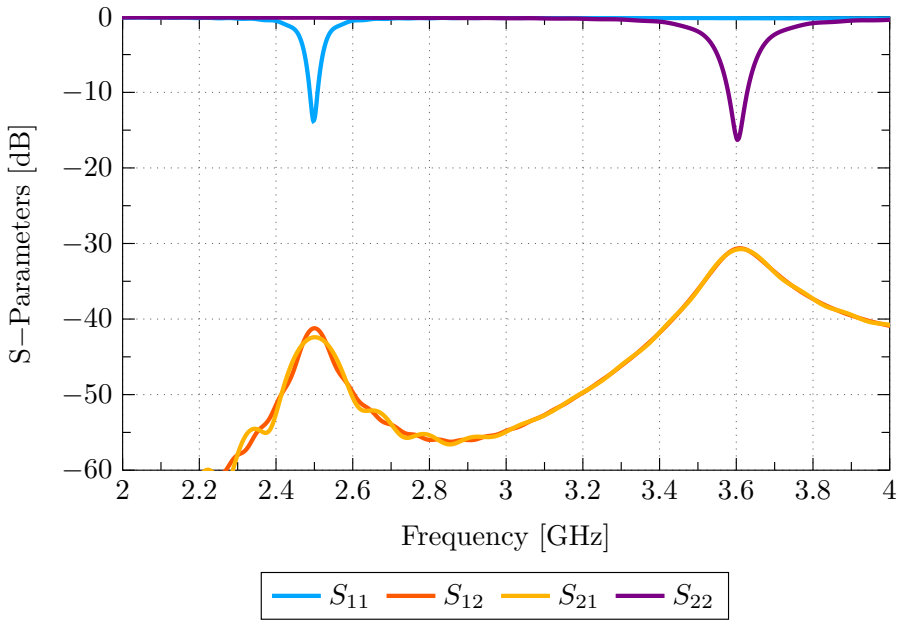

Figure 6.22: S-Parameters of Semi-elliptical antennas optimized at 2.5GHz and 3.6 GHz

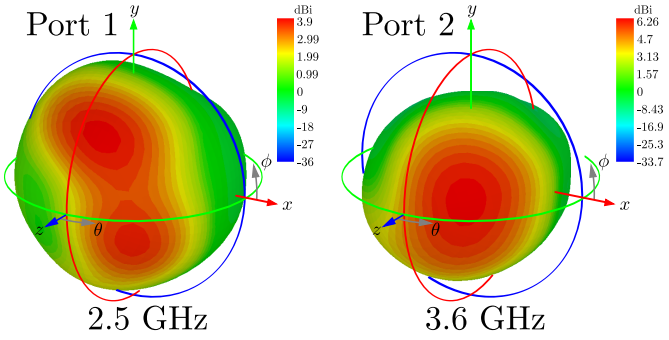

Figure 6.23: Radiation Pattern of Semi-elliptical antennas optimized at 2.5GHz and 3.6 GHz

optimized parameters are: $W_1 = 26.45$ mm, $W_2 = 13.95$ mm, $L_p = 28$ mm, $l_f = 1.2$ mm , $g = 0.5$ mm, $h_2 = 0.93$ mm and, $\theta_1 = 6.43$ mm.

The scattering parameters of the 2 prototypes mounted on the chassis have been represented in Fig. 6.22, the reflection coefficients of each of the antennas show that the two structures are resonant at the frequencies that were initially established i.e. at 2.5 GHz and 3.6 GHz, the isolation generated between the ports are very good, for all cases there will be values lower than -30 dB. The radiation patterns obtained are unidirectional with a directivity of 3.9 dBi for 2.5 GHz, and 6.21 dBi for 3.6 GHz respectively, a 3D view of the two generated patterns is displayed in Fig. 6.23.

Once the structures have been designed in isolation and demonstrated that they work at the 2 necessary frequencies, 6 more antennas with the same characteristics have been integrated into the mobile platform, to avoid mutual coupling between the ports, the antennas have been placed in an interleaved as seen in Fig. 6.24. After submitting to a full-wave analysis, the scattering parameters allow us to demonstrate that the antennas are really resonant at the desired frequency, however, in the reflection coefficients for the antennas designed at 3.6 GHz (the small ones that are located in the extremes) it is seen that there is a shifter frequency towards a lower frequency, this variation in frequency is due to the change of the boundary conditions that were used to design the antenna as an isolated element, then, a minimum reduction of the dimension W_2 in the antennas that are fed by port 4 and 8 can be adapted as a solution to force the resonances will be 3.6 GHz.

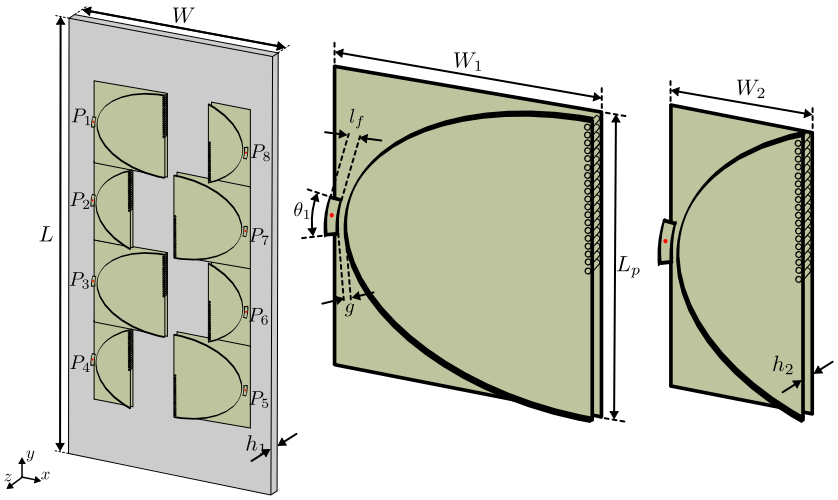

Figure 6.24: 4x2 MIMO antennas optimized at 2.5 GHz and 3.6 GHz for a tablet chassis.

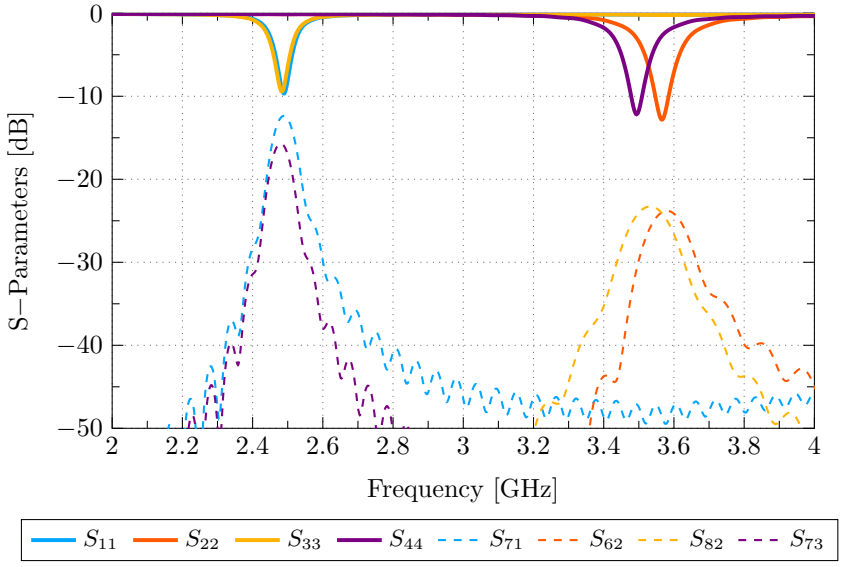

Figure 6.25: S-Parameters of 4x2 MIMO antennas optimized at 2.5GHz and 3.6 GHz.

In the array antenna generated, the worst scenario that has been presented is the interaction between similar continuous elements, for example, the antenna excited by port 1 and 7, causing the isolation between these ports to be affected compared to the isolated elements of la Fig. 6.22, for the other cases the isolation is much better with values lower than −15 dB. To increase the isolation that has been considered critical, all antennas that are mounted on the platform can be moved towards the edge of the chassis. In order to achieve that the platform works as beamforming, a distribution network described in Section 6.2, power dividers with phase shifter or Radio defined by Software can be used to excite the 4x2 MIMO antennas optimized at 2.5 GHz and 3.6 GHz.

The configuration of the second option proposed in this section can be seen in the Fig. 6.26, the chassis in which the structure will be mounted maintains the same characteristics and dimensions as that shown in the first proposal ($W = 75$ mm and $L = 150$ mm). If we focus on the design, the antenna that is proposed at this point is very similar to the previous proposal, part of an ellipse that folds on itself in the direction of its semi-major axis, in the lower layer the ellipse comes to be modified until it has the shape of a rectangle. The first resonance frequency will be produced by the total dimensions on the $x-$ axis of the ellipse, the currents will go from the upper layer to the lower layer passing through the electrical wall cast at the linear edge.

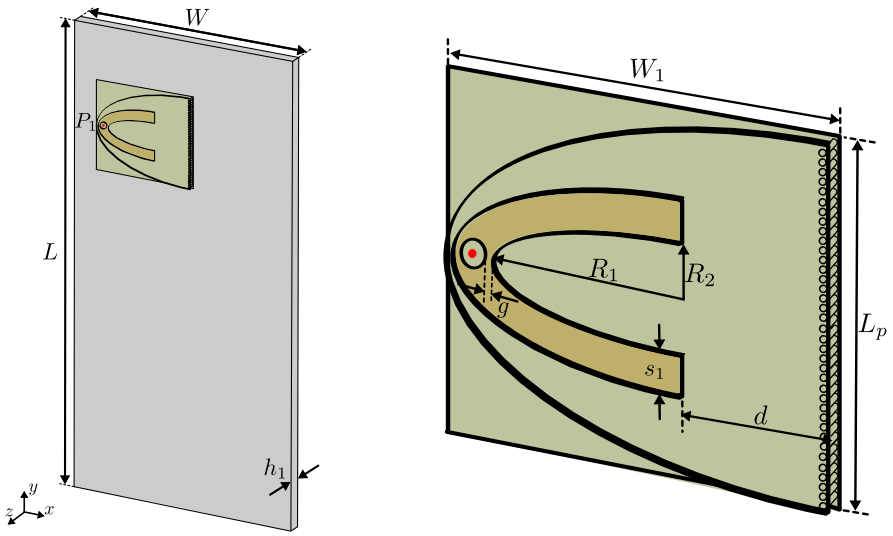

Figure 6.26: Dual band semi-elliptical antenna optimized at 2.5 GHz and 3.6 GHz.

To add an additional frequency and convert the antenna into dual band, a slot is inserted in the upper layer, this slot has the shape of an elliptical half-ring. The proposed way to excite the structure is to use a capacitive element, this element has a circular shape with radius $R_3 = 1$ mm and, is located in the area of maximum radius of the semi-elliptic ring slot. In this way, an induction of currents can be forced, the first one that travels along the edge will generate the lowest frequency, and the high frequency that is produced by the currents that flow through the central zone. In any case, the optimized parameters that have been used to design the antenna would be: $W_1 = 28$ mm, $L_p = 26$ mm, $g = 0.3$ mm, $R_1 = 13$ mm, $R_2 = 5$ mm, $s_1 = 2$ mm, and the height between the lower and higher layers is $h_2 = 0.93$ mm.

The reflection coefficient that has been generated in the structure through the full wave analysis has been plotted in the Fig. 6.27, it can clearly be seen that for values $S_{11} < -6$ dB there is a coupling, although this is true the bandwidth being very limited, the resonances are very well fixed at the design frequencies. One way to improve these S−parameters is by inserting coupling circuits through concentrated elements. The radiation patterns at 2.5 GHz and 3.6 GHz can be seen in Fig. 6.28, for both cases the patterns are unidirectional,

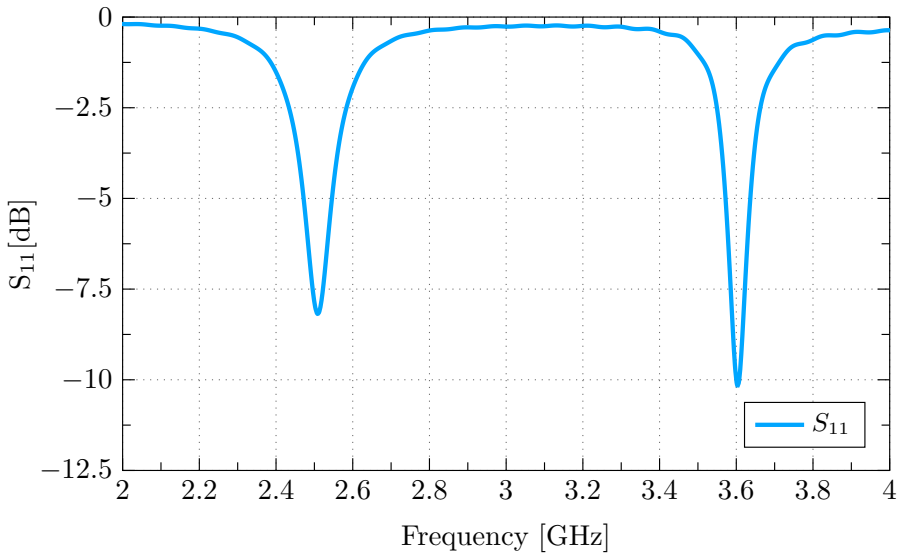

Figure 6.27: S-Parameters of Dual band semi-elliptical antenna optimized at 2.5GHz and 3.6 GHz for a tablet application.

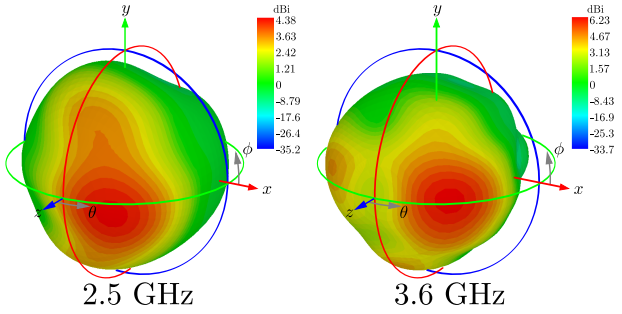

Figure 6.28: Radiation Pattern of dual-band semi elliptical antenna optimized at 2.5GHz and 3.6 GHz.

and the maximums are being shifted in the opposite direction to the excitation point in the form of a travelling wave.

6.5 Boeing 737 Analysis

During the process of academic preparation and development of this thesis, I have been concerned about the possibility that a arbitrary structure can be resonant, even having the ability to select the directions of the currents and radiation patterns independently of the excitement. As each of the analyzes of the various structures shown in this document has been carried out, this concept has been gradually clarified. However, the structures presented are generally homogeneous, so in this section, with the help of the Theory of characteristic modes, an arbitrary shape will be analyzed. Also, it will try to propose the best way and the best place to be able to excite certain modes, and achieve the radiation characteristics very good controlled as well.

Thus, to achieve our stated objective, from the web, the free access model of a scale Boeing 737 airplane has been taken. To be able to analyze it, the structure has been re-scaled to a frequency of interest, the length of the airplane that goes from the nose to the tail is approximately a wavelength at the frequency of 2.45 GHz, this dimension is linear length, i.e. the dimension is not consider the shape of the aircraft's fuselage.

Illuminating with a plane wave and, carrying out the analysis with the characteristic modes theory, the result of the characteristic angles of the first 4 modes has been shown in Fig. 6.29. The natural modes will go from the nose to the tail of the airplane and the degenerate ones will go from the right wing to the left wing (or vice versa). The intention was that the fundamental

mode resonates at a frequency of 2.5 GHz as it was thought when the airplane was scaled. However, due to the curved shape of the structure, the resonance frequencies of the characteristic angles have shifted towards a lower frequency, for the case of the fundamental mode J_1 the resonance is at 1 GHz.

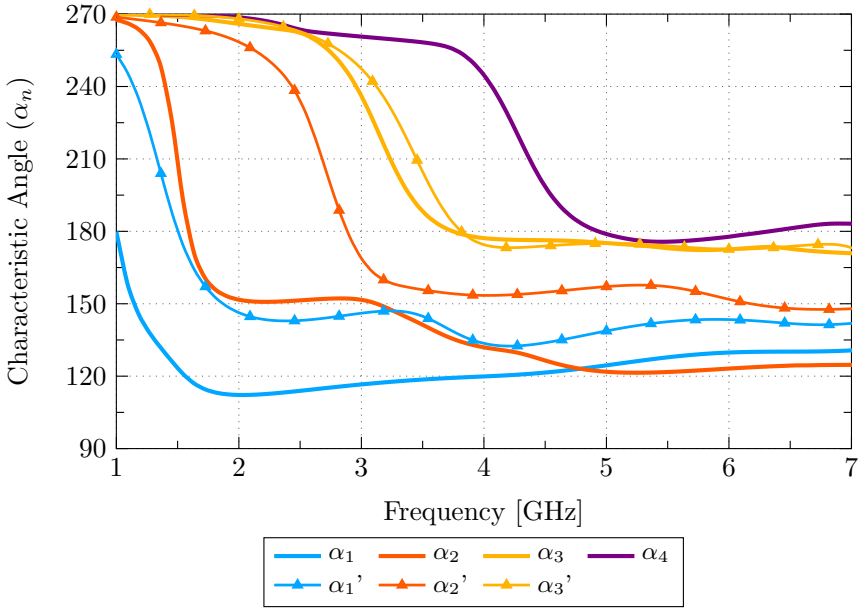

Figure 6.29: Characteristic Angle generated by scaled Boeing 737 airplane.

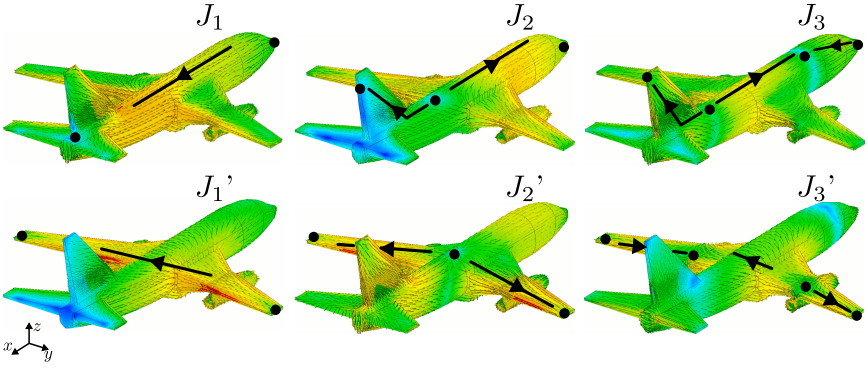

Figure 6.30: Characteristic Current distributions presented in a scaled Boeing 737 airplane.

It is important to say that as Increasing the order of the mode will generate a better bandwidth, whether in the case of natural modes or for degenerate modes. The characteristic currents for each 1 of the modes at their resonance frequency has been shown in Fig. 6.30.

With this information it gives us the idea of where to put or insert the feeding ports, the main objective is to generate a unidirectional radiation pattern, so that excite the mode J_1 would be the most logical thing to do. As we have seen throughout this thesis, there are two ways of feeding a structure, using capacitive or inductive elements. To excite inductively, the air-plane should be cut off in the area where the greatest intensity of currents is generated, this process being not easy in reality.

Therefore, the best option will be to use a capacitive excitation with a differential feeding, these elements should be located on the current nulls, however, due to the shape of the plane it is a bit complicated to introduce capacitive elements in the nulls, then, a pair of antennas closest to the zero currents have been located on the roof of the air-plane, the antennas have a shape very similar to the surface of the aircraft fuselage with one of its ends short-circuited towards the structure.

Figure 6.31: The manufactured prototype of a scaled Boeing 737 airplane, excited by 2 pifa antennas.

In Fig. 6.31, a side view of the proposed scale prototype has been represented, the aircraft has been manufactured through 3D printing using the Prusa I3 Multi Material printer, in view of the need for the structure is conductive, the air-plane has been painted through a commercial golden sprite doped with copper particles. The feeding points have been driven through two coaxial cables that go from the belly of the aircraft to the antenna in the top. In order to fixed the power ports and weld the coaxial cable, adhesive copper sheets have been used around the holes made. The final physical dimensions considering feeding would be 10.8 cm x 11.4 cm.

After the full wave analysis using CST Studio suite and the characterization of the prototype through a Vector network Analyzer, a comparative graph of the scattering parameters of the Boeing 737 has been made in the Fig. 6.32, the simulated S−parameters when the antennas are excited as single isolated elements, they show 2 resonances that are very close, the first one at 4.8 GHz for port 1 and at 4.9 GHz for port 2, for both cases with an isolation between ports lower than −15 dB. However, in the measured parameters it is seen that there are 2 well-marked resonances that have been shifted to a higher frequency than those generated by simulation, in the case of the measured S_{22} parameter there is an additional resonance at a lower frequency that generates a very good bandwidth with respect to the simulated S_{22}, these frequency shifts are linked to the efficiency with which the manufacturing process is carried out.

On the other hand, making a feeding using a combination of ports, the excitation or exclusion of certain modes can be forced, with balanced supply (+1, +1) the even modes are forced and, with the differential (+1, −1) the odd modes. In Fig. 6.32(b), the results of the two types of combination have been plotted, for both cases, in the simulation a resonance is generated at the same frequency with a limited bandwidth. However, the measurements have generated a large bandwidth ranging from 3.6 GHz to a frequency higher than 6 GHz.

The simulations of the total radiation patterns and currents of the prototype at the frequencies (where the resonance has the better coupling) have been shown in Fig. 6.33. When a port is excited as single isolated element, it can clearly be seen that the greatest intensity of currents will be around the excited feed point, generating a maximum in the radiation pattern in the direction of the feed point. Using the combination of ports has forced the excitation of certain modes, with balanced power, the J_2 mode is excited on the surface of the aircraft fuselage, this causes a radiation pattern with 2 lobes in the direction of the power points. Meanwhile, with differential feeding, the excitation of the mode J_1 was forced, which means that a unidirectional diagram orthogonal

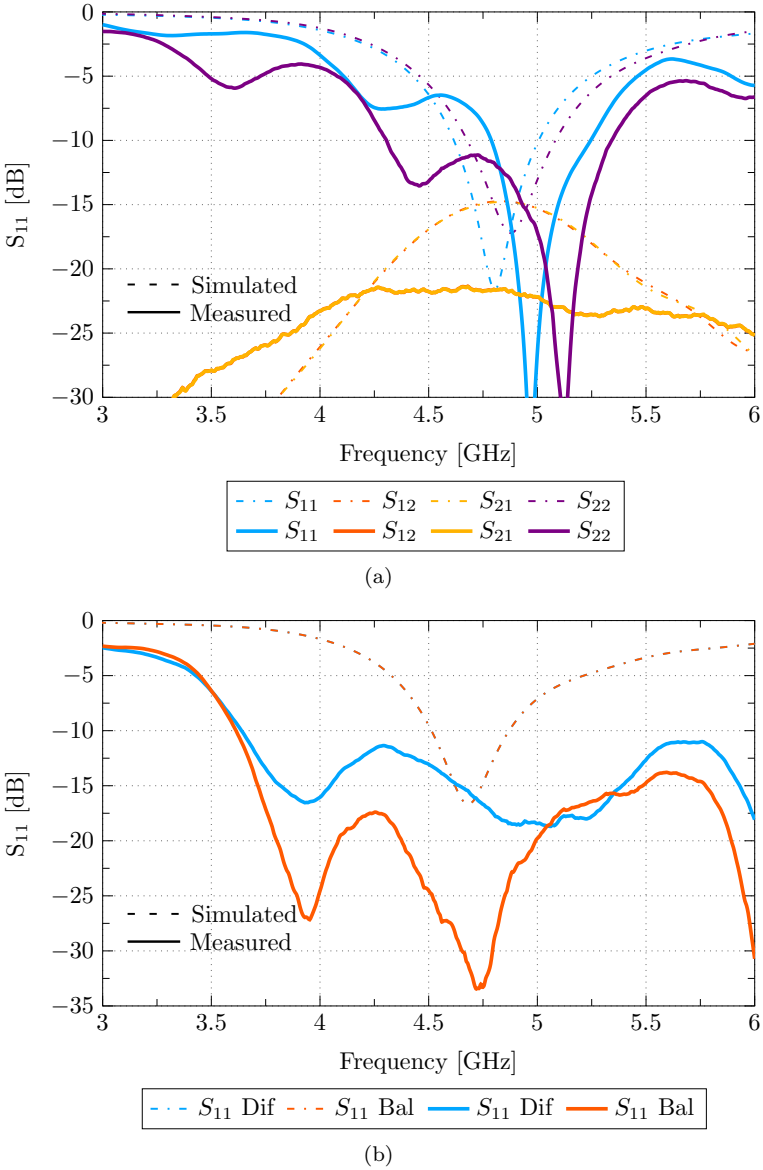

Figure 6.32: Scattering parameters of a scaled Boeing 737 airplane. (a) With isolated ports and, (b) With balanced and Differential excitation.

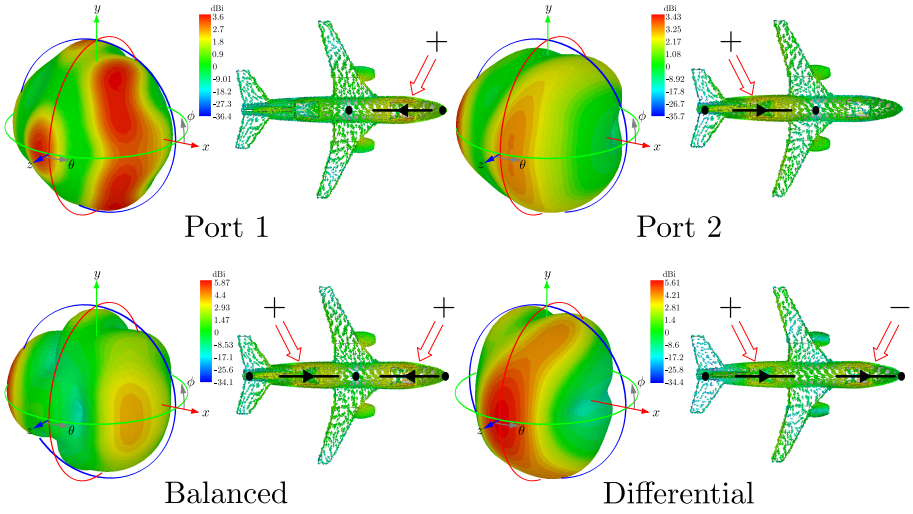

Figure 6.33: Total current distribution and radiation pattern for a scaled Boeing 737 airplane.

to the structure will be generated. Thus complying with the generation of a controlled current distribution and radiation patterns using multiple feeding points.

6.6 Metasurface Antenna Absorber

The stealth technology since the second world war has been one of the most studied topics because this type of technology allows reducing the observability of radiant structures through the reduction of the radar cross-section (RCS), which has been integrated into aircraft, submarines, missiles. The first applications in fighter aircrafts beyond the angle of the fuselage used a special type of paint as absorbent, causing electromagnetic waves that reached the object not to be reflected [173]. Subsequently, structures with corrugated surfaces were used, generating a deviation from the electromagnetic waves impinging on the surface of the object [174].

However, in recent years absorbents using metamaterials have become a structure of great interest, due to their versatility to integrate with several devices [175, 176]. There are some methods to reduce RCS in a structure such as radar absorbing materials (RAM) [177–179], shaping [180, 181], artificial magnetic conductive surfaces [182] and meta-surfaces of polarization conversion

[183, 184]. The most common forms used to design absorbent metamaterials are split ring resonators [185, 186], as well as geometries that have rectangular, circular or triangular shapes.

In some preliminary studies in addition to using metamaterials as absorbs, resistive loads have been integrated into the structure. An example of an absorbent with resistive loads is presented in [187], the electromagnetic waves inside the structure will be consumed by the resistive loads, generating a maximum power transfer, the impedance values have been obtained from the analysis of full-wave of the analyzed structure as radiator element, afterward the reciprocity theorem is applied and through it, the load values have been obtained. The bandwidth obtained in the reference work is very large around 105%, however, it cannot be considered a low-profile structure because the distance between the ground plane and the structure is very large. On the other hand, the absorber design is optimal, as long as the optimal point of excitation is known, however, in cases where the structures are arbitrary, a different type of analysis is required. Thus, the Theory of Characteristic Modes (TCM) is a great option that can be used to design the structure.

Therefore, in this section, the procedure for the design of the metasurface material is presented and it has been optimized to achieve high absorption starting from an arbitrary unit cell formed by 8x8 pixels matrix, each pixel

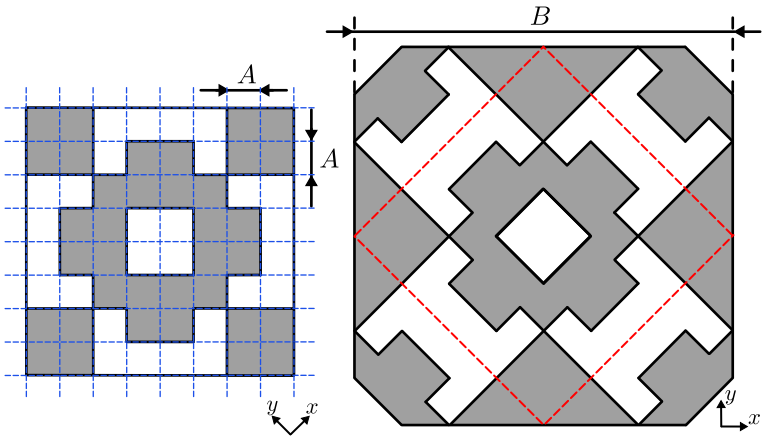

Figure 6.34: (a) The optimized unit cell metasurface structure of 8x8 pixels, (b) the proposed unit cell rotated 90°, completed at its vertices periodically.

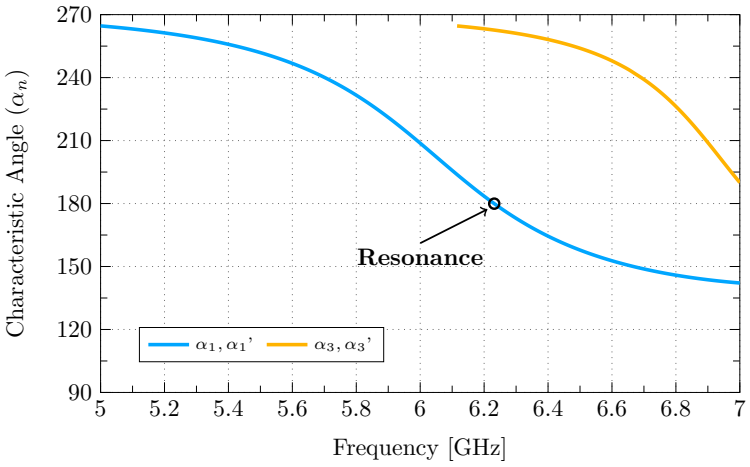

Figure 6.35: Characteristic angle the proposed metasurface unit cell analyzed such as a periodical structure.

N describes a dimension of A x A, where $A = 1.78$ mm and can be coded binary (1 is metal and 0 is air) such as shown in Fig.6.34(a). In order to facilitate the analysis, the unit cell has been rotated 90° and its vertices have been complimented as a periodic structure, leaving a structure of dimensions B x B, where $B = \sqrt{2(N^2)(A^2)}$ as seen in Fig.6.34(b).

In Fig.6.35, the characteristic angles of the fundamental modes (mode J_1 and mode J_1') that appear in the structure depicted in Fig. 6.34 has been represented, mode J_1 and its degenerate mode J_1' resonates at the same frequency at 6.23 GHz.

The objective to use the characteristic modes is not only to obtain information about the resonant frequency of the structure but also to know how the characteristic currents are distributed on its surface and to obtain a specific behavior, with this distribution it can describe the zones with the optimal points to insert the feeding to excite the desired mode. Therefore, the intention in this work is to excite the fundamental mode J_1 and its degenerate mode J_1' showing in Fig.6.36.

Then, according to the current distribution that describes the fundamental mode in the structure, it can be seen that there is a symmetry at -45° of the vertical axis, in this axis of symmetry a pair of nulls is presented. Clearly the

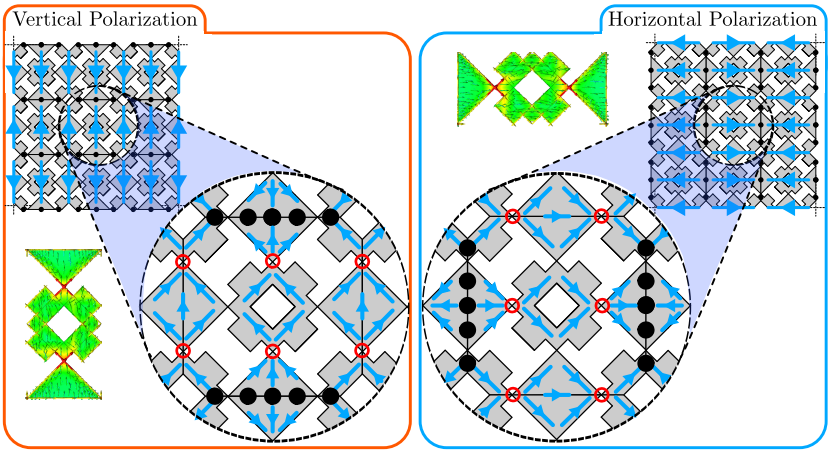

Figure 6.36: Characteristic current distribution of fundamental mode in the proposed metasurface unit cell analyzed such as a periodical structure. Vertical and Horizontal polarization at 6.23 GHz.

currents are distributed throughout the structure, generating in some areas a greater intensity and describing as an optimal place to insert the feeding point.

Therefore, to excite the J_1 modes or their degenerate, the feeding points must be placed in each of the vertices that have been marked with red circles, as evidenced in Fig.6.36 (a), the position of each of the feeding points will depend on the structure area, being able to be located horizontally or vertically, for both cases an inductive feeding will be used.

The proposed design has been mounted over a substrate with the following characteristics: $\epsilon_r = 4.3$ and a height $h = 1.6$ mm, after to the design in the simulator the boundary conditions of the sidewalls of the unit cell (X and Y direction) must be configured as a periodic structure and the Z-axis as open free space, and taking into account the information provided in the previous section through Fig.6.36, small slots with a value $Gap = 0.8$ mm are designed in the areas that have been considered as optimal points to insert a feeding port.

In these slots, the sources will be placed such as depicted in Fig.6.37(a), and through a full-wave analysis the values of the characteristic impedance will be obtained in the real and imaginary part, these complex values of the impedance

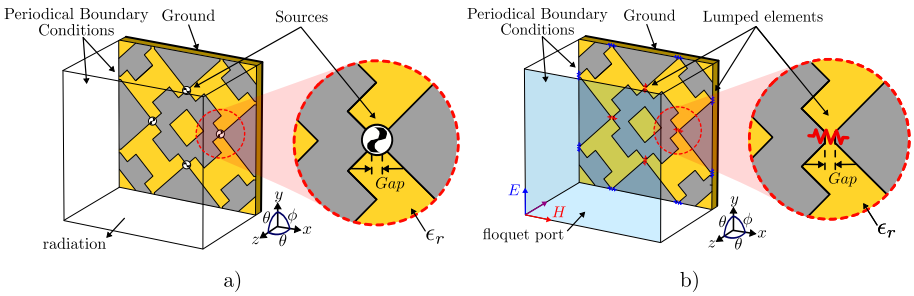

Figure 6.37: Setup of the unit cell in the simulator. a) In transmission mode using feeding ports, and b) In reception mode using resistive loads.

will be used to calculate the lumped elements that must be used to design the absorber that is shown in Fig.6.37(b).

The characteristic impedance of the proposed structure has been plotted in Fig.6.38 (see right vertical axis). At 6 GHz the impedance is decomposed in resistance and reactance $Z = 422 + \text{j}170.79\ \Omega$, using the mathematical formulation presented in [187] the elements can be calculated through its admittance:

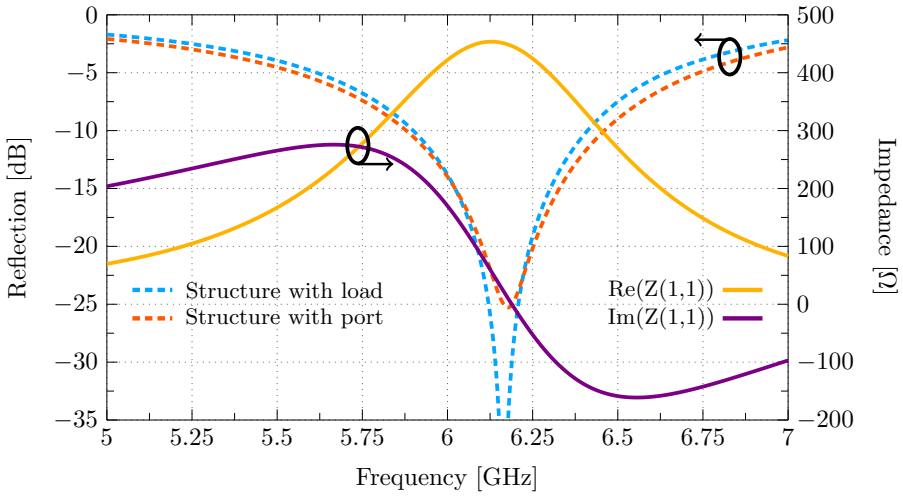

Figure 6.38: Input impedance of the periodical structure and the reflection coefficient comparison of the structure with port and resistor, respectively.

$$Y_{in} = \frac{1}{Z_{in}} = \frac{1}{422 + j170,7\Omega} = 0,0020 - j0,0008 \ (S) \tag{6.2}$$

The reactance should be cancelled using a capacitive or inductive element and this depends if the reactance is positive or negative. Hence, for this case, the element can be obtained according to below:

$$C_p = \frac{-im(Y_{in})}{(\omega)} = \frac{0,008}{2\pi f} = 0.0218 \text{ pF} \tag{6.3}$$

Once the reactance has been cancelled, the value of the input resistance must be calculated, obtaining it as follows:

$$Z_{in} \parallel Z_c = \frac{1}{Y_{in} + Y_c} = \frac{1}{0,0020} = 500 \ \Omega \tag{6.4}$$

Therefore, to obtain the maximum transfer of power in the structure, these 2 calculated elements must be inserted in each of the slots that have been previously designed. However, obtaining or designing an inductive element with these characteristics is complicated, hence a frequency will be selected in which the reactance is equal to 0, so the reference frequency will be at 6.19 GHz, now according to the Equations 6.2, 6.3, 6.4, the resistance value is equal to $R_{in} = 446 \ \Omega$ and the reactance will be zero. The resistance of 446 Ω has been approximated to a more commercial value that is 500 Ω.

At this point, it is important to highlight that when the structure is analyzed in transmission mode as seen in Fig. 6.37(a) the power is distributed on both sides of the top layer, while for the model in reception when the structure has been illuminated by the floquet port as it is the case of Fig. 6.37(b), the currents only flow in the surface of the top layer. Then, the value of the input resistance in reception will be twice that in transmission. The input impedance for the transmission analysis will be 500 Ω and the load values for the analysis in reception will be 1K Ω. In Fig. 6.38, in addition to the impedance, the reflection coefficients for the case in transmission and reception have been shown (see the right axis of Fig. 6.38). The results are similar in both cases with a small variation in frequency.

The proposed metasurface has been scaled to a constant $K = 1.78$ keeping its original height, increasing the size the problem of milling is avoided, in addition the spaces to soldering the resistive loads will be optimal, the final size of the proposed metasurface is: 180 mm x 180 mm x 1.6 mm and its resonance frequency will be around at 6.1 GHz.

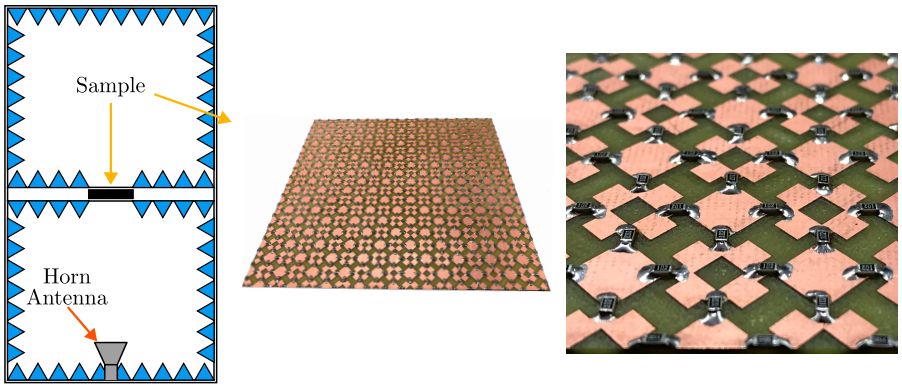

Figure 6.39: Measured reflection from the metasurface absorber. The insert shows a photograph of the fabricated absorber with chip resistors.

On the structure, a lot of a number of resistive loads have been soldered, which have been distributed over each slot as can be seen in Fig.6.39(c), the absorption parameters of the metasurface has been measured within an anechoic chamber using a horn-type antenna according to the configuration described in Fig.6.39(a)(b),

The measurement procedure consists in using the concept of total reflection, that is, performing a measurement in reception using a perfect reflector and then comparing it with the reflection value of the prototype. In Fig.6.40, a comparative graph is shown with the simulated and measured results of the reflection coefficient of the metasurface. For simulation, it has been considered only for a polarization ($E_{in} = 0°$), meanwhile, for measurements case, the metasurface has been characterized in 4 positions when E_{in} is = 0°, 30°, 60° and, 90° clockwise.

The measurements have a very good characteristics to be a very low profile device, the bandwidth considered to work in optimal conditions as an absorbent is 10% (under -10 dB) from 5.8 GHz to 6.44 GHz, and it is also independent of polarization, however, It has a small variation in frequency with respect to the simulated results, this variation is produced by the soldering of the load since it does not coincide with the edges of each of the slots.

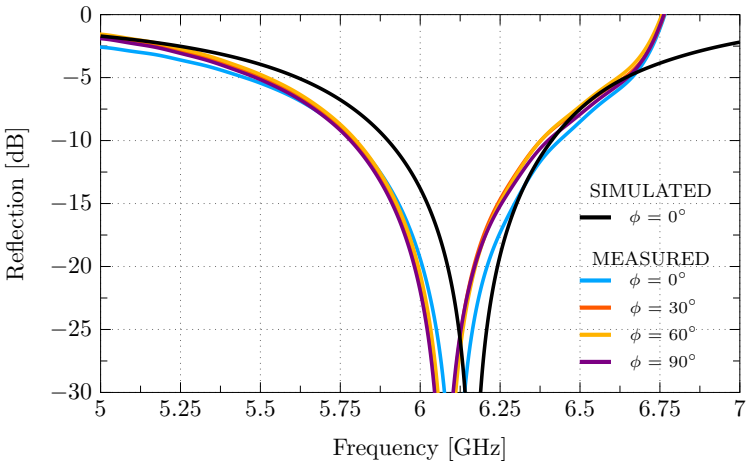

Figure 6.40: Simulated metasurface absorber reflection coefficient for different incident angles (θ) with adjusted matched load values.

6.7 Conclusion

All the knowledge gained in previous chapters from the modal analysis of the different structures is applied in this final chapter to propose new antenna designs for different applications.

Along this thesis, some prototypes have been analyzed and designed, each one of them operating as an isolated element. The possibility of generating characteristic modes in arrays using microwave networks such as Butler matrices has been investigated. In section 6.2, a distribution network has been presented consisting of 4 input ports and 4 output ports that allow generating 4 independent beams. The device has been designed to work at a frequency of 2.4 GHz and optimized so that the structure is as compact as possible. It has been tested with a commercial array of antennas to demonstrate its optimal performance.

In section 6.3, the design of an antenna that presents a large bandwidth has been proposed. The structure is composed of 4 asymmetric cavities. The external walls of these cavities have been partially short-circuited with the ground plane. The four asymmetrical cavities are fed with a common optimized capacitive element. This concept of making a piece of cavity resonate can be used for any type of shape.

Through the thesis development, there has been collaboration with an International Mobile Company for the development of new 5G antennas for mobile devices. Two types of very low-profile antennas have been proposed that can be integrated into the chassis of a handset device. Each one of the proposals has been obtained using folded structures, excited with capacitive elements. Up to 8 antennas have been integrated operating at two different frequencies, yielding an appropriate solution for MIMO technology.

In section 6.4, a scaled model of a Boeing 737 has been taken as a reference, in order to demonstrate the utility of TCM to analyze the radiating properties structure. The structure has been illuminated with a plane wave to determine a optimum feeding positions. Then, multiple feeding ports have been inserted to force the excitation or exclusion of certain modes. The device has been manufactured and it demonstrates that it is possible to generate a radiation pattern with unidirectional radiation pattern in broadside direction.

Finally, in section 6.5, periodic structure has been analyzed in order to design an absorbing surface at a fixed frequency. TCM has been used to analyze the unit cell to determine the optimum position and value of the resistive loads. With the optimum resistive a maximum power transfer is obtained, the device has been manufactured and good agreement between the measurements and simulations has been observed.

Chapter 7

Conclusions and Future works

""Everyday we know more and understand less.""

— Albert Einstein

7.1 Summary of obtained results

The main objective of this thesis has been to use a methodology to design antennas that have a high bandwidth using multiple feeds. In recent years, the theory of characteristic modes has become a great tool that provides important information for antenna design.

From a general perspective through a mathematical formulation it has been possible to describe the behavior of arbitrary structures in the absence of power supply, the characteristic modes start from the definition of an eigenvalue problem involving the impedance matrix, this impedance matrix can be solved through integral equations which basically would be the use of the method of moments.

Each eigenvalue is associated with a characteristic mode, therefore, knowing its magnitude can provide information on the resonance frequency, current distribution and characteristic radiation patterns of the arbitrary structure. However, eigenvalues are not frequently used, there are other alternatives that allow providing the physical interpretation of the modes such as modal signif-

icance and characteristic angles. In addition, by integrating a power source to the structure and performing the analysis with the TCM, it is possible to know the modes that participate in the generation of a resonance, and also the percentage of contribution of each one of them to the generation of the total radiation.

Using all this mathematical formulation described and that comes developed in some commercial electromagnetic simulators, it has been made of the analysis of modes of several planar structures where their resonance characteristics, radiation patterns and current distributions have been shown, it is important to mention that there will be an infinite number of modes, but can be limited to a minimum number according to the frequency range of analysis, for most of the examples shown in this thesis only the first 4 or 5 modes are considered.

When two or more flat elements interact, for example two circular plates separated by an air gap, they generate 2n fundamental modes (J_1) that resonate at the same frequency, where n is the number of elements, each of them with a specific nomenclature (J_1 antenna mode, J_1 transmission line mode, J_1' antenna mode, J_1' transmission line mode). As they are isolated elements, they need a feeding ports, for which there are two alternatives: capacitive excitation or inductive excitation, the capacitive form can be placed at the point where the currents are zero, while the inductive feed can be inserted where the currents are maximum.

Therefore, to know the location of the feeding point, a short circuit has to be placed between the two elements, this modification allows to generate a resonance at a lower frequency, since the length of the structure has been increased to double, degenerating not those of current and the two ends of the plates and a maximum in the short circuit, Therefore, the short circuit can be replaced by an inductive excitation, to improve the bandwidth can be used 2 power supply points as presented in the example of the 2 ellipses, the interesting thing about this is that it has been shown that not only one mode can generate a resonance, if not it turns out to be the combination of some.

On the other hand, circular and square rings have also been analyzed, taking into account the direction of the currents and their intensity, one or more power supply points can be inserted, making a combination between ports can force the excitation of certain modes and the exclusion of others. Using the balanced excitation (+1, +1) with 2 ports forces the excitation of the even modes, while using the differential excitation (+1, −1) will excite only the odd modes. For the purpose of this thesis the ideal has been to force the excitation of the odd modes, because it allows to generate a radiation pattern in broadside direction.

Once arbitrary 2D structures have been studied, their information and physical dimension can be taken advantage of to generate a resonance, for this these structures are folded on themselves until they reach the point where their ends come together, as the folding of the structure is performed, the current distribution will be modified. For example, in the fundamental mode, the null currents of the planar plate will no longer be at the edges of the structure when folded, these nulls have been shifted to the side walls, this shifted of the nulls allows to insert a feeding port inductively between the two edges of the structure, thus achieving a unidirectional radiation pattern.

As the height between the top layer and the bottom layer decreases, the characteristic angle tends to have a steep slope, in other words the bandwidth will be reduced, an alternative to improve the bandwidth is to slightly deform the edges that are between the feed point. Using this type of configuration a couple of prototypes have been fabricated, the measured and simulated results are similar allowing us to validate this design concept.

Subsequently, using the same waveguide, the study of the characteristic modes has been presented, in this case the distribution of currents on the surface of the waveguide and the resonances through the analysis of the characteristic angles, in addition a study of the modes that would be excited and their power contribution when the waveguides are illuminated for a plane wave has been shown. By analyzing the structure as a resonator of length $L/2$ in open circuit configuration at one end and short circuit at the other, it is possible to discriminate half of the current distribution on the surface of the structure, making the modes more capacitive than those generated in the waveguide.

Then, once the modes have been obtained in the structures and in the same way as for the planar plates, the waveguides can be excited capacitively or inductively. Two devices have been designed based on the circular and rectangular waveguide of length $L/2$ with open circuit at one end and open circuit at the other end. The structures have been fed with two capacitive elements, combining the ports has generated unidirectional radiation patterns and also with a large bandwidth, one of them has been fabricated and its results are close to those obtained in simulations.

Finally, in chapter 6, some devices have been designed using the concepts that have been shown throughout the development of the thesis. Although antennas have been designed as simple and isolated elements, it has also been necessary to design a device to feed a, array antennas and get multiple independent beams or called beamforming, therefore, it has been designed and manufactured a compact Butler matrix at 2.4 GHz.

Based on the concept of cavities, a very low profile antenna has been designed, the antenna consists of 4 semi-cavities with open circuits in the center and short circuits at the ends, each of the semi-cavities share the capacitive feed point that was located in the center, generating a wide bandwidth. Under this same criterion has been designed an antenna capable of working in two different frequencies and that can be integrated into a smart watch, the antenna consists of 4 semi-cavities, two resonating at one frequency and two at another, the isolation between the ports is less than -15dB.

Using the concepts of structures folded on themselves, a pair of antennas have been designed that work in the WIFI bands, because of their low profile they have been integrated into a tablet chassis. To achieve multiple beams, the prototype consists of 4 antennas resonating at 2.4 GHz and 4 antennas at 3.6 GHz.

Throughout the development of the thesis, structures with homogeneous surfaces have been analyzed, however, it has not been possible to study non-homogeneous surfaces, therefore, to complement the study we have analyzed a structure that has the shape of an airplane, through a mode analysis we have located the feeding points, and using a combination of ports we have generated radiation patterns in the broadside direction.

And finally, a meta surface of periodic characteristics has been analyzed, this antenna works as an absorber, its impedance values have been changed by resistive loads generating a maximum power transfer, i.e., the waves incident on this surface will not be reflected but consumed by the loads.

7.2 Conclusions

The general objective of the Thesis is to apply the Theory of Characteristic Modes for the design of antennas. The antennas, that will be based on planar or three-dimensional structures, should be broadband, with multiple simultaneous radiation modes and dual in polarization.

The specific objectives that were raised at the beginning of the thesis were:

- Analysis of three-dimensional structures with characteristic modes
- Multi-port structure feeding with orthogonal radiation patterns
- Design of antennas for applications in 5G systems, at the user level and MIMO multibeam base stations and in the WiFi bands and other innovative applications.

The objectives of the thesis have been fully met, using new analysis methodologies and proposing multiple innovative designs, with applications for the new communication standards.

The most relevant contributions of the thesis are the following:

1. The most relevant contribution includes the study of structures of different shapes interconnected with each other. Such as combinations of loops with circles, squares or triangles, shapes or semi-elliptic shapes with multiple feeding points and parallel or coplanar 3D structures.

2. Structures with multiple feed points have been shown to have relative bandwidth characteristics in excess of 100% in same cases, due to the combination of modes that compensate for electrical and magnetic energies.

3. The folded planar structures have been proven to maintain the current modes of the planar original structure and are well suited as antennas, due to the ease of feeding, their compact size and the integrated design of the ground plane and matching elements.

4. Low-profile, high-bandwidth 3D radiating elements designed from folded structures have been integrated into a compact base station structure with multiple independent beams.

5. Waveguides and cavities have been extensively studied in the literature. In this thesis we present for the first time in a unified way the radiation of open cavities and open guides from the characteristic modes analysis.

6. It has been verified that the characteristic modes of open canonical structures, calculated numerically by integral equation methods, have a direct correlation with the analytical modes TE_{mnl} and TM_{mnl} of closed cavities.

7. Multi-fed cavity antennas have been designed in rectangular and cylindrical geometries, obtaining adaptations in large bandwidths.

8. Newly developed concepts have enabled the design of antennas in different frequency bands and applications, such as airplane radiation, smart watch, absorbing metasurfaces or multiple coupled resonators with exceptional bandwidths.

As a general conclusion, a design methodology based on the analysis of characteristic modes in complex 3D structures, with efficient coupling to multiple input ports and optimized radiation parameters, has been employed.

7.3 Future work

The Ph.D. Thesis has opened up new perspectives for antenna design, but some issues have been left open and are considered to be of strategic importance for future research.

The topics to be investigated are as follows

- Analysis and design of antennas including dielectrics using characteristic mode theory. This study is necessary since most antennas include dielectric substrates.
- Scalar formulation of potentials and calculation of currents from electric fields normal to metallic surfaces. This study is justified by the information obtained from the modal near fields and by the simplification of the vector sum of currents.
- Proposal of new design parameters, such as stability of patterns, correlation of modal fields (ECC), decoupling of modes, etc.
- Antenna design for new 5G systems in the millimeter frequency bands using characteristic modes.

References

[1] COMSOL, "COMSOL Multiphysics," Available at www.comsol.com, 2019.

[2] D. M. Pozar, *Microwave engineering*. John Wiley & Sons, 2009.

[3] S. Shukla, V. Khare, S. Garg, and P. Sharma, "Comparative study of 1G, 2G, 3G and 4G," *J. Eng. Comput. Appl. Sci*, vol. 2, no. 4, pp. 55–63, 2013.

[4] C. Yan, B. Wang, Y. Han *et al.*, "Why time reversal for future 5G wireless," *IEEE Signal Processing Magazine*, vol. 33, no. 2, pp. 17–26, 2016.

[5] N. Panwar, S. Sharma, and A. K. Singh, "A survey on 5G: The next generation of mobile communication," *Physical Communication*, vol. 18, pp. 64–84, 2016.

[6] I. Oppermann, M. Hämäläinen, and J. Iinatti, *UWB: theory and applications*. John Wiley & Sons, 2005.

[7] P. S. Hall and Y. Hao, *Antennas and propagation for body-centric wireless communications*. Artech house, 2012.

[8] D. Porcino and W. Hirt, "Ultra-wideband radio technology: potential and challenges ahead," *IEEE communications magazine*, vol. 41, no. 7, pp. 66–74, 2003.

[9] R. Garbacz, "A generalized expansion for radiated and scattered fields," Ph.D. dissertation, The Ohio State University, 1968.

[10] R. Garbacz and R. Turpin, "A generalized expansion for radiated and scattered fields," *IEEE Transactions on Antennas and Propagation*, vol. 19, no. 3, pp. 348–358, 1971.

[11] R. Harrington and J. Mautz, "Theory of characteristic modes for conducting bodies," *IEEE Transactions on Antennas and Propagation*, vol. 19, no. 5, pp. 622–628, 1971.

[12] ——, "Computation of characteristic modes for conducting bodies," *IEEE Transactions on Antennas and Propagation*, vol. 19, no. 5, pp. 629–639, 1971.

[13] R. Harrington, *Field computation by moment methods*. Wiley-IEEE Press, 1993.

[14] R. Harrington, J. Mautz, and Y. Chang, "Characteristic modes for dielectric and magnetic bodies," *IEEE Transactions on Antennas and Propagation*, vol. 20, no. 2, pp. 194–198, 1972.

[15] Y. Chang and R. Harrington, "A surface formulation for characteristic modes of material bodies," *IEEE transactions on antennas and propagation*, vol. 25, no. 6, pp. 789–795, 1977.

[16] M. Cabedo-Fabres, A. Valero-Nogueira, and M. Ferrando-Bataller, "Systematic study of elliptical loop antennas using characteristic modes," in *IEEE Antennas and Propagation Society International Symposium (IEEE Cat. No. 02CH37313)*, vol. 1. IEEE, 2002, pp. 156–159.

[17] M. Cabedo-Fabres, E. Antonio-Daviu, M. Ferrando-Bataller, and A. Valero-Nogueira, "On the use of characteristic modes to describe patch antenna performance," in *IEEE Antennas and Propagation Society International Symposium. Digest. Held in conjunction with: USNC/CNC/URSI North American Radio Sci. Meeting (Cat. No. 03CH37450)*, vol. 2. IEEE, 2003, pp. 712–715.

[18] M. Cabedo-Fabres, E. Antonino-Daviu, A. Valero-Nogueira, and M. Ferrando-Bataller, "Analysis of wide band planar monopole antennas using characteristic modes," in *IEEE Antennas and Propagation Society International Symposium. Digest. Held in conjunction with: USNC/CNC/URSI North American Radio Sci. Meeting (Cat. No. 03CH37450)*, vol. 3. IEEE, 2003, pp. 733–736.

[19] M. Cabedo-Fabres, A. Valero-Nogueira, J. Herranz-Herruzo, and M. Ferrando-Bataller, "A discussion on the characteristic mode theory limitations and its improvement for the effective modeling of antennas and arrays," in *IEEE Antennas and Propagation Society Symposium, 2004.*, vol. 1. IEEE, 2004, pp. 121–124.

[20] E. Antonino-Daviu, M. Cabedo-Fabres, M. Ferrando-Bataller, and A. Valero-Nogueira, "A discussion on the feed configuration of planar monopole antennas to obtain ultra wide band performance," in *IEEE Antennas and Propagation Society Symposium, 2004.*, vol. 2. IEEE, 2004, pp. 1867–1870.

[21] E. Antonino-Daviu, M. Cabedo-Fabres, M. Ferrando-Bataller, A. Valero-Nogueira, and M. Martinez-Vazquez, "Novel antenna for mobile terminals based on the chassis-antenna coupling," in *2005 IEEE Antennas and Propagation Society International Symposium*, vol. 1. IEEE, 2005, pp. 503–506.

[22] M. Cabedo-Fabres, E. Antonino-Daviu, A. Valero-Nogueira, and M. Ferrando-Bataller, "Wideband radiating ground plane with notches," in *2005 IEEE Antennas and Propagation Society International Symposium*, vol. 2. IEEE, 2005, pp. 560–563.

[23] E. Antonino-Daviu, M. Cabedo-Fabres, M. Gallo, M. Ferrando-Bataller, and M. Bozzetti, "Design of a multimode MIMO antenna using characteristic modes," in *2009 3rd European Conference on Antennas and Propagation*. IEEE, 2009, pp. 1840–1844.

[24] E. Antonino-Daviu, M. Fabres, M. Ferrando-Bataller, and V. M. R. Peñarrocha, "Modal analysis and design of band-notched UWB planar monopole antennas," *IEEE Transactions on Antennas and Propagation*, vol. 58, no. 5, pp. 1457–1467, 2010.

[25] M. Cabedo-Fabres, E. Antonino-Daviu, A. Valero-Nogueira, and M. F. Bataller, "The theory of characteristic modes revisited: A contribution to the design of antennas for modern applications," *IEEE Antennas and Propagation Magazine*, vol. 49, no. 5, pp. 52–68, 2007.

[26] M. Cabedo Fabres, "Systematic design of antennas using the theory of characteristic modes," Ph.D. dissertation, Universitat Politècnica de València, 2008.

[27] E. Antonino Daviu, "Analysis and design of antennas for wireless communications using modal methods," Ph.D. dissertation, Universitat Politècnica de València, 2008.

[28] E. Safin, "Modal analysis methods for small antenna design," Ph.D. dissertation, Kiel University, 2016.

[29] B. D. Raines, "Systematic design of multiple antenna systems using characteristic modes," Ph.D. dissertation, The Ohio State University, 2011.

[30] J. L. Ethier, "Antenna shape synthesis using characteristic mode concepts," Ph.D. dissertation, Université d'Ottawa/University of Ottawa, 2012.

[31] L. Fenghan, "Study of microwave metasurface antennas using characteristic mode analysis," 2018.

[32] D. A. Santillán Haro, "Diseño de lentes metálicas usando la teoría de modos característicos." Ph.D. dissertation, Universitat Politècnica de València, 2020.

[33] V. Prakash, , and R. Mittra, "Characteristic basis function method: A new technique for efficient solution of method of moments matrix equations," *Microwave and Optical Technology Letters*, vol. 36, no. 2, pp. 95–100, 2003.

[34] B. K. Lau, D. Manteuffel, H. Arai, and S. V. Hum, "Guest editorial theory and applications of characteristic modes," *IEEE Transactions on Antennas and Propagation*, vol. 64, no. 7, pp. 2590–2594, 2016.

[35] E. Safin and D. Manteuffel, "Manipulation of characteristic wave modes by impedance loading," *IEEE Transactions on Antennas and Propagation*, vol. 63, no. 4, pp. 1756–1764, 2015.

[36] K. R. Schab, J. M. Outwater, M. W. Young, and J. T. Bernhard, "Eigenvalue crossing avoidance in characteristic modes," *IEEE Transactions on Antennas and Propagation*, vol. 64, no. 7, pp. 2617–2627, 2016.

[37] M. Capek, P. Hazdra, P. Hamouz, and J. Eichler, "A method for tracking characteristic numbers and vectors," *Progress In Electromagnetics Research*, vol. 33, pp. 115–134, 2011.

[38] J. G. Van Bladel, *Electromagnetic fields*. John Wiley & Sons, 2007, vol. 19.

[39] E. Safin and D. Manteuffel, "Advanced eigenvalue tracking of characteristic modes," *IEEE Transactions on Antennas and Propagation*, vol. 64, no. 7, pp. 2628–2636, 2016.

[40] L. Akrou and H. J. da Silva, "Enhanced modal tracking for characteristic modes," *IEEE Transactions on Antennas and Propagation*, vol. 67, no. 1, pp. 356–360, 2018.

[41] L. Chettri and R. Bera, "A comprehensive survey on internet of things (iot) toward 5g wireless systems," *IEEE Internet of Things Journal*, vol. 7, no. 1, pp. 16–32, 2019.

[42] S. Kumar, A. S. Dixit, R. R. Malekar, H. D. Raut, and L. K. Shevada, "Fifth generation antennas: a comprehensive review of design and performance enhancement techniques," *IEEE Access*, vol. 8, pp. 163 568–163 593, 2020.

[43] A. Bekasiewicz and S. Koziel, "Compact UWB monopole antenna for internet of things applications," *Electronics Letters*, vol. 52, no. 7, pp. 492–494, 2016.

[44] W.-C. Liu, C.-M. Wu, and Y.-J. Tseng, "Parasitically loaded CPW-fed monopole antenna for broadband operation," *IEEE Transactions on Antennas and Propagation*, vol. 59, no. 6, pp. 2415–2419, 2011.

[45] Z. Chen *et al.*, "Wideband multilayered microstrip antennas fed by coplanar waveguide-loop with and without via combinations," *IET microwaves, antennas & propagation*, vol. 3, no. 1, pp. 85–91, 2009.

[46] C. A. Balanis, *Antenna theory: analysis and design*. John wiley & sons, 2016.

[47] W.-C. Liu, "Design of a multiband CPW-fed monopole antenna using a particle swarm optimization approach," *IEEE Transactions on Antennas and Propagation*, vol. 53, no. 10, pp. 3273–3279, 2005.

[48] N. M. Mohamed-Hicho, E. Antonino-Daviu, M. Cabedo-Fabrés, and M. Ferrando-Bataller, "A novel low-profile high-gain UHF antenna using high-impedance surfaces," *IEEE Antennas and Wireless Propagation Letters*, vol. 14, pp. 1014–1017, 2015.

[49] M. I. Hussein, A. Hakam, M. Ouda, and R. M. Shubair, "Compact low-profile planar elliptical antenna for UWB applications," in *2016 10th European Conference on Antennas and Propagation (EuCAP)*. IEEE, 2016, pp. 1–2.

[50] H. Ullah and F. A. Tahir, "Broadband planar antenna array for future 5g communication standards," *IET Microwaves, Antennas & Propagation*, vol. 13, no. 15, pp. 2661–2668, 2019.

[51] L. Zhao, Z.-M. Chen, and J. Wang, "A wideband dual-polarized omnidirectional antenna for 5g/wlan," *IEEE Access*, vol. 7, pp. 14 266–14 272, 2019.

[52] E. Antonino-Daviu, M. Cabedo-Fabrés, M. Sonkki, N. M. Mohamed-Hicho, and M. Ferrando-Bataller, "Design guidelines for the excitation of characteristic modes in slotted planar structures," *IEEE Transactions on Antennas and Propagation*, vol. 64, no. 12, pp. 5020–5029, 2016.

[53] E. Antonino-Daviu, M. Cabedo-Fabres, M. Ferrando-Bataller, and A. Valero-Nogueira, "Wideband double-fed planar monopole antennas," *Electronics Letters*, vol. 39, no. 23, p. 1635, 2003.

[54] K. Saurav, D. Sarkar, A. Singh, and K. V. Srivastava, "Multiband circularly polarized cavity-backed crossed dipole antenna," *IEEE Transactions on Antennas and Propagation*, vol. 63, no. 10, pp. 4286–4296, 2015.

[55] E. G. Tianang, M. A. Elmansouri, and D. S. Filipovic, "Cavity-backed vivaldi array antenna," in *2016 10th European Conference on Antennas and Propagation (EuCAP)*. IEEE, 2016, pp. 1–4.

[56] A. S. Dixit and S. Kumar, "A miniaturized antipodal vivaldi antenna for 5g communication applications," in *2020 7th International Conference on Signal Processing and Integrated Networks (SPIN)*. IEEE, 2020, pp. 800–803.

[57] T. Goel and A. Patnaik, "Novel broadband antennas for future mobile communications," *IEEE Transactions on antennas and propagation*, vol. 66, no. 5, pp. 2299–2308, 2018.

[58] A. S. Dixit and S. Kumar, "A survey of performance enhancement techniques of antipodal vivaldi antenna," *IEEE Access*, vol. 8, pp. 45 774–45 796, 2020.

[59] N. K. Darimireddy, R. R. Reddy, and A. M. Prasad, "A miniaturized hexagonal-triangular fractal antenna for wide-band applications [antenna applications corner]," *IEEE Antennas and Propagation Magazine*, vol. 60, no. 2, pp. 104–110, 2018.

[60] H. Ullah and F. A. Tahir, "A novel snowflake fractal antenna for dual-beam applications in 28 ghz band," *IEEE Access*, vol. 8, pp. 19 873–19 879, 2020.

[61] D. Wen, Y. Hao, H. Wang, and H. Zhou, "Design of a wideband antenna with stable omnidirectional radiation pattern using the theory of characteristic modes," *IEEE Transactions on Antennas and Propagation*, vol. 65, no. 5, pp. 2671–2676, 2017.

[62] Y. Luo, Z. N. Chen, and K. Ma, "Enhanced bandwidth and directivity of a dual-mode compressed high-order mode stub-loaded dipole using characteristic mode analysis," *IEEE Transactions on Antennas and Propagation*, vol. 67, no. 3, pp. 1922–1925, 2018.

[63] R. Li, D. McNamara, and G. Wei, "Characteristic modes evaluation for metallic small antennas with unidirectional pattern," *IEEE Antennas and Wireless Propagation Letters*, vol. 16, pp. 3026–3029, 2017.

[64] L. Zhang, Y. Sun, Y. He, S.-W. Wong, C. Mao, L. Ge, and S. Gao, "A quad-polarization reconfigurable antenna with suppressed cross polarization based on characteristic mode theory," *IEEE Transactions on Antennas and Propagation*, 2020.

[65] Z. Zhang, X. Fu, and S. Cao, "Design of a vertically polarized patch antenna with switchable near-endfire beam using characteristic mode analysis," *IEEE Antennas and Wireless Propagation Letters*, vol. 19, no. 7, pp. 1157–1161, 2020.

[66] Q. Li and T.-Y. Shih, "Characteristic-mode-based design of planar in-band full-duplex antennas," *IEEE Open Journal of Antennas and Propagation*, vol. 1, pp. 329–338, 2020.

[67] Y. Shi, Z. K. Meng, W. Y. Wei, W. Zheng, and L. Li, "Characteristic mode cancellation method and its application for antenna rcs reduction," *IEEE Antennas and Wireless Propagation Letters*, vol. 18, no. 9, pp. 1784–1788, 2019.

[68] N. M. Mohamed-Hicho, E. Antonino-Daviu, M. Cabedo-Fabres, and M. Ferrando-Bataller, "Designing slot antennas in finite platforms using characteristic modes," *IEEE Access*, vol. 6, pp. 41 346–41 355, 2018.

[69] J.-F. Lin and L. Zhu, "Low-profile high-directivity circularly-polarized differential-fed patch antenna with characteristic modes analysis," *IEEE Transactions on Antennas and Propagation*, 2020.

[70] K. Li, Y. Shi, H. Shen, and L. Li, "A characteristic-mode-based polarization-reconfigurable antenna and its array," *IEEE Access*, vol. 6, pp. 64 587–64 595, 2018.

[71] C. Wang, Y. Chen, and S. Yang, "Bandwidth enhancement of a dual-polarized slot antenna using characteristic modes," *IEEE Antennas and Wireless Propagation Letters*, vol. 17, no. 6, pp. 988–992, 2018.

[72] J. Zhao, Y. Chen, and S. Yang, "In-band radar cross-section reduction of slot antenna using characteristic modes," *IEEE Antennas and Wireless Propagation Letters*, vol. 17, no. 7, pp. 1166–1170, 2018.

[73] N. L. Johannsen, N. Peitzmeier, P. A. Hoeher, and D. Manteuffel, "On the feasibility of multi-mode antennas in uwb and iot applications below 10 ghz," *IEEE Communications Magazine*, vol. 58, no. 3, pp. 69–75, 2020.

[74] D. Manteuffel and R. Martens, "Compact multimode multielement antenna for indoor UWB massive MIMO," *IEEE Transactions on Antennas and Propagation*, vol. 64, no. 7, pp. 2689–2697, 2016.

[75] N. Peitzmeier and D. Manteuffel, "Upper bounds and design guidelines for realizing uncorrelated ports on multimode antennas based on symmetry analysis of characteristic modes," *IEEE Transactions on Antennas and Propagation*, vol. 67, no. 6, pp. 3902–3914, 2019.

[76] K. Li and Y. Shi, "A pattern reconfigurable mimo antenna design using characteristic modes," *IEEE Access*, vol. 6, pp. 43 526–43 534, 2018.

[77] F. H. Lin and Z. N. Chen, "Low-profile wideband metasurface antennas using characteristic mode analysis," *IEEE Transactions on Antennas and Propagation*, vol. 65, no. 4, pp. 1706–1713, 2017.

[78] A. A. Salih, Z. N. Chen, and K. Mouthaan, "Characteristic mode analysis and metasurface-based suppression of higher order modes of a 2×2 closely spaced phased array," *IEEE Transactions on Antennas and Propagation*, vol. 65, no. 3, pp. 1141–1150, 2017.

[79] T. Li and Z. N. Chen, "Metasurface-based shared-aperture 5G $S-/K$-band antenna using characteristic mode analysis," *IEEE Transactions on Antennas and Propagation*, vol. 66, no. 12, pp. 6742–6750, 2018.

[80] X. Gao, G. W. Tian, Z. Shou, and S. M. Li, "A low-profile broadband circularly polarized patch antenna based on characteristic mode analysis," *IEEE Antennas and Wireless Propagation Letters*, 2020.

[81] G. Gao, R.-F. Zhang, W.-F. Geng, H.-J. Meng, and B. Hu, "Characteristic mode analysis of a nonuniform metasurface antenna for wearable applications," *IEEE Antennas and Wireless Propagation Letters*, vol. 19, no. 8, pp. 1355–1359, 2020.

[82] X. Yang, Y. Liu, and S.-X. Gong, "Design of a wideband omnidirectional antenna with characteristic mode analysis," *IEEE Antennas and Wireless Propagation Letters*, vol. 17, no. 6, pp. 993–997, 2018.

[83] F. H. Lin and Z. N. Chen, "Truncated impedance sheet model for low-profile broadband nonresonant-cell metasurface antennas using characteristic mode analysis," *IEEE Transactions on Antennas and Propagation*, vol. 66, no. 10, pp. 5043–5051, 2018.

[84] ——, "A method of suppressing higher order modes for improving radiation performance of metasurface multiport antennas using characteristic mode analysis," *IEEE Transactions on Antennas and Propagation*, vol. 66, no. 4, pp. 1894–1902, 2018.

[85] T. Li and Z. N. Chen, "A dual-band metasurface antenna using characteristic mode analysis," *IEEE Transactions on Antennas and Propagation*, vol. 66, no. 10, pp. 5620–5624, 2018.

[86] Z. Liang, J. Ouyang, F. Yang, and L. Zhou, "Design of license plate rfid tag antenna using characteristic mode pattern synthesis," *IEEE Transactions on Antennas and Propagation*, vol. 65, no. 10, pp. 4964–4970, 2017.

[87] R. Rezaiesarlak and M. Manteghi, "Design of chipless rfid tags based on characteristic mode theory (cmt)," *IEEE Transactions on Antennas and Propagation*, vol. 63, no. 2, pp. 711–718, 2014.

[88] A. Sharif, J. Ouyang, F. Yang, H. T. Chattha, M. A. Imran, A. Alomainy, and Q. H. Abbasi, "Low-cost, inkjet-printed UHF RFID tag based system for internet of things applications using characteristic modes," *IEEE Internet of Things Journal*, 2019.

[89] J. Butler, "Beam-forming matrix simplifies design of electronically scanned antenna," *Electron. Design*, vol. 9, pp. 170–173, 1961.

[90] A. K. Vallappil, M. K. A. Rahim, B. A. Khawaja, N. A. Murad, and M. M. Gajibo, "Butler matrix based beamforming networks for phased array antenna systems: A comprehensive review and future directions for 5g applications," *IEEE Access*, 2020.

[91] S. Weiss and R. Dahlstrom, "Rotman lens development at the army research lab," in *2006 IEEE Aerospace Conference*. IEEE, 2006, pp. 7–pp.

[92] Y. Wang, M. Bialkowski, and A. Abbosh, "Double microstrip-slot transitions for broadband 90° microstrip phase shifters," *IEEE microwave and wireless components letters*, vol. 22, no. 2, pp. 58–60, 2012.

[93] J. Wang, Z. Shen, and L. Zhao, "UWB 90° phase shifter based on broadside coupler and T-shaped stub," *Electronics Letters*, vol. 52, no. 25, pp. 2048–2050, 2016.

[94] A. M. Peñarrubia, M. F. Bataller, M. C. Fabrés, and E. A. Daviu, "Uwb multi-beam antenna array for the microwave band," in *2016 10th European Conference on Antennas and Propagation (EuCAP)*. IEEE, 2016, pp. 1–5.

[95] L. M. Abdelghani, T. A. Denidni, and M. Nedil, "Ultra-broadband 4× 4 compact butler matrix using multilayer directional couplers and phase shifters," in *2012 IEEE/MTT-S International Microwave Symposium Digest*. IEEE, 2012, pp. 1–3.

[96] L. Abdelghani, T. A. Denidni, and M. Nedil, "Design of a new ultra-wideband 4× 4 butler matrix for beamforming antenna applications," in *Proceedings of the 2012 IEEE International Symposium on Antennas and Propagation*. IEEE, 2012, pp. 1–2.

[97] M. E. Bialkowski, F.-C. E. Tsai, Y.-C. Su, and K.-H. Cheng, "Design of fully integrated 4x4 and 8x8 butler matrices in microstrip/slot technology for ultra wideband smart antennas," in *2008 IEEE Antennas and Propagation Society International Symposium*. IEEE, 2008, pp. 1–4.

[98] A. Moscoso-Martir, I. Molina-Fernandez, and A. Ortega-Monux, "Wideband slot-coupled butler matrix," *IEEE Microwave and Wireless Components Letters*, vol. 24, no. 12, pp. 848–850, 2014.

[99] R. L. Sturdivant and E. K. Chong, "Systems engineering of a terabit elliptic orbit satellite and phased array ground station for IoT connectivity and consumer internet access," *IEEE Access*, vol. 4, pp. 9941–9957, 2016.

[100] R. C. Williams and S. Bissessar, "Strengthening cooperation between telecommunications operators and national disaster offices in caribbean countries," 2017.

[101] T. Bernabeu Jiménez, "Contribution to the physical interpretation of characteristic mode resonances. application to dielectric resonator antennas," Ph.D. dissertation, Universitat Politècnica de València, 2017.

[102] W. C. Gibson, *The method of moments in electromagnetics*. Chapman and Hall/CRC, 2007.

[103] T. Bernabeu-Jimenez, A. Valero-Nogueira, F. Vico-Bondia, and A. A. Kishk, "On the contribution to the field of the nonphysical characteristic modes in infinite dielectric circular cylinders under normal excitation," *IEEE Transactions on Antennas and Propagation*, vol. 66, no. 1, pp. 505–510, 2017.

[104] Z. Miers, "Systematic antenna design using the theory of characteristic modes," Ph.D. dissertation, Lund University, 2016.

[105] E. A. Elghannai, "Novel method to control antenna currents based on theory of characteristic modes," Ph.D. dissertation, The Ohio State University, 2016.

[106] N. L. Bohannon, "Synthesis process using characteristic modes for multiple in situ antennas for system radiation requirements," Ph.D. dissertation, University of Illinois at Urbana-Champaign, 2016.

[107] B. Yang, "A modal approach to compact MIMO antenna design," Ph.D. dissertation, North Carolina State University, 2017.

[108] R. F. Harrington, "Fields, time-harmonic electromagnetic," *IEEE, press*, 2001.

[109] ——, "Matrix methods for field problems," *Proceedings of the IEEE*, vol. 55, no. 2, pp. 136–149, 1967.

[110] R. Garbacz, "Modal expansions for resonance scattering phenomena," *Proceedings of the IEEE*, vol. 53, no. 8, pp. 856–864, 1965.

[111] R. Harrington, "Origin and development of the method of moments for field computation," *IEEE Antennas and Propagation Magazine*, vol. 32, no. 3, pp. 31–35, 1990.

[112] ANSYS, "ANSYS," Available at www.mscsoftware.com, 2019.

[113] M. Software, "PATRAN," Available at www.ansys.com, 2019.

[114] A. HyperWorks, "Altair hyperworks," Available at www.altairhyperworks.com, 2019.

[115] D. Systemes, "CST computer simulation technology," Available at www.cst.com, 2019.

[116] Y. Chen and C.-F. Wang, *Characteristic modes: Theory and applications in antenna engineering*. John Wiley & Sons, 2015.

[117] S. Rao, D. Wilton, and A. Glisson, "Electromagnetic scattering by surfaces of arbitrary shape," *IEEE Transactions on antennas and propagation*, vol. 30, no. 3, pp. 409–418, 1982.

[118] K. M. Abadir and J. R. Magnus, *Matrix algebra*. Cambridge University Press, 2005, vol. 1.

[119] J. Ethier, E. Lanoue, and D. McNamara, "MIMO handheld antenna design approach using characteristic mode concepts," *Microwave and Optical Technology Letters*, vol. 50, no. 7, pp. 1724–1727, 2008.

[120] W. Geyi, P. Jarmuszewski, and Y. Qi, "The foster reactance theorem for antennas and radiation Q," *IEEE Transactions on Antennas and Propagation*, vol. 48, no. 3, pp. 401–408, 2000.

[121] S. R. Best, "The foster reactance theorem and quality factor for antennas," *IEEE Antennas and Wireless Propagation Letters*, vol. 3, no. 1, pp. 306–309, 2004.

[122] R. Harrington and J. Mautz, "Control of radar scattering by reactive loading," *IEEE Transactions on Antennas and Propagation*, vol. 20, no. 4, pp. 446–454, 1972.

[123] E. Newman, "Small antenna location synthesis using characteristic modes," *IEEE Transactions on Antennas and Propagation*, vol. 27, no. 4, pp. 530–531, 1979.

[124] A. Yee and R. Garbacz, "Self-and mutual-admittances of wire antennas in terms of characteristic modes," *IEEE Transactions on Antennas and Propagation*, vol. 21, no. 6, pp. 868–871, 1973.

[125] R. Martens, E. Safin, and D. Manteuffel, "Inductive and capacitive excitation of the characteristic modes of small terminals," in *2011 Loughborough Antennas & Propagation Conference*. IEEE, 2011, pp. 1–4.

[126] J. Holopainen, R. Valkonen, O. Kivekas, J. Ilvonen, and P. Vainikainen, "Broadband equivalent circuit model for capacitive coupling element–based mobile terminal antenna," *IEEE Antennas and Wireless Propagation Letters*, vol. 9, pp. 716–719, 2010.

[127] Q. Zhang, R. Ma, W. Su, and Y. Gao, "Design of a multimode UWB antenna using characteristic mode analysis," *IEEE Transactions on Antennas and Propagation*, vol. 66, no. 7, pp. 3712–3717, 2018.

[128] W. Li, Y. Liu, J. Li, L. Ye, and Q. H. Liu, "Modal proportion analysis in antenna characteristic mode theory," *International Journal of Antennas and Propagation*, vol. 2019, 2019.

[129] W. R. Eisenstadt, *Microwave differential circuit design using mixed mode s-parameters*. Artech House, 2006.

[130] Q. Xue, S. W. Liao, and J. H. Xu, "A differentially-driven dual-polarized magneto-electric dipole antenna," *IEEE Transactions on antennas and propagation*, vol. 61, no. 1, pp. 425–430, 2012.

[131] Z.-h. Tu, W.-A. Li, and Q.-X. Chu, "Single-layer differential CPW-fed notch-band tapered-slot UWB antenna," *IEEE Antennas and Wireless Propagation Letters*, vol. 13, pp. 1296–1299, 2014.

[132] R. N. Simons, *Coplanar waveguide circuits, components, and systems*. John Wiley & Sons, 2004, vol. 165.

[133] A. Smida, A. Iqbal, A. J. Alazemi, M. I. Waly, R. Ghayoula, and S. Kim, "Wideband wearable antenna for biomedical telemetry applications," *IEEE Access*, vol. 8, pp. 15 687–15 694, 2020.

[134] A. S. Alqadami, N. Nguyen-Trong, B. Mohammed, A. E. Stancombe, M. T. Heitzmann, and A. Abbosh, "Compact unidirectional conformal antenna based on flexible high-permittivity custom-made substrate for

wearable wideband electromagnetic head imaging system," *IEEE Transactions on Antennas and Propagation*, vol. 68, no. 1, pp. 183–194, 2019.

[135] O. M. Sanusi, F. A. Ghaffar, A. Shamim, M. Vaseem, Y. Wang, and L. Roy, "Development of a 2.45 ghz antenna for flexible compact radiation dosimeter tags," *IEEE Transactions on Antennas and Propagation*, vol. 67, no. 8, pp. 5063–5072, 2019.

[136] A. Sharif, J. Guo, J. Ouyang, S. Sun, K. Arshad, M. A. Imran, and Q. H. Abbasi, "Compact base station antenna based on image theory for UWB/5G RTLS embraced smart parking of driverless cars," *IEEE Access*, vol. 7, pp. 180 898–180 909, 2019.

[137] H.-J. Kim, H. Hirayama, S. Kim, K. J. Han, R. Zhang, and J.-W. Choi, "Review of near-field wireless power and communication for biomedical applications," *IEEE Access*, vol. 5, pp. 21 264–21 285, 2017.

[138] R. Scheeler, E. F. Kuester, and Z. Popović, "Sensing depth of microwave radiation for internal body temperature measurement," *IEEE Transactions on antennas and propagation*, vol. 62, no. 3, pp. 1293–1303, 2013.

[139] B. Kibret, A. K. Teshome, and D. T. Lai, "Analysis of the human body as an antenna for wireless implant communication," *IEEE Transactions on antennas and propagation*, vol. 64, no. 4, pp. 1466–1476, 2016.

[140] H. Xue, H. Liu, Q. Shao, Q. Feng, and L. Li, "Double-deflection vortex beam generation using a single elliptical patch with the theory of characteristic modes," *Optics express*, vol. 28, no. 8, pp. 12 322–12 330, 2020.

[141] C. R. Penafiel-Ojeda, M. Cabedo-Fabrés, E. Antonino-Daviu, and M. Ferrando-Bataller, "Compact antenna with unidirectional radiation patterns," 2018.

[142] Z. Mahlaoui, E. Antonino-Daviu, A. Latif, M. Ferrando-Bataller, and C. R. Peńafiel-Ojeda, "Frequency reconfigurable patch antenna using pin diodes with directive and fixed radiation pattern," in *2018 International Conference on Selected Topics in Mobile and Wireless Networking (MoWNeT)*. IEEE, 2018, pp. 1–3.

[143] R. E. Collin, *Foundations for microwave engineering*. John Wiley & Sons, 2007.

[144] C. Lee, S. Lee, and S. Chuang, "Plot of modal field distribution in rectangular and circular waveguides," *IEEE transactions on microwave theory and techniques*, vol. 33, no. 3, pp. 271–274, 1985.

[145] K. Zhang, D. Li, K. Chang, K. Zhang, and D. Li, *Electromagnetic theory for microwaves and optoelectronics*. Springer, 1998.

[146] M. Capek, P. Hazdra, M. Masek, and V. Losenicky, "Analytical representation of characteristic mode decomposition," *IEEE Transactions on Antennas and Propagation*, vol. 65, no. 2, pp. 713–720, 2016.

[147] E. Merkley, B. Jackson, C. Saavedra, and Y. Antar, "A compact cavity-backed monopole antenna for UWB applications," in *2017 IEEE International Symposium on Antennas and Propagation & USNC/URSI National Radio Science Meeting*. IEEE, 2017, pp. 495–496.

[148] S.-W. Qu, C.-H. Chan, and Q. Xue, "Ultrawideband composite cavity-backed folded sectorial bowtie antenna with stable pattern and high gain," *IEEE transactions on antennas and propagation*, vol. 57, no. 8, pp. 2478–2483, 2009.

[149] H. Lee and B. Lee, "Compact broadband dual-polarized antenna for indoor MIMO wireless communication systems," *IEEE Transactions on Antennas and Propagation*, vol. 64, no. 2, pp. 766–770, 2015.

[150] R. Martens and D. Manteuffel, "Systematic design method of a mobile multiple antenna system using the theory of characteristic modes," *IET Microwaves, Antennas & Propagation*, vol. 8, no. 12, pp. 887–893, 2014.

[151] M. E. Bialkowski and Y. Wang, "Wideband microstrip 180° hybrid utilizing ground slots," *IEEE microwave and wireless components letters*, vol. 20, no. 9, pp. 495–497, 2010.

[152] Y. Abdalla and H. Hammad, "Ultra-wideband compact slot-coupled 180 hybrid based on ultra-wideband wilkinson power divider," in *2014 44th European Microwave Conference*. IEEE, 2014, pp. 231–234.

[153] C. R. Peñafiel, L. F. Carrera, D. V. Navarro, M. Baquero, and M. Ferrando-Bataller, "Beamforming networks for antenna array, useful in wifi applications," *NOVASINERGIA, ISSN 2631-2654*, vol. 1, no. 1, pp. 59–66, 2018.

[154] Y. T. Lo and S. Lee, *Antenna Handbook: theory, applications, and design*. Springer Science & Business Media, 2013.

[155] R. C. Hansen, *Phased array antennas*. John Wiley & Sons, 2009, vol. 213.

[156] L. Josefsson and P. Persson, *Conformal array antenna theory and design*. John wiley & sons, 2006, vol. 29.

[157] P. Aghabeyki, G. Moradi, and R. S. Shirazi, "Low-profile ring slot siw antenna based on higher-order cylindrical cavity modes," *IET Microwaves, Antennas & Propagation*, vol. 14, no. 14, pp. 1779–1785, 2020.

[158] T. Y. Yang, W. Hong, and Y. Zhang, "Wideband millimeter-wave substrate integrated waveguide cavity-backed rectangular patch antenna," *IEEE Antennas and Wireless Propagation Letters*, vol. 13, pp. 205–208, 2014.

[159] W. Abdel-Wahab, H. Al-Saedi, S. Safavi-Naeini, and Y. Wang, "SIW-integrated patch antenna backed air-filled cavity for 5G MMW appilcations," in *2016 IEEE International Symposium on Antennas and Propagation (APSURSI)*. IEEE, 2016, pp. 1233–1234.

[160] C. R. Peñafiel-Ojeda, M. Cabedo-Fabrés, E. Antonino-Daviu, and M. Ferrando-Bataller, "Air-filled substrate integrate waveguide antenna analyzed with theory of characteristic modes," in *2019 13th European Conference on Antennas and Propagation (EuCAP)*. IEEE, 2019, pp. 1–5.

[161] C.-M. Liu, S. Xiao, Z. Zhang, and J. Feng, "Low profile SIW slot antenna with wide beam-width radiation pattern," *Electronics Letters*, vol. 54, no. 3, pp. 116–118, 2017.

[162] S. X. Ta and I. Park, "Crossed dipole loaded with magneto-electric dipole for wideband and wide-beam circularly polarized radiation," *IEEE Antennas and Wireless Propagation Letters*, vol. 14, pp. 358–361, 2014.

[163] D. Wen, Y. Hao, M. O. Munoz, H. Wang, and H. Zhou, "A compact and low-profile MIMO antenna using a miniature circular high-impedance surface for wearable applications," *IEEE Transactions on Antennas and Propagation*, vol. 66, no. 1, pp. 96–104, 2017.

[164] L. J. Chu, "Physical limitations of omni-directional antennas," *Journal of applied physics*, vol. 19, no. 12, pp. 1163–1175, 1948.

[165] J. S. McLean, "A re-examination of the fundamental limits on the radiation Q of electrically small antennas," *IEEE Transactions on antennas and propagation*, vol. 44, no. 5, p. 672, 1996.

[166] W. Hong, "Solving the 5G mobile antenna puzzle: Assessing future directions for the 5G mobile antenna paradigm shift," *IEEE Microwave Magazine*, vol. 18, no. 7, pp. 86–102, 2017.

[167] E. Antonino-Daviu, M. Cabedo-Fabres, M. Ferrando-Bataller, and J. Herranz-Herruzo, "Analysis of the coupled chassis-antenna modes in

mobile handsets," in *IEEE Antennas and Propagation Society Symposium, 2004.*, vol. 3. IEEE, 2004, pp. 2751–2754.

[168] P. Vainikainen, J. Ollikainen, O. Kivekas, and K. Kelander, "Resonator-based analysis of the combination of mobile handset antenna and chassis," *IEEE Transactions on Antennas and Propagation*, vol. 50, no. 10, pp. 1433–1444, 2002.

[169] E. Safin and D. Manteuffel, "Reconstruction of the characteristic modes on an antenna based on the radiated far field," *IEEE Transactions on Antennas and Propagation*, vol. 61, no. 6, pp. 2964–2971, 2013.

[170] Y. Park and Y. Sung, "A reconfigurable antenna for quad-band mobile handset applications," *IEEE Transactions on Antennas and Propagation*, vol. 60, no. 6, pp. 3003–3006, 2012.

[171] H. Li, Z. T. Miers, and B. K. Lau, "Design of orthogonal MIMO handset antennas based on characteristic mode manipulation at frequency bands below 1 Ghz," *IEEE Transactions on Antennas and Propagation*, vol. 62, no. 5, pp. 2756–2766, 2014.

[172] C. Deng, Z. Feng, and S. V. Hum, "MIMO mobile handset antenna merging characteristic modes for increased bandwidth," *IEEE Transactions on Antennas and Propagation*, vol. 64, no. 7, pp. 2660–2667, 2016.

[173] B. Sweetman, "Stealth aircraft-history, technology and outlook," in *ASME 1990 International Gas Turbine and Aeroengine Congress and Exposition*. Citeseer, 1990.

[174] W. Jiang, H. Ma, L. Yan, J. Wang, Y. Han, L. Zheng, and S. Qu, "A microwave absorption/transmission integrated sandwich structure based on composite corrugation channel: Design, fabrication and experiment," *Composite Structures*, vol. 229, p. 111425, 2019.

[175] S. U. Rahman, Q. Cao, I. Gil, M. Sajjad, and Y. Wang, "Design of wideband beamforming metasurface with alternate absorption," *IEEE access*, vol. 8, pp. 21 393–21 400, 2020.

[176] C. M. Watts, X. Liu, and W. J. Padilla, "Metamaterial electromagnetic wave absorbers," *Advanced materials*, vol. 24, no. 23, pp. OP98–OP120, 2012.

[177] Y. Liu and X. Zhao, "Perfect absorber metamaterial for designing low-RCS patch antenna," *IEEE Antennas and Wireless Propagation Letters*, vol. 13, pp. 1473–1476, 2014.

[178] T. Liu, X. Cao, J. Gao, Q. Zheng, W. Li, and H. Yang, "RCS reduction of waveguide slot antenna with metamaterial absorber," *IEEE Transactions on Antennas and Propagation*, vol. 61, no. 3, pp. 1479–1484, 2012.

[179] Y.-Q. Li, H. Zhang, Y.-Q. Fu, and N.-C. Yuan, "RCS reduction of ridged waveguide slot antenna array using EBG radar absorbing material," *IEEE Antennas and Wireless Propagation Letters*, vol. 7, pp. 473–476, 2008.

[180] W. Jiang, Y. Liu, S. Gong, and T. Hong, "Application of bionics in antenna radar cross section reduction," *IEEE Antennas and Wireless Propagation Letters*, vol. 8, pp. 1275–1278, 2009.

[181] W. Wang, S. Gong, X. Wang, Y. Guan, and W. Jiang, "Differential evolution algorithm and method of moments for the design of low-RCS antenna," *IEEE Antennas and Wireless Propagation Letters*, vol. 9, pp. 295–298, 2010.

[182] Y. Zhao, X.-y. Cao, J. Gao, and W.-q. Li, "Broadband RCS reduction and high gain waveguide slot antenna with orthogonal array of polarisation-dependent AMC," *Electronics letters*, vol. 49, no. 21, pp. 1312–1313, 2013.

[183] Y. Liu, Y. Hao, K. Li, and S. Gong, "Wideband and polarization-independent radar cross section reduction using holographic metasurface," *IEEE Antennas and Wireless Propagation Letters*, vol. 15, pp. 1028–1031, 2015.

[184] Y. Liu, K. Li, Y. Jia, Y. Hao, S. Gong, and Y. J. Guo, "Wideband rcs reduction of a slot array antenna using polarization conversion metasurfaces," *IEEE Transactions on Antennas and Propagation*, vol. 64, no. 1, pp. 326–331, 2015.

[185] B.-X. Wang, G.-Z. Wang, L.-L. Wang, and X. Zhai, "Design of a five-band terahertz absorber based on three nested split-ring resonators," *IEEE Photonics Technology Letters*, vol. 28, no. 3, pp. 307–310, 2015.

[186] Y. Cheng, H. Yang, Z. Cheng, and N. Wu, "Perfect metamaterial absorber based on a split-ring-cross resonator," *Applied Physics A*, vol. 102, no. 1, pp. 99–103, 2011.

[187] X. Q. Lin, P. Mei, P. C. Zhang, Z. Z. D. Chen, and Y. Fan, "Development of a resistor-loaded ultrawideband absorber with antenna reciprocity," *IEEE Transactions on Antennas and Propagation*, vol. 64, no. 11, pp. 4910–4913, 2016.

Related Publications

JCR indexed journals

- **C.R. Peñafiel-Ojeda**, R. Baez, V.G. Santos and C.E. Andrade, "An Ultrawideband Printed Monopole Antenna Analyzed with the Theory of Characteristic Modes," *IEEE Latin America Transactions*, TBD. 2021.

- **C.R. Peñafiel-Ojeda**, H. Giddens, M. Cabedo-Fabrès, M. Ferrando-Bataller, and Y. Hao, "Multi-Functional Metasurface Described by the Theory of Characteristic Modes," *Applied Physics Letters*, TBD. 2021.

Other journals

- A. Llanga-Vargas, M. Ferrando-Bataller, M. Cabedo-Fabrès, and **C.R. Peñafiel-Ojeda**, "Sistema de Agrupación de Antenas Definidas por Software de Bajo Costo, como Instrumento de Medida para Sistemas MIMO," *Revista NOVASINERGIA de la Universidad Nacional de Chimborazo*, vol. 2, no. 1, pp. 59–66, December 2018.

- **C.R. Peñafiel-Ojeda**, L. Carrera-Suárez, D. Navarro-Méndez, M. Baquero-Escudero, and M. Ferrando-Bataller, "Beamforming Networks for antenna array, useful in WiFi applications," *Revista NOVASINERGIA de la Universidad Nacional de Chimborazo*, vol. 1, no. 1, pp. 59–66, June 2018.

International conferences

- A. Llanga-Vargas, M. Cabedo-Fabrès, M. Ferrando-Bataller, and **C.R. Peñafiel-Ojeda** "Multiport broadband 5G MIMO antenna with very high isolation," in *Antennas and Propagation Society International Symposium, 2021 IEEE*, December 2021. (submitted)

- F. Toasa, **C.R. Peñafiel-Ojeda**, A. Llanga-Vargas, G. Cuzco, "Efficient Digital Beamforming for Bluetooth 5.1 using Software Defined Radio," in *The 5th International Conference on Telecommunications and Communication Engineering, 2021*, November 2021 (submitted)

- F. Toasa, L. Tello-Oquendo, **C.R. Peñafiel-Ojeda**, G. Cuzco, "Experimental Demonstration for Indoor Localization Based on AoA of Bluetooth 5.1 Using Software Defined Radio," in *2021 IEEE 18th Annual Consumer Communications & Networking Conference (CCNC), 2021 IEEE*, March 2021, pp. 1–4.

- **C.R. Peñafiel-Ojeda**, A. Llanga-Vargas, M. Cabedo-Fabrès, and M. Ferrando-Bataller, "Elliptical Disk Cavity Backed Antenna for UWB Systems," in *Antennas and Propagation Society International Symposium, 2019 IEEE*, July 2019, pp. 1–2.

- **C.R. Peñafiel-Ojeda**, M. Cabedo-Fabrès, E. Antonino-Daviu, and M. Ferrando-Bataller, "Air-Filled Substrate Integrate Waveguide Antenna Analyzed with Theory of Characteristic Modes," in *2019 13th European Conference on Antennas and Propagation (EuCAP)*. IEEE, 2019, pp. 1–5.

- **C.R. Peñafiel-Ojeda**, M. Cabedo-Fabrès, E. Antonino-Daviu, and M. Ferrando-Bataller, "Multi-Beam Wideband Antenna Useful in MIMO Applications," in *Antennas and Propagation Society International Symposium, 2018 IEEE*, July 2018, pp. 1–2.

- Z. Mahlaoui, E. Antonino-Daviu, A. Latif, , M. Ferrando-Bataller, and **C.R. Peñafiel-Ojeda**, "Frequency Reconfigurable Patch Antenna Using Pin Diodes with Directive and Fixed Radiation Pattern," in *2018 International Conference on Selected Topics in Mobile and Wireless Networking (MoWNeT)*. IEEE, 2018, pp. 1–3.

- **C.R. Peñafiel-Ojeda**, M. Cabedo-Fabrès, E. Antonino-Daviu, and M. Ferrando-Bataller, "Compact Antenna with Unidirectional Radiation Patterns," in *2018 12th European Conference on Antennas and Propagation (EuCAP)*. IEEE, 2018, pp. 1–5.

- **C.R. Peñafiel-Ojeda**, M. Cabedo-Fabrès, E. Antonino-Daviu, and M. Ferrando-Bataller, "Design of an Unidirectional UWB Cavity Backed Antenna," in *2017 IEEE MTT-S International Conference on Numerical Electromagnetic and Multiphysics Modeling and Optimization for RF, Microwave, and Terahertz Applications (NEMO)*. IEEE, 2017, pp. 28–30.

- **C.R. Peñafiel-Ojeda**, M. Cabedo-Fabrès, N.M. Mohamed-Hicho, and M. Ferrando-Bataller, "Design of a Low Profile Unidirectional UWB Antenna for Multi-service Base Station," in *2017 11th European Conference on Antennas and Propagation (EuCAP)*. IEEE, 2017, pp. 3575–3579.

National conferences

- G. Ramírez-Arroyave, **C.R. Peñafiel-Ojeda**, J. Araque-Quijano, M. Cabedo-Fabrès, J. Romeu, M. Ferrando-Bataller, L. Jofre, "Characteristic mode analysis of planar dual-port static and reconfigurable antennas," in *XXXIV Simposium Nacional de la Unión Científica Internacional de Radio*, Sep. 2019.

- A. Llanga-Vargas, **C.R. Peñafiel-Ojeda**, D. Santillán-Haro, M. Cabedo-Fabrès, E. Antonino-Daviu, M. Ferrando-Bataller, "Antenas para estaciones base 5G definidas por software," in *XXXIII Simposium Nacional de la Unión Científica Internacional de Radio*, Sep. 2018.

- **C.R. Peñafiel-Ojeda**, S. Rashid, M. Ferrando-Bataller, L. Jofre, M. Cabedo-Fabrès, J. Romeu, "Antena UWB de ranuras sobre cavidad cargada para radiación en el cuerpo humano," in *XXXII Simposium Nacional de la Unión Científica Internacional de Radio*, Sep. 2017.

- **C.R. Peñafiel-Ojeda**, E. Antonino-Daviu, M. Cabedo-Fabrès, M. Ferrando-Bataller, "Red formadora de haz para agrupación de antenas a 2.45 GHz," in *XXXI Simposium Nacional de la Unión Científica Internacional de Radio*, Sep. 2016.